Extreme Hydrological Events during the last 3500 years and their Changes in the Future

Inauguraldissertation

der Philosophisch–naturwissenschaftlichen Fakultät
der Universität Bern

vorgelegt von

Woon Mi Kim

von Seoul, Südkorea

Leiter der Arbeit:

Prof. Dr. Christoph C. Raible
Prof. Dr. Thomas F. Stocker

Abteilung für Klima– und Umweltphysik
Physikalisches Institut der Universität Bern

Bern, 29. Oktober 2021

Copyright Notice

Contents

Thesis summary

The Earth's climate has constantly varied over time due to the influence of internal processes and external factors. Together with the mean climate, spatial and temporal characteristics of extreme hydrological events, such as droughts and extreme precipitation, have also changed over time. For instance, droughts with multi-decadal duration, which have never been detected in the instrumental era, occurred during the Medieval climate anomaly (approximately 950–1200 CE) in North America and northern Europe. Devastating floods associated with heavy rainfall occurred more frequently during the Little Ice Age (about 1250–1850 CE) compared to other periods in the Common Era (the last 2k years) over Europe. These past extreme events significantly impacted the environment and ancient societies, sometimes influencing societal disruptions.

Despite their impacts on the environment and society, until now, less attention has been paid to the variations of past extreme hydrological events and their drivers compared to the variations in mean precipitation. Among many factors that hinder the investigations of past extreme hydrological events, the main problem arises from the limited availability of observations and past reconstructions for this kind of sporadic events.

Nowadays, complex climate models have become essential tools to examine the underlying dynamics of the Earth's climate. As these models can simulate the response of the climate to internal and external perturbations, they offer a possibility to address responsible drivers of climate variations and also extreme events on the global scale. In addition, simulations with climate models cover long time periods that can go far beyond the modern instrumental era. Hence, information from simulations can complement observations and reconstructions to illustrate better the characteristics of past droughts and extreme precipitation.

This thesis uses a state-of-the-art earth system model, the Community Earth System Model (CESM), as the main investigation tool to understand the variability and dynamics of past extreme hydrological events, namely droughts and extreme precipitation, during the past three millennia. It also aims to address the effects of an external factor, i.e., volcanic eruptions, on the climate and the impacts of past change in the climate on ancient European society. The thesis mainly consists of three studies.

The first study focuses on the dynamics of persistent Mediterranean droughts during 850–2099 CE. The Mediterranean region is one of the drought hot spots which is projected to experience an intensified drying by the end of the 21$^{\text{st}}$ century compared to the historical period. Hence, a more comprehensive understanding of the underlying mechanisms of past droughts over the region is necessary to better assess the changes of drought drivers in the historical and future period. In the study, temporal characteristics of Mediterranean droughts are assessed, and drivers of persistent long droughts are identified. In addition, the sensitivity of Mediterranean droughts to various drought metrics is tested.

The second study deals with daily extreme precipitation during the last three millennia previous to the Industrial Era (1501 BCE–1849 CE). The study is based on the newly conducted 3500-year long CESM simulations, which include a new proxy record of reconstructed volcanic eruptions. Internal and externally generated processes that influence the long-term variability of extreme precipitation are identified across the globe using a statistical method based on the extreme value theory. Among the externally generated processes, the impacts of volcanic eruptions on extreme precipitation are analyzed in more detail.

The third research topic concentrates on examining the impacts of the 43 BCE Okmok eruption in Alaska on the climate and early Mediterranean civilization. Abrupt large-scale changes of the Mediterranean climate after this large extratropical volcanic eruption are detected in various climate-related records, and the magnitudes of these changes are quantified with CESM. This change in climate is as a possible driver of the societal changes that occurred during the ancient Roman period.

Lastly, an outlook and a general conclusion of the thesis are presented, also proposing some potential follow-up investigations.

Chapter 1

Introduction

All life forms on the Earth are tightly connected to the climate and dependent on its variation over time. In the history of humankind, the climate has played a pivotal role in the advent of organized human civilizations, including their cultural and societal prosperity and decays (Hodell et al., 1995; DeMenocal, 2001; Büntgen et al., 2011; Xoplaki et al., 2016; McConnell et al., 2020). Some societal disruptions that are marked in history had followed after calamities caused by extreme climate events, such as extreme cold and wet periods, floods, and droughts (e.g., Peterson and Haug, 2005; Dugmore et al., 2012; McLeman et al., 2014; McConnell et al., 2020). Hence, the nature of the climate and extreme events and drivers of their changes have always been important subjects of study. In addition, the present-day rapid warming (IPCC, 2021) that shows an unprecedented rate of changes makes it more important than ever to better understand the long-term variability of the climate and its underlying physical mechanisms. This fact also holds true for extreme hydrological events whose their frequency and intensity are expected to vary in the future warmer climate (Trenberth et al., 2003; Donat et al., 2019; Cook et al., 2020a; Seneviratne et al., 2021).

Despite their devastating impacts on society, the long-term variability and past characteristics of extreme hydrological events, such as droughts and extreme precipitation, are less investigated than those of the mean climate. In the case of droughts, many studies related to the Common Era (the last 2k) are concentrated on the North American region (e.g., Cook et al., 2014; Coats et al., 2016b; Cook et al., 2016b). Investigations on past droughts, including their underlying mechanisms in other regions are still not fully explored. For instance, in Europe, one of the areas, which will be strongly affected by the intensification of droughts in the future is the Mediterranean sector (Seneviratne et al., 2021). Hence, more knowledge on the natural variability of Mediterranean droughts is required to better assess the contributions of anthropogenic changes.

For extreme precipitation, an understanding of its long-term variability and a global-scale analysis is clearly missing. In many cases, investigations on drivers of extreme precipitation cover the period starting from the mid-20th century. Same as droughts, extreme precipitation is changing in the present and is also expected to change more strongly in the future. Hence, understanding the pre-industrial extreme precipitation events will be necessary to quantify the present and future changes of extreme precipitation across the globe.

This lack of studies on droughts and extreme precipitation can be attributed to the limited availability of long proxy and documentary records across the globe for such intense and rare events. It is undeniable that there is a clear necessity for more research on extreme hydrological events using various available tools, for instance, complex climate models, to examine their nature from the past to the present, thereby, assessing their potential changes in the future.

This thesis investigates extreme hydrological events from the past three millennia to the future hundred years using an earth system model. In addition, the last part of the thesis (Chapter 5) deals with the influences of external processes on the past climate variation and early European societies. The main questions I aim to answer in this thesis are:

(i) How do extreme hydrological events (droughts and extreme precipitation) vary over time, and how are they influenced by external and internal processes of the climate system?
(ii) How does an external process influence the climate, and what was the implication of this influence on an ancient civilization in Europe?

Prior to introducing the research outcome, some necessary background concepts and definitions to understand the topics of the thesis are given in this chapter. In the first section, I briefly introduce the definitions of the climate and its related components, and processes that induce climate variations, such as external forcing, internal variability, and feedbacks. In the following sections, I provide details on the overarching topics of this thesis which are on extreme hydrological events. The definitions of extreme hydrological events and temporal variations of these events during the study period are introduced. Finally, in the last section, a brief description of complex climate models and climate simulations are elaborated.

1.1 The Earth's climate system and its components

Climate can be defined as average weather in terms of its mean and variability for a certain period and a certain location (Baede et al., 2001). At the same time, the climate is a mean state of the climate system, a global system that is composed of five major components: the atmosphere, which is a layer of gases surrounding the Earth, the hydrosphere, which consists of all liquid water, the cryosphere, which is all solid water, the lithosphere, the solid outer part of the Earth, and the biosphere, which encompasses all living things and their interactions. A small portion of the atmosphere is composed of the trace gases such as CO_2, CH_4 and N_2O occupying 0.1% of the atmospheric composition, and water vapor with a varying proportion from 1 to 4% depending on the air temperature. These gases play crucial roles in the Earth's energy budget by absorbing and emitting radiation. They absorb a part of the infrared radiation emitted by the Earth and radiate it back to the surface increasing the surface temperature. This process of retaining thermal radiation is known as the greenhouse effect, an essential phenomenon for the maintenance of the habitable temperature in our planet with a mean value of roughly 15°C.

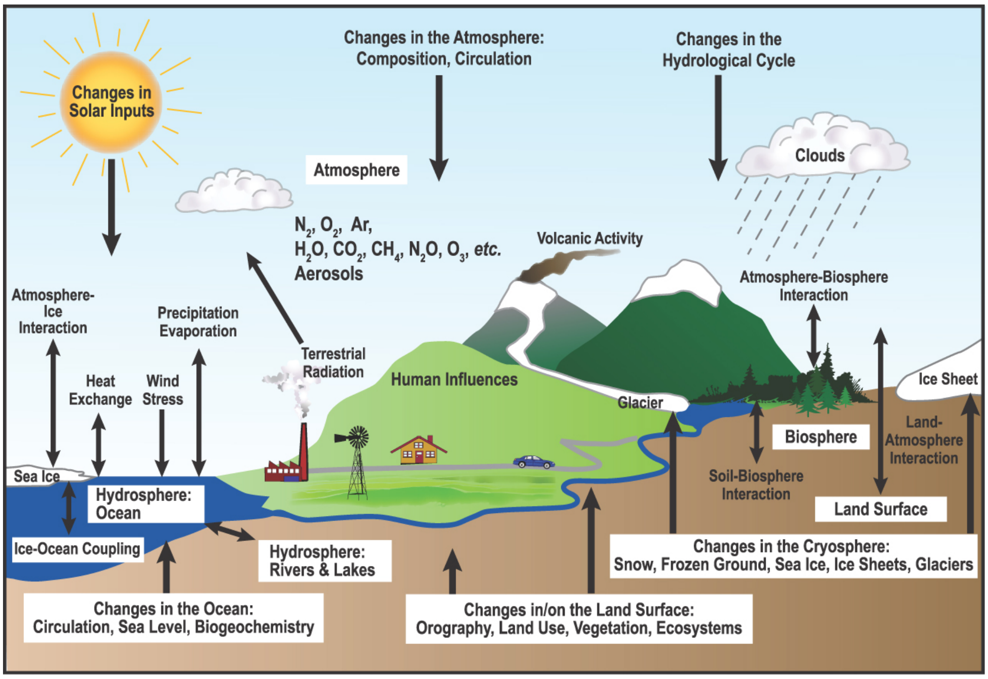

Figure 1.1: Component of the climate system and interactions among them. Figure retrieved from Baede et al. (2001).

All the components of the climate system constantly interact with each other exchanging energy and masses using the incoming solar radiation as an input energy (Fig. 1.1). One of these interactions leads to the hydrological cycle, a complex global cycle that allows exchanges of water masses among the climate components (Trenberth et al., 2007; Rodell et al., 2015; Douville et al., 2021). The Earth's hydrological cycle is the continuous movement of water masses within the climate system (Fig. 1.2) that can be simplified as follows: water is evaporated from oceans (with estimated mean annual fluxes of 449,400 ± 22,200 $\text{km}^3\ \text{yr}^{-1}$ for 2000–2010 CE) and land (70,600 ± 5000 $\text{km}^3\ \text{yr}^{-1}$), then transported to the atmosphere to be condensed and forms clouds. When the upper atmosphere reaches saturation levels, precipitation falls to oceans (403,500 ± 22,200 $\text{km}^3\ \text{yr}^{-1}$) and land (116,500 ± 5,100 $\text{km}^3\ \text{yr}^{-1}$). Excess precipitation over land runs off to streams and rivers, in which subsequently flow to oceans (45,900 ± 4,400 $\text{km}^3\ \text{yr}^{-1}$). Also during the cycle, water masses are stored in liquid forms in oceans and land, as snow and glaciers on land, and as water vapor and clouds in the atmosphere. An illustration of the hydrological cycle with its estimated mean annual fluxes for 2000-2010 CE is presented in Fig. 1.2 (Rodell et al., 2015). In addition, nutrients and minerals over land and oceans are redistributed with the movement of water masses.

Another importance of the hydrological cycle is also related to the roles of involved water masses in atmospheric circulations and the Earth's energy budget (Douville et al., 2021). Throughout the hydrological cycle, water continuously releases latent heat fluxes by condensation and evaporation. These latent heat fluxes are the key drivers of atmospheric circulations on various temporal and spatial scales. In addition, water vapor transported to the upper atmosphere is an important greenhouse gas that directly influences the Earth's radiative budget.

Due to the constant interactions among the components and external influences, the Earth's climate always changes and never stays at its mean equilibrium temperature of 15°C (Baede et al., 2001). It presents variations on several time scales from seasons to millennia and even longer, and these climate variations are termed climate change.

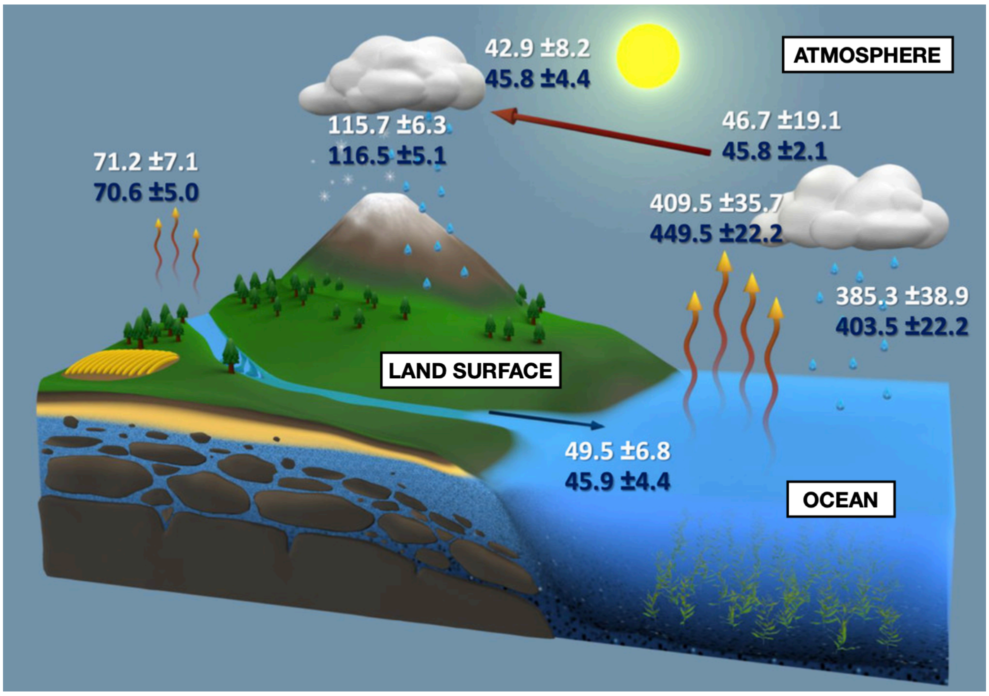

Figure 1.2: A schematic of the global hydrological cycle with its estimated mean annual fluxes for 2000-2010 CE. The unit of the fluxes is in 10^3 km^3 yr^{-1}. Figure adapted from Rodell et al. (2015).

1.2 Perturbations in the climate system

Climate variations take place on various time scales and are caused by processes that perturb the Earth's radiative balance (Baede et al., 2001; Gulev et al., 2021). Such processes can originate externally from the climate system and internally from interactions among the climate components. The former is known as external forcing, and the latter is internal variability. There are also secondary processes called feedbacks that can amplify or diminish the initial perturbations in the climate system.

The net change in the Earth's radiative balance due to some perturbations introduced in the climate system is referred to as radiative forcing (RF; Myhre et al., 2013). More specifically, RF is defined as the change in net downward radiative fluxes after allowing an equilibrium in stratospheric temperatures while fixing tropospheric temperatures, water vapor, and cloud cover at the unperturbed values. RF is positive when the change in net incoming radiation is positive, and vice versa for negative RF. The response of the climate to RF can be expressed through a change in the global mean surface temperature at the equilibrium state (ΔT), which can be simplified as:

$$\Delta T = \lambda RF \tag{1.1}$$

where λ is the climate sensitivity parameter whose value varies across different RF agents. The relationship indicates that the global mean surface temperature (ΔT) response to a given RF depends on the RF and the responses inherent in λ (Myhre et al., 2013). The climate response to a RF is by warming up (positive ΔT) and cooling down (negative ΔT) the Earth's surface. The RF estimated for different agents are shown in Fig. 1.3.

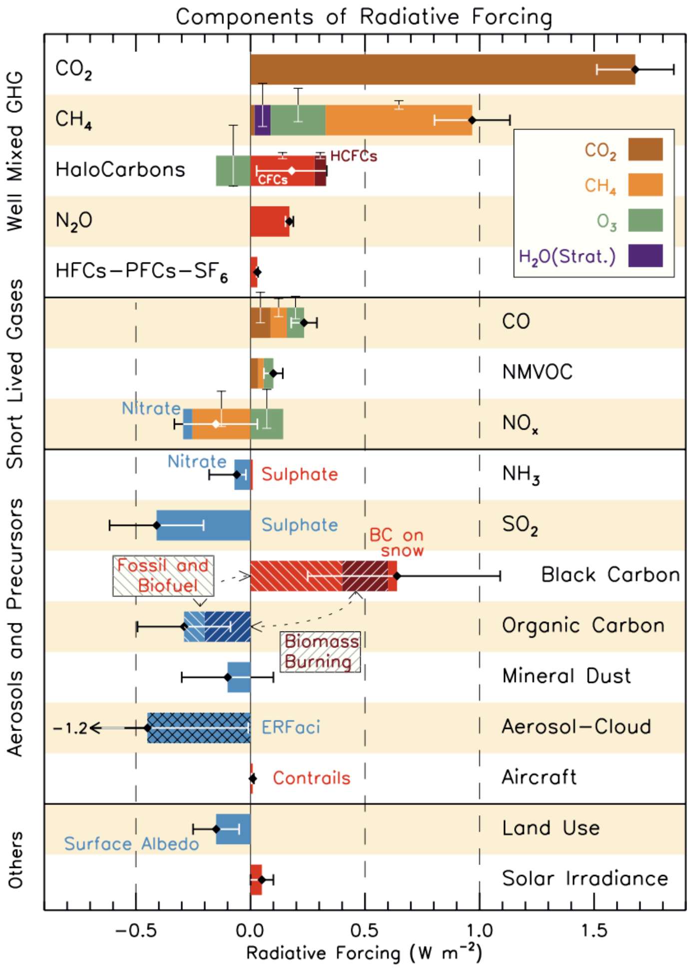

Figure 1.3: RF for different agents from 1750 to 2005 CE. Black lines indicate the range of uncertainties in the estimation. Figure retrieved from Myhre et al. (2013).

External forcing

RF can have natural or anthropogenic origins. All processes that drive *RF* are termed external forcing. Naturally originated external forcings are the changes in the orbital parameters and solar irradiance, and volcanic eruptions.

- The changes in the orbital parameters are influential on the climate on time scales of millennia and longer (Berger, 1988; Paillard, 2010). Hence, changes in radiative balance driven by this forcing are hard to be detected in the instrumental era. From the mid- to late-Holocene, the changes in the orbital parameters have progressively decreased the Earth's mean surface temperature (Wanner et al., 2008; Bader et al., 2020).

- Solar forcing operates on various time scales (Myhre et al., 2013; Gulev et al., 2021). Similar to the orbital forcing, solar forcing presents variations on millennia and longer related to astronomical alignments, and on relatively shorter time scales from decadal, given by its 11-year cycle, to centennial. The amplitudes of the 11-year solar cycle range between 0.5 and 2 W m^{-2} (Muscheler et al., 2007; Fröhlich, 2009). During the last millennium, there was an extended period with relatively low solar activities between 1250 and 1850 CE, later named as the Little Ice Age (LIA; e.g., Pfister and Brázdil, 2006; Camenisch et al., 2016), During the LIA, some of the most notable reductions in solar activities occurred with the Maunder Minimum (1645–1715 CE; Shindell et al., 2001) and Dalton Minimum (1790–1830 CE; Wagner and Zorita, 2005), among others. There was also a period with relatively high solar activities around 950–1200 CE known as the Medieval Warm Anomaly (MCA; e.g., Mann et al., 2009; Goosse et al., 2012). During the LIA, reduced regional temperatures and cold winters were documented, while opposite warm conditions prevailed during the MCA in many regions of the Northern Hemisphere (Fig. 1.4). The overall *RF* due to the changes in TSI for the period 1750–2011 CE is estimated at 0.05-0.10 W m^{-2} (Myhre et al., 2013).

- Among natural external forcings, volcanic forcing imposes more perceivable short-term impacts on the climate (Robock, 2000). Large volcanic eruptions inject a substantial amount of SO_2 aerosols into the stratosphere. These aerosols that can reside at least a year in the tropical or a few months in the extratropical stratosphere scatter the incoming solar radiation and reduce the amount of radiation that can reach the Earth's surface. Therefore, the global mean surface temperature is decreased. The volcanic forcing shows annual to multi-decadal variability, although the occurrences of the events are rather sporadic compared to the previous two forcings. The driver of the Northern Hemispheric cooling during the LIA was not only the decrease in solar activities but also the frequent volcanic eruptions occurred during the same period (Wagner and Zorita, 2005; Miller et al., 2012). The aerosol *RF* of the 1991 Pinatubo eruption was stronger than –6 W m^{-2} (Stenchikov et al., 1998), while during the period with several smaller eruptions in 2008–2011 CE the *RF* was –0.11 W m^{-2} (Myhre et al., 2013)

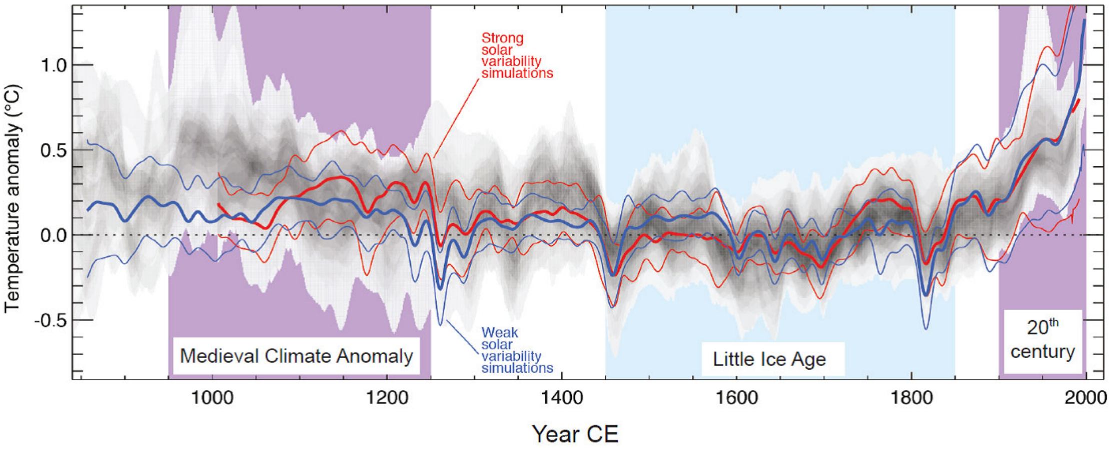

Figure 1.4: Comparison of simulated (color lines) and proxy-based reconstructed (grey shaded) Northern Hemisphere mean temperature changes relative to their 1500–1850 means and smoothed with a 30-year filter. Red lines are from models forced by stronger solar variability and blue lines are from models forced by weaker solar variability. Thick colored lines are the means of multiple models and thin lines indicate the 90% confidence ranges of these means. Figure retrieved from `https://www.ncdc.noaa.gov/global-warming/last-1000-years`, which is adapted from Pachauri et al. (2014).

The most important long-term radiative imbalance originate from human activities through the changes in land use and land covers, and in the composition of gases in the atmosphere.

- Changes in land use and land cover (LULC) alter the surface radiative balance mainly through the changes in surface albedo (Gulev et al., 2021). LULC has already been detected since the 17th century with the expansion of agricultural activities (Pongratz et al., 2008; Hurtt et al., 2011), although with relatively small impacts on the global scale until the 19th century (Gulev et al., 2021). Since then, deforestation and agricultural lands have substantially expanded. In 1980 CE, 60% of all land cover changes were associated with human activities. The LULC has imposed *RF* of –0.15 W m^{-2} for 1700–2019 CE, which resulted in a global cooling of 0.1°C since 1750 CE.

- Human activities have changed the composition of the atmospheric gases (Gulev et al., 2021). The concentrations of the gases that induce the greenhouse effect, the so-called greenhouse gases (GHGs), have substantially increased since the Industrial Era. In addition, some new GHGs of a purely anthropogenic origin, the halogenated gases (CFCs, HCFCs, HFCs, PFCs, and SF6), were inserted into the atmosphere in the 20th century. The annual CO_2 concentration has increased globally from 278 ± 2 ppm in 1750 CE to 409.9 ± 0.4 ppm in 2019 CE. This concentration is the highest value of CO_2 since the last 800,000 years. For CH_4, the increase for the same period is from 722 ± 25 ppb to 1866 ± 3.3 ppb, and for N_2O, it is from 270 ± 7 to 332.1 ± 0.4 ppb. The combined *RF* imposed by these three GHGs from 1750 to 2019 CE is 2.9 ± 0.5 W m^{-2}. For the halogenated GHGs, although their *RF* has increased 3.5% compared to 2011 CE, the total amount of these gases has significantly decreased by a factor of seven in 2019 CE compared to 1970–1980 CE. The total *RF* of the halogenated GHGs are 0.41 ±

0.07 W m^{-2} until 2019 CE. These increases in GHGs intensify the greenhouse effect, hence, causing an overall warming of the troposphere. This warming, in turn, leads to an increase in water vapor, which is another strong GHG that can amplify even more the ongoing warming through water vapor feedback (Forster et al., 2021).

Internal variability

Besides external forcing, there are internal processes in the climate system that perturb the climate even in the absence of external forcing called internal variability. These processes arise from the non-linear dynamical mechanisms intrinsic in each climate component and coupling between them, for example, the coupling of the ocean-atmosphere system (Baede et al., 2001; Deser et al., 2012). The processes of internal variability operate on various time scales. For instance, internal variability in the atmosphere presents short-term variability related to the memory of the atmosphere that goes hardly beyond a few weeks, and the long-term variability that arises from the processes of coupled ocean-atmosphere via dynamic and thermodynamic interactions.

The complex non-linear interactions among the climate components complicate the predictability of the climate on interannual to decadal time scales and the assessment of influences of external forcing on the climate (Deser et al., 2012). Distinguishing the influences of external forcing and internal variability is a key task for a proper assessment of drivers of climate variations and extreme climate events. One way to achieve this task is by employing climate models to simulate a climate under a certain condition, for instance, with a fixed external forcing and with a time-varying forcing. Then, statistical tests should be applied to these climate simulations under the hypothesis that detected differences arise solely due to internal variability or external forcing.

Processes of internal variability can also cause regular fluctuations of the climate leading to recurrent spatial climate patterns known as modes of variability (Phillips et al., 2014). Some of the modes are El Niño-Southern Oscillation (ENSO) that involves a complex coupling between the atmosphere and ocean over the tropical equatorial Pacific (Rasmusson and Wallace, 1983), and the Pacific Decadal Oscillation (PDO), which occurs over the north Pacific influenced by wind-driven ocean-gyre fluctuations (Trenberth and Hurrell, 1994; Mantua and Hare, 2002). Besides ENSO and PDO, other modes, that are used for the studies in this thesis (Chapters 3 and 4), include the Northern Annular Mode (NAM) in the Northern Hemisphere (Thompson and Wallace, 2000), the Southern Annular Mode (SAM) in the Southern Hemisphere (Marshall, 2003), the North Atlantic Oscillation (NAO; Wallace and Gutzler, 1981; Wanner et al., 2001), the East Atlantic-West Russia (EA-WR; Barnston and Livezey, 1987; Washington et al., 2000), Pacific South American-1 (PSA; Mo and Paegle, 2001; Irving and Simmonds, 2016), and the Pacific North American (PNA; Wallace and Gutzler, 1981; Leathers and Palecki, 1992) patterns.

- ENSO is one of the most important modes of variability that affects temperature and precipitation across the globe through teleconnection mechanisms (Dai and Wigley, 2000). It occurs in the tropical Equatorial Pacific with recurrent fluctuations in the atmosphere and oceans. The atmospheric branch of ENSO is known as Southern Oscillation which is expressed by an alternation of sea level pressure anomalies between Darwin in Australia and Tahiti. The ocean branch is associated with a positive-negative alternation of sea surface temperature anomalies (SSTA) over the tropical equatorial Pacific. When the positive SSTA persists above a certain threshold for a certain period (Trenberth and Stepaniak, 2001), the event is called El Niño. The negative SSTA belongs to La Ninña event, and the SSTA state between El Niño and La Ninña to a neutral state. The large-scale atmospheric meridional circulation associated with ENSO over the equatorial Pacific is the Walker circulation characterized by a rising motion over the western Pacific and a subsidence over the eastern Pacific (Wang, 2004). ENSO presents an interphase fluctuation of 3 to 7 years, although it also exhibits interseasonal and interannual variability.

- PDO is known as a long-lived El Niño-like pattern that occurs over the North Pacific basin. The positive PDO is associated with negative SSTA in central and western North Pacific and positive SSTA in the eastern North Pacific. The opposite SSTA condition corresponds to the negative PDO. PDO strongly influences the climate over the north Pacific Sector, and it presents a recurrence of one to few decades.

- NAM (also known as Arctic Oscillation) is a hemispheric-scale pattern characterized by an increase in the pressure gradient between the mid-latitudes and polar regions. It is the leading mode of variability in the Northern Hemispheric (NH) mid-high latitudes. NAM influences the positions of the stormtracks and associated weather systems. The positive phase of NAM (with relatively reduced pressures in polar regions) is associated with poleward displacement and increased zonality of the stormtrack, and the negative phase (with relatively higher pressures in polar regions) with more southward displacement and meridional expansion of stormtrack. NAM presents seasonal to annual variability.

- SAM (also known as Antarctic Oscillation) is an analog to NAM in the Southern Hemisphere (SH) and is the leading mode of variability in the SH mid-high latitudes. It represents the fluctuations of pressures between Antarctica and mid-latitudes. The positive phase of SAM occurs when the pressure anomalies in Antarctica are lower than the pressure anomalies at the mid-latitudes and vice versa for the negative phase. The phases of SAM are associated with the contraction of the westerly wind belts at the mid-latitudes toward poles (positive phase) and the expansion toward the north (negative phase). In general, SAM presents a variation of a few weeks to months.

- NAO is a regional expression of NAM with dominance over the North Atlantic and European sector. It is associated with the fluctuations of pressures between the subtropical high system near the Azores and the subpolar low system near Iceland. During the positive NAO, the pressure gradient between the subtropical high system and subpolar low system is relatively high and vice versa during the negative NAO. It is the most important leading mode of variability in the North Atlantic and European domain, influencing the displacement and expansion of low-pressure systems and stormtrack. More poleward displacement of stormtrack occurs during the positive NAO. In general, NAO presents a seasonal to annual variability.

- EA-WR is a zonally extended pressure pattern occurring over Eurasia and one of the leading modes in Europe and Asia. The positive phase of EA-WR is associated with positive geopotential height anomalies in Europe and northern China, and negative geopotential height anomalies in central North Atlantic and north of the Caspian Sea. The pattern influences temperature and precipitation mostly in Eurasia, but it also shows connections to precipitation in North America (Lim, 2015) and Amazon (Gonsamo et al., 2015).

- PNA is the second dominant mode of variability in the NH mid-to-high latitudes following the NAM, and it represents a wave train pattern that extends along the mid-high latitudes. The positive PNA shows high geopotential height anomalies around Hawaii and in western North America, and low geopotential height anomalies in the south of Aleutian Islands and the southeastern United States. It largely influences the climate in North America and presents a week to seasonal variability.

- PSA is an analog to PNA over the SH, and it is a large-scale pattern that explains the most variance in the mid-high latitudes following the SAM. The wave train of PSA extends from the central Pacific Ocean to the Amundsen and Weddell Seas. During the positive PSA, positive centers of geopotential height anomalies are located over the Weddell Sea and southern Indian ocean, and negative geopotential height anomalies are in between the positive anomalies. PSA affects the SST over the central and eastern Pacific and strongly influences South American and Antarctic climates.

Feedbacks

Feedbacks are processes that can amplify or diminish the response of the climate to a perturbation introduced by an internal variability or external forcing (Baede et al., 2001; Forster et al., 2021). When a feedback process takes place, the response of the climate is non-linear, hence, it does not scale with the amplitude of the introduced perturbation. Mathematically, feedbacks are quantified as changes in the net energy budget at the top of the atmosphere (TOA) due to a change in the global surface air temperature (Forster et al., 2021). When the response is amplified, the feedback is positive, and when the response is diminished, the feedback is negative. Numerous feedbacks occur within the climate system. Among them, two important examples of feedback processes are the water vapor and lapse rate feedbacks.

The water vapor feedback is a positive feedback that occurs when the net radiation changes due to the changes in the atmospheric water content (Forster et al., 2021). The mechanism functions as follows: when a surface air temperature is increased, the concentration of water vapor in the upper troposphere is also increased. More water vapor, which is a strong GHG, absorbs more incoming and outgoing radiation, leading in turn to an increase in the surface air temperature.

The lapse rate feedback is related to the radiative change initiated by a non-uniform change in the vertical temperature profile in the troposphere (Forster et al., 2021). Over the tropics, the mean vertical temperature profile closely follows a moist adiabatic lapse rate of roughly 5 K km^{-1}, with the lower troposphere warmer than the upper troposphere. If the warming increases in the upper troposphere, for instance, caused by the increase in GHGs, the lapse rate changes, and more long-wave radiation is emitted from the upper troposphere to the space. More emitted radiation induces a decrease in the surface air temperature. The process is a negative feedback that diminishes the initial radiative condition. The situation is opposite at mid-to-high latitudes, where strong temperature inversions occur in winter in the lower troposphere. Enhanced warming is expected in the lower troposphere than the upper troposphere leading to a positive lapse rate feedback.

Additional feedbacks that are relevant to the topic of the thesis and take place on the land surface are the feedback processes that arise from the coupling between the atmosphere and land surface (Seneviratne et al., 2010). These are the feedbacks that are involved during the soil moisture - temperature interaction and the soil moisture - precipitation interaction (Fig. 1.5). The mechanisms are explained as follows:

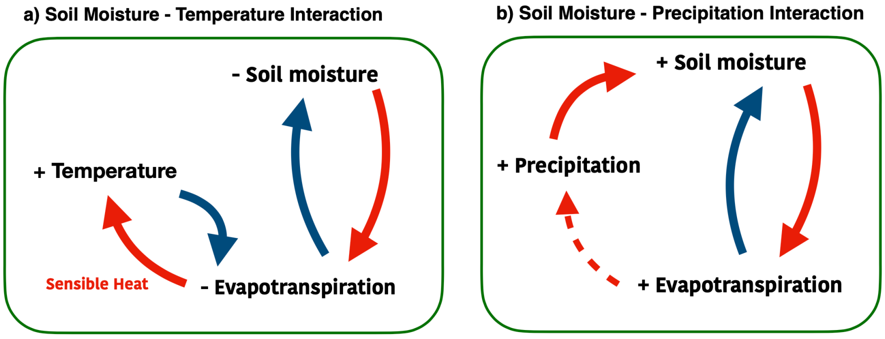

Figure 1.5: Feedback processes involved during the atmosphere-land surface interaction: (a) soil moisture - temperature, and (b) soil moisture - precipitation. Red arrows indicate positive feedbacks that intensify, and blue arrows indicate negative feedbacks that weaken the initial conditions. Dotted arrow denotes a possible feedback but with large uncertainties. Figure adapted from Seneviratne et al. (2010).

In the soil moisture - temperature interaction (Fig. 1.5a), a dry condition with a low soil moisture level leads to a decrease in evapotranspiration which causes an increase in sensible heat flux. In turn, more sensible heat flux leads to an increase in surface air temperature. High temperature increases evapotranspiration, although the magnitude of the increase is limited by the already depleted soil moisture. Then, more evapotranspiration induces a subsequent loss of soil moisture. This mechanism that amplifies the initial loss of soil moisture will continue until the soil is completely dried out if no other factor breaks the interaction.

In the soil moisture - precipitation interaction (Fig. 1.5b), an increase in precipitation leads to an increase in soil moisture, which subsequently increases evapotranspiration. There is also a potential negative feedback involved during this process as an increase in evapotranspiration leads to a reduction in soil moisture. Then, more evapotranspiration will potentially increase precipitation. However, the positive link between evapotranspiration and precipitation are uncertain as physical processes related to this coupling is more complex and still not fully understood (Seneviratne et al., 2010). Some studies have shown that the positive coupling is valid only under specific conditions and depends on the region. Nevertheless, a large number of observational and model-based studies have supported the positive association of the evapotranspiration-precipitation coupling with varying magnitudes of strength (refer to the literature mentioned in Seneviratne et al. (2010)).

1.3 Extreme hydrological events

Extreme events are phenomena whose frequencies and intensities depart from their mean normal values (Coles et al., 2001). From a statistical perspective, these events are located at the tails of probability distributions, either at the upper or at the lower tail. The thresholds for the upper and lower tails are defined based on the percentiles, such as the 90^{th} percentile or above for the upper tail, and the 10^{th} percentile or below for the lower tail. In other words, the occurrence of such events is relatively low. The term extreme “weather” event defines the phenomena themselves, and the term extreme “climate” event describes the overall characteristics of a number of extreme weather events as a whole over a certain period. In general, extreme events occur temporarily for a short time period compared to the mean climate fluctuation, and spatially on the regional scales, although in some cases they can expand to continental scales.

Two extreme climate events that are investigated in this thesis are droughts and extreme daily precipitation. For droughts, the study period is from 850 to 2099 CE with a spatial focus on the west-central Mediterranean (Chapter 3). The work aims to understand the variability and underlying mechanisms of persistent droughts over the region. For extreme precipitation, the study concentrates on the long-term variability of the events across the globe during the last 3500 years before the Industrial Era (1501BCE – 1849 CE; Chapter 4). In addition, the associations of external forcing and internal variability with extreme precipitation are statistically examined. This section introduces the definitions and methods to quantify and analyze these two types of extreme hydrological events.

1.3.1 Droughts

Drought is an extreme hydrological event characterized by a prolonged period of negative water balance in the environment relative to normal conditions (Mishra and Singh, 2010; Dai, 2011).

The event is characterized by its slow development, which makes its impacts less perceivable during the initial stage of the event. The socio-economic impacts of drought become more severe with the duration of drought, and the implicated damages are more perceivable when the event is already intensified. Droughts detected in the present day have a typical duration of a few weeks to several years. However, reconstructions from tree rings indicate the existence of some past droughts with decadal to multi-decadal duration in North America (Cook et al., 2010b) and northern Europe (Helama et al., 2009) during the last millennium.

Traditionally droughts are classified into four types (Mishra and Singh, 2010):
(i) Meteorological drought, which is identified by a reduction of precipitation relative to its normal value. In many cases, meteorological drought is the cause of other types of droughts.
(ii) Agricultural or soil moisture drought, which is characterized by a depletion of soil moisture, and as its name indicates, is a type of drought that impacts crops and plant ecosystems. During agricultural drought, the state of soil cannot fulfill the water demand required for the normal growth of vegetation. Agricultural drought is not only caused by a decrease in precipitation but also by excessive evapotranspiration from the surface and plants.
(iii) Hydrological drought is the period when available water in natural reservoirs, such as lakes, aquifers, and rivers, is reduced. It can be caused by a meteorological drought, but the geology of a region is another important factor that drives this type of drought.
(iv) Lastly, socio-economic drought, which occurs when the availability of water resources cannot meet the demand of society and the impacts of the water shortage become perceivable by society. This type of drought can be caused by a natural propagation from other types of drought, but also by poor infrastructure and bad management to distribute and control the available water resources.

Besides these traditionally defined four types of drought, a new type is added, which is groundwater drought (Mishra and Singh, 2010). Groundwater drought is defined as a period with a depletion of groundwater level. It also can be defined as a period with a decrease in recharge and discharge of groundwater. Usually, it results from other types of droughts when their effects are propagated to the underground system, which can take from a month to several years. Until now, few studies have been conducted on groundwater drought compared to other types of drought (e.g., Peters et al., 2006; Bloomfield et al., 2019). This can partially be attributed to the difficulty of quantifying the total amount of available groundwater storage.

Knowing the exact causes either of initiation or intensification of droughts is a difficult task for several reasons. First, slow developments of droughts make it difficult to determine the exact initiation of the events, hence, complicating the assessment of initial drivers (Dai, 2011). Second, drought is a multivariate phenomenon that many physical and biological processes are superposed (Cook et al., 2018). Therefore, it is difficult to attribute only to one or a few specific factors as causal drivers. In addition, when a long dry period persists, different types of drought can be connected to each other (Mo, 2008). For instance, meteorological droughts are often the cause of other droughts (Wang et al., 2016). Distinguishing one drought type from others becomes difficult when various droughts are connected as well as separating drivers of each type of drought.

These complexities make droughts impossible to be quantified using one universal metric (Lloyd-Hughes, 2014). Various drought indices exist and each index catches certain aspects of droughts (Mishra and Singh, 2010; Dai, 2011; Raible et al., 2017; Mukherjee et al., 2018). The choice of the drought index depends on the research question to deal with. Drought indices that were employed in this thesis are the Self Calibrated Palmer Drought Severity Index (scPDSI; Wells et al., 2004), Standardized Precipitation Index (SPI; McKee et al., 1993), and Standardized Precipitation Evapotranspiration Index (SPEI; Vicente-Serrano et al., 2009) which are explained below:

- scPDSI is a modified version of Palmer Drought Severity Index (Palmer, 1965). The estimation relies on a two-layer soil model where the upper layer can hold a inch (2.54 cm) of soil moisture (Wells et al., 2004). Precipitation P is required in the initial step, then other involved variables related to water balance such as actual evapotranspiration ET, recharge to the soils R, runoff RO, moisture loss L including their potential values, are produced within the model. The potential evapotranspiration PET for the scPDSI is estimated following Eq. 1.13.

  To calculate the scPDSI, first, the Climatically Appropriate For Existing Conditions (CAFEC) precipitation $\hat{P}$ that represents the amount of necessary precipitation to maintain a normal soil moisture level is estimated:

  $$\hat{P} = \alpha_i PET + \beta_i PR + \gamma_i PRO - \delta_i PL \tag{1.2}$$

  where PR, PRO, PL are the time series of potential recharge, potential runoff, and potential loss, respectively. α_i, β_i, γ_i, and δ_i are the weighting coefficients for the potential values for each month i with $i = 1, ..., 12$. These coefficients are calculated as the ratio between the multi-year monthly averages of actual and potential values of the water balance variables during the chosen calibration period (Eq. 1.3):

  $$\begin{aligned} \alpha_i &= \frac{\overline{ET_i}}{\overline{PET_i}} \quad \beta_i = \frac{\overline{R_i}}{\overline{PR_i}} \\ \gamma_i &= \frac{\overline{RO_i}}{\overline{PRO_i}} \quad \delta_i = \frac{\overline{L_i}}{\overline{PL_i}} \end{aligned} \tag{1.3}$$

  The moisture departure d is estimated as a difference between the actual precipitation P and CAFEC precipitation $\hat{P}$ as $d = P - \hat{P}$. Then, the weighting coefficient for d, K that varies with the climate of the site is introduced, first by defining K".

  $$K" = 1.5^{10} \log[(\frac{\overline{PET} + \overline{R} + \overline{RO}}{\overline{P} + \overline{L}} + 2.8)/\overline{D}] + 0.5 \tag{1.4}$$

  where $\overline{D}$ is an average of d over the calibration period. Then, K is calculated by weighting K" by a certain factor that makes the percentage of months classified as scPDSI ≤ -4 or scPDSI ≥ 4 as 2% over the calibration period (Wells et al., 2004; Van der Schrier et al., 2011).

The moisture anomaly index or the Z index is obtained as:

$$Z = dK \tag{1.5}$$

The Z index is also often used as a metric to quantify departures from a mean hydroclimate condition. Finally, the scPDSI at time j, X_j, is derived by considering the moisture condition of the preceding month X_{j-1} as:

$$X_j = pX_{j-1} + qZ_j \tag{1.6}$$

where p and q are the duration factors that arise from a linear relationship between the summation of the Z index values and a current scPDSI value (Wells et al., 2004). The values of the duration factors vary with the sites.

The scPDSI has an inherent time scale that ranges from 9 to 14 months depending on the region (Vicente-Serrano et al., 2010, 2015). Therefore, it is an index for droughts with relatively long duration, ideally for agricultural droughts.

- SPI is a normalized drought metric that only requires a long-term precipitation record, ideally at least of 30 years (McKee et al., 1993; Wu et al., 2005), as an input. In other words, it quantifies meteorological drought. The estimation is based on a probabilistic approach that a time series of monthly precipitation is modeled using different statistical distributions (Lloyd-Hughes and Saunders, 2002).

  One commonly used distribution for precipitation records, also used in this thesis, is the gamma distribution. The cumulative probability distribution $G(x)$ according to the gamma distribution is given as:

$$G(x) = \frac{1}{\beta^{\alpha}\Gamma(\alpha)} \int_0^x x^{\alpha} e^{-x/\beta} dx \tag{1.7}$$

  where x is the precipitation record, α is the shape parameter, and β is the scale parameter. Γ is the gamma function which is expressed as:

$$\Gamma(\alpha) = \int_0^{\infty} x^{\alpha-1} e^{-x} dx \tag{1.8}$$

  Fitting the gamma distribution to precipitation over a calibration period requires proper estimation of α and β. For the estimation, an approximated maximum likelihood method proposed by Thom (1958) is usually used. Since the gamma distribution is undefined for $x = 0$, the cumulative probability needs to be modified to:

$$H(x) = q + (1 - q)G(x) \tag{1.9}$$

where $q = P(x = 0)$ is the probability of zero precipitation with $q > 0$. The $H(x)$ is then converted to a standard normal distribution which results in the final SPI. In general, for the conversion, an approximation given by Abramowitz and Stegun (1965) is used:

$$SPI = \begin{cases} -(t - \frac{c_0+c_1t+c_2t^2}{1+d_1t+d_2t^2+d_3t^3}) & 0 < H(x) \leq 0.5 \\ +(t - \frac{c_0+c_1t+c_2t^2}{1+d_1t+d_2t^2+d_3t^3}) & 0.5 < H(x) < 1 \end{cases} \tag{1.10}$$

where c_0 = 2.51517, c_1 = 0.802853, c_2 = 0.010328, d_1 = 1.432788, d_2 = 0.189269, and d_3 = 0.001308. The t is given as:

$$t = \begin{cases} \sqrt{\ln[\frac{1}{H(x)^2}]} & 0 < H(x) \leq 0.5 \\ \sqrt{\ln[\frac{1}{(1-H(x))^2}]} & 0.5 < H(x) < 1 \end{cases} \tag{1.11}$$

The computation of SPI is much simpler than scPDSI, and the index is more flexible in terms of time scales allowing the estimation on various time ranges by aggregating precipitation of several months. However, as it only considers precipitation to identify meteorological droughts, it is not appropriate for droughts that are driven by vapor pressure deficit (VPD) caused by an increase in temperature. VPD-driven droughts are the cases of many present-day droughts (Mukherjee et al., 2018).

- SPEI follows the same calculation steps of SPI, but instead of considering only a precipitation record, it uses a record of the water balance b given as the difference between precipitation and PET (Eq. 1.13). Hence, SPEI quantifies agricultural drought. The water balance b is modeled using a log-logistic distribution, then similarly to SPI, transformed to a normal distribution. The probability distribution function according to the log-logistic distribution is:

  $$F(b) = [1 + (\frac{\alpha}{b - \gamma})^{\beta}]^{-1} \tag{1.12}$$

  where α, β, and γ are the scale, shape, and origin parameters of the log-logistic distribution. The parameters can be estimating with the L-moment procedure (Ahmad et al., 1988).

  Considering P, which the probability of exceeding a determined b value given as $P(b) = 1 - F(b)$, the final SPEI is estimated following the conversion to a normal distribution using Eqs. (1.10) and (1.11), replacing $H(x)$ to $P(b)$.

The ranges of drought classification by scPDSI and SPI are shown in tables 1.1 and 1.2.

The necessary potential evapotranspiration (PET[mm mon^{-1}]), which represents the moisture demand of the atmosphere, for scPDSI and SPEI are calculated by the Thornwaite equation (Thornthwaite et al., 1948; Willmott et al., 1985; Van der Schrier et al., 2011). The

Table 1.1: Drought classification by scPDSI

scPDSI value	Classification
4.00 ≤	Extremely wet
3.00 to 3.99	Very wet
2.00 to 2.99	Moderately wet
1.00 to 1.99	Slightly wet
0.50 to 0.99	Incipient wet spell
0.49 to -0.49	Near normal
-0.50 to -0.99	Incipient dry spell
-1.00 to -1.99	Mild drought
-2.00 to -2.99	Moderate drought
-3.00 to -3.99	Severe drought
-4.00 ≤	Extreme drought

Table 1.2: Drought classification by SPI and SPEI

SPI value	Classification	Probability
2.00 ≤	Extremely wet	2.3
1.50 to 1.99	Severely wet	4.4
1.00 to 1.49	Moderately wet	9.2
0.00 to 0.99	Mildly wet	34.1
0.00 to -0.99	Mild drought	34.1
-1.00 to -1.49	Moderate drought	9.2
-1.50 to -1.99	Severe drought	4.4
-2.00 ≤	Extreme drought	2.3

Thornwaite equation expresses an empirical association between monthly means of daily averaged temperatures T[°C] and PET as:

$$PET_{initial} = \begin{cases} 0 & T < 0°\text{C} \\ 16(10T/I)^a & 0°\text{C} \leq T < 26.5°\text{C} \\ -415.85 + 32.24T - 0.43T^2 & T \geq 26.5°\text{C} \end{cases} \tag{1.13}$$

where I is the heat index:

$$I = \sum_{i=1}^{12} (T/5)^{1.514} \tag{1.14}$$

and a is a third-order polynomial in the heat index I:

$$a = 6.75 \times 10^{-7} I^3 - 7.71 \times 10^{-5} I^2 + 1.792 \times 10^{-2} I + 0.49239 \tag{1.15}$$

Finally, $PET_{initial}$ is adjusted with the duration of the day and month lengths (Willmott et al., 1985):

$$PET = PET_{initial}(\theta/30)(h/12) \tag{1.16}$$

where θ[days] is the length of the month and h[hours] is the duration of daylight on the fifteenth day of the month that varies depending on the latitude.

As shown, the Thornwaite equation uses the monthly mean temperature and the latitude of the site to estimate PET. A more sophisticated method to calculate PET is the Penman-Monteith equation (Allen et al., 1994; Van der Schrier et al., 2011) which includes not only air temperatures but more variables such as wind speeds and radiation as inputs. In this thesis, the Thornwaite equation was employed, as Van der Schrier et al. (2011) have shown that the scPDSI are rather insensitive to the choice of the PET scheme.

1.3.2 Extreme precipitation

Extreme precipitation is weather events that are located at the upper tail of probability distributions of precipitation in terms of the occurrence and intensity. The duration of these events is much shorter than those of droughts, with a typical time scales of several days. However, the events produce clearly perceivable impacts on society, often being the causes of torrential floods. Although drivers of extreme precipitation are more regional, such as synoptic-scale weather phenomena (e.g., Pfahl, 2014; Messmer et al., 2015, 2017; Cannon et al., 2018), extreme precipitation is also influenced by large-scale modes of variability, such as ENSO or the North Atlantic Oscillation (NAO) among others (Kenyon and Hegerl, 2010; Sun et al., 2015), and surface temperatures (Pendergrass et al., 2015, 2017; Sillmann et al., 2017).

There are various metrics to define extreme precipitation and the choice of the metric usually depends on the research question. These metrics can be percentile-based such as the 90th, 95th and 99th percentiles of probability distributions (Coles et al., 2001; Thiombiano et al., 2017), or universally-defined climate indices (Donat et al., 2013) such as Rx1day (monthly maximum 1 day precipitation), R10mm (number of heavy precipitation days, which is the total number of days in a year with more than 10mm), CWD (consecutive wet days which is the number of consecutive days when precipitation is more than 1mm) among others, or block-maxima approach-based (Coles et al., 2001) such as the monthly or annual maximum daily or monthly accumulated precipitation. For this thesis, the percentile-based metric was used.

One of the most widely used methods to examine extreme precipitation is based on the extreme value theory (EVT; Coles et al., 2001). The EVT provides the statistical foundation on sample values that deviate extremely from their medians, and are located at the tails of probability distributions. The assumption lies in the sample values that are independent and randomly distributed. Two approaches exist in the EVT: the block-maxima approach that studies statistical behaviors of maximum values in time-defined blocks, for instance, monthly or annual maximum precipitation, and the peak-over-threshold (POT) approach that deals with maxima defined above a certain threshold, for instance, above a certain a percentile. The POT approach is the method employed in this thesis.

The POT approach (Coles et al., 2001) states that the values y of a sequence of an independent random variable x that exceed a certain threshold u is asymptotically distributed following a generalized Pareto distribution (GPD) with the density distribution function given as:

$$H(y) = \begin{cases} 1 - (1 + \frac{\xi y}{\sigma})^{-1/\xi} & \text{for} \quad \xi \neq 0 \\ 1 - \exp(-\frac{y}{\sigma}) & \text{for} \quad \xi = 0 \end{cases} \tag{1.17}$$

where $y = x - u$ are the positive exceedances, σ is the scale parameter that characterizes the spread of the distribution of y, and ξ is the shape parameter that represents the tail behavior of the distribution. The parameter estimation for a stationary GPD model is achieved through a maximum likelihood procedure (Sugahara et al., 2009).

Based on the GPD distribution, it is possible to estimate the T-year return level y_T associated with the return period T (Coles et al., 2001; Khaliq et al., 2006) as:

$$y_T = \sigma[\zeta_u T^{\xi} - 1]/\xi \tag{1.18}$$

$\zeta_u = P(x > u)$ is the ratio of exceedances in the sample. For the 95^{th} percentile, this is $\zeta_u = 0.05$, and for the $99^{\text{ th}}$ percentile is $\zeta_u = 0.01$.

The y_T gives a probability of occurrence of extreme levels, and is a widely used metric for future projection and planning for this kind of event (Sugahara et al., 2009). More details on the theoretical basis of the POT approach are given in the method section of Chapter 4.

1.3.3 Past and present changes in extreme hydrological events

Past variations (850 – 1949 CE)

Numerous studies on paleo-extreme hydrological events are focused on the last millennium (850 – 1849CE). This fact can be explained by the abundance of high-quality natural proxy and documentary reconstructions that cover this period (e.g., Fernández-Donado et al., 2013; PAGES Hydro2k Consortium, 2017; Jungclaus et al., 2017), which are required for investigating these kinds of regional and sporadic events. In addition, the mean climate during the last millennium presents less variations compared to those of the glacial-interglacial cycles. Hence, in many cases, the period serves as a test-bed for studies of natural climate variability (Schmidt et al., 2011; Jungclaus et al., 2017). Temporally high-resolved proxy records, for instance, continental-scale annually-resolved tree ring-based reconstructions of wet and dry conditions known as tree-ring Drought Atlas (Data available on `http://drought.memphis.edu/`; Cook et al., 2010b,a, 2015, 2020b), have significantly improved the detection of such rare events in

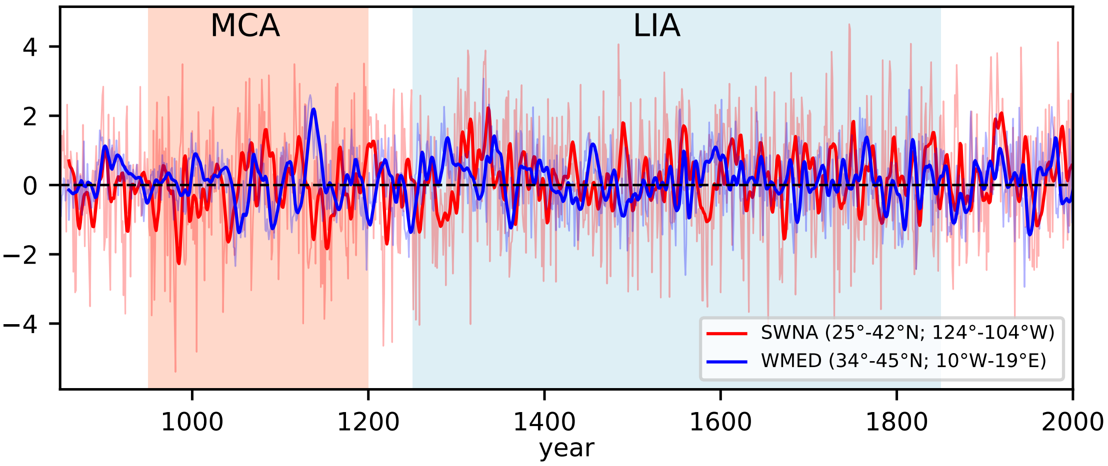

Figure 1.6: Time series of tree-ring-based reconstructed scPDSI averaged over southwest North America (SWNA) and the western Mediterranean (WMED). Thick lines are the 10-year running mean. Data obtained from `http://drought.memphis.edu/`.

the past. Mainly, these reconstructions have allowed more understanding of temporal variations and spatial characteristics of droughts during the last millennium (Fig. 1.6).

In the last millennium, there has always been some sporadic occurrence of regional-scale droughts in all continents in the Northern Hemisphere. Some of the events caused more catastrophic impacts on the environment and society than others, such as the 1850 Civil War drought (Herweijer et al., 2006) and the 1930 Dust Bowl drought (Cook et al., 2008) in North America, and droughts occurred in 1473 (Camenisch et al., 2020), and 1842 (Brázdil et al., 2019) in Europe, which were accompanied by extremely warm conditions.

In North America, the tree-ring reconstructions indicate the occurrence of droughts with exceptional spatial and temporal extents during the MCA (Cook et al., 2010b, 2016b). These MCA droughts extended over a large part of the U.S. continent, covering the southwest and Central Plain exhibiting a pan-continental characteristic (Cook et al., 2007, 2014). In addition, the MCA droughts in the southwest U.S. showed a duration of multi-decadal to centennial long. Such droughts with exceptional spatial and temporal extents which have not been observed in the instrumental era are called megadroughts. The MCA megadroughts were possibly induced by internal variability associated with a strong La Niña and a persistent positive Atlantic Multidecadal Oscillation (Coats et al., 2015, 2016a).

Megadroughts have also occurred in Europe during the MCA over southern Finland and north-central Europe (Helama et al., 2009; Cook et al., 2015). During this period, a larger part of Europe experienced relatively dry conditions than the LIA, with dryness covering southern Scandinavia, central Europe, and the eastern Mediterranean (Cook et al., 2015). Also, several intense droughts occurred in the mid-15th century in north-central Europe, with some regions experiencing dry conditions that lasted for about 30 years. Between 1531–1540 CE, dryness predominated over central Europe (Brázdil et al., 2020), and in 1540 CE presenting an intense drought accompanied with an exceptionally strong heat wave (Wetter and Pfister, 2013; Pfister, 2018). Over the Mediterranean region, temporal coherence of wet and dry fluctuations on decadal to centennial time scales are found between the western and eastern regions during the last millennium (Cook et al., 2016a). The wet-dry fluctuations over this region seem to be associated with NAO (Cook et al., 2016a). This finding agrees with Xoplaki et al. (2018) who have shown that the multidecadal variability of hydroclimate, including droughts, over the Mediterranean during the last millennium is driven by internal variability.

Extreme precipitation before the Industrial Era is less investigated than droughts. This can be explained by the lack of proxy and historical data that includes this kind of short-lived extreme events. Nevertheless, some natural proxy-based reconstructions and documentary records (e.g., Büntgen et al., 2011; Brázdil et al., 2012; Kjeldsen et al., 2014; Machado et al., 2015) provide a description of past extreme precipitation on the regional scale. In the semi-arid regions in the western United States, the frequency of extreme precipitation is inferred from tree ring-based reconstructions of the summer scPDSI for the last 500 years (Steinschneider et al., 2016). The reconstruction indicates that the regions present a low-frequency variability of extreme precipitation that ranges over ample frequency bands, showing a variability from 2 to 30 years.

Over Europe, flood events that are recorded in documentary sources are often linked to extreme precipitation (e.g., Brázdil et al., 2012; Kjeldsen et al., 2014). However, caution is required to interpret such records, as floods are not always caused by heavy rainfall. Based on the reconstructions from the historical documents (Brázdil et al., 2012), extreme floods associated with torrential rainfall occurred over many parts of Europe during the last millennium. For instance, the events in November 1617 in the Mediterranean, September 1763 over England and Scotland, July 1342, and winter of 1783/1784 in central Europe are some of the strongest events which implicated devastating economic losses. Mostly, the event in July 1342 was caused after consecutive 8 days of heavy precipitation. Natural and documentary proxies indicate an increase of extreme precipitation events over Europe during the LIA (Glaser et al., 2010; Wilhelm et al., 2012). This increase seems to be associated with large-scale atmospheric circulation patterns such as the Atlantic low and Russian high (Jacobeit et al., 2003; Brázdil et al., 2012).

Changes during the historical period (1950 CE – present)

The modern instrumental period has clearly allowed more detection of intense hydrological events with rare occurrences across the globe. In addition, high-quality global observational networks available since the mid-20th century have facilitated assessments of changes and variability of extreme hydrological events and their associated drivers (e.g., Lloyd-Hughes and Saunders, 2002; Donat et al., 2013; Spinoni et al., 2015; Sun et al., 2021). Moreover, this network of data also has led to the development of drought and flood maps for the observational period (e.g., Barredo, 2007; He et al., 2020).

In the last few decades, changes in the intensities and frequencies of droughts and extreme precipitation have been reported in many parts of the continents (Seneviratne et al., 2021).

These changes in extreme hydrological events are linked to the intensification of the global hydrological cycle, which also affects its associated atmospheric circulations. The cause of the present-day intensification of the hydrological cycle is mainly attributed to the increase in the tropospheric temperature caused by the increase in the atmospheric GHG (Trenberth et al., 2003).

Changes in droughts vary with the regions. Intensification of severity and duration of droughts has been observed over southern and central Europe, and West Africa (Seneviratne et al., 2021). On the other hand, little changes or even decreases in droughts have been detected in the central U.S. and northern Australia. In west-southern and central Europe, droughts are mainly driven by the vapor pressure deficit (VPD) rather than the precipitation deficit (Mukherjee et al., 2018; Cook et al., 2020a). Although drivers of VPD depend on various factors and on the regions, one of the important drivers is the increase in atmospheric temperatures. The amplified VPD strongly contributes to the ongoing dryness in the Mediterranean region (Vicente-Serrano et al., 2021).

In the case of extreme precipitation, a global-scale intensification has been observed since the mid-20th century. Same as droughts, this change is attributed to the present-day increase in the tropospheric temperature. The intensification of extreme precipitation is based on the Clausius–Clapeyron (C-C) relationship (Allen and Ingram, 2002) which states that the rate of increase in extreme precipitation is 6-7% per 1 degree of warming (Pall et al., 2007; Fischer and Knutti, 2016). This value holds mostly true over higher latitudes, but some land areas and tropical regions show more various increase rates (O'Gorman, 2012; Kharin et al., 2013; Pfahl et al., 2017).

1.4 Modeling climate and extreme events

Coupled climate models became a crucial tool for investigating climate variations on various time scales and their underlying mechanisms by assessing the influences of internal variability and external forcing on the climate (Flato et al., 2014). Currently used complex climate models can be classified into two kinds: atmosphere-ocean general circulation models (AOGCM) and earth system models (ESM). AOGCMs include the physical processes in the atmosphere, ocean, land, sea ice, and interactions among these components. ESMs are more advanced than AOGCMs, as they expand on AOGCMs by including various biogeochemical cycles such as the carbon, sulfur, or ozone cycles. Both kinds of models simulate relevant aspects of the climate system, including the atmosphere, the ocean, sea, ice, land surface. However, some caution is required when using complex climate models and interpreting simulations from them, as these models still contain limitations related to the representations of real-world phenomena, which are based on mathematical terms (Flato et al., 2014).

In general, complex climate models are able to reproduce relatively well large-scale characteristics of mean precipitation. However, almost all models still share some degree of uncertainties in reproducing regional scale precipitation, which involves more spatial heterogeneity (Flato et al., 2014). This is reflected in the magnitudes of simulated precipitation that strongly vary from region to region. For the same reasons, more discrepancies in extreme precipitation are found between model simulations and observations. The discrepancy is even larger over the tropical regions (O'Gorman and Schneider, 2009; O'Gorman, 2012). In the case of droughts, climate models largely underestimate the persistence of events (Ault et al., 2014; Moon et al., 2018).

In terms of internal variability, the amplitudes and intensities of internal variability are largely model-dependent (Bellenger et al., 2014; Fasullo et al., 2020), and there are still some limitations in climate models in reproducing some aspects of modes of variability, for instance, the cold tongue in the western Pacific associated with ENSO (Flato et al., 2014; Seager et al., 2019). Large internal variability often can mask a signal of external forcing complicating assessing influences of an individual forcing on the climate. In such cases, a certain number of ensemble simulations is required to robustly assess the signals of external forcing (Deser et al., 2012; Evans et al., 2013; Deser et al., 2020). However, for long transient simulations, this ensemble approach is computationally expensive, which is not always possible to conduct.

These limitations need to be considered when using AOGCM and ESM simulations. Reducing such uncertainties is an active on-going work in the climate science community, for example by increasing model resolutions (e.g., Champion et al., 2011; Delworth et al., 2012; Scher et al., 2017) and improving cloud microphysics related parametrizations (e.g., Neale et al., 2010). In addition, a prior evaluation of model performance compared to observations is always necessary. However, such evaluations are also not always easy to conduct due to the lack of high-quality temporarily long observations (Flato et al., 2014). Despite these drawbacks, there is no doubt that AOGCMs and ESMs provide valuable information on the climate to complement those given by proxy records that generally focus on the regional climate and also have their inherent biases. Moreover, model simulations can reach far beyond the spatial and temporal extent that instrumental and proxy records can cover.

Complex climate models have been utilized to understand the variability and mechanisms of past extreme events. For instance, various model simulations have provided explanations about the potential drivers of the past MCA megadroughts (Coats et al., 2013, 2015, 2016a), hydroclimate variations and extremes during the last millennium (Stevenson et al., 2018; Xoplaki et al., 2018), and the 1540 drought and heatwave (Orth et al., 2016).

The work on this thesis which aims to investigate extreme hydrological events from the past to the future was performed using simulations from a state-of-the-art ESM, the Community Earth System Model (Hurrell et al., 2013). More details on this specific ESM are given in Chapter 2. The implications of the above-mentioned limitations on the results of this thesis are elaborated throughout the research chapters from Chapters 3 to 5.

Future projection on extreme hydrological events (present – the end of 21st century)

AOGCMs and ESMs have been useful tools to quantify the present and future changes in droughts and extreme precipitation under the increase in GHG concentrations. Future projections with AOGCMs and ESMs indicate that the drying trend together with the increases in dry days and droughts will be intensified over large parts of the land under the business-as-usual scenario causing substantial socio-economic impacts and changes (Lehner et al., 2017; Cook et al., 2018; Naumann et al., 2018; Lu et al., 2019; Cook et al., 2020a; Seneviratne et al., 2021). These regions include the Mediterranean, southwest Africa, and southern Australia, among others. In the case of the Mediterranean region, the drying trend will continue even under a stricter mitigation scenario (Lehner et al., 2017; Seneviratne et al., 2021).

For extreme precipitation, the intensification in its severity and frequency will continue in most of the mid-latitude lands if the current warming of the troposphere continues (Kharin et al., 2013; Pendergrass et al., 2015; Donat et al., 2016; Wang et al., 2017; Pendergrass et al., 2017; Seneviratne et al., 2021). The rate of change in extreme precipitation is proportional to the amount of surface warming regardless of the causing drivers such as GHGs or solar forcing (Pendergrass et al., 2015; Sillmann et al., 2017; Seneviratne et al., 2021).

1.5 Outline of the thesis

The work on this thesis is conducted under the umbrella of the project “PleistoCEP #172745” supported by the Swiss National Science Foundation. The research objective is to better understand the past to future variability in the climate with more focus on extreme climate events, such as droughts, floods, and extreme temperature episodes. The study period (1501 BCE to 2099 CE) pertains to the late Holocene and Anthropocene (Lewis and Maslin, 2015), which are marked by the prosperity and collapses of many early human civilizations (Hodell et al., 1995; DeMenocal, 2001; Büntgen et al., 2011; McConnell et al., 2020), and later, with rapid developments of modern societies. The role of changes in climate on the societal changes during this period has been highly debated, and it is still a research topic that is necessary to be addressed in order to understand the impacts of climate events in our past, present, and future societies. The presented thesis aims to address:

(i) the external forcing imprint in extreme events during the last 3500 years, and
(ii) hydrological variability, including extreme events during historical periods of cultural prosperity and decline in Europe.

The thesis is composed of the following chapters in which each covers a different research topic:

- Chapter 2 provides detailed descriptions on the Community Earth System Model including the here used model simulations, the implemented external forcing, and the procedure to conduct the simulations. In addition, proxy and observational records used for the study are introduced.

- Chapter 3 investigates the mechanisms of multi-year Mediterranean droughts from 850–2099 CE using CESM simulations and tree-ring-based hydroclimate reconstruction. First, the sensitivity of paleo-droughts to various drought indices is assessed; second, drivers of multi-year Mediterranean droughts are discovered at different stages of the evolution of droughts, and lastly, the changes of these drivers under the RCP8.5 scenario are quantified. Moreover, the impacts of volcanic eruptions on Mediterranean droughts are particularly addressed. This study emphasizes the importance of variables related to the land-atmosphere interactions during the development phase of droughts, which has been mostly disregarded in the paleo-drought context so far. The study is published in Climate of the Past (Kim and Raible, 2021).

- Chapter 4 examines the long-term characteristics of pre-industrial extreme precipitation on the global scale for 1501 BCE–1849 CE using CESM transient simulations. It addresses the roles of externally forced and internal variability and atmospheric temperatures on extreme precipitation and distinguishes regions where each variable plays a more dominant role in the variability of extreme precipitation using the extreme value analysis (Coles et al., 2001). This work is one of the few that attempts to understand the characteristics of pre-industrial extreme precipitation, particularly with a modeling perspective. The work is in press in Climate of the Past (Kim et al., 2021).

- Chapter 5 studies the impacts of 43 BCE Okmok eruption in Alaska on the climate and early Mediterranean civilization. A massive cooling detected around this period in Arctic ice cores is supported by the CESM ensemble simulations. The simulations also indicate that the period is characterized by relatively wet conditions. The cold and wet conditions could have caused crop failures and famines, and triggered societal unrest over the region. Other natural proxies and historical records are compiled together to illustrate the climate and societal situations during that epoch and to support the argument. It is important to highlight that this work is a result of an interdisciplinary collaboration among various disciplines in climate sciences such as glaciology, modeling, archeology, and history. The study was published in Proceedings of the National Academy of Sciences (McConnell et al., 2020).

- Chapter 6 provides an outlook of the all presented work and potential future studies.

- Appendix A is a study on the Southern Hemispheric (SH) droughts for the historical period 1957–2016 CE using observational data. A novel computational method known as Causal Discovery Algorithm (CDA; Runge et al., 2019) is used to find time-lagged drivers of SH droughts, and a performance of a CDA-based-model to predict droughts over the study regions is evaluated. The work is in preparation.

- Appendix B provides a technical setup of CESM 1.2.2 on the Cray XC40 at the Swiss National Supercomputer Centre.

References

Abramowitz, M. and Stegun, I. A.: Handbook of mathematical functions with formulas, graphs, and mathematical table, in: US Department of Commerce, National Bureau of Standards Applied Mathematics series 55, URL `https://water.usgs.gov/osw/bulletin17b/1964_Zelen_Severo.pdf`, 1965.

Ahmad, M., Sinclair, C., and Werritty, A.: Log-logistic flood frequency analysis, Journal of Hydrology, 98, 205–224, doi:10.1016/0022-1694(88)90015-7, 1988.

Allen, M. R. and Ingram, W. J.: Constraints on future changes in climate and the hydrologic cycle, Nature, 419, 228–232, doi:10.1038/nature01092, 2002.

Allen, R., Smith, M., Pereira, L., and Perrier, A.: An update for the calculation of reference evapotranspiration, ICID bulletin, 43, 35–92, 1994.

Ault, T. R., Cole, J. E., Overpeck, J. T., Pederson, G. T., and Meko, D. M.: Assessing the risk of persistent drought using climate model simulations and paleoclimate data, Journal of Climate, 27, 7529–7549, doi:10.1175/JCLI-D-12-00282.1, 2014.

Bader, J., Jungclaus, J., Krivova, N., Lorenz, S., Maycock, A., Raddatz, T., Schmidt, H., Toohey, M., Wu, C.-J., and Claussen, M.: Global temperature modes shed light on the Holocene temperature conundrum, Nature communications, 11, 1–8, doi:10.1038/s41467-020-18478-6, 2020.

Baede, A. P., Ahlonsou, E., and Schimel, D.: The Climate System: an Overview. In Third Assessment Report (TAR) Climate Change 2001: The Scientific Basis, Climate change 2001: the scientific basis, pp. 38–47, URL `https://www.ipcc.ch/report/ar3/wg1/chapter-1-the-climate-system-an-overview/`, 2001.

Barnston, A. G. and Livezey, R. E.: Classification, seasonality and persistence of low-frequency atmospheric circulation patterns, Monthly weather review, 115, 1083–1126, doi:10.1175/1520-0493(1987)115⟨1083:CSAPOL⟩2.0.CO;2, 1987.

Barredo, J. I.: Major flood disasters in Europe: 1950–2005, Natural Hazards, 42, 125–148, doi:10.1016/j.quascirev.2011.10.010, 2007.

Bellenger, H., Guilyardi, É., Leloup, J., Lengaigne, M., and Vialard, J.: ENSO representation in climate models: From CMIP3 to CMIP5, Climate Dynamics, 42, 1999–2018, doi:10.1007/s00382-013-1783-z, 2014.

Berger, A.: Milankovitch theory and climate, Reviews of geophysics, 26, 624–657, doi:10.1029/RG026i004p00624, 1988.

Bloomfield, J. P., Marchant, B. P., and McKenzie, A. A.: Changes in groundwater drought associated with anthropogenic warming, Hydrology and Earth System Sciences, 23, 1393–1408, doi:10.5194/hess-23-1393-2019, 2019.

Brázdil, R., Kundzewicz, Z. W., Benito, G., Demarée, G., Macdonald, N., Roald, L. A., et al.: Historical floods in Europe in the past millennium, Changes in Flood Risk in Europe, edited by: Kundzewicz, ZW, IAHS Press, Wallingford, pp. 121–166, 2012.

Brázdil, R., Demarée, G. R., Kiss, A., Dobrovolnỳ, P., Chromá, K., Trnka, M., Dolák, L., Řezníčková, L., Zahradníček, P., Limanowka, D., et al.: The extreme drought of 1842 in Europe as described by both documentary data and instrumental measurements, Climate of the Past, 15, 1861–1884, doi:10.5194/cp-15-1861-2019, 2019.

Brázdil, R., Dobrovolnỳ, P., Bauch, M., Camenisch, C., Kiss, A., Kotyza, O., Oliński, P., and Řezníčková, L.: Central Europe, 1531–1540 CE: The driest summer decade of the past five centuries?, Climate of the Past, 16, 2125–2151, doi:10.5194/cp-16-2125-2020, 2020.

Büntgen, U., Brázdil, R., Heussner, K.-U., Hofmann, J., Kontic, R., Kyncl, T., Pfister, C., Chromá, K., and Tegel, W.: Combined dendro-documentary evidence of Central European hydroclimatic springtime extremes over the last millennium, Quaternary Science Reviews, 30, 3947–3959, doi:10.1016/j.quascirev.2011.10.010, 2011.

Büntgen, U., Tegel, W., Nicolussi, K., McCormick, M., Frank, D., Trouet, V., Kaplan, J. O., Herzig, F., Heussner, K.-U., Wanner, H., Luterbacher, J., and Esper, J.: 2500 years of European climate variability and human susceptibility, Science, 331, 578–582, doi:10.1126/science.1197175, 2011.

Camenisch, C., Keller, K., Salvisberg, M., Amann, B. J.-F., Bauch, M., Blumer, S. R., Brázdil, R., Brönnimann, S., Büntgen, U., Campbell, B., et al.: The early Spörer Minimum–a period of extraordinary climate and socio-economic changes in Western and Central Europe, Climate of the Past, 12, 1–33, doi:10.5194/cp-2016-7, 2016.

Camenisch, C., Brázdil, R., Kiss, A., Pfister, C., Wetter, O., Rohr, C., Contino, A., and Retsö, D.: Extreme heat and drought in 1473 and their impacts in Europe in the context of the early 1470s, Regional environmental change, 20, 1–15, doi:10.1007/s10113-020-01601-0, 2020.

Cannon, F., Hecht, C. W., Cordeira, J. M., and Ralph, F. M.: Synoptic and mesoscale forcing of Southern California extreme precipitation, Journal of Geophysical Research: Atmospheres, 123, 13–714, doi:10.1029/2018JD029045, 2018.

Champion, A. J., Hodges, K. I., Bengtsson, L. O., Keenlyside, N. S., and Esch, M.: Impact of increasing resolution and a warmer climate on extreme weather from Northern Hemisphere extratropical cyclones, Tellus A: Dynamic meteorology and oceanography, 63, 893–906, doi:10.1111/j.1600-0870.2011.00538.x, 2011.

Coats, S., Smerdon, J. E., Seager, R., Cook, B. I., and González-Rouco, J. F.: Megadroughts in southwestern North America in ECHO-G millennial simulations and their comparison to proxy drought reconstructions, Journal of climate, 26, 7635–7649, doi:10.1175/JCLI-D-12-00603.1, 2013.

Coats, S., Cook, B. I., Smerdon, J. E., and Seager, R.: North American pancontinental droughts in model simulations of the last millennium, Journal of Climate, 28, 2025–2043, doi:https://doi.org/10.1175/JCLI-D-14-00634.1, 2015.

Coats, S., Smerdon, J. E., Cook, B., Seager, R., Cook, E. R., and Anchukaitis, K. J.: Internal ocean-atmosphere variability drives megadroughts in Western North America, Geophysical research letters, 43, 9886–9894, doi:10.1002/2016GL070105, 2016a.

Coats, S., Smerdon, J. E., Karnauskas, K. B., and Seager, R.: The improbable but unexceptional occurrence of megadrought clustering in the American West during the Medieval Climate Anomaly, Environmental Research Letters, 11, 074 025, doi:10.1088/1748-9326/11/7/074025, 2016b.

Coles, S., Bawa, J., Trenner, L., and Dorazio, P.: An introduction to statistical modeling of extreme values, vol. 208, Springer, 2001.

Cook, B., Mankin, J. S., Marvel, K., Williams, A., Smerdon, J., and Anchukaitis, K.: Twenty-first century drought projections in the CMIP6 forcing scenarios, Earth's Future, 8, e2019EF001 461, doi:10.1029/2019EF001461, 2020a.

Cook, B. I., Miller, R. L., and Seager, R.: Dust and sea surface temperature forcing of the 1930s "Dust Bowl" drought, Geophysical Research Letters, 35, doi:10.1029/2008GL033486, 2008.

Cook, B. I., Smerdon, J. E., Seager, R., and Cook, E. R.: Pan-continental droughts in North America over the last millennium, Journal of Climate, 27, 383–397, doi:10.1175/JCLI-D-13-00100.1, 2014.

Cook, B. I., Anchukaitis, K. J., Touchan, R., Meko, D. M., and Cook, E. R.: Spatiotemporal drought variability in the Mediterranean over the last 900 years, Journal of Geophysical Research: Atmospheres, 121, 2060–2074, doi:10.1002/2015JD023929, 2016a.

Cook, B. I., Cook, E. R., Smerdon, J. E., Seager, R., Williams, A. P., Coats, S., Stahle, D. W., and Díaz, J. V.: North American megadroughts in the Common Era: Reconstructions and simulations, Wiley Interdisciplinary Reviews: Climate Change, 7, 411–432, doi:10.1002/wcc.394, 2016b.

Cook, B. I., Mankin, J. S., and Anchukaitis, K. J.: Climate change and drought: From past to future, Current Climate Change Reports, 4, 164–179, doi:10.1007/s40641-018-0093-2, 2018.

Cook, E. R., Seager, R., Cane, M. A., and Stahle, D. W.: North American drought: Reconstructions, causes, and consequences, Earth-Science Reviews, 81, 93–134, doi:10.1016/j.earscirev.2006.12.002, 2007.

Cook, E. R., Anchukaitis, K. J., Buckley, B. M., D'Arrigo, R. D., Jacoby, G. C., and Wright, W. E.: Asian monsoon failure and megadrought during the last millennium, science, 328, 486–489, doi:10.1126/science.1185188, 2010a.

Cook, E. R., Seager, R., Heim Jr, R. R., Vose, R. S., Herweijer, C., and Woodhouse, C.: Megadroughts in North America: Placing IPCC projections of hydroclimatic change in a long-term palaeoclimate context, Journal of Quaternary Science, 25, 48–61, doi:10.1002/jqs.1303, 2010b.

Cook, E. R., Seager, R., Kushnir, Y., Briffa, K. R., Büntgen, U., Frank, D., Krusic, P. J., Tegel, W., van der Schrier, G., Andreu-Hayles, L., et al.: Old World megadroughts and pluvials during the Common Era, Science advances, 1, e1500 561, doi:10.1126/sciadv.1500561, 2015.

Cook, E. R., Solomina, O., Matskovsky, V., Cook, B. I., Agafonov, L., Berdnikova, A., Dolgova, E., Karpukhin, A., Knysh, N., Kulakova, M., et al.: The european russia drought atlas (1400–2016 ce), Climate Dynamics, 54, 2317–2335, doi:10.1007/s00382-019-05115-2, 2020b.

Dai, A.: Drought under global warming: a review, Wiley Interdisciplinary Reviews: Climate Change, 2, 45–65, doi:10.1002/wcc.81, 2011.

Dai, A. and Wigley, T.: Global patterns of ENSO-induced precipitation, Geophysical Research Letters, 27, 1283–1286, doi:10.1029/1999GL011140, 2000.

Delworth, T. L., Rosati, A., Anderson, W., Adcroft, A. J., Balaji, V., Benson, R., Dixon, K., Griffies, S. M., Lee, H.-C., Pacanowski, R. C., et al.: Simulated climate and climate change in the GFDL CM2. 5 high-resolution coupled climate model, Journal of Climate, 25, 2755–2781, doi:10.1175/JCLI-D-11-00316.1, 2012.

DeMenocal, P. B.: Cultural responses to climate change during the late Holocene, Science, 292, 667–673, doi:10.1126/science.1059287, 2001.

Deser, C., Phillips, A., Bourdette, V., and Teng, H.: Uncertainty in climate change projections: the role of internal variability, Climate dynamics, 38, 527–546, doi:10.1007/s00382-010-0977-x, 2012.

Deser, C., Lehner, F., Rodgers, K. B., Ault, T., Delworth, T. L., DiNezio, P. N., Fiore, A., Frankignoul, C., Fyfe, J. C., Horton, D. E., et al.: Insights from Earth system model initial-condition large ensembles and future prospects, Nature Climate Change, 10, 277–286, doi:10.1038/s41558-020-0731-2, 2020.

Donat, M., Alexander, L., Yang, H., Durre, I., Vose, R., Dunn, R., Willett, K., Aguilar, E., Brunet, M., Caesar, J., et al.: Updated analyses of temperature and precipitation extreme indices since the beginning of the twentieth century: The HadEX2 dataset, Journal of Geophysical Research: Atmospheres, 118, 2098–2118, doi:10.1002/jgrd.50150, 2013.

Donat, M. G., Lowry, A. L., Alexander, L. V., O'Gorman, P. A., and Maher, N.: More extreme precipitation in the world's dry and wet regions, Nature Climate Change, 6, 508–513, doi:10.1038/nclimate2941, number: 5 Publisher: Nature Publishing Group, 2016.

Donat, M. G., Angélil, O., and Ukkola, A. M.: Intensification of precipitation extremes in the world's humid and water-limited regions, Environmental Research Letters, 14, 065 003, doi:10.1088/1748-9326/ab1c8e, publisher: IOP Publishing, 2019.

Douville, H., Raghavan, K., Renwick, J., Allan, R. P., Arias, A, P., Barlow, M., Cerezo-Mota, R., Cherchi, A., Gan, T. Y., Gergis, J., Jiang, D., Khan, A., Pokam Mba, W., Rosenfeld, D., Tierney, J., and Zolina, O.: Water Cycle Changes. In Climate Change 2021: The Physical Science Basis Contribution of Working Group I to the Sixth Assessment Report of the Intergovernmental Panel on Climate Change, URL `https://wwwipccch/report/sixth-assessment-report-working-group-i/`, in press, 2021.

Dugmore, A. J., McGovern, T. H., Vésteinsson, O., Arneborg, J., Streeter, R., and Keller, C.: Cultural adaptation, compounding vulnerabilities and conjunctures in Norse Greenland, Proceedings of the National Academy of Sciences, 109, 3658–3663, doi:10.1073/pnas.1115292109, 2012.

Evans, J. P., Ji, F., Abramowitz, G., and Ekström, M.: Optimally choosing small ensemble members to produce robust climate simulations, Environmental Research Letters, 8, 044 050, doi:10.1088/1748-9326/8/4/044050, 2013.

Fasullo, J. T., Phillips, A., and Deser, C.: Evaluation of Leading Modes of Climate Variability in the CMIP Archives, Journal of Climate, 33, 5527–5545, doi:10.1175/JCLI-D-19-1024.1, 2020.

Fernández-Donado, L., González-Rouco, J., Raible, C., Ammann, C., Barriopedro, D., García-Bustamante, E., Jungclaus, J. H., Lorenz, S., Luterbacher, J., Phipps, S., et al.: Large-scale temperature response to external forcing in simulations and reconstructions of the last millennium, Climate of the Past, 9, 393–421, doi:10.5194/cp-9-393-2013, 2013.

Fischer, E. M. and Knutti, R.: Observed heavy precipitation increase confirms theory and early models, Nature Climate Change, 6, 986–991, doi:10.1038/nclimate3110, number: 11 Publisher: Nature Publishing Group, 2016.

Flato, G., Marotzke, J., Abiodun, B., Braconnot, P., Chou, S. C., Collins, W., Cox, P., Driouech, F., Emori, S., Eyring, V., et al.: Evaluation of climate models, in: Climate change 2013: the physical science basis. Contribution of Working Group I to the Fifth Assessment Report of the Intergovernmental Panel on Climate Change, edited by Stocker, T., Qin, D., Plattner, Tignor, M., Allen, S., Boschung, J., Nauels, A., Xia, Y., Bex, V., and Midgley, P., pp. 741–866, Cambridge University Press, 2014.

Forster, P., Storelvmo, T., Armour, K., Collins, W., Dufresne, J. L., Frame, D., Lunt, D. J., Mauritsen, T., Palmer, M. D., Watanabe, M., Wild, M., and Zhang, H.: The Earth's Energy Budget, Climate Feedbacks, and Climate Sensitivity. In Climate Change 2021: The Physical Science Basis Contribution of Working Group I to the Sixth Assessment Report of the Intergovernmental Panel on Climate Change, URL `https://wwwipccch/report/sixth-assessment-report-working-group-i/`, in press, 2021.

Fröhlich, C.: Evidence of a long-term trend in total solar irradiance, Astronomy & Astrophysics, 501, L27–L30, doi:10.1051/0004-6361/200912318, 2009.

Glaser, R., Riemann, D., Schönbein, J., Barriendos, M., Brázdil, R., Bertolin, C., Camuffo, D., Deutsch, M., Dobrovolný, P., van Engelen, A., Enzi, S., Halíčková, M., Koenig, S. J., Kotyza, O., Limanówka, D., Macková, J., Sghedoni, M., Martin, B., and Himmelsbach, I.: The variability of European floods since AD 1500, Climatic Change, 101, 235–256, doi:10.1007/s10584-010-9816-7, 2010.

Gonsamo, A., Chen, J. M., and D'Odorico, P.: Underestimated role of East Atlantic-West Russia pattern on Amazon vegetation productivity, Proceedings of the National Academy of Sciences, 112, E1054–E1055, doi:10.1073/pnas.1420834112, 2015.

Goosse, H., Crespin, E., Dubinkina, S., Loutre, M.-F., Mann, M. E., Renssen, H., Sallaz-Damaz, Y., and Shindell, D.: The role of forcing and internal dynamics in explaining the "Medieval Climate Anomaly", Climate dynamics, 39, 2847–2866, doi:10.1007/s00382-012-1297-0, 2012.

Gulev, S. K., W, T. P., Ahn, J., Dentener, F. J., Domingues, C M Gerland, S., Gong, D., Kaufman, D. S., Nnamchi, H. C., Quaas, J., Rivera, J. A., Sathyendranath, S., Smith, S. L., Trewin, B., von Shuckmann, K., and Vose, R. S.: Changing State of the Climate System. In: Climate Change 2021: The Physical Science Basis Contribution of Working Group I to the Sixth Assessment Report of the Intergovernmental Panel on Climate Change, URL `https://wwwipccch/report/sixth-assessment-report-working-group-i/`, in press, 2021.

He, X., Pan, M., Wei, Z., Wood, E. F., and Sheffield, J.: A global drought and flood catalogue from 1950 to 2016, Bulletin of the American Meteorological Society, 101, E508–E535, doi:10.1175/BAMS-D-18-0269.1, 2020.

Helama, S., Meriläinen, J., and Tuomenvirta, H.: Multicentennial megadrought in northern Europe coincided with a global El Niño–Southern Oscillation drought pattern during the Medieval Climate Anomaly, Geology, 37, 175–178, doi:10.1130/G25329A.1, 2009.

Herweijer, C., Seager, R., and Cook, E. R.: North American droughts of the mid to late nineteenth century: a history, simulation and implication for Mediaeval drought, The Holocene, 16, 159–171, doi:10.1191/0959683606hl917rp, 2006.

Hodell, D. A., Curtis, J. H., and Brenner, M.: Possible role of climate in the collapse of Classic Maya civilization, Nature, 375, 391–394, doi:10.1038/375391a0, 1995.

Hurrell, J. W., Holland, M. M., Gent, P. R., Ghan, S., Kay, J. E., Kushner, P. J., Lamarque, J.-F., Large, W. G., Lawrence, D., Lindsay, K., Lipscomb, W. H., Long, M. C., Mahowald, N., Marsh, D. R., Neale, R. B., Rasch, P., Vavrus, S., Vertenstein, M., Bader, D., Collins, W. D., Hack, J. J., Kiehl, J., and Marshall, S.: The community earth system model: a framework for collaborative research, Bulletin of the American Meteorological Society, 94, 1339–1360, doi:10.1175/BAMS-D-12-00121.1, 2013.

Hurtt, G. C., Chini, L. P., Frolking, S., Betts, R., Feddema, J., Fischer, G., Fisk, J., Hibbard, K., Houghton, R., Janetos, A., et al.: Harmonization of land-use scenarios for the period 1500–2100: 600 years of global gridded annual land-use transitions, wood harvest, and resulting secondary lands, Climatic change, 109, 117–161, doi:10.1007/s10584-011-0153-2, 2011.

IPCC: IPCC, 2021: Climate Change 2021: The Physical Science Basis. Contribution of Working Group I to the Sixth Assessment Report of the Intergovernmental Panel on Climate Change, URL `https://www.ipcc.ch/report/sixth-assessment-report-working-group-i/`, in press, 2021.

Irving, D. and Simmonds, I.: A new method for identifying the Pacific–South American pattern and its influence on regional climate variability, Journal of Climate, 29, 6109–6125, doi:10.1175/JCLI-D-15-0843.1, 2016.

Jacobeit, J., Glaser, R., Luterbacher, J., and Wanner, H.: Links between flood events in central Europe since AD 1500 and large-scale atmospheric circulation modes, Geophysical Research Letters, 30, doi:10.1029/2002GL016433, 2003.

Jungclaus, J. H., Bard, E., Baroni, M., Braconnot, P., Cao, J., Chini, L. P., Egorova, T., Evans, M., González-Rouco, J. F., Goosse, H., Hurtt, G. C., Joos, F., Kaplan, J. O., Khodri, M., Klein Goldewijk, K., Krivova, N., LeGrande, A. N., Lorenz, S. J., Luterbacher, J., Man, W., Maycock, A. C., Meinshausen, M., Moberg, A., Muscheler, R., Nehrbass-Ahles, C., Otto-Bliesner, B. I., Phipps, S. J., Pongratz, J., Rozanov, E., Schmidt,

G. A., Schmidt, H., Schmutz, W., Schurer, A., Shapiro, A. I., Sigl, M., Smerdon, J. E., Solanki, S. K., Timmreck, C., Toohey, M., Usoskin, I. G., Wagner, S., Wu, C.-J., Yeo, K. L., Zanchettin, D., Zhang, Q., and Zorita, E.: The PMIP4 contribution to CMIP6–Part 3: The last millennium, scientific objective, and experimental design for the PMIP4 past1000 simulations, Geoscientific Model Development, 10, 4005–4033, doi:10.5194/gmd-10-4005-2017, 2017.

Kenyon, J. and Hegerl, G. C.: Influence of Modes of Climate Variability on Global Precipitation Extremes, Journal of Climate, 23, 6248–6262, doi:10.1175/2010JCLI3617.1, 2010.

Khaliq, M. N., Ouarda, T. B., Ondo, J.-C., Gachon, P., and Bobée, B.: Frequency analysis of a sequence of dependent and/or non-stationary hydro-meteorological observations: A review, Journal of hydrology, 329, 534–552, doi:10.1016/j.jhydrol.2006.03.004, 2006.

Kharin, V. V., Zwiers, F. W., Zhang, X., and Wehner, M.: Changes in temperature and precipitation extremes in the CMIP5 ensemble, Climatic Change, 119, 345–357, doi:10.1007/s10584-013-0705-8, 2013.

Kim, W. M. and Raible, C. C.: Dynamics of the Mediterranean droughts from 850 to 2099 CE in the Community Earth System Model, Climate of the Past, 17, 887–911, doi:10.5194/cp-17-887-2021, 2021.

Kim, W. M., Blender, R., Sigl, M., Messmer, M., and Raible, C. C.: Statistical characteristics of extreme daily precipitation during 1501 BCE–1849 CE in the Community Earth System Model, Climate of the Past Discussions, pp. 1–38, doi:10.5194/cp-2021-61, 2021.

Kjeldsen, T. R., Macdonald, N., Lang, M., Mediero, L., Albuquerque, T., Bogdanowicz, E., Brázdil, R., Castellarin, A., David, V., Fleig, A., Gül, G. O., Kriauciuniene, J., Kohnová, S., Merz, B., Nicholson, O., Roald, L. A., Salinas, J. L., Sarauskiene, D., Šraj, M., Strupczewski, W., Szolgay, J., Toumazis, A., Vanneuville, W., Veijalainen, N., and Wilson, D.: Documentary evidence of past floods in Europe and their utility in flood frequency estimation, Journal of Hydrology, 517, 963–973, doi:10.1016/j.jhydrol.2014.06.038, 2014.

Leathers, D. J. and Palecki, M. A.: The Pacific/North American teleconnection pattern and United States climate. Part II: Temporal characteristics and index specification, Journal of Climate, 5, 707–716, doi: 10.1175/1520-0442(1992)005⟨0707:TPATPA⟩2.0.CO;2, 1992.

Lehner, F., Coats, S., Stocker, T. F., Pendergrass, A. G., Sanderson, B. M., Raible, C. C., and Smerdon, J. E.: Projected drought risk in 1.5 C and 2 C warmer climates, Geophysical Research Letters, 44, 7419–7428, doi:10.1002/2017GL074117, 2017.

Lewis, S. L. and Maslin, M. A.: Defining the anthropocene, Nature, 519, 171–180, doi:10.1038/nature14258, 2015.

Lim, Y.-K.: The East Atlantic/West Russia (EA/WR) teleconnection in the North Atlantic: climate impact and relation to Rossby wave propagation, Climate Dynamics, 44, 3211–3222, doi:s00382-014-2381-4, 2015.

Lloyd-Hughes, B.: The impracticality of a universal drought definition, Theoretical and Applied Climatology, 117, 607–611, doi:10.1007/s00704-013-1025-7, 2014.

Lloyd-Hughes, B. and Saunders, M. A.: A drought climatology for Europe, International Journal of Climatology: A Journal of the Royal Meteorological Society, 22, 1571–1592, doi:10.1002/joc.846, 2002.

Lu, J., Carbone, G. J., and Grego, J. M.: Uncertainty and hotspots in 21st century projections of agricultural drought from CMIP5 models, Scientific reports, 9, 1–12, doi:10.1038/s41598-019-41196-z, 2019.

Machado, M. J., Botero, B. A., López, J., Francés, F., Díez-Herrero, A., and Benito, G.: Flood frequency analysis of historical flood data under stationary and non-stationary modelling, Hydrology and Earth System Sciences, 19, 2561–2576, doi:10.5194/hess-19-2561-2015, 2015.

Mann, M. E., Zhang, Z., Rutherford, S., Bradley, R. S., Hughes, M. K., Shindell, D., Ammann, C., Faluvegi, G., and Ni, F.: Global signatures and dynamical origins of the Little Ice Age and Medieval Climate Anomaly, Science, 326, 1256–1260, doi:10.1126/science.1177303, 2009.

Mantua, N. J. and Hare, S. R.: The Pacific decadal oscillation, Journal of oceanography, 58, 35–44, doi: 10.1023/A:1015820616384, 2002.

Marshall, G. J.: Trends in the Southern Annular Mode from observations and reanalyses, Journal of climate, 16, 4134–4143, doi:10.1175/1520-0442(2003)016⟨4134:TITSAM⟩2.0.CO;2, 2003.

McConnell, J. R., Sigl, M., Plunkett, G., Burke, A., Kim, W. M., Raible, C. C., Wilson, A. I., Manning, J. G., Ludlow, F., Chellman, N. J., et al.: Extreme climate after massive eruption of Alaska's Okmok volcano in 43 BCE and effects on the late Roman Republic and Ptolemaic Kingdom, Proceedings of the National Academy of Sciences, 117, 15 443–15 449, doi:10.1073/pnas.2002722117, 2020.

McKee, T. B., Doesken, N. J., Kleist, J., et al.: The relationship of drought frequency and duration to time scales, in: Proceedings of the 8th Conference on Applied Climatology, vol. 17, pp. 179–183, American Meteorological Society Boston, MA, 1993.

McLeman, R. A., Dupre, J., Ford, L. B., Ford, J., Gajewski, K., and Marchildon, G.: What we learned from the Dust Bowl: lessons in science, policy, and adaptation, Population and environment, 35, 417–440, doi:s11111-013-0190-z, 2014.

Messmer, M., Gómez-Navarro, J. J., and Raible, C. C.: Climatology of Vb cyclones, physical mechanisms and their impact on extreme precipitation over Central Europe, Earth system dynamics, 6, 541–553, doi:10.5194/esd-6-541-2015, 2015.

Messmer, M., Gómez-Navarro, J. J., and Raible, C. C.: Sensitivity experiments on the response of Vb cyclones to sea surface temperature and soil moisture changes, Earth system dynamics, 8, 477–493, doi:10.5194/esd-8-477-2017, 2017.

Miller, G. H., Geirsdóttir, Á., Zhong, Y., Larsen, D. J., Otto-Bliesner, B. L., Holland, M. M., Bailey, D. A., Refsnider, K. A., Lehman, S. J., Southon, J. R., et al.: Abrupt onset of the Little Ice Age triggered by volcanism and sustained by sea-ice/ocean feedbacks, Geophysical Research Letters, 39, doi:10.1029/2011GL050168, 2012.

Mishra, A. K. and Singh, V. P.: A review of drought concepts, Journal of Hydrology, 391, 202–216, doi: 10.1016/j.jhydrol.2010.07.012, 2010.

Mo, K. C.: Model-based drought indices over the United States, Journal of Hydrometeorology, 9, 1212–1230, doi:10.1175/2008JHM1002.1, 2008.

Mo, K. C. and Paegle, J. N.: The Pacific–South American modes and their downstream effects, International Journal of Climatology: A Journal of the Royal Meteorological Society, 21, 1211–1229, doi:10.1002/joc.685, 2001.

Moon, H., Gudmundsson, L., and Seneviratne, S. I.: Drought persistence errors in global climate models, Journal of Geophysical Research: Atmospheres, 123, 3483–3496, doi:10.1002/2017JD027577, 2018.

Mukherjee, S., Mishra, A., and Trenberth, K. E.: Climate Change and Drought: a Perspective on Drought Indices, Current Climate Change Reports, 4, 145–163, doi:10.1007/s40641-018-0098-x, 2018.

Muscheler, R., Joos, F., Beer, J., Müller, S. A., Vonmoos, M., and Snowball, I.: Solar activity during the last 1000 yr inferred from radionuclide records, Quaternary Science Reviews, 26, 82–97, doi:10.1016/j.quascirev.2006.07.012, 2007.

Myhre, G., Shindell, D., Breón, F., Collins, W., Fuglestvedt, J., Huang, J., Koch, D., Lamarque, J., Lee, D., Mendoza, B., Nakajima, T., Robock, A., Stephens, G., Takemura, T., and Zhang, H.: Anthropogenic and natural radiative forcing. In Climate Change 2013: The Physical Science Basis Contribution of Working Group I to the Fifth Assessment Report of the Intergovernmental Panel on Climate Change, URL `https://wwwipccch/site/assets/uploads/2018/02/WG1AR5_Chapter08_FINALpdf`, 2013.

Naumann, G., Alfieri, L., Wyser, K., Mentaschi, L., Betts, R., Carrao, H., Spinoni, J., Vogt, J., and Feyen, L.: Global changes in drought conditions under different levels of warming, Geophysical Research Letters, 45, 3285–3296, doi:10.1002/2017GL076521, 2018.

Neale, R. B., Chen, C.-C., Gettelman, A., Lauritzen, P. H., Park, S., Williamson, D. L., Conley, A. J., Garcia, R., Kinnison, D., and Lamarque, J.-F.: Description of the NCAR community atmosphere model (CAM 5.0), NCAR Tech. Note NCAR/TN-486+ STR, 1, 1–12, 2010.

O'Gorman, P. A. and Schneider, T.: The physical basis for increases in precipitation extremes in simulations of 21st-century climate change, Proceedings of the National Academy of Sciences, 106, 14 773–14 777, doi:10.1073/pnas.0907610106, publisher: National Academy of Sciences Section: Physical Sciences, 2009.

Orth, R., Vogel, M. M., Luterbacher, J., Pfister, C., and Seneviratne, S. I.: Did European temperatures in 1540 exceed present-day records?, Environmental Research Letters, 11, 114 021, doi:10.1088/1748-9326/11/11/114021, 2016.

O'Gorman, P. A.: Sensitivity of tropical precipitation extremes to climate change, Nature Geoscience, 5, 697–700, doi:10.1038/ngeo1568, 2012.

Pachauri, R. K., Allen, M. R., Barros, V. R., Broome, J., Cramer, W., Christ, R., Church, J. A., Clarke, L., Dahe, Q., Dasgupta, P., et al.: Climate change 2014: synthesis report. Contribution of Working Groups I, II and III to the fifth assessment report of the Intergovernmental Panel on Climate Change, Ipcc, URL `https://www.ipcc.ch/report/ar5/syr/`, 2014.

PAGES Hydro2k Consortium: Comparing proxy and model estimates of hydroclimate variability and change over the Common Era, Climate of the Past, 13, 1851–1900, doi:10.5194/cp-13-1851-2017, 2017.

Paillard, D.: Climate and the orbital parameters of the Earth, Comptes Rendus Geoscience, 342, 273–285, doi:10.1016/j.crte.2009.12.006, 2010.

Pall, P., Allen, M. R., and Stone, D. A.: Testing the Clausius–Clapeyron constraint on changes in extreme precipitation under CO2 warming, Climate Dynamics, 28, 351–363, doi:10.1007/s00382-006-0180-2, 2007.

Palmer, W. C.: Meteorological drought, vol. 30, US Department of Commerce, Weather Bureau, 1965.

Pendergrass, A. G., Lehner, F., Sanderson, B. M., and Xu, Y.: Does extreme precipitation intensity depend on the emissions scenario?, Geophysical Research Letters, 42, 8767–8774, doi:10.1002/2015GL065854, 2015.

Pendergrass, A. G., Knutti, R., Lehner, F., Deser, C., and Sanderson, B. M.: Precipitation variability increases in a warmer climate, Scientific reports, 7, 1–9, doi:10.1038/s41598-017-17966-y, 2017.

Peters, E., Bier, G., Van Lanen, H. A., and Torfs, P.: Propagation and spatial distribution of drought in a groundwater catchment, Journal of Hydrology, 321, 257–275, doi:10.1016/j.jhydrol.2005.08.004, 2006.

Peterson, L. C. and Haug, G. H.: Climate and the collapse of Maya civilization: A series of multi-year droughts helped to doom an ancient culture, American Scientist, 93, 322–329, URL `http://www.jstor.org/stable/27858607`, 2005.

Pfahl, S.: Characterising the relationship between weather extremes in Europe and synoptic circulation features, Natural Hazards and Earth System Sciences, 14, 1461–1475, doi:10.5194/nhess-14-1461-2014, publisher: Copernicus GmbH, 2014.

Pfahl, S., O'Gorman, P. A., and Fischer, E. M.: Understanding the regional pattern of projected future changes in extreme precipitation, Nature Climate Change, 7, 423–427, doi:10.1038/nclimate3287, number: 6 Publisher: Nature Publishing Group, 2017.

Pfister, C.: 5 The "Black Swan" of 1540: Aspects of a European Megadrought, in: Climate Change and Cultural Transition in Europe, pp. 156–194, Brill, doi:10.1163/9789004356825_007, 2018.

Pfister, C. and Brázdil, R.: Social vulnerability to climate in the" Little Ice Age": an example from Central Europe in the early 1770s, Climate of the Past, 2, 115–129, doi:10.5194/cp-2-115-2006, 2006.

Phillips, A. S., Deser, C., and Fasullo, J.: Evaluating modes of variability in climate models, Eos, Transactions American Geophysical Union, 95, 453–455, doi:10.1002/2014EO490002, 2014.

Pongratz, J., Reick, C., Raddatz, T., and Claussen, M.: A reconstruction of global agricultural areas and land cover for the last millennium, Global Biogeochemical Cycles, 22, doi:10.1029/2007GB003153, 2008.

Raible, C. C., Bärenbold, O., and Gómez-navarro, J. J.: Drought indices revisited – improving and testing of drought indices in a simulation of the last two millennia for Europe, Tellus A: Dynamic Meteorology and Oceanography, 69, 1287 492, doi:10.1080/16000870.2017.1296226, 2017.

Rasmusson, E. M. and Wallace, J. M.: Meteorological aspects of the El Nino/southern oscillation, Science, 222, 1195–1202, doi:10.1126/science.222.4629.1195, 1983.

Robock, A.: Volcanic eruptions and climate, Reviews of geophysics, 38, 191–219, doi:10.1029/1998RG000054, 2000.

Rodell, M., Beaudoing, H. K., L'ecuyer, T., Olson, W. S., Famiglietti, J. S., Houser, P. R., Adler, R., Bosilovich, M. G., Clayson, C. A., Chambers, D., et al.: The observed state of the water cycle in the early twenty-first century, Journal of Climate, 28, 8289–8318, doi:10.1175/JCLI-D-14-00555.1, 2015.

Runge, J., Bathiany, S., Bollt, E., Camps-Valls, G., Coumou, D., Deyle, E., Glymour, C., Kretschmer, M., Mahecha, M. D., Muñoz-Marí, J., et al.: Inferring causation from time series in Earth system sciences, Nature communications, 10, 1–13, doi:10.1038/s41467-019-10105-3, 2019.

Scher, S., Haarsma, R. J., Vries, H. d., Drijfhout, S. S., and Delden, A. J. v.: Resolution dependence of extreme precipitation and deep convection over the Gulf Stream, Journal of Advances in Modeling Earth Systems, 9, 1186–1194, doi:https://doi.org/10.1002/2016MS000903, 2017.

Schmidt, G. A., Jungclaus, J. H., Ammann, C. M., Bard, E., Braconnot, P., Crowley, T. J., Delaygue, G., Joos, F., Krivova, N. A., Muscheler, R., Otto-Bliesner, B. L., Pongratz, J., Shindell, D. T., Solanki, S. K., Steinhilber, F., and Vieira, L. E. A.: Climate forcing reconstructions for use in PMIP simulations of the last millennium (v1. 0), Geoscientific Model Development, 4, 33–45, doi:10.5194/gmd-4-33-2011, 2011.

Seager, R., Cane, M., Henderson, N., Lee, D.-E., Abernathey, R., and Zhang, H.: Strengthening tropical Pacific zonal sea surface temperature gradient consistent with rising greenhouse gases, Nature Climate Change, 9, 517–522, doi:10.1038/s41558-019-0505-x, 2019.

Seneviratne, S. I., Corti, T., Davin, E. L., Hirschi, M., Jaeger, E. B., Lehner, I., Orlowsky, B., and Teuling, A. J.: Investigating soil moisture–climate interactions in a changing climate: A review, Earth-Science Reviews, 99, 125–161, doi:10.1016/j.earscirev.2010.02.004, 2010.

Seneviratne, S. I., Zhang, X., Adnan, M., Badi, W., Dereczynski, C., Di Luca, A., Ghosh, S., Iskandar, I., Kossin, J., Lewis, S., Otto, F., Pinto, I., Satoh, M., Vicente-Serrano, S. M., Wehner, M., and Zhou, B.: Weather and Climate Extreme Events in a Changing Climate. In Climate Change 2021: The Physical Science Basis. Contribution of Working Group I to the Sixth Assessment Report of the Intergovernmental Panel on Climate Change, URL `https://www.ipcc.ch/report/sixth-assessment-report-working-group-i/`, in press, 2021.

Shindell, D. T., Schmidt, G. A., Mann, M. E., Rind, D., and Waple, A.: Solar forcing of regional climate change during the Maunder Minimum, science, 294, 2149–2152, doi:10.1126/science.1064363, 2001.

Sillmann, J., Stjern, C. W., Myhre, G., and Forster, P. M.: Slow and fast responses of mean and extreme precipitation to different forcing in CMIP5 simulations, Geophysical Research Letters, 44, 6383–6390, doi:10.1002/2017GL073229, 2017.

Spinoni, J., Naumann, G., Vogt, J. V., and Barbosa, P.: The biggest drought events in Europe from 1950 to 2012, Journal of Hydrology: Regional Studies, 3, 509–524, doi:10.1002/joc.5291, 2015.

Steinschneider, S., Ho, M., Cook, E. R., and Lall, U.: Can PDSI inform extreme precipitation?: An exploration with a 500 year long paleoclimate reconstruction over the U.S., Water Resources Research, 52, 3866–3880, doi:https://doi.org/10.1002/2016WR018712, 2016.

Stenchikov, G. L., Kirchner, I., Robock, A., Graf, H.-F., Antuña, J. C., Grainger, R. G., Lambert, A., and Thomason, L.: Radiative forcing from the 1991 Mount Pinatubo volcanic eruption, Journal of Geophysical Research: Atmospheres, 103, 13 837–13 857, 1998.

Stevenson, S., Overpeck, J. T., Fasullo, J., Coats, S., Parsons, L., Otto-Bliesner, B., Ault, T., Loope, G., and Cole, J.: Climate variability, volcanic forcing, and last millennium hydroclimate extremes, Journal of Climate, 31, 4309–4327, doi:10.1175/JCLI-D-17-0407.1, 2018.

Sugahara, S., Rocha, R. P. d., and Silveira, R.: Non-stationary frequency analysis of extreme daily rainfall in Sao Paulo, Brazil, International Journal of Climatology, 29, 1339–1349, doi:10.1002/joc.1760, 2009.

Sun, Q., Zhang, X., Zwiers, F., Westra, S., and Alexander, L. V.: A global, continental, and regional analysis of changes in extreme precipitation, Journal of Climate, 34, 243–258, doi:10.1175/JCLI-D-19-0892.1, 2021.

Sun, X., Renard, B., Thyer, M., Westra, S., and Lang, M.: A global analysis of the asymmetric effect of ENSO on extreme precipitation, Journal of Hydrology, 530, 51–65, doi:10.1016/j.jhydrol.2015.09.016, 2015.

Thiombiano, A. N., El Adlouni, S., St-Hilaire, A., Ouarda, T. B., and El-Jabi, N.: Nonstationary frequency analysis of extreme daily precipitation amounts in Southeastern Canada using a peaks-over-threshold approach, Theoretical and Applied Climatology, 129, 413–426, doi:10.1007/s00704-016-1789-7, 2017.

Thom, H. C.: A note on the gamma distribution, Monthly weather review, 86, 117–122, doi:10.1175/1520-0493(1958)086⟨0117:ANOTGD⟩2.0.CO;2, 1958.

Thompson, D. W. and Wallace, J. M.: Annular modes in the extratropical circulation. Part I: Month-to-month variability, Journal of climate, 13, 1000–1016, doi:10.1175/1520-0442(2000)013⟨1000:AMITEC⟩2.0.CO;2, 2000.

Thornthwaite, C. W. et al.: An approach toward a rational classification of climate, Geographical review, 38, 55–94, doi:10.2307/210739, 1948.

Trenberth, K. E. and Hurrell, J. W.: Decadal atmosphere-ocean variations in the Pacific, Climate Dynamics, 9, 303–319, doi:10.1007/BF00204745, 1994.

Trenberth, K. E. and Stepaniak, D. P.: Indices of el Niño evolution, Journal of climate, 14, 1697–1701, doi:10.1175/1520-0442(2001)014⟨1697:LIOENO⟩2.0.CO;2, 2001.

Trenberth, K. E., Dai, A., Rasmussen, R. M., and Parsons, D. B.: The Changing Character of Precipitation, Bulletin of the American Meteorological Society, 84, 1205–1218, doi:10.1175/BAMS-84-9-1205, publisher: American Meteorological Society Section: Bulletin of the American Meteorological Society, 2003.

Trenberth, K. E., Smith, L., Qian, T., Dai, A., and Fasullo, J.: Estimates of the global water budget and its annual cycle using observational and model data, Journal of Hydrometeorology, 8, 758–769, doi:10.1175/JHM600.1, 2007.

Van der Schrier, G., Jones, P., and Briffa, K.: The sensitivity of the PDSI to the Thornthwaite and Penman-Monteith parameterizations for potential evapotranspiration, Journal of Geophysical Research: Atmospheres, 116, doi:10.1029/2010JD015001, 2011.

Vicente-Serrano, S. M., Beguería, S., and López-Moreno, J. I.: A Multiscalar Drought Index Sensitive to Global Warming: The Standardized Precipitation Evapotranspiration Index, Journal of Climate, 23, 1696–1718, doi:10.1175/2009JCLI2909.1, URL `https://journals.ametsoc.org/doi/full/10.1175/2009JCLI2909.1`, 2009.

Vicente-Serrano, S. M., Beguería, S., López-Moreno, J. I., Angulo, M., and El Kenawy, A.: A new global 0.5 gridded dataset (1901–2006) of a multiscalar drought index: comparison with current drought index datasets based on the Palmer Drought Severity Index, Journal of Hydrometeorology, 11, 1033–1043, doi:10.1175/2010JHM1224.1, 2010.

Vicente-Serrano, S. M., Van der Schrier, G., Beguería, S., Azorin-Molina, C., and Lopez-Moreno, J.-I.: Contribution of precipitation and reference evapotranspiration to drought indices under different climates, Journal of Hydrology, 526, 42–54, doi:10.1016/j.jhydrol.2014.11.025, 2015.

Vicente-Serrano, S. M., Domínguez-Castro, F., Murphy, C., Hannaford, J., Reig, F., Peña-Angulo, D., Tramblay, Y., Trigo, R. M., Mac Donald, N., Luna, M. Y., et al.: Long-term variability and trends in meteorological droughts in Western Europe (1851–2018), International journal of climatology, 41, E690–E717, doi:10.1002/joc.6719, 2021.

Wagner, S. and Zorita, E.: The influence of volcanic, solar and CO 2 forcing on the temperatures in the Dalton Minimum (1790–1830): a model study, Climate Dynamics, 25, 205–218, doi:https://doi.org/10.1007/s00382-005-0029-0, 2005.

Wallace, J. M. and Gutzler, D. S.: Teleconnections in the geopotential height field during the Northern Hemisphere winter, Monthly weather review, 109, 784–812, doi:10.1175/1520-0493(1981)109⟨0784:TITGHF⟩2.0.CO;2, 1981.

Wang, C.: ENSO, Atlantic climate variability, and the Walker and Hadley circulations, in: The Hadley circulation: present, past and future, pp. 173–202, Springer, doi:10.1007/978-1-4020-2944-8_7, 2004.

Wang, W., Ertsen, M. W., Svoboda, M. D., and Hafeez, M.: Propagation of drought: from meteorological drought to agricultural and hydrological drought, doi:10.1155/2016/6547209, 2016.

Wang, X., Jiang, D., and Lang, X.: Future extreme climate changes linked to global warming intensity, Science Bulletin, 62, 1673–1680, doi:10.1016/j.scib.2017.11.004, 2017.

Wanner, H., Brönnimann, S., Casty, C., Gyalistras, D., Luterbacher, J., Schmutz, C., Stephenson, D. B., and Xoplaki, E.: North Atlantic Oscillation–concepts and studies, Surveys in geophysics, 22, 321–381, doi:10.1023/A:1014217317898, 2001.

Wanner, H., Beer, J., Bütikofer, J., Crowley, T. J., Cubasch, U., Flückiger, J., Goosse, H., Grosjean, M., Joos, F., Kaplan, J. O., et al.: Mid-to Late Holocene climate change: an overview, Quaternary Science Reviews, 27, 1791–1828, doi:10.1016/j.quascirev.2008.06.013, 2008.

Washington, R., Hodson, A., Isaksson, E., and Macdonald, O.: Northern hemisphere teleconnection indices and the mass balance of Svalbard glaciers, International Journal of Climatology: A Journal of the Royal Meteorological Society, 20, 473–487, doi:10.1002/(SICI)1097-0088(200004)20:5⟨473::AID-JOC506⟩3.0.CO;2-O, 2000.

Wells, N., Goddard, S., and Hayes, M. J.: A Self-Calibrating Palmer Drought Severity Index, Journal of Climate, 17, 2335–2351, doi:10.1175/1520-0442(2004)017⟨2335:ASPDSI⟩2.0.CO;2, 2004.

Wetter, O. and Pfister, C.: An underestimated record breaking event–why summer 1540 was likely warmer than 2003, Climate of the Past, 9, 41–56, doi:10.5194/cp-9-41-2013, 2013.

Wilhelm, B., Arnaud, F., Sabatier, P., Crouzet, C., Brisset, E., Chaumillon, E., Disnar, J.-R., Guiter, F., Malet, E., Reyss, J.-L., Tachikawa, K., Bard, E., and Delannoy, J.-J.: 1400years of extreme precipitation patterns over the Mediterranean French Alps and possible forcing mechanisms, Quaternary Research, 78, 1–12, doi:10.1016/j.yqres.2012.03.003, 2012.

Willmott, C. J., Rowe, C. M., and Mintz, Y.: Climatology of the terrestrial seasonal water cycle, Journal of Climatology, 5, 589–606, doi:10.1002/joc.3370050602, 1985.

Wu, H., Hayes, M. J., Wilhite, D. A., and Svoboda, M. D.: The effect of the length of record on the standardized precipitation index calculation, International Journal of Climatology: A Journal of the Royal Meteorological Society, 25, 505–520, doi:10.1002/joc.1142, 2005.

Xoplaki, E., Fleitmann, D., Luterbacher, J., Wagner, S., Haldon, J. F., Zorita, E., Telelis, I., Toreti, A., and Izdebski, A.: The Medieval Climate Anomaly and Byzantium: A review of the evidence on climatic fluctuations, economic performance and societal change, Quaternary Science Reviews, 136, 229–252, doi:10.1016/j.quascirev.2015.10.004, 2016.

Xoplaki, E., Luterbacher, J., Wagner, S., Zorita, E., Fleitmann, D., Preiser-Kapeller, J., Sargent, A. M., White, S., Toreti, A., Haldon, J. F., et al.: Modelling climate and societal resilience in the Eastern Mediterranean in the last millennium, Human Ecology, 46, 363–379, doi:10.1007/s10745-018-9995-9, 2018.

Chapter 2

Methods

2.1 Community Earth System Model

The Community Earth System Model (CESM; Hurrell et al., 2013) is a fully coupled Earth System Model developed by the National Center of Atmospheric Research (NCAR) in the U.S. The model is composed of separate component models for the atmosphere, land, ocean, sea ice and a coupler component that enables exchanges of fluxes and information among all the components. The component models are the Community Atmosphere Model for the atmosphere (CAM; Neale et al., 2010), the Community Land Model for the land (CLM; Lawrence et al., 2011), the Parallel Ocean Program version 2 for the ocean (POP; Smith et al., 2010) and Los Alamos Sea Ice Model for the sea ice (CICE; Hunke et al., 2010). Up to date, two CESM model series and several versions of each series are freely available for scientific use. Following the CESM 1.x series, the new series CESM 2 became available in 2018. The versions used for this thesis are CESM 1.0.1 (CESM101), released in 2010, and CESM 1.2.2 (CESM122), released in 2014.

From CESM1.0.x to CESM1.2.x, some technical updates and improvements are implemented in the component models (`https://www.cesm.ucar.edu/models/cesm1.2/tags/cesm1_2/whatsnew_science.html`, Neale et al., 2010). An important change is the update of the atmospheric component CAM4 to CAM5. In this thesis, CESM101 consists of CAM4, CLM4, POP2, and CICE4, and CESM122 has the same component models as CESM101 except for CAM, and it uses CAM5.

CAM4 (Neale et al., 2010) has a horizontal resolution of 1.25° × 0.9° at 26 vertical levels in a hybrid sigma-pressure coordinate system. In a hybrid sigma-pressure system, the upper levels of the atmosphere are represented by pressure only, and the lower levels by a sigma vertical coordinate. In this system, the pressure P at a given grid point with a latitude i, longitude j, and level k, is defined as $P(i, j, k) = A_{\mathrm{k}} P_0 + B_{\mathrm{k}} P_{\mathrm{s}}(i, j)$. A and B are the coefficients for the coordinate system that vary with the levels, P_{s} is the model's current surface pressure, and P_0 is the reference pressure which is 1000 hPa. The vertical levels in CAM4 extend approximately from 992.64 to 2.92 hPa. In CAM4, the core is changed from a spectral core used in CAM3 to a Lin-Rood finite volume core (Lin and Rood, 1996). Compared to the preceding version CAM3, CAM4 is improved in the physical representation of deep convection (Neale et al., 2010). For instance, the modification based on the conservation of moist entropy and mixing methods of Raymond and Blyth (1986, 1992) are implemented, improving the convection sensitivity to tropospheric moisture and reducing the amplitude of the diurnal cycle of precipitation over land. Sub-grid scale Convective Momentum Transports (CMT) (CMT; Gregory et al., 1997; Richter and Rasch, 2008) are added to the deep convection scheme, resulting in an improved representation of Hadley circulation during northern winter, and reductions in biases in annual means of tropical easterly, subtropical westerly, and excessive southern hemisphere mid-latitude jet (Neale et al., 2010). Moreover, the overall improvement of deep convection-related physics leads to a better representation of the amplitude and spatial anomaly patterns of the simulated El Niño. Additionally, the calculation of cloud fraction in polar climates is modified to the calculation of stratiform cloud following Vavrus and Waliser (2008).

CAM5 (Neale et al., 2010) is used in its coarser horizontal resolution version of $1.9^\circ \times 2.5^\circ$ at 30 vertical levels in the same hybrid sigma-pressure coordinate system as CAM4. In CAM5, a change from an Eulerian to a Lagrangian calculation for vertical advection and a new calculation scheme for cloud microphysics are added. CAM5 contains a substantial range of improvements in the representation of cloud physical processes compared to CAM4 (Neale et al., 2010). New physical parametrizations and processes included in CAM5 enable the model to simulate full cloud-aerosol interaction including cloud droplet activation by aerosols, precipitation processes due to particle size-dependent behavior, and explicit radiative interaction of cloud particles. The new parametrization schemes and processes are: a moist turbulence scheme based on a diagnostic Turbulent Kinetic Energy (TKE) formulation (Bretherton and Park, 2009) which allows simulating full aerosol indirect effects within stratus; a shallow convection scheme that uses a realistic plume dilution equation and closure (Park and Bretherton, 2009) that can accurately simulate the spatial distribution of shallow convective activity; a revised cloud macrophysics scheme that improves treatment of cloud processes (Park et al., 2014); stratiform microphysical processes represented by a prognostic, two-moment formulation for cloud droplet and cloud ice following Morrison and Gettelman (2008); a three-mode model aerosol scheme (Liu and Ghan, 2010); and an update of the radiation scheme to the Rapid Radiative Transfer Method for GCMs (RRTMG; Mlawer et al., 1997; Iacono et al., 2008) that provides a speed-up for long climate integrations.

CLM4 (Lawrence et al., 2011) operates on the same horizontal resolution as CAM4 and 5. For the land subsurface, which includes vegetated land, wetland, and glacier, the model has 15 vertical layers extending from the surface to 35.18 m deep. The vertical layers are not distributed evenly. The upper 1 meter of the subsurface is distributed across the first 8 layers, and the upper 10 meters across the first 12 layers. Unlike the land subsurface, the lake model (Zeng et al., 2002) included in CLM4 simulates with 10 vertical layers which reaches 44.78 m. Compared to the preceding versions CLM3 and CLM3.5, CLM4 is improved in hydrological properties, plant functional type dependency on the soil moisture stress function, and it includes a prognostic carbon and nitrogen cycle. The prognostic carbon and nitrogen cycle is based on the terrestrial biogeochemistry Biome-BGC model (Thornton and Rosenbloom, 2005) and it calculates vegetation, litter, soil carbon, vegetation phenology, and nitrogen states. Further, CLM4 includes a prognostic fire module, which is governed by near-surface soil moisture conditions and fuel availability. It also allows simulating a transient land cover and land-use changes.

POP2 (Smith et al., 2010) succeeds the old version POP, and it operates on nominal 1° horizontal resolution with the North pole displaced into Greenland. In this horizontal resolution system, the longitudinal resolution is approximately 1° and the latitudinal resolutions are various with the finer resolution close to the equator with approximately 0.3°. The vertical resolution is 60 levels distributed from the surface to approximately 5500 m deep. From the surface to 160 m, the layers are separated evenly every 10 m, and below the 160 m, the depth of the layers vary until 5500 m. The improvements in POP2 are: changes to the parametrization for the transition of meso-scale eddies from the deeper ocean to the surface and the introduction of time and space dependent thickness and isopycnal diffusivity coefficients (Danabasoglu and Marshall, 2007; Danabasoglu et al., 2008) that provides a more realistic representation of ocean eddy energy; the adjustment to the vertical mixing terms and the new parametrization for sub-meso-scale eddies that allows more realistic mixing and stratification properties; and a new parametrization improving the penetration depth of deep ocean overflows (Danabasoglu et al., 2010). The new parametrizations including the increase in the vertical resolution of the upper ocean in POP2 improve the representation of ENSO variability, the Atlantic Meridional Overturning Circulation, and the sea surface temperature correlations within the Pacific Ocean (Gent et al., 2011).

CICE4 (Hunke et al., 2010; Bailey et al., 2011) operates on the same horizontal resolution as POP2, and it follows the Community Sea Ice Model, CSIM5, which is based on CICE3. Some technical upgrades in CICE 4 are the incremental remapping transport and mechanical redistribution schemes (Bailey et al., 2011). CICE4 is based on a dynamic-thermodynamic model that includes a subgrid-scale ice thickness distribution (Bitz et al., 2001; Lipscomb, 2001) and energy-conserving thermodynamics (Bitz and Lipscomb, 1999). The ice dynamics relies on the elastic viscous plastic dynamics (Hunke and Dukowicz, 1997).

Several simulations from CESM101 and CESM122 with different configurations have been used in this thesis. Details on the here used simulations are presented in the following sections. More details are given on the external forcings and experimental design for the CESM122 simulations, which were performed under the project "PleistoCEP #172745".

2.2 Implementation of the external forcings in CESM 1.2.2

To simulate the 1501 BCE–2099 CE transient climate using CESM122, proper external forcings based on reconstructions and observations are needed. As external forcings, CESM uses the prescribed spectral solar irradiance (SSI), greenhouse gases concentration (GHG), land use and land-use change (LULUC), and stratospheric volcanic aerosol (VOL) (Fig. 2.1). The Earth's orbital configuration is calculated online in CESM according to (Berger, 1978). The necessary reconstructions for the external forcings are obtained from different sources, then converted to the CESM mountable formats. The here used forcings largely agree with the PMIP3-CMIP5 (Braconnot et al., 2012; Taylor et al., 2012) and PMIP4-CMIP6 (Eyring et al., 2016; Kageyama et al., 2018) protocols for the last millennium experiment (Schmidt et al., 2011; Jungclaus et al., 2017).

Solar Spectral Irradiance (SSI)

For the SSI (Fig. 2.1a), a reconstruction based on cosmogenic ^{14}C isotopes available in PMIP4 repository (`https://pmip4.lsce.ipsl.fr/`, Jungclaus et al., 2017) is used. To generate the pre-industrial total solar irradiance (TSI) and SSI forcings, initially, solar surface magnetic flux and equivalent sunspot numbers are reconstructed from the isotope data through a chain of physics-based models (Vieira et al., 2011; Usoskin et al., 2014, 2016). Then, the 11-year solar cycle is added separately to the reconstructed annual sunspot number by employing statistical relationships relating various properties of the solar cycle based on direct sunspot observations. This reconstructed annual sunspot number with the 11-year cycle is incorporated into a SATIRE-M irradiance model (Vieira et al., 2011) to result a SSI forcing. This pre-industrial SSI is merged to the CMIP6 historical solar forcing (Matthes et al., 2017) which is generated as a mean of SSI resulting from two models, NRLSSI2 (Coddington et al., 2015) and SATIRE (Krivova et al., 2010; Yeo et al., 2015). NRLSSI2 takes observations of TSI and SSI, and SATIRE relies on solar images in visible light, solar magnetic field intensity and polarity, and the sunspot number as input variables. When these inputs are not available, both NRLSSI2 and SATIRE use the sunspot number. The solar cycles for 2015–2099 CE is assumed stationary following Lean and Rind (2009) by repeating the solar cycle from April 1996 to June 2008 CE until 2099 CE as proposed in the CMIP5 experiments (Taylor et al., 2012).

Greenhouse gases (GHG) and aerosols

For the pre-industrial (1501 BCE–1849 CE) well-mixed greenhouse gases (Fig. 2.1b), CH_4, N_2O and CO_2, high-resolution GHG reconstructions based on Greenland and Antarctic ice cores are used. The CH_4 and N_2O records are obtained from Joos and Spahni (2008) which combine Antarctica and Greenland ice cores. These records are already smoothed using a spline with a 40-year cutoff period. Hence, only a decadal and longer variation of CH_4 and N_2O are retained.

For the CO_2, the record is obtained from Bereiter et al. (2015) which bases on the Antarctica Dome C ice cores. The reason for using a different CO_2 record from the one provided by Joos and Spahni (2008) is because the spline fit employed by Joos and Spahni (2008) smoothed out excessively the reduced CO_2 concentration during the Little Ice Age ca. 1600–1800 CE. The CO_2 concentration from Bereiter et al. (2015) exhibits clearly the decreased CO_2 values during this particular period. As the temporal resolution of the CO_2 reconstruction is not uniform over time, its time step is linearly interpolated to the annual resolution. Then, this annually resolved CO_2 time series is smoothed using the cubic spline interpolation to eliminate high-frequency fluctuations.

From 1850 to 2015 CE, the annual GHG are extended using the records from Meinshausen et al. (2017), which follows the CMIP6 protocol. The concentrations of chlorofluorocarbons (Fig. 2.1c) are negligible before the pre-industrial era, and they change from 1850 CE according to Meinshausen et al. (2017). For the GHG concentration from 2015 to 2099 CE, the emission based on RCP8.5 scenario is used. The RCP8.5 represents the "business-as-usual" emission scenario without any strong mitigation attempts, and it corresponds to a forcing scenario of approximately 8.5 W m^{-2} by the end of the 21^{st} century (Moss et al., 2010). Other aerosols such as sulfate, dust, black and organic carbons are set constant up to 1850 CE (Lamarque et al., 2010). The afterward changes are given by Lamarque et al. (2010) in the historical period and by Lamarque et al. (2011) up to 2099 CE.

Land Use and Land Use Change (LULUC)

For LULUC (Fig. 2.1d), the same forcing for the PMIP3-CMIP5 last millennium experiment (Schmidt et al., 2011) is used. The LULUC up to 1500 CE is based on Pongratz et al. (2008). The LULUC is set constant to 850 CE level up to 850 CE and from 850–1500 CE varies following (Pongratz et al., 2008). From 1500 CE, the forcing is merged with a synthesis data from Hurtt et al. (2011) which continues until 2099 CE. The two datasets do not merge smoothly at 1500 CE as each relies on different sources for the past LULUC, thus, showing step-wise changes in the distribution of cropland and pasture (Fig. 2.1d). Pongratz et al. (2008) reconstruction relies on the published maps of agricultural areas and a population-based approach on country level. Hurtt et al. (2011) is reconstructed using the HYDE land-use database v3.1 (Klein Goldewijk et al., 2011) from 1500–2005 CE and afterward, the future LULUC from 2005–2099 CE bases on Integrated Assessment Models (IAM). Nevertheless, the global impacts of the 1500 CE step-wise change can be negligible as the global variability of LULUC is rather small up until 1850 CE, although it can present some regional implications. After 1850 CE, the changes in LULUC is accelerated due to the expansion and crop and pasture continuing until 2099 CE (Hurtt et al., 2011).

Stratospheric Volcanic aerosols (VOL)

The record of volcanic sulfate aerosols from 1501 BCE to 1979 CE is obtained from Sigl et al. (2021) (HolVol), which is a newly compiled re-dated high-resolution record from Greenland and Antarctica. The Holvol dataset covers almost the entire Holocene starting from 9500 BCE. The last 1150 years of the record (Toohey and Sigl, 2017) is the recommended forcing for the PMIP4 last millennium experiment (Jungclaus et al., 2017). In this record, the dating of volcanic eruptions is much improved by using a new method for absolute dating of ice core records (Sigl et al., 2015). For the eruptions whose exact timings of occurrence are not clear, the months of eruptions are set to January. For 1979–2015 CE, a record of sulfate aerosols derived from satellite measurements by Carn et al. (2016) is considered. After 2015 CE, it is assumed that

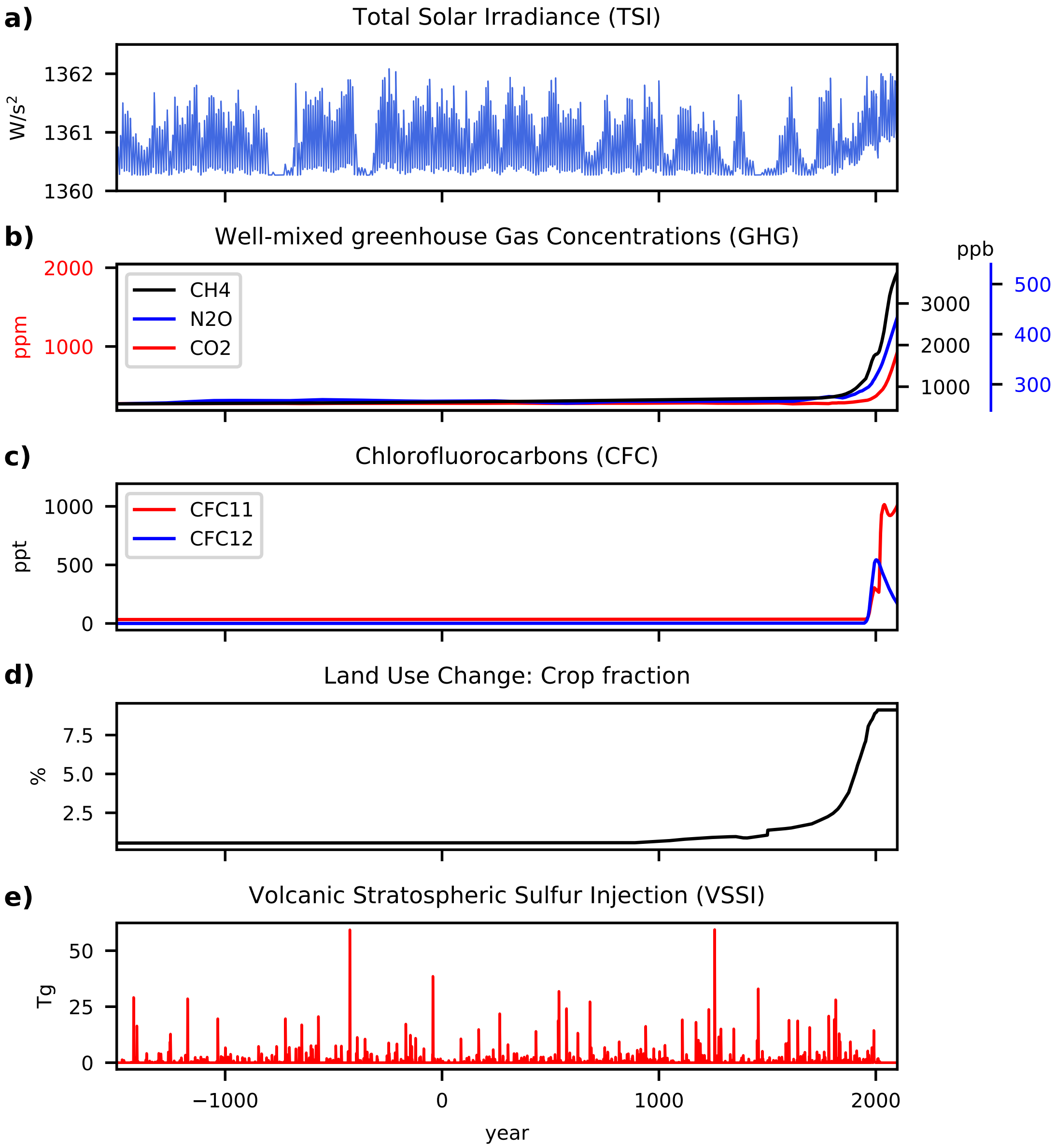

Figure 2.1: Time series of the forcings for 1501BCE–2099CE used for TRA1501.

no volcanic eruption occurs. Both Holvol and Carn's datasets provide information on volcanic eruptions in volcanic stratospheric sulfur injections (VSSI, Fig. 2.1e). As input for a volcanic forcing, CESM uses a prescribed latitudinal and monthly means of stratospheric volcanic aerosols. Hence, the Easy Volcanic Aerosol Model version 1.2 (EVA; Toohey et al., 2016) is employed to generate the temporal, vertical, and latitudinal distribution of volcanic masses that fits CESM. The Holvol and Carn's records are merged and inserted into EVA.

EVA is a three-box model of stratospheric transport that separates the stratosphere into three regions: equatorial, Northern and Southern Hemisphere extratropics (Toohey et al., 2016). The spatial stratospheric aerosol distribution is determined by the superposition of these three zonally symmetric global-scale aerosol plumes. The meridional structure of volcanic aerosol distribution in each region is defined by static Gaussian functions, which are derived from the fits of the aerosol extinction of Pinatubo from the Chemistry-Climate Model Initiative reconstruction (Eyring et al., 2013). The temporal evolution of volcanic sulfate masses in each box bases on a simple single-box model of stratospheric aerosol evolution from Bluth et al. (1997). The evolution of volcanic aerosols depends on the initial injections of SO_2, then the conversion of SO_2 to sulfate aerosols SO_4, the loss of sulfate aerosol to the troposphere, and lastly, the transport of masses between the regions. The transport of aerosols between the regions depends on two time constant τ_{mix}, the rate of two-way mixing, and τ_{res}, the poleward residual circulation. The values of these constant vary sinusoidally with the calendar months. In the end, EVA generates the monthly, vertically, and latitudinally resolved parameters related to the aerosol optical properties. These parameters are the aerosol extinction (EXT) that describes the total attenuation of incident radiation, the single scattering albedo (SSA) that represents the proportion of scattered EXT, the scattering asymmetry factory (ASY) that is the average cosine of scattering angle weighted by the intensity of the scattered light as a function of the angle, and the aerosol optical depth (AOD), calculated as the integral of the vertical profile of EXT (Toohey et al., 2016).

Instead of these optical properties, CESM takes as an input a monthly-resolved, vertical and latitudinal distribution of volcanic aerosols, and it calculates the optical properties of volcanic aerosols for different spectral bands in the radiation part of the model under several assumptions. CESM assumes that volcanic aerosols are composed of 25% water and 75% sulfuric acid, and the aerosol sizes are distributed log-normally with an effective radius of 0.426 μm and σ of 1.25. To make the EVA-generated forcing to a CESM mountable format, a small modification is introduced in the original EVA code. The scheme for the transformation from the sulfate aerosols to the optical properties is excluded, thereby the model can directly produce the distribution of sulfate aerosols. The resulted sulfate aerosol distribution is converted to have the composition of 25% of water and 75% of sulfuric acid, and its vertical coordinate is transformed from the absolute heights in km to the pressure levels in Pa, the isobaric coordinate system. The necessary atmospheric variables for converting to an isobaric coordinate system are obtained from the 200-year climatological mean of the 1501 BCE control simulation (CTR1501).

The resulting volcanic forcing implemented in CESM shows reduced post-volcanic changes of atmospheric temperatures and net solar radiation at the surface compared to the former volcanic forcing used in the PMIP3 last millennium experiment (Schmidt et al., 2011; Lehner et al., 2015; Otto-Bliesner et al., 2016) from Gao et al. (2008). It is assumed that this difference arises from the different temporal and vertical distributions of sulfate aerosols between the two volcanic forcings (For instance, see the 1991 Pinatubo and the 1815 Tambora eruptions of HolVol-EVA (dashed blue lines) and Gao et al. (2008) (black lines) in Fig. 2.2a and b).

Hence, two technical modifications are applied to this 3500-year EVA-based CESM volcanic forcing (from now on, just called the HolVol-EVA forcing) in order to attain a similar atmospheric response for the 1991 Pinatubo eruption to the respective response in Gao et al. (2008) in CESM. For this procedure, the 1991 Pinatubo from HolVol (Sigl et al., 2021) is first

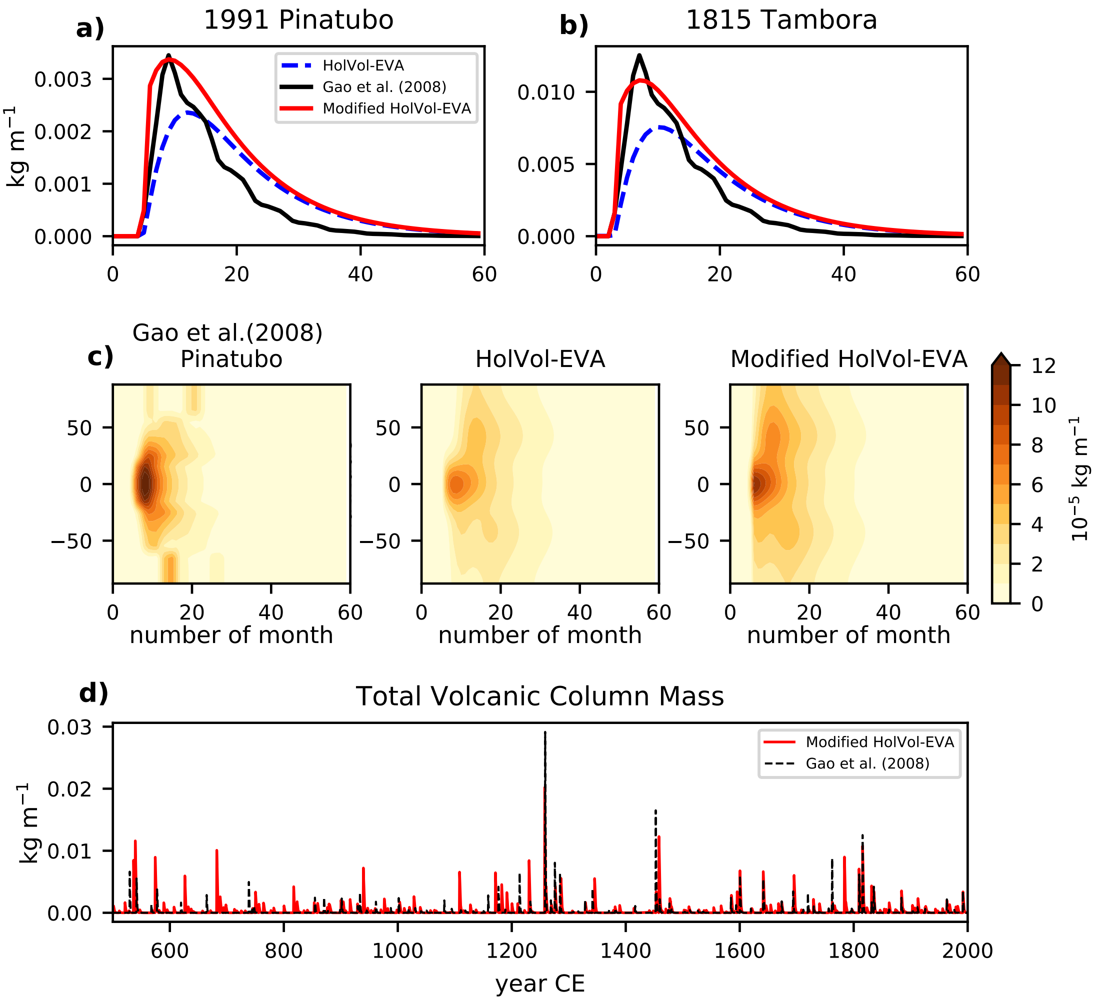

Figure 2.2: Total volcanic aerosol column mass in CESM for (a) the 1991 Pinatubo, and (b) the 1815 Tambora eruptions. Black lines are for Gao et al. (2008), dashed blue lines are for the initial HolVol-EVA's ((Gao et al., 2008)), and red blue lines are the modified HolVol-EVA's forcings. (c) Temporal-latitudinal distribution of volcanic aerosol column mass for Gao et al. (2008)'s, the initial HolVol-EVA's, and the modified HolVol-EVA's forcings. (a) 500–2000 CE time series of volcanic forcings of Gao et al. (2008) (dashed black lines) and HolVol-EVA (red lines).

used for the comparison to Gao et al. (2008)'s Pinatubo (Fig. 2.2a) instead of using Carn et al. (2016). The reason for this is because both HolVol's and Gao et al. (2008)'s Pinatubo eruptions are reconstructed from the Greenland and Antarctica ice cores, while Carn et al. (2016)'s Pinatubo eruption bases purely on the satellite measurement. The sulfate aerosols of the Pinatubo eruption in both reconstructions are then transformed to EVA-based CESM forcings and compared to each other. After comparing these Holvol's and Gao et al. (2008)'s Pinatubo eruptions, the following modifications are applied to the HolVol-EVA volcanic forcing:

First, the total volcanic aerosols are scaled by a factor of 1.49 (Fig. 2.2). The scaling factor is derived by comparing the total amount of volcanic aerosol masses during 10 years after the 1991 Pinatubo in HolVol and Gao et al. (2008), making both have similar total values. A similar scaling approach was used by Zhong et al. (2018) which also used the EVA model to

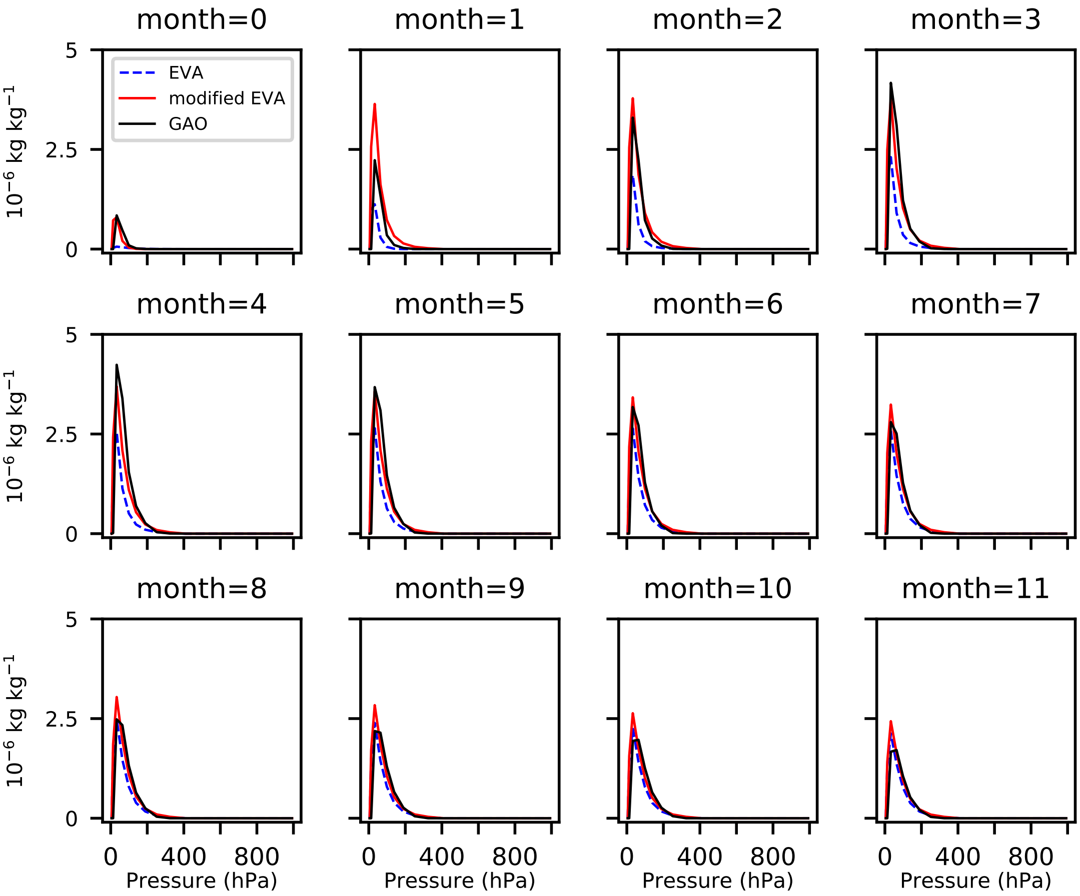

Figure 2.3: Temporal evolution of vertical distribution of volcanic aerosols from the first month of eruption (month=0).

generate a volcanic forcing during the last 2k years. They used a slightly higher scaling factor of 1.79, as the 1815 Tambora eruption was used as reference.

Second, the timing of the maximum peaks of the eruptions is shifted by four months in time after the respective eruption following the approach in Gao et al. (2008) (Fig. 2.2). After this peak, the volcanic aerosols decay smoothly as estimated by EVA. The temporal evolution of the shifted vertical aerosol distribution of HolVol resembles the one of Gao et al. (2008) almost perfectly (Fig. 2.3).

After these modifications, the HolVol-EVA forcing and Gao et al. (2008) show a similar amount of total sulfates for the 1991 Pinatubo eruption (Fig. 2.2d), hence, similar atmospheric responses after this eruption is expected. This scaling does not substantially amplify the effects of other large eruptions in HolVol, as even after the modification, the HoVol-EVA forcing presents less amount of sulfate masses for other large eruptions than Gao et al. (2008). This is also the cases for the 1815 Tambora and the 1257 Samalas eruptions.

2.3 Experimental design

An overview of the configurations for the CESM101 and CESM122 simulations used for the studies in Chapters 3 to 5 is presented in tables 2.1 and 2.2. The descriptions on each of the simulation are given in the following subsections.

2.3.1 Simulation of the period 850 to 2099 CE in CESM 1.0.1

Two CESM101 simulations conducted by Lehner et al. (2015) are used for the study in Chapter 3. The first simulation is the control simulation of 400 year-long with perpetual forcings and the second one is the seamless transient simulation with time-varying external forcings covering 850–2099 CE. The transient simulation is the first simulation with CESM that includes the interactive carbon cycle for the entire last millennium.

The control simulation is run with perpetual external forcings (CTR850 in table 2.1) at 850 CE values except for the orbital parameters. The land use and land-use change (LULUC), total solar irradiance (TSI), and greenhouse gas concentrations (GHG) are set constant at 850 CE values, and the orbital parameters at 1990 CE levels. No volcanic eruption is included in the control simulation.

The transient simulation includes time-varying external forcings (TRA850 in table 2.1) that largely follow the PMIP3 (Schmidt et al., 2011)-CMIP5 (Taylor et al., 2012) protocol. The evolution of GHG concentrations is based on the estimates from high-resolution Antarctic ice cores, later merged with measurements in the mid-20$^{\text{th}}$ century (Schmidt et al., 2011). The LULUC and aerosols are the same as the forcings used in the CESM122 simulations. The volcanic forcing relies on Gao et al. (2008). For the solar forcing, a small modification was introduced in the TSI, by scaling it up by a factor of 2.2635. The scaling was applied according to an enlarged amplitude of TSI in some reconstructions (Shapiro et al., 2011; Schmidt et al., 2012). This scaling makes the amplitude of TSI in CESM by a factor of two larger than those in other PMIP3 simulations. The amplitude of the scaled TSI lies between the reconstruction by Shapiro et al. (2011) and other TSI in the PMIP3 simulations (Schmidt et al., 2011).

2.3.2 Simulation of the period 1501 BCE to 2099 CE in CESM 1.2.2

A newly available long reconstruction of volcanic eruptions reaching the entire past three millennia (1500 BCE–2000 CE) by Sigl et al. (2013, 2015) and Toohey and Sigl (2017) motivated the plan to perform a new seamless simulation with an updated CESM model, CESM122. The plan conducted under the project "PleistoCEP #172745" aimed to assess better the roles of internal and externally forced variability, particularly of the volcanic forcing, on the climate and extreme hydrological events from the past to the future. The time span of the new simulations is from 1501 BCE to 2099 CE covering the period of the reconstructed volcanic eruptions by Sigl et al. (2013, 2015) and Toohey and Sigl (2017). The new transient simulation extends the simulation from Lehner et al. (2015).

Table 2.1: Values of forcings in CESM 1.0.1 simulations

	CESM 1.0.1 (Lehner et al., 2015)	
	CTR850	**TRA850**
time (year)	400	1250 (850–2099 CE)
Orbital	Berger (1978) at 1990 CE	
CO$_2$ (ppm)	279.3	Schmidt et al. (2011) Moss et al. (2010)
CH$_4$ (ppb)	674.5	
N$_2$O (ppb)	266.5	
f11 (ppb)	–	
f12 (ppb)	–	
Aerosol	Lamarque et al. (2010) at 1850 CE	Lamarque et al. (2010, 2011)
TSI (W m^{-2})	1360.228	adjusted Vieira and Solanki (2010)
VOL	–	Gao et al. (2008)
LULUC	Pongratz et al. (2008) at 850 CE	Pongratz et al. (2008) Hurtt et al. (2011)

Table 2.2: Values of forcings in CESM 1.2.2 simulations

	CESM 1.2.2 (McConnell et al., 2020; Kim et al., 2021)			
	CTR1501	**ORB1501**	**TRA1501**	**TRA-ENS**
time (year)	400	3601 (1501BCE–2099 CE)		30 (30–60 BCE)
Orbital	Berger (1978) at 1501 BCE	Berger (1978)		
CO$_2$ (ppm)	274.21		Bereiter et al. (2015) Meinshausen et al. (2017) Moss et al. (2010)	
CH$_4$ (ppb)	572.88		Joos and Spahni (2008) Meinshausen et al. (2017) Moss et al. (2010)	
N$_2$O (ppb)	262.79			
f11 (ppb)	–			
f12 (ppb)	–			
Aerosol	Lamarque et al. (2010) at 1850 CE		Lamarque et al. (2010, 2011)	Lamarque et al. (2010) at 1850 CE
TSI (W m^{-2})	1360.38		Vieira et al. (2011) Usoskin et al. (2014, 2016)	
VOL	–		Sigl et al. (2021) Carn et al. (2016)	
LULUC	Pongratz et al. (2008) at 850 CE		Pongratz et al. (2008) Hurtt et al. (2011)	Pongratz et al. (2008) at 850 CE

It is also important to mention that at the beginning of the project in October of 2017, the record of reconstructed volcanic eruptions covered 1500 BCE–2000 CE (Sigl et al., 2013, 2015; Toohey and Sigl, 2017). Now this record is extended to the almost entire Holocene back to 9500 BCE (HolVol; Sigl et al., 2021), being one of the longest continuous chronologies of volcanic eruptions available for scientific use.

Three CESM122 simulations were conducted to be used for the study in Chapter 4: a control simulation with perpetual external forcings at 1501 BCE values (CTR1501 in table 2.2), a simulation with all external forcings set constant at 1501 BCE values same as CTR1501 but with the time-varying orbital parameters for 1501 BCE–2008 CE (ORB1501 in table 2.2), and a transient simulation with all time-varying external forcings also for 1501 BCE–2008 CE (TRA1501 in table 2.2). Unlike the CESM101 simulations in Chapter 3, these simulations include CAM5 and do not contain an active carbon cycle but a prognostic carbon and nitrogen cycle.

Before conducting the control and transient simulations, a spin-up simulation with perpetual external forcings at 1501 BCE was initiated from the restart file with the perpetual 850 CE climate condition. The corresponding restart file was obtained from the CESM repository (`https://svn-ccsm-models.cgd.ucar.edu`). In the spin-up simulation, all the external forcings were set constant at 1501 BCE values except the LULUC. The LULUC was set to the reconstructed condition at 850 CE (Pongratz et al., 2008). The values of the external forcings at 1501 BCE clearly differ from those at 850 CE (table. 2.2). Therefore, the spin-up simulation was needed to be run until the variables related to the atmospheric radiative balance and ocean conditions were adjusted to the new climate conditions. Whether the climate was adjusted to the new condition was evaluated by examining the trends of the globally and hemispherically averaged annual mean atmosphere and ocean temperatures at different levels, and the annual mean net shortwave surface radiation. The trends of these variables for the last 100 years of the runs were estimated and tested through the Mann-Kendall trend (M-K) tests at 99% confidence interval (Mann, 1945). The M-K test is valid for non-parametric distributions, and its null hypothesis states the existence of a monotonic trend in a time series. The null hypothesis must be accepted at a given confidence interval to confirm that a variable has reached an equilibrium, thus, no apparent monotonic trend is present in the time series of the variable. This indicates that the climate is already adjusted to the new forcing conditions.

The atmospheric temperatures and the net surface radiation had reached acceptable equilibrium states after a few hundred years of the simulated years. However, the ocean, particularly the deep subsurface levels, reacts slowly to the changes caused by the forcings compared to the atmosphere and land due to its large thermal inertia. Therefore, it is expected that the ocean variables take much longer to achieve a radiative stability. Because of the technical limitation related to the available computational resources, it was not possible to continue the spin-up simulation until the deep ocean layers reached a full equilibrium state. Hence, the simulation was run until the mean temperature of the surface ocean layer (from 0 to 500 m) did not show any statistically significant drift, while other deep layers were allowed presenting some monotonic trends with a magnitude of less than 0.05°C per century. To achieve this condition, the spin-up simulation was run for 1463 model years.

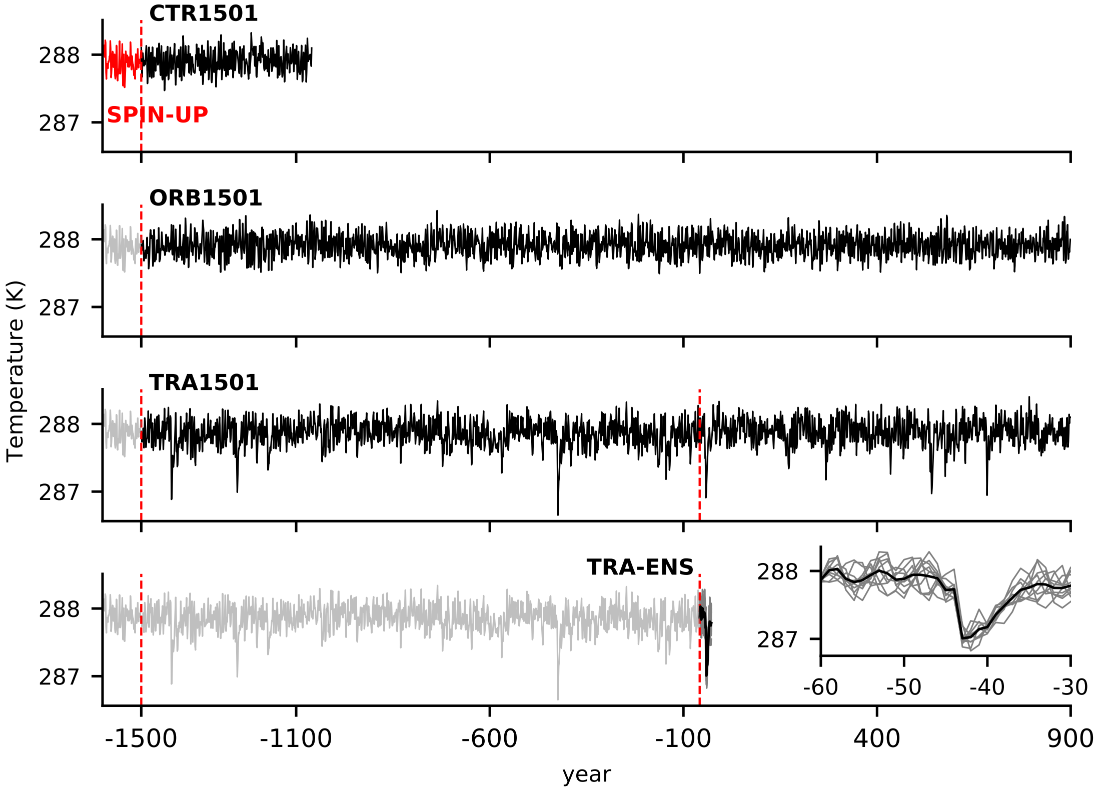

Figure 2.4: Overview of simulations performed in CESM 1.2.2 illustrated using the annually averaged global surface temperature. For the spin-up simulation only the last 100 years of the simulated years are shown (in red), and for the transient simulations from 1501 BCE to 900 CE. Red vertical lines indicate where the control and transient simulations are branched off from the spin-up simulation, and where the TRA-ENS is branched off from TRA1501.

From the model year 1463, the simulation was continued for another 400 model years to produce the control simulation with perpetual 1501 BCE conditions and with the LULUC at 850 CE (Table 2.2 and Fig. 2.4). From the same year, the two transient simulations, ORB1501 and TRA1501, were branched off and run continuously until 2099 CE (Fig. 2.4). ORB1501 shares the same configuration with the control simulation, but only the orbital parameters, the eccentricity, the obliquity, and the longitude of perihelion, vary with time following Berger (1978). TRA1501 contains all time-varying external forcings shown in Fig. 2.1.

2.3.3 Initial condition ensemble simulations for the period 60 BCE to 30 CE

The study in Chapter 5 is based on an ensemble of ten transient simulations from CESM122 for the period 60 BCE–30 CE (TRA-ENS in table 2.2). To start the ensemble, ten simulations are branched off from 60BCE in TRA1501 (Fig. 2.4). Then, a small temperature perturbation is introduced at the first time step in the atmosphere to generate the ensemble members.

The introduced temperature perturbations vary from 1.10^{-14} to 1.10^{-13} K and increase monotonically with ΔT of 1.10^{-14} K for each ensemble member. The simulations are continuously run with the same time-varying external forcings as TRA1501 but only for the period up to 30 BCE. This 30-year period includes three volcanic eruptions occurred in 45 BCE, 43 BCE (The Okmok eruption) and 34 BCE, all in the Northern Hemisphere.

2.4 Proxy records and observations

Several natural proxy reconstructions, observational-based and reanalysis data are used, first to understand better the past and present climate mechanisms together with the CESM output, and second, to validate the past simulated climate by CESM. The datasets are the tree-ring-based reconstructions of summer drought and wetness, also known as Old World Drought Atlas (OWDA; Cook et al., 2015), the University of Delaware Air Temperature and Precipitation version 5.01 (U.Del; Willmott and Matsuura, 2001), both used for the study in Chapter 3, and the ERA5 reanalysis (Hersbach et al., 2020) for Chapter 4.

The OWDA (Cook et al., 2015) is a reconstructed gridded map of the summer season self-calibrated Palmer Severity Drought Index (scPDSI; Wells et al., 2004) based on the tree-ring network in Europe, North Africa, and the Middle East. The map covers the areas of 27.25°N–70.75°N and 11.75°W–44.75°E and it is resolved at half-degree longitude-by-latitude. The temporal resolution is annual providing mean summer season hydroclimate conditions from 0 to 2000 CE. The OWDA is generated with a regression-based climate field of reconstructions which is calibrated for 1928–1978 CE. The reconstructed values are validated against the instrumental scPDSI for the period 1901 – 1928 CE. The OWDA shows a good coherence with some historical extreme hydrological episodes such as the 1921 drought and the great European famine of 1315—1317 CE caused by an abnormally wet climate condition. This dataset is employed to understand past hydroclimate conditions over the Mediterranean region together with the CESM101 simulations in Chapter 3.

The U.Del (Willmott and Matsuura, 2001) is the monthly climatology of gridded station data for air temperatures and precipitation over land, and it covers the period 1900–2014 CE. It is a compilation of monthly station data from several sources which includes the Global Historical Climatology Network (GHCN2; Peterson and Vose, 1997) and the archive of Legates and Willmott (Legates and Willmott, 1990). The compiled temperature and precipitation data are interpolated to the spatial resolution of a half-degree longitude-by-latitude grid. The datasets are provided by the NOAA/OAR/ESRL PSL from their website `https://psl.noaa.gov/data/gridded/data.UDel_AirT_Precip.html`. This U.Del temperature and precipitation are employed to calculate the scPDSI in order to validate the CESM101 simulations in Chapter 3.

The ERA5 (Hersbach et al., 2020) is the latest reanalysis product of ECMWF that covers the period from 1979 CE to the present. ERA5 uses the 2016 version of the ECMWF numerical weather prediction model and the integrated forecasting system Cy41r2 data assimilation (Hersbach et al., 2020). The datasets are provided by the Copernicus Climate Data store `https://www.ecmwf.int/en/forecasts/datasets/reanalysis-datasets/era5`. From ERA5, the total precipitation at a temporal resolution of an hour and a spatial resolution of 0.75° x 0.75° is used to validate extreme daily precipitation output in the CESM122 simulations in Chapter 4.

References

Bailey, D., Holland, M., Hunke, E., Lipscomb, B., Briegleb, B., Bitz, C., and Schramm, J.: Community Ice CodE (CICE) user's guide version 4.0 released with CCSM 4.0, Tech. rep., Tech. rep., Los Alamos National Library, URL `https://www.cesm.ucar.edu/models/ccsm4.0/cice/doc/index.html`, 2011.

Bereiter, B., Eggleston, S., Schmitt, J., Nehrbass-Ahles, C., Stocker, T. F., Fischer, H., Kipfstuhl, S., and Chappellaz, J.: Revision of the EPICA Dome C CO2 record from 800 to 600 kyr before present, Geophysical Research Letters, 42, 542–549, 2015.

Berger, A.: Long-term variations of daily insolation and Quaternary climatic changes, Journal of Atmospheric Sciences, 35, 2362–2367, doi:10.1175/1520-0469(1978)035⟨2362:LTVODI⟩2.0.CO;2, 1978.

Bitz, C., Holland, M., Weaver, A., and Eby, M.: Simulating the ice-thickness distribution in a coupled climate model, Journal of Geophysical Research: Oceans, 106, 2441–2463, doi:10.1029/1999JC000113, 2001.

Bitz, C. M. and Lipscomb, W. H.: An energy-conserving thermodynamic model of sea ice, Journal of Geophysical Research: Oceans, 104, 15 669–15 677, doi:10.1029/1999JC900100, 1999.

Bluth, G. J., Rose, W. I., Sprod, I. E., and Krueger, A. J.: Stratospheric loading of sulfur from explosive volcanic eruptions, The Journal of Geology, 105, 671–684, 1997.

Braconnot, P., Harrison, S. P., Kageyama, M., Bartlein, P. J., Masson-Delmotte, V., Abe-Ouchi, A., Otto-Bliesner, B., and Zhao, Y.: Evaluation of climate models using palaeoclimatic data, Nature Climate Change, 2, 417–424, doi:10.1038/nclimate1456, 2012.

Bretherton, C. S. and Park, S.: A new moist turbulence parameterization in the Community Atmosphere Model, Journal of Climate, 22, 3422–3448, doi:10.1175/2008JCLI2556.1, 2009.

Carn, S., Clarisse, L., and Prata, A. J.: Multi-decadal satellite measurements of global volcanic degassing, Journal of Volcanology and Geothermal Research, 311, 99–134, doi:10.1016/j.jvolgeores.2016.01.002, 2016.

Coddington, O., Lean, J., Lindholm, D., Pilewskie, P., and Snow, M.: Program: NOAA Climate Data Record (CDR) of Solar Spectral Irradiance (SSI), Version 2. NOAA National Centers for Environmental Information, doi:10.7289/V51J97P6, 2015.

Cook, E. R., Seager, R., Kushnir, Y., Briffa, K. R., Büntgen, U., Frank, D., Krusic, P. J., Tegel, W., van der Schrier, G., Andreu-Hayles, L., et al.: Old World megadroughts and pluvials during the Common Era, Science advances, 1, e1500 561, doi:10.1126/sciadv.1500561, 2015.

Danabasoglu, G. and Marshall, J.: Effects of vertical variations of thickness diffusivity in an ocean general circulation model, Ocean Modelling, 18, 122–141, doi:10.1016/j.ocemod.2007.03.006, 2007.

Danabasoglu, G., Ferrari, R., and McWilliams, J. C.: Sensitivity of an ocean general circulation model to a parameterization of near-surface eddy fluxes, Journal of Climate, 21, 1192–1208, doi:10.1175/2007JCLI1508.1, 2008.

Danabasoglu, G., Large, W. G., and Briegleb, B. P.: Climate impacts of parameterized Nordic Sea overflows, Journal of Geophysical Research: Oceans, 115, doi:10.1029/2010JC006243, 2010.

Eyring, V., Lamarque, J.-F., Hess, P., Arfeuille, F., Bowman, K., Chipperfiel, M. P., Duncan, B., Fiore, A., Gettelman, A., Giorgetta, M. A., et al.: Overview of IGAC/SPARC Chemistry-Climate Model Initiative (CCMI) community simulations in support of upcoming ozone and climate assessments, SPARC newsletter, 40, 48–66, URL `http://oceanrep.geomar.de/id/eprint/20227`, 2013.

Eyring, V., Bony, S., Meehl, G. A., Senior, C. A., Stevens, B., Stouffer, R. J., and Taylor, K. E.: Overview of the Coupled Model Intercomparison Project Phase 6 (CMIP6) experimental design and organization, Geoscientific Model Development, 9, 1937–1958, doi:10.5194/gmd-9-1937-2016, 2016.

Gao, C., Robock, A., and Ammann, C.: Volcanic forcing of climate over the past 1500 years: An improved ice core-based index for climate models, Journal of Geophysical Research: Atmospheres, 113, doi:10.1029/2008JD010239, 2008.

Gent, P. R., Danabasoglu, G., Donner, L. J., Holland, M. M., Hunke, E. C., Jayne, S. R., Lawrence, D. M., Neale, R. B., Rasch, P. J., Vertenstein, M., et al.: The community climate system model version 4, Journal of climate, 24, 4973–4991, doi:10.1175/2011JCLI4083.1, 2011.

Gregory, D., Kershaw, R., and Inness, P.: Parametrization of momentum transport by convection. II: Tests in single-column and general circulation models, Quarterly Journal of the Royal Meteorological Society, 123, 1153–1183, doi:10.1002/qj.49712354103, 1997.

Hersbach, H., Bell, B., Berrisford, P., Hirahara, S., Horányi, A., Muñoz-Sabater, J., Nicolas, J., Peubey, C., Radu, R., Schepers, D., Simmons, A., Soci, C., Abdalla, S., Abellan, X., Balsamo, G., Bechtold, P., Biavati, G., Bidlot, J., Bonavita, M., Chiara, G. D., Dahlgren, P., Dee, D., Diamantakis, M., Dragani, R., Flemming, J., Forbes, R., Fuentes, M., Geer, A., Haimberger, L., Healy, S., Hogan, R. J., Hólm, E., Janisková, M., Keeley, S., Laloyaux, P., Lopez, P., Lupu, C., Radnoti, G., Rosnay, P. d., Rozum, I., Vamborg, F., Villaume, S., and Thépaut, J.-N.: The ERA5 global reanalysis, Quarterly Journal of the Royal Meteorological Society, 146, 1999–2049, doi:10.1002/qj.3803, 2020.

Hunke, E. C. and Dukowicz, J. K.: An elastic–viscous–plastic model for sea ice dynamics, Journal of Physical Oceanography, 27, 1849–1867, doi:10.1175/1520-0485(1997)027⟨1849:AEVPMF⟩2.0.CO;2, 1997.

Hunke, E. C., Lipscomb, W. H., Turner, A. K., Jeffery, N., and Elliott, S.: CICE: the Los Alamos Sea Ice Model Documentation and Software User's Manual Version 4.1 LA-CC-06-012, T-3 Fluid Dynamics Group, Los Alamos National Laboratory, 675, URL `http://www.ccpo.odu.edu/~klinck/Reprints/PDF/cicedoc2015.pdf`, 2010.

Hurrell, J. W., Holland, M. M., Gent, P. R., Ghan, S., Kay, J. E., Kushner, P. J., Lamarque, J.-F., Large, W. G., Lawrence, D., Lindsay, K., Lipscomb, W. H., Long, M. C., Mahowald, N., Marsh, D. R., Neale, R. B., Rasch, P., Vavrus, S., Vertenstein, M., Bader, D., Collins, W. D., Hack, J. J., Kiehl, J., and Marshall, S.: The community earth system model: a framework for collaborative research, Bulletin of the American Meteorological Society, 94, 1339–1360, doi:10.1175/BAMS-D-12-00121.1, 2013.

Hurtt, G. C., Chini, L. P., Frolking, S., Betts, R., Feddema, J., Fischer, G., Fisk, J., Hibbard, K., Houghton, R., Janetos, A., et al.: Harmonization of land-use scenarios for the period 1500–2100: 600 years of global gridded annual land-use transitions, wood harvest, and resulting secondary lands, Climatic change, 109, 117–161, doi:10.1007/s10584-011-0153-2, 2011.

Iacono, M. J., Delamere, J. S., Mlawer, E. J., Shephard, M. W., Clough, S. A., and Collins, W. D.: Radiative forcing by long-lived greenhouse gases: Calculations with the AER radiative transfer models, Journal of Geophysical Research: Atmospheres, 113, doi:10.1029/2008JD009944, 2008.

Joos, F. and Spahni, R.: Rates of change in natural and anthropogenic radiative forcing over the past 20,000 years, Proceedings of the National Academy of Sciences, 105, 1425–1430, doi:10.1073/pnas.0707386105, 2008.

Jungclaus, J. H., Bard, E., Baroni, M., Braconnot, P., Cao, J., Chini, L. P., Egorova, T., Evans, M., González-Rouco, J. F., Goosse, H., Hurtt, G. C., Joos, F., Kaplan, J. O., Khodri, M., Klein Goldewijk, K., Krivova, N., LeGrande, A. N., Lorenz, S. J., Luterbacher, J., Man, W., Maycock, A. C., Meinshausen, M., Moberg, A., Muscheler, R., Nehrbass-Ahles, C., Otto-Bliesner, B. I., Phipps, S. J., Pongratz, J., Rozanov, E., Schmidt, G. A., Schmidt, H., Schmutz, W., Schurer, A., Shapiro, A. I., Sigl, M., Smerdon, J. E., Solanki, S. K., Timmreck, C., Toohey, M., Usoskin, I. G., Wagner, S., Wu, C.-J., Yeo, K. L., Zanchettin, D., Zhang, Q., and Zorita, E.: The PMIP4 contribution to CMIP6–Part 3: The last millennium, scientific objective, and experimental design for the PMIP4 past1000 simulations, Geoscientific Model Development, 10, 4005–4033, doi:10.5194/gmd-10-4005-2017, 2017.

Kageyama, M., Braconnot, P., Harrison, S. P., Haywood, A. M., Jungclaus, J. H., Otto-Bliesner, B. L., Peterschmitt, J.-Y., Abe-Ouchi, A., Albani, S., Bartlein, P. J., et al.: The PMIP4 contribution to CMIP6–Part 1: Overview and over-arching analysis plan, Geoscientific Model Development, 11, 1033–1057, doi:10.5194/gmd-11-1033-2018, 2018.

Kim, W. M., Blender, R., Sigl, M., Messmer, M., and Raible, C. C.: Statistical characteristics of extreme daily precipitation during 1501 BCE–1849 CE in the Community Earth System Model, Climate of the Past Discussions, pp. 1–38, doi:10.5194/cp-2021-61, 2021.

Klein Goldewijk, K., Beusen, A., Van Drecht, G., and De Vos, M.: The HYDE 3.1 spatially explicit database of human-induced global land-use change over the past 12,000 years, Global Ecology and Biogeography, 20, 73–86, doi:10.1111/j.1466-8238.2010.00587.x, 2011.

Krivova, N., Vieira, L., and Solanki, S.: Reconstruction of solar spectral irradiance since the Maunder minimum, Journal of Geophysical Research: Space Physics, 115, doi:10.1029/2010JA015431, 2010.

Lamarque, J.-F., Bond, T. C., Eyring, V., Granier, C., Heil, A., Klimont, Z., Lee, D., Liousse, C., Mieville, A., Owen, B., et al.: Historical (1850–2000) gridded anthropogenic and biomass burning emissions of reactive gases and aerosols: methodology and application, Atmospheric Chemistry and Physics, 10, 7017–7039, doi:10.5194/acp-10-7017-2010, 2010.

Lamarque, J.-F., Kyle, G. P., Meinshausen, M., Riahi, K., Smith, S. J., van Vuuren, D. P., Conley, A. J., and Vitt, F.: Global and regional evolution of short-lived radiatively-active gases and aerosols in the Representative Concentration Pathways, Climatic change, 109, 191–212, doi:10.1007/s10584-011-0155-0, 2011.

Lawrence, D. M., Oleson, K. W., Flanner, M. G., Thornton, P. E., Swenson, S. C., Lawrence, P. J., Zeng, X., Yang, Z.-L., Levis, S., Sakaguchi, K., et al.: Parameterization improvements and functional and structural advances in version 4 of the Community Land Model, Journal of Advances in Modeling Earth Systems, 3, doi:10.1029/2011MS00045, 2011.

Lean, J. L. and Rind, D. H.: How will Earth's surface temperature change in future decades?, Geophysical research letters, 36, doi:10.1029/2009GL038932, 2009.

Legates, D. R. and Willmott, C. J.: Mean seasonal and spatial variability in gauge-corrected, global precipitation, International Journal of Climatology, 10, 111–127, doi:10.1002/joc.3370100202, 1990.

Lehner, F., Joos, F., Raible, C. C., Mignot, J., Born, A., Keller, K. M., and Stocker, T. F.: Climate and carbon cycle dynamics in a CESM simulation from 850 to 2100 CE, Earth system dynamics, 6, 411–434, doi:10.5194/esd-6-411-2015, 2015.

Lin, S.-J. and Rood, R. B.: Multidimensional flux-form semi-Lagrangian transport schemes, Monthly Weather Review, 124, 2046–2070, doi:10.1175/1520-0493(1996)124⟨2046:MFFSLT⟩2.0.CO;2, 1996.

Lipscomb, W. H.: Remapping the thickness distribution in sea ice models, Journal of Geophysical Research: Oceans, 106, 13 989–14 000, doi:10.1029/2000JC000518, 2001.

Liu, X. and Ghan, S.: A modal aerosol model implementation in the Community Atmosphere 4741 Model, version 5 (CAM5), J. Atmos. Sci, 4742, 2010.

Mann, H. B.: Nonparametric tests against trend, Econometrica: Journal of the econometric society, pp. 245–259, doi:10.2307/1907187, 1945.

Matthes, K., Funke, B., Andersson, M. E., Barnard, L., Beer, J., Charbonneau, P., Clilverd, M. A., Dudok de Wit, T., Haberreiter, M., Hendry, A., et al.: Solar forcing for CMIP6 (v3. 2), Geoscientific Model Development, 10, 2247–2302, doi:10.5194/gmd-10-2247-2017, 2017.

McConnell, J. R., Sigl, M., Plunkett, G., Burke, A., Kim, W. M., Raible, C. C., Wilson, A. I., Manning, J. G., Ludlow, F., Chellman, N. J., et al.: Extreme climate after massive eruption of Alaska's Okmok volcano in 43 BCE and effects on the late Roman Republic and Ptolemaic Kingdom, Proceedings of the National Academy of Sciences, 117, 15 443–15 449, doi:10.1073/pnas.2002722117, 2020.

Meinshausen, M., Vogel, E., Nauels, A., Lorbacher, K., Meinshausen, N., Etheridge, D. M., Fraser, P. J., Montzka, S. A., Rayner, P. J., Trudinger, C. M., Krummel, P. B., Beyerle, U., Canadell, J. G., Daniel, J. S., Enting, I. G., Law, R. M., Lunder, C. R., O'Doherty, S., Prinn, R. G., Reimann, S., Rubino, M., Velders, G. J. M., Vollmer, M. K., Wang, R. H. J., and Weiss, R.: Historical greenhouse gas concentrations for climate modelling (CMIP6), Geoscientific Model Development, 10, 2057–2116, doi:10.5194/gmd-10-2057-2017, publisher: Copernicus GmbH, 2017.

Mlawer, E. J., Taubman, S. J., Brown, P. D., Iacono, M. J., and Clough, S. A.: Radiative transfer for inhomogeneous atmospheres: RRTM, a validated correlated-k model for the longwave, Journal of Geophysical Research: Atmospheres, 102, 16 663–16 682, doi:10.1029/97JD00237, 1997.

Morrison, H. and Gettelman, A.: A new two-moment bulk stratiform cloud microphysics scheme in the Community Atmosphere Model, version 3 (CAM3). Part I: Description and numerical tests, Journal of Climate, 21, 3642–3659, doi:10.1175/2008JCLI2105.1, 2008.

Moss, R. H., Edmonds, J. A., Hibbard, K. A., Manning, M. R., Rose, S. K., Van Vuuren, D. P., Carter, T. R., Emori, S., Kainuma, M., Kram, T., et al.: The next generation of scenarios for climate change research and assessment, Nature, 463, 747–756, doi:10.1038/nature08823, 2010.

Neale, R. B., Chen, C.-C., Gettelman, A., Lauritzen, P. H., Park, S., Williamson, D. L., Conley, A. J., Garcia, R., Kinnison, D., and Lamarque, J.-F.: Description of the NCAR community atmosphere model (CAM 5.0), NCAR Tech. Note NCAR/TN-486+ STR, 1, 1–12, 2010.

Otto-Bliesner, B. L., Brady, E. C., Fasullo, J., Jahn, A., Landrum, L., Stevenson, S., Rosenbloom, N., Mai, A., and Strand, G.: Climate variability and change since 850 CE: An ensemble approach with the Community Earth System Model, Bulletin of the American Meteorological Society, 97, 735–754, doi:10.1175/BAMS-D-14-00233.1, 2016.

Park, S. and Bretherton, C. S.: The University of Washington shallow convection and moist turbulence schemes and their impact on climate simulations with the Community Atmosphere Model, Journal of Climate, 22, 3449–3469, doi:10.1175/2008JCLI2557.1, 2009.

Park, S., Bretherton, C. S., and Rasch, P. J.: Integrating cloud processes in the Community Atmosphere Model, version 5, Journal of Climate, 27, 6821–6856, doi:10.1175/JCLI-D-14-00087.1, 2014.

Peterson, T. C. and Vose, R. S.: An overview of the Global Historical Climatology Network temperature database, Bulletin of the American Meteorological Society, 78, 2837–2850, doi:10.1175/1520-0477(1997)078⟨2837:AOOTGH⟩2.0.CO;2, 1997.

Pongratz, J., Reick, C., Raddatz, T., and Claussen, M.: A reconstruction of global agricultural areas and land cover for the last millennium, Global Biogeochemical Cycles, 22, doi:10.1029/2007GB003153, 2008.

Raymond, D. J. and Blyth, A. M.: A stochastic mixing model for nonprecipitating cumulus clouds, Journal of Atmospheric Sciences, 43, 2708–2718, doi:10.1175/1520-0469(1986)043⟨2708:ASMMFN⟩2.0.CO;2, 1986.

Raymond, D. J. and Blyth, A. M.: Extension of the stochastic mixing model to cumulonimbus clouds, Journal of Atmospheric Sciences, 49, 1968–1983, doi:10.1175/1520-0469(1992)049⟨1968:EOTSMM⟩2.0.CO;2, 1992.

Richter, J. H. and Rasch, P. J.: Effects of convective momentum transport on the atmospheric circulation in the Community Atmosphere Model, version 3, Journal of Climate, 21, 1487–1499, doi:10.1175/2007JCLI1789.1, 2008.

Schmidt, G., Jungclaus, J. H., Ammann, C., Bard, E., Braconnot, P., Crowley, T., Delaygue, G., Joos, F., Krivova, N., Muscheler, R., et al.: Climate forcing reconstructions for use in PMIP simulations of the Last Millennium (v1. 1), Geoscientific Model Development, 5, 185–191, doi:10.5194/gmd-5-185-2012, 2012.

Schmidt, G. A., Jungclaus, J. H., Ammann, C. M., Bard, E., Braconnot, P., Crowley, T. J., Delaygue, G., Joos, F., Krivova, N. A., Muscheler, R., Otto-Bliesner, B. L., Pongratz, J., Shindell, D. T., Solanki, S. K., Steinhilber, F., and Vieira, L. E. A.: Climate forcing reconstructions for use in PMIP simulations of the last millennium (v1. 0), Geoscientific Model Development, 4, 33–45, doi:10.5194/gmd-4-33-2011, 2011.

Shapiro, A., Schmutz, W., Rozanov, E., Schoell, M., Haberreiter, M., Shapiro, A., and Nyeki, S.: A new approach to the long-term reconstruction of the solar irradiance leads to large historical solar forcing, Astronomy & Astrophysics, 529, A67, doi:10.1051/0004-6361/201016173, 2011.

Sigl, M., McConnell, J. R., Layman, L., Maselli, O., McGwire, K., Pasteris, D., Dahl-Jensen, D., Steffensen, J. P., Vinther, B., Edwards, R., et al.: A new bipolar ice core record of volcanism from WAIS Divide and NEEM and implications for climate forcing of the last 2000 years, Journal of Geophysical Research: Atmospheres, 118, 1151–1169, doi:10.1029/2012JD018603, 2013.

Sigl, M., Winstrup, M., McConnell, J. R., Welten, K. C., Plunkett, G., Ludlow, F., Büntgen, U., Caffee, M., Chellman, N., Dahl-Jensen, D., et al.: Timing and climate forcing of volcanic eruptions for the past 2,500 years, Nature, 523, 543–549, doi:10.1038/nature14565, 2015.

Sigl, M., Toohey, M., McConnell, J. R., Cole-Dai, J., and Severi, M.: HolVol: Reconstructed volcanic stratospheric sulfur injections and aerosol optical depth for the Holocene (9500 BCE to 1900 CE), doi:10.1594/PANGAEA.928646(DOIregistrationinprogress), last access = 5 May 2021, 2021.

Smith, R., Jones, P., Briegleb, B., Bryan, F., Danabasoglu, G., Dennis, J., Dukowicz, J., Eden, C., Fox-Kemper, B., Gent, P., Hecht, M., Jayne, S., Jochum, M., Large, W., Lindsay, K., Maltrud, M., Norton, N., Peacock, S., Vertenstein, M., and Yeager, S.: The parallel ocean program (POP) reference manual ocean component of the community climate system model (CCSM) and community earth system model (CESM), LAUR-01853, 141, 1–140, 2010.

Taylor, K. E., Stouffer, R. J., and Meehl, G. A.: An overview of CMIP5 and the experiment design, Bulletin of the American meteorological Society, 93, 485–498, doi:10.1175/BAMS-D-11-00094.1, 2012.

Thornton, P. E. and Rosenbloom, N. A.: Ecosystem model spin-up: Estimating steady state conditions in a coupled terrestrial carbon and nitrogen cycle model, Ecological Modelling, 189, 25–48, doi:10.1016/j.ecolmodel.2005.04.008, 2005.

Toohey, M. and Sigl, M.: Volcanic stratospheric sulfur injections and aerosol optical depth from 500 BCE to 1900 CE, Earth System Science Data, 9, 809–831, doi:10.5194/essd-9-809-2017, 2017.

Toohey, M., Stevens, B., Schmidt, H., and Timmreck, C.: Easy Volcanic Aerosol (EVA v1. 0): an idealized forcing generator for climate simulations, Geoscientific Model Development, 9, 4049–4070, doi:10.5194/gmd-9-4049-2016, 2016.

Usoskin, I., Hulot, G., Gallet, Y., Roth, R., Licht, A., Joos, F., Kovaltsov, G., Thébault, E., and Khokhlov, A.: Evidence for distinct modes of solar activity, Astronomy & Astrophysics, 562, L10, doi:10.1051/0004-6361/201423391, 2014.

Usoskin, I., Gallet, Y., Lopes, F., Kovaltsov, G., and Hulot, G.: Solar activity during the Holocene: the Hallstatt cycle and its consequence for grand minima and maxima, Astronomy & Astrophysics, 587, A150, doi:10.1051/0004-6361/201527295, 2016.

Vavrus, S. and Waliser, D.: An improved parameterization for simulating Arctic cloud amount in the CCSM3 climate model, Journal of Climate, 21, 5673–5687, doi:10.1175/2008JCLI2299.1, 2008.

Vieira, L. E. A. and Solanki, S. K.: Evolution of the solar magnetic flux on time scales of years to millenia, Astronomy & Astrophysics, 509, A100, doi:10.1051/0004-6361/200913276, 2010.

Vieira, L. E. A., Solanki, S. K., Krivova, N. A., and Usoskin, I.: Evolution of the solar irradiance during the Holocene, Astronomy & Astrophysics, 531, A6, doi:10.1051/0004-6361/201015843, 2011.

Wells, N., Goddard, S., and Hayes, M. J.: A Self-Calibrating Palmer Drought Severity Index, Journal of Climate, 17, 2335–2351, doi:10.1175/1520-0442(2004)017⟨2335:ASPDSI⟩2.0.CO;2, 2004.

Willmott, C. J. and Matsuura, K.: Terrestrial air temperature and precipitation: Monthly and annual time series (1950–1999) Version 1.02, Center for Climatic Research, University of Delaware, Newark, 1155, URL `http://climate.geog.udel.edu/~climate/html_pages/README.ghcn_ts2.html.`, 2001.

Yeo, K., Ball, W., Krivova, N., Solanki, S., Unruh, Y., and Morrill, J.: UV solar irradiance in observations and the NRLSSI and SATIRE-S models, Journal of Geophysical Research: Space Physics, 120, 6055–6070, doi:10.1002/2015JA021277, 2015.

Zeng, X., Shaikh, M., Dai, Y., Dickinson, R. E., and Myneni, R.: Coupling of the common land model to the NCAR community climate model, Journal of Climate, 15, 1832–1854, doi:10.1175/1520-0442(2002)015⟨1832:COTCLM⟩2.0.CO;2, 2002.

Zhong, Y., Jahn, A., Miller, G., and Geirsdottir, A.: Asymmetric Cooling of the Atlantic and Pacific Arctic During the Past Two Millennia: A Dual Observation-Modeling Study, Geophysical Research Letters, 45, 12–497, doi:10.1029/2018GL079447, 2018.

Chapter 3

Dynamics of the Mediterranean droughts from 850 to 2099 CE in the Community Earth System Model

Woon Mi Kim and Christoph C. Raible

Published in *Climate of the Past*, Volume 17, 887 – 911, 2021

The chapter is published under the link:
`https://doi.org/10.5194/cp-17-887-2021`

Clim. Past, 17, 887–911, 2021
https://doi.org/10.5194/cp-17-887-2021

Climate of the Past
Open Access

Dynamics of the Mediterranean droughts from 850 to 2099 CE in the Community Earth System Model

Woon Mi Kim[1,2] **and Christoph C. Raible**[1,2]

[1]Climate and Environmental Physics, University of Bern, Bern, Switzerland
[2]Oeschger Centre for Climate Change Research, University of Bern, Bern, Switzerland

Correspondence: Woon Mi Kim (woonmi.kim@climate.unibe.ch)

Received: 5 June 2020 – Discussion started: 6 July 2020
Revised: 15 March 2021 – Accepted: 17 March 2021 – Published: 22 April 2021

Abstract. In this study, we analyze the dynamics of multi-year droughts over the western and central Mediterranean for the period of 850–2099 CE using the Community Earth System Model version 1.0.1. Overall, the model is able to realistically represent droughts over this region, although it shows some biases in representing El Niño–Southern Oscillation (ENSO) variability and mesoscale phenomena that are relevant in the context of droughts over the region.

The analysis of the simulations shows that there is a discrepancy among diverse drought metrics in representing duration and frequencies of past droughts in the western and central Mediterranean. The self-calibrated Palmer drought severity index identifies droughts with significantly longer duration than other drought indices during 850–1849 CE. This re-affirms the necessity of assessing a variety of drought indices in drought studies in the paleoclimate context as well.

Independent of the choice of the drought index, the analysis of the period 850–1849 CE suggests that Mediterranean droughts are mainly driven by internal variability of the climate system rather than external forcing. Strong volcanic eruptions show no connection to dry conditions but instead are connected to wet conditions over the Mediterranean. The analysis further shows that Mediterranean droughts are characterized by a barotropic high-pressure system together with a positive temperature anomaly over central Europe. This pattern occurs in all seasons of drought years, with stronger amplitudes during winter and spring. The North Atlantic Oscillation (NAO) and ENSO are also involved during Mediterranean multi-year droughts, showing that droughts occur more frequently with positive NAO and La Niña-like conditions. These modes of variability play a more important role during the initial stage of droughts. As a result, the persistence of multi-year droughts is determined by the interaction between the regional atmospheric and soil moisture variables, i.e., the land–atmosphere feedbacks, during the transition years of droughts.

These feedbacks are intensified during the period 1850–2099 CE due to the anthropogenic influence, thus reducing the role of modes of variability on droughts in this period. Eventually, the land–atmosphere feedbacks induce a constant dryness over the Mediterranean region for the late 21st century relative to the period 1000–1849 CE.

1 Introduction

Drought is an extreme weather and climate event characterized by a prolonged period with persistent depletion of atmospheric moisture and surface water balance from its mean average condition. Drought is also characterized by a slow onset and devastating impacts on society, the economy, and the environment (Wilhite, 1993; Dai, 2011; Mishra and Singh, 2010), and it can be classified into four types: meteorological drought, associated with the decrease in precipitation; agricultural drought, associated with the depletion of soil moisture and impacts on crops and plants; hydrological drought, characterized by the depletion of streamflow and water reservoirs; and lastly socio-economic drought that occurs when the other types of droughts cause impacts on society, in a way that the water supply cannot meet the demand from society (Mishra and Singh, 2010). If a meteorological drought lasts for a longer period, it has the potential to propagate to other types of droughts, such as agricultural or hydrological drought. In this sense, different types of droughts

Published by Copernicus Publications on behalf of the European Geosciences Union.

can become connected to each other. Thus, meteorological drought is one of the causes of other types of droughts, among other processes such as seasonal changes of run-off or an increase in evapotranspiration demand (Wang et al., 2016; Zhu et al., 2019). The severity and duration of a drought can be quantified through different indices that capture hydrological conditions associated with a regional water balance (Dai, 2011). However, a single universal index cannot characterize the entire complex nature of droughts (Lloyd-Hughes, 2014) and the connection among different types of droughts (Mukherjee et al., 2018). Thus, one index does not necessarily show a similar value to other indices even for the same region and period (Raible et al., 2017; Mukherjee et al., 2018). Some of the widely used indices are the self-calibrated Palmer drought severity index (Wells et al., 2004), the Standardized Precipitation Index (McKee et al., 1993), and the Standardized Precipitation Evapotranspiration Index (Vicente-Serrano et al., 2009), among many others.

The Mediterranean region is known as a climate change hot spot (Giorgi, 2006), i.e., the region is highly responsive to current and future global warming, showing a decrease in precipitation and an increase in drought episodes (Dubrovský et al., 2014; Liu et al., 2018). The climate of the Mediterranean is characterized as semi-arid with a pronounced annual cycle, which means a high temporal variability of the availability of water resources (Lionello et al., 2006). Therefore, droughts or periods with scarcity of water are intrinsic parts of the climatic conditions over the Mediterranean. Overall, the region shows mild and wet winters and hot and dry summers (Lionello et al., 2006). The variability of precipitation is not uniform across the entire Mediterranean. The western and eastern regions show different precipitation regimes, in particular in winter. A regional mode of circulation that explains this spatial difference is the Mediterranean Oscillation, characterized by the opposite pressure and precipitation patterns between the western and eastern region (Dünkeloh and Jacobeit, 2003). Besides, the regional precipitation is strongly influenced by the midlatitude storm tracks and cyclones, which become stronger during the winter (Lionello et al., 2016; Raible et al., 2007, 2010; Ulbrich et al., 2009); regional cyclones (Alpert et al., 1990); and large-scale modes of variability, such as the North Atlantic Oscillation (NAO), East Atlantic–West Russian pattern (EA–WR) and El Niño–Southern Oscillation (ENSO) (Lionello et al., 2006; Raible, 2007). The influence of these large-scale patterns varies within the Mediterranean region. The NAO exerts its control on precipitation by affecting the strength of westerlies and latitudinal movement of storm tracks. Precipitation decreases during the positive phase of the NAO, mostly in the western and central Mediterranean, whereas it increases during the negative phase of NAO (Wallace and Gutzler, 1981; Hurrell, 1995). The EA-WR influences the southeastern Mediterranean hydroclimate causing drier conditions during its positive phase (Barnston and Livezey, 1987; Krichak and Alpert, 2005). The response of the Mediterranean climate to ENSO is more complex: it varies over time, as illustrated by historical cases (Brönnimann, 2007; Brönnimann et al., 2007), and it depends on the maturity of the ENSO state (Vicente-Serrano, 2005), the seasons (Mariotti et al., 2002), and the co-occurrence with NAO (Brönnimann, 2007; Raible et al., 2001, 2003). Mariotti et al. (2002) demonstrated that precipitation decreases over the western Mediterranean during La Niña in autumn and spring. Brönnimann (2007) showed a connection between La Niña (El Niño) and the positive (negative) phase of the NAO in the late winter.

In the Mediterranean, increases in the severity and number of droughts have been already observed since the mid to late 20th century (e.g., Mariotti et al., 2008; Philandras et al., 2011; Sousa et al., 2011; Seager et al., 2014; Vicente-Serrano et al., 2014; Spinoni et al., 2015). In recent decades, the occurrence of droughts with a pan-European characteristic that cover a large part of the western and central Mediterranean region have been also detected (García-Herrera et al., 2019; Spinoni et al., 2017). The increase in dryness is attributed to the increase in the atmospheric greenhouse gas (GHG) concentrations, which causes a strong increase in the surface temperature and a decrease in precipitation over this region (Mariotti et al., 2008). General circulation models (GCMs) project that this drying trend, together with the increases in dry days and drought episodes, will be intensified in the future under the business-as-usual scenario, causing substantial socio-economic impacts and changes in the region (Mariotti et al., 2008; Field et al., 2012; Lehner et al., 2017; Naumann et al., 2018). The future changes in the Mediterranean droughts are due to increasing tropical SSTs (Hoerling et al., 2011), changes in the mean regional circulation associated with intensified subsidence and low-level mass divergence (Seager et al., 2014), the expansion of the Hadley cell and of the subtropical subsidence zones (Previdi and Liepert, 2007), an intensification of subtropical highs (Li et al., 2012), and a northward shift of the storm tracks (Raible et al., 2010).

Although the dryness projected in the future scenarios is unprecedentedly intense, multi-year dry periods are not a completely new phenomenon over the Mediterranean. Using the summer self-calibrated Palmer drought severity index (scPDSI) based on tree ring reconstructions (also known as the Old World Drought Atlas; OWDA; Cook et al., 2015), Cook et al. (2016a) found that the region has experienced several dry periods during the last 900 years, some with persistent pan-Mediterranean characteristics. The variability of these Mediterranean droughts shows the frequencies of not only interannual but also multidecadal timescales.The causes of these past droughts are still unclear, but a connection to large-scale patterns, such as the NAO, Eastern Atlantic, and Scandinavian patterns may be relevant.

Besides paleoclimate proxies, GCMs have been used to study long-term changes and continuous variability of global and regional hydroclimate and extreme events during the last millennium (PAGES Hydro2k Consortium, 2017; Haywood et al., 2019). Modeling studies on the long-term variability of droughts are focused on the continental US, mainly to investigate the variability and mechanisms of southwestern United States (SW) droughts (Coats et al., 2013, 2016; Parsons et al., 2018; Parsons and Coats, 2019) and North American pan-continental droughts (Coats et al., 2015; Cook et al., 2016b). The results show that different GCMs are able to reproduce the duration and intensity of SW megadroughts and North American pan-continental droughts. The authors further suggest that internal variability is the main driver of these droughts, although the specific processes are largely model dependent.

Globally, Stevenson et al. (2018) used the Community Earth System Last Millennium Ensemble (CESM-LME; Otto-Bliesner et al., 2016) to examine the connection between past global hydrological mega-events and climate variability and external forcings during the last millennium. Among the major modes of climate variability, ENSO and AMO are identified as having an influence on mega-events; both modes significantly alter the megadrought risks and persistence in drought-prone regions, such as southern Australia, the Sahel, and the southern United States. The study provides insights into the dynamic of megadroughts associated with different mode of variability on global scales. However, a detailed analysis on Europe and the Mediterranean is missing.

Over the European domain, Ljungqvist et al. (2019) examined a long-term covariability between the summer temperature and hydroclimate during the Common Era. By comparing the instrumental records, tree-ring-based reconstructions, and model simulations, they found that a warm dry relationship with multidecadal variability is more dominant in southern Europe. Though all datasets share some common leading modes of covariability across different time frequencies, there are some discrepancies among instrumental records, proxies, and models. The proxies present a stronger positive temperature–hydroclimate relationship, while the model exhibits a stronger negative relationship than the instrumental records. Xoplaki et al. (2018) investigated the interaction between past central and eastern Mediterranean societies and the hydroclimate conditions, including droughts, by comparing the historical records, proxies, and GCM simulations. Analyzing three particular historical periods, they concluded that the multidecadal variability of precipitation in the region is driven by internal dynamics of the climate system: large discrepancies between the model trajectories are detected. Therefore, no agreement in timing between models, proxies, and historical records can be expected. Nevertheless, the models elucidate some possible explanations about the dynamics of extreme dry and wet events in some past periods.

Despite a number of studies on past hydrological variability, a long-term continuous perspective on the mechanisms of past extreme hydrological events, specifically of droughts over the Mediterranean during the last millennium, is still missing. As a long trend of dryness has already been detected in the instrumental era and is expected to intensify in the future scenario, it is necessary to provide a long-term picture on the variability and changes of past dry events and their mechanisms. Therefore, we aim to examine the physical mechanisms involved in yearly and multi-year long droughts during the Common Era (850–1849 CE) and historical, present, and future periods (1850–2099 CE) over the western and central Mediterranean region. We choose this specific area, as this region has been affected by recent large-scale droughts (García-Herrera et al., 2019; Spinoni et al., 2017), which can be seen as pan-western–central Mediterranean droughts. Moreover, the region shows coherent desiccation in the future scenario (Dubrovský et al., 2014). From now on, for simplicity, we refer to the western and central Mediterranean region in our study simply as the Mediterranean region. We focus on understanding the dynamics that induce past persistent pan-regional multi-year droughts and whether the dynamics that induce droughts in the past will change in the historical and future periods with the anthropogenic increase in GHG.

For our purpose, we use the Community Earth System Model version 1.0.1 (CESM), which includes the active biogeochemical cycle and has a horizontal resolution of $1.25^\circ \times 0.9^\circ$ (Lehner et al., 2015). The spatial resolution of the model is a clear advantage for our study on a relatively small confined area. The precipitation of the region is strongly influenced by extratropical cyclones and in general, GCMs have difficulties in reproducing the dynamics and precipitation associated with these mesoscale phenomena (Raible et al., 2007; Watterson, 2006). Nevertheless, these atmospheric dynamics and precipitation are better represented in GCMs with finer spatial resolutions (Champion et al., 2011; Watterson, 2006). Hence, using a model that provides a seamless simulation for the period 850–2099 CE with a relatively finer spatial resolution can improve a representation of precipitation-related processes and thus drought-associated mechanisms over the region.

This paper is composed of the following sections: in Sect. 2, we introduce the model and simulations; the hydrological variables given by the model; the definitions of droughts and drought indices; the proxy and observation datasets; and methods. In Sect. 3, we present the results of the analysis: first, we compare the simulation, proxy reconstruction, and observations to validate the model simulation; second, we describe how the model depicts past droughts, whether the quantification of past droughts over the region is sensitive to the choice of drought metrics, and whether there is some possible connection between the volcanic eruptions and droughts; third, we present the climate conditions associated with the past Mediterranean droughts and their connection with regional-scale circulation and modes of variability, i.e., the NAO and ENSO; lastly, we discuss whether mechanisms that induce past droughts have changed in the historical and future periods. Finally, the conclusions are presented in Sect. 4.

2 Model description and methods

2.1 Description of the model and simulations

We use the Community Earth System model version 1.0.1 in this study. Two simulations are used: a continuous transient simulation of 1250 years (850–2099 CE) and a control simulation of 400 years at perpetual 850 CE conditions (Lehner et al., 2015). In the simulations, the atmosphere has the horizontal resolution of 1.25° × 0.9° and 26 vertical layers, and the land has the same horizontal resolution as the atmosphere with 15 sub-surface layers. The ocean has the horizontal resolution of 1.25° × 0.9° with displaced pole grids with 60 ocean layers. The sea ice component shares the same horizontal resolution as the ocean.

The control simulation uses constant forcing parameters set to the 850 CE values: the land use and land use changes (LULUC), the total solar irradiance in which the value is 1360.228 W m^{-2}, and the greenhouse gas (GHG) concentrations, such as the CO_2 of 279.3 ppm, CH_4 of 674.5 ppb, and the N_2O of 266.9 ppb. Unlike other forcings, the orbital parameters are set to 1990 CE conditions.

The transient simulation includes the active biogeochemical cycle and forcing, such as the LULUC, total solar irradiance, volcanic eruptions, and GHG concentrations that vary over time. The GHG concentrations and LULUC vary little before 1850, showing pronounced changes and increases after that year. Then, the period 2005–2099 CE is run with the RCP 8.5 scenario. The transient forcing follows the third Paleoclimate Modeling Intercomparison Project (PMIP4; Schmidt et al., 2012) – Fifth Coupled Model Intercomparison Project (CMIP5; Taylor et al., 2012) protocols. A more detailed overview of the forcing and initial set-up of the simulations is presented in Lehner et al. (2015).

2.2 Region of study, analysis, and methods

The focus area of the study is the western and central Mediterranean region (33–45° N, 15° W–28° E; Fig. 1). The extent of the region is selected based on empirical orthogonal function (EOF) analysis on the monthly precipitation from the observation (gridded station precipitation from U.Delaware v5.01; Willmott and Matsuura, 2001). The region overall shares a similar variability in the first EOF (13.28 %) and second EOF (11.01 %); this similarity can also be attributed to the influence of the NAO on the precipitation over the region (Dünkeloh and Jacobeit, 2003).

For the analysis, the monthly anomalies of variables associated with the hydrological condition, such as the surface and air temperatures, precipitation, zonal and meridional winds, geopotential heights, and sea level pressure are calculated with respect to the 1000–1849 CE (850 years) mean annual cycle for each grid point in the transient simulation. For the control simulation, the entire 400 years is taken as a reference period to calculate the anomalies.

We split the transient simulation into two parts: the first period from 850 to 1849 CE is used to study the natural variability of droughts excluding the effect of an accelerated increase in the GHGs, and the second period from 1850 to 2099 CE is used to examine the effects of anthropogenic changes on the natural variability of droughts. For the first period (850–1849 CE), the drought condition in the transient simulation is compared to that in the control simulation to assess the influence of the natural variability and forcings. A Mann–Whitney U test is performed to statistically compare the distributions between the transient and the control simulation. The null hypothesis of a Mann–Whitney U test states that the distributions of both populations (in this case, the transient and the control simulations) are equal. For the second period (1850–2099 CE), a linear detrending method is applied to the anomalies in order to examine changes in the variability and mechanisms associated with droughts during this period. For this, the time period is split into two and the least-squares method is applied to each of the periods separately: from 1850 to 2000 and from 2001 to 2099 CE (Fig. A1). Following this, the detrended anomalies are compared to the anomalies in the non-detrended (1850–2099 CE) and the first (850–1849 CE) periods.

Composites of positive and negative phases of two modes of variability, NAO and ENSO, are also investigated. The NAO is taken as the difference in the sea level pressure anomalies between the regions confined to 35–39° N, 33–21° W and 63–67° N, 25–13° W, which reflect the Azores high and the Iceland low, respectively (Wallace and Gutzler, 1981; Trigo et al., 2002). The ENSO is characterized by the annual mean sea surface temperature anomalies over Niño 3.4 region in the tropical equatorial Pacific (5° S–5° N, 170–120° W) (Trenberth, 1997).

We further perform a wavelet coherence analysis (Grinsted et al., 2004; Gouhier et al., 2018) and a superposed epoch analysis (e.g., Malevich, 2018; Rao et al., 2017) in order to find a possible connections between droughts and volcanic eruptions. Thereby, we use the time series of the drought indices (Sect. 2.3) and of volcanic eruptions (Gao et al., 2008). Note that all time series for these analysis are normalized to have a zero mean and 1 standard deviation.

2.3 Drought definitions

We use four drought metrics to quantify droughts and to perform the comparison among them: the Standardized Precipitation Index (SPI), Standardized Precipitation Evapotranspiration Index (SPEI), self-calibrated Palmer drought severity index (scPDSI), and annual soil moisture anomaly (SOIL).

The SPI only requires a long-term precipitation record, and the accumulated precipitation is fitted to a probabilistic distribution, in our case a gamma distribution. Following this, the fitted distribution is transformed to a normalized Gaussian distribution (McKee et al., 1993). The SPEI is similar to the SPI, but instead of only using a precipitation record,

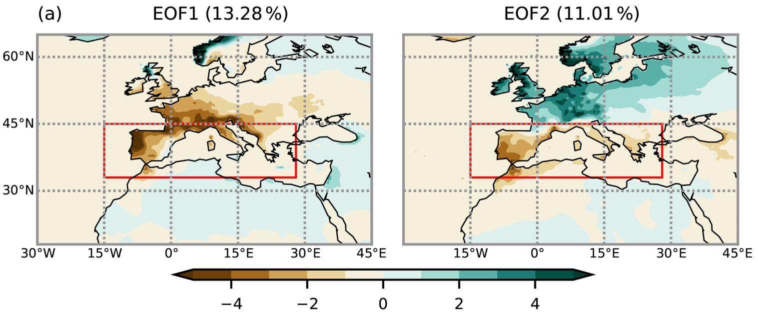

(b) Percentage of Area with anomaly < 0 mm/mon (mean=75 %)

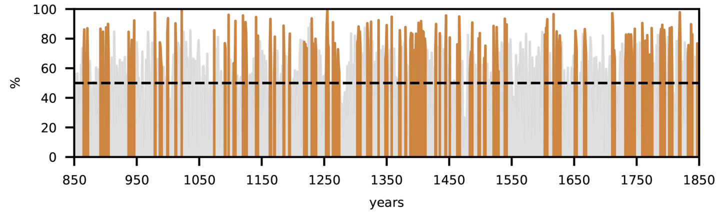

Figure 1. **(a)** Variance explained by the first EOF and second EOF in the observed monthly precipitation from the U.Delaware v5.01 dataset for the period of 1901–2000 CE. The red rectangle indicates the region of study: western and central Mediterranean. **(b)** Percentage of area with the soil moisture anomaly below 0 mm per month in the region of study during the last millennium in CESM. Brown shading indicates the years with droughts.

it considers the climate water balance given by the difference between the precipitation and atmospheric evaporative demand. This difference is fitted to a log-logistic probability distribution and then transformed to a normal distribution (Vicente-Serrano et al., 2009). For the atmospheric evaporative demands, we use the potential evapotranspiration derived from the Thornthwaite equation, which only requires surface temperature and latitude (Thornthwaite, 1948). The scPDSI computes the water balance by assuming a two-layer soil bucket model, and it requires temperature and potential evapotranspiration records. Other necessary variables, such as runoff and losses, are estimated from the temperature and potential evapotranspiration (Palmer, 1965; Wells et al., 2004; Zhong et al., 2018). Again, the potential evapotranspiration is calculated by using Thornthwaite equation similar to for the SPEI. The SOIL is the upper 10 cm soil moisture anomaly calculated with respect to the 850-year mean (1000–1849 CE) annual cycles. The soil moisture is a direct output from the model.

All indices are calculated with respect to the same reference period (1000–1849 CE) and with the 12-months annual timescale for the SPI, SPEI, and SOIL. The scPDSI has an inherent timescale that ranges from 9 to 14 months depending on the region (Vicente-Serrano et al., 2010, 2015). Thus, we use a 12-month timescale for the other indices in order to be comparable to the scPDSI. Then, the area-weighted average of each index is calculated over the Mediterranean region (Fig. 1). The summer scPDSI is also calculated by averaging the June–July–August scPDSI, in order to compare with the summer scPDSI from the tree-ring-based reconstruction, the Old Word Drought Atlas (OWDA; Cook et al., 2015).

For all indices, we define a drought event as consecutive years with negative indices, in which at least 1 year with the index falls below the 10th percentile of its 850-year (1000–1849 CE) distribution. In such a way, we assure that the dry condition is maintained consistently during drought years, without being interrupted by a single wet year or season. This method, which imposes a threshold based on the extreme percentiles, assures that strong negative anomalies persist throughout the entire year with droughts. Thus, we only include relatively severe droughts in the analysis.

Droughts with a duration of more than 3 years are considered multi-year droughts. In Sect. 3.3., we analyze the mean condition during droughts in the control and transient simulations taking into account all short (1 and 2 years in duration) and long (more than 3 years in duration) Mediterranean droughts. For the next part of the analysis in Sect. 3.4., we examine the dynamics associated with persistent multi-year droughts (more than 3 years in duration). These long droughts are separated into three stages: the initiation years as the first years of droughts, the termination years as the last years, and the rest as the transition years. The evolution of droughts is analyzed for each of the stages. This separation method is similar to the one used by Parsons and Coats (2019).

Lastly, in order to define droughts with pan-western–central Mediterranean characteristics, we select only drought events where more than 70 % of the region of study is occupied by negative indices (Fig. 1b). However, for multi-year droughts, we concede that this condition does not need to be fulfilled for the initiation and termination years but only needs to be fulfilled for the transition years: a drought can start weak and with a more local characteristic, expand to a larger proportion of the Mediterranean, and weaken again in the termination years.

2.4 Observation and proxy reconstruction datasets for the validation

To validate the model simulation, we compare mean seasonal and annual precipitation, time series of droughts and climate conditions associated with droughts among the observation, and proxy reconstruction and model simulations for the period 1901–2000 CE. We use the gridded station data for temperature and precipitation from U.Delaware v5.01 (Willmott and Matsuura, 2001), the sea surface temperature from the Extended Reconstructed Sea Surface Temperature v5 (ERSST v5; Huang et al., 2017a), and geopotential heights from the 20th Century Reanalysis v2 (CR v2; Compo et al., 2011). The anomalies of variables are calculated by extracting the mean annual cycles with respect to 1950–1979 CE. The scPDSI is calculated using the U.Delaware v5.01 temperature and precipitation. The same calibration period 1950–1979 is used to calculate the scPDSI for the observation and model. Furthermore, we take the gridded tree-ring-based reconstruction of European summer scPDSI: OWDA (Cook et al., 2015). Among all drought indices, we use only scPDSI for comparison and validation, as the OWDA only provides this specific drought metric. The time series of scPDSI during this period are statistically compared to each other using the *t* tests with the null hypothesis of equal means between two time series. The analysis of patterns associated with droughts is performed by calculating the spatial correlations between the scPDSI and SST, scPDSI, and geopotential height fields.

3 Results

3.1 Validation of CESM: comparison among observation, proxy and model (1901–2000 CE)

In this section, we compare the mean precipitation, mean scPDSI, number and duration of droughts, and atmospheric conditions associated with Mediterranean dry conditions among the observation, OWDA, and CESM simulation for the period of 1901–2000 CE.

The model simulation exhibits similar spatial patterns of mean seasonal precipitation to those from the observation (Fig. 2), although some regions are statistically different. In the summer, both the central and western Mediterranean present dry conditions, whereas in the winter both regions are less dry than the summer, with wet conditions over Portugal and Balkans. For the mean annual cycle, the model in general shows less precipitation than the observed values over both the central and western Mediterranean. Nevertheless, the model reproduces the annual precipitation cycle well, correctly depicting the maximum and minimum periods of precipitation.

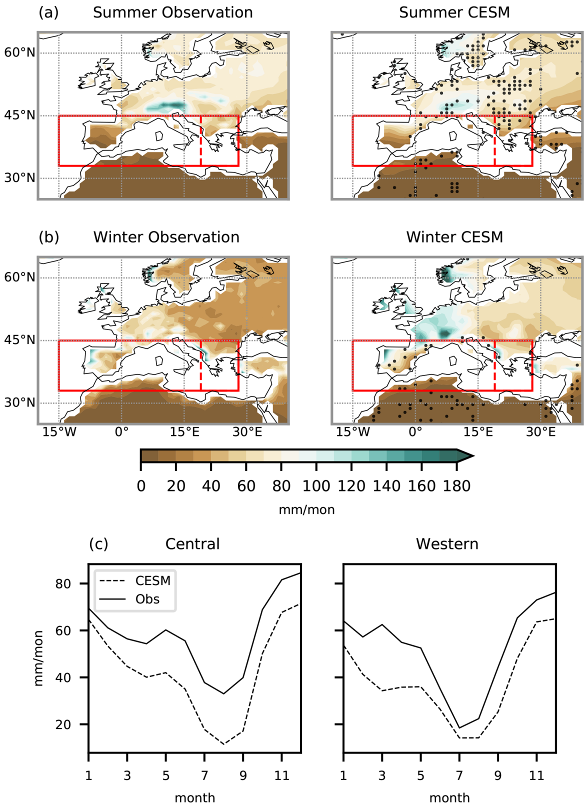

Figure 2. Mean seasonal precipitation for the observation (left) and CESM (right) in the **(a)** summer and **(b)** winter for the period of 1901–2000 CE. Black dots on the composites of CESM indicate the regions where the means between the observation and model are not statistically similar at a 5 % confidence level from the *t* tests. **(c)** Mean annual cycles of precipitation for the same period over the areas in the rectangles. The observation is in continuous lines, and CESM is in dashed lines.

Comparing the time series of scPDSI (Fig. 3a and c), the summer means between the model and OWDA are statistically similar to each other (*p* value from the *t* test of 0.28). The same happens between the OWDA and observation but with much lower confidence level of 1 % (*p* value of 0.01). However, the means of both summer and annual scPDSI in the model are statistically different to those in the observation (*p* values of 0.001). Nevertheless, all three scPDSI show negative trends during 1901–2000 CE (Fig. 3c) and in each sub-

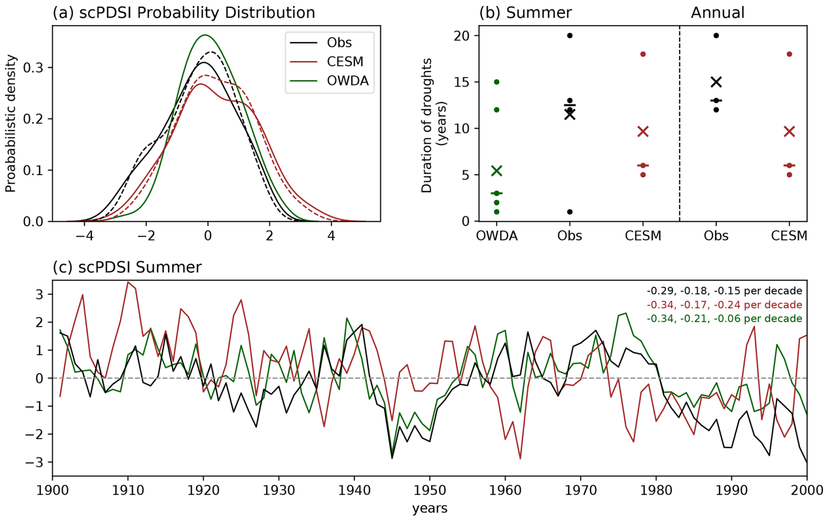

Figure 3. **(a)** Probabilistic distribution of the yearly self-calibrated Palmer drought severity indices (scPDSIs) from the U.Delaware v5.01 observation (black), CESM (red), and OWDA (green) smoothed by kernel density estimates using Gaussian kernels. Continuous lines indicate the summer, and dashed lines indicate the annual scPDSIs. The t tests are applied among these distribution under the null hypothesis of equal means between two time series.The p value between the summer scPDSI from CESM and OWDA is 0.28, between the OWDA and observation it is 0.01, and between the CESM and observation it is 0.001 for both summer and annual values. **(b)** Distribution of duration of annual droughts in different datasets. Crosses are the means and horizontal dashes the medians of the duration of droughts. **(c)** Time series of summer scPDSIs from the observation (black), CESM (red), and OWDA (green) for 1901–2000 CE. The numbers on the upper right indicate the values of the trends per decade, from left to right, for the periods 1901–1950 CE, 1951–2000 CE, and 1901–2000 CE. All of these trends are statistically significant at 95 % confidence interval based on the Mann–Kendall tests.

period (1901–1950 and 1951–2000 CE), indicating a continuous increase of drying over the region, which is in line with the previous studies (Mariotti et al., 2008; Sousa et al., 2011; Spinoni et al., 2015). Based on the Mann–Kendall tests, these trends are all statistically significant at the 95 % confidence interval. For the number of droughts (Fig. 3b), the observation presents 4 events, OWDA presents 7 events, and CESM presents 3 events during the last century. For the duration of droughts, the mean (5.43 years) and median (3 years) in OWDA are lower than those in the observation (11.50 and 12.50 years, respectively). CESM also exhibits a lower median (6 years) compared to the observation, although its mean (9.67 years) better resembles the observation than the one in OWDA. These differences in the means and medians between the observation and CESM are also present in annual scPDSI.

Overall, the model tends to underestimate the duration of present-day droughts more than those from the observation. However, the model to a certain extent still shows its ability to reproduce persistent droughts of multi-year duration. Additionally, the mean duration of droughts in CESM is longer than in OWDA. Still, it is important to note that the analysis of annual-scale extreme dry events based on a relatively short present period of 100 years is not sufficient to draw comprehensive conclusions on present-day multi-year droughts due to the limited number of events.

One reason for the difference in the scPDSI between the model and observations is potentially related to the model performance on mesoscale phenomena, which play an important role for the regional precipitation during the wet season (Alpert et al., 1990; Ulbrich et al., 2009; Champion et al., 2011; Watterson, 2006). Additionally, the model performance on internal variability may contribute to this discrepancy, which will be discussed in the following paragraphs. The difference in scPDSI between OWDA and the observation, which shows a p value at the limit of 1 % confidence level, can be explained by some characteristics of tree-ring-based reconstructions. The annually resolved summer (JJA) OWDA is based on tree ring reconstructions, which are known to be biased towards the growing season. Thus, the annual signal is not fully preserved (Franke et al., 2013). Moreover, tree-ring-based reconstructions for droughts tend to overestimate low-frequency variability compared to the instrumental observations (Franke et al., 2013), and the distribution of tree rings used to generate the gridded reconstruction over the Mediterranean may not be enough to capture precipitation events associated with regional-scale cyclones and fully depict dry–wet variability for the entire region (Babst et al., 2018).

After all, the model simulation and observation share many common patterns associated with the variability of scPDSI. Figure 4 shows the correlation patterns between the

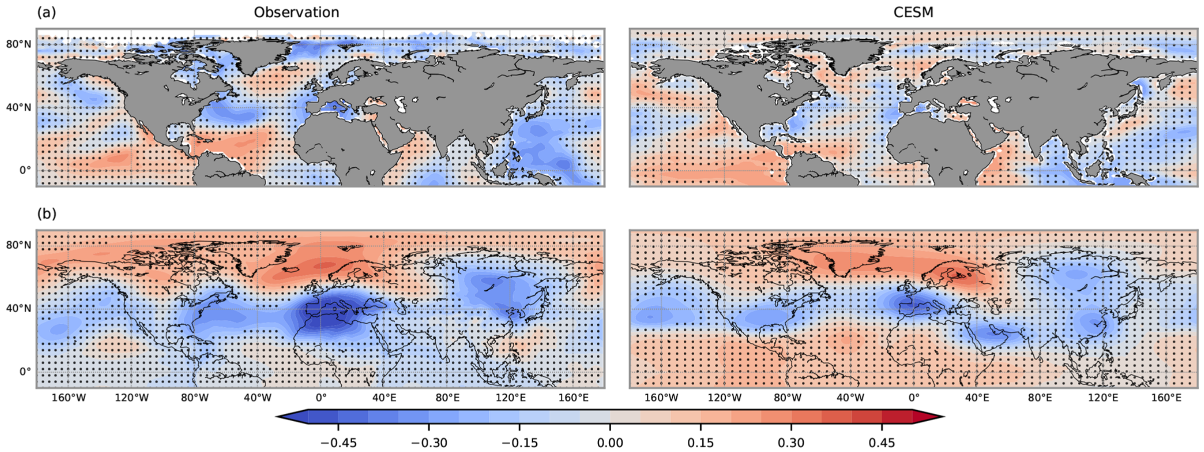

Figure 4. Pearson correlation coefficients between the scPDSI and anomalies of **(a)** sea surface temperature from ERSST v5 and **(b)** geopotential height at 850 hPa from the CR20 for the observation (left) and CESM (right) during the period of 1901–2000 CE. The linear trends of variables are removed before applying the correlation. Black dots on the maps show the regions where correlations are statistically not significant at 5 % confidence level.

scPDSI and SST and the scPDSI and geopotential height at 850 hPa. The observation and model exhibit significant positive correlations over the central equatorial Pacific, though in the observation the region with statistically significant correlation is located more in the central North Pacific than in the model. The observation and model simulation share a common wave-like pattern from the North Pacific to Siberia over the extratropical latitudinal belt. Within this wave-like pattern, there is a prominent bipolar pattern with a significant negative correlation centered over the Mediterranean region and a positive correlation over the northern high latitudes. In the observation, the area of negative correlation of this bipolar pattern is larger over Europe, and the positive correlation is shifted to the Scandinavian region compared to the model simulation. Additionally, the observation and model present some common patterns occurring over the regions of ENSO (the tropical equatorial Pacific) and NAO (the North Atlantic).

As these two modes of variability are important in the climate system, including the European climate, it is necessary to point out that the amplitude of ENSO is too strong in this version of CESM (Parsons et al., 2017; Stevenson et al., 2018). In the case of the NAO, the seasonal variability of this mode seems to be amplified, similar to many other CMIP models (Fasullo et al., 2020). These inherent biases related to the modes of variability can partially explain the differences we observe here between the model simulation and observation. Nevertheless, it is found that CESM is still able to capture the hydroclimate condition associated with the ENSO teleconnection relatively well (Stevenson et al., 2018). The model also resembles the present-day NAO pattern well, including the spatial precipitation and temperature associated with this mode of variability in Europe (Deser et al., 2017).

Although there are some discrepancies between the model simulation and the observation, the model is able to reproduce the climate conditions associated with the variability of present-day scPDSI. In particular, the model is able to simulate multi-year droughts, and these droughts have a longer duration than those in OWDA. As it also shows statistical similarity to OWDA over the region, the model is suitable to analyze past Mediterranean droughts. The biases mentioned here are considered in detail in Sect. 4 when discussing the results of this study.

3.2 Variability of Mediterranean droughts during the 850–1849 CE and their connection to the volcanic forcing

To gain an overview of drought conditions in the Mediterranean, we assess the indices defined in the Sect. 2.3 using the period 850 to 1849 CE by focusing on the drought events and their duration. We compare the variability and duration of droughts of the summertime scPDSI in CESM with those in OWDA. Note that a direct comparison between the proxies and the model simulation is not possible due to the different initial conditions and the chaotic behavior of the climate system (PAGES Hydro2k Consortium, 2017; Xoplaki et al., 2018). Thus, we focus on comparing the simulated summer drought variability with the one of OWDA. Following this, we assess whether the simulated and reconstructed droughts respond similarly to the same external forcing, i.e., the volcanic eruptions.

Figure 5a and c exhibit the distributions and the 100-year running means of duration of summer droughts in OWDA and CESM. For the duration of summer droughts in 850–1849 CE (Fig. 5a), the discrepancy between CESM

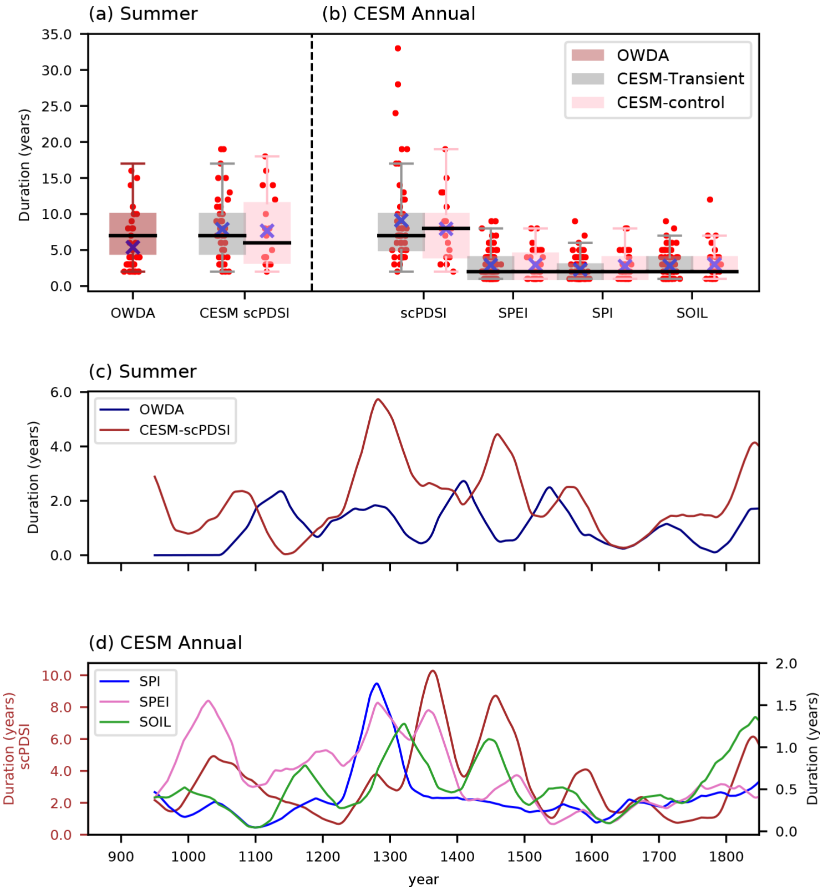

Figure 5. **(a)** Distribution of the duration of droughts for the summer scPDSIs from OWDA and the transient and control simulations, and for **(b)** the annual drought indices from the transient and control simulations in CESM. Red points indicate individual drought events, black lines on the boxes are the medians of the duration, and blue crosses are the means of duration. **(c)** The 100-year running means of the duration of droughts for the summer scPDSIs and **(d)** the annual drought indices. The indices are the self-calibrated Palmer drought index (scPDSI) from OWDA, summer scPDSI (CESM-scPDSI), annual Standardized Precipitation Index (SPI), Standardized Precipitation Evapotranspiration Index (SPEI), soil moisture anomaly (SOIL), and annual scPDSI from CESM. Note that the annual scPDSI (brown line in **d**) has a separate y axis for its duration. The Mann–Whitney U tests (MW tests) are applied to the duration of droughts in **(a)** and **(b)** under the null hypothesis of an equal distribution between two time series of duration of droughts. The p value between the duration of summer scPDSI in OWDA and CESM is 0.003, which indicates that their distributions are statistically different from each other. This is also the case for all the annual indices, except between the SPEI and SOIL, with a p value of 0.87. The p values between the indices in the transient and control simulations are all statistically similar, indicating that the distribution of duration of droughts in the transient simulation is in the range of variability of the control simulation. The p values from the MW tests between the transient and control simulations are presented in Table A1.

and OWDA is clear, with OWDA presenting the mean duration of 5.38 years and CESM presenting a mean duration of 7.89 years. The distributions associated with these means are statistically different from each other. This seems to be consistent with the result in the previous section (Sect. 3.1) that shows that OWDA identifies droughts with shorter duration compared to the present-day observation and CESM in the Mediterranean region. Thus, this characteristic is still present during the entire last millennium. The variability of droughts over time in OWDA and CESM are also different from each other (Fig. 5c). A period of increase in droughts, which is common in OWDA and CESM, is not identified. This gives us a first hint that the occurrence of droughts over the region is not mainly driven by the external natural forcings. However, both time series present a common period of decrease in droughts around 1600 CE.

Similarly, Fig. 5b and d show the distributions and the running means of duration of annual Mediterranean droughts in CESM using different indices. As expected, different indices do not exactly behave similarly in terms of the occurrence, number of events, and duration (Raible et al., 2017; Mukherjee et al., 2018). However, in the 850–1849 CE period, the indices coincide for some years: over 89 years, all indices indicate the same overlapped drought periods. In terms of duration in 850–1849 CE, the scPDSI is the one which shows more longer-lasting droughts than other indices, with a mean duration of 9.1 years. Following this, the SPEI, SOIL, and SPI present the mean durations of 2.9, 2.8, and 2.3 years, respectively. The SPI shows more events than other indices but with shorter duration. All of these means are statistically different from each other, except the means between SPEI and SOIL, which are statistically similar (p value of 0.87). This difference in the duration of droughts among the indices is also evident in the control simulation.

The difference in the duration of droughts among indices can be explained by the water balance variables involved in the computation of each index. For instance, the SPI only takes precipitation as its input variable. Thus, it does not consider the atmospheric evaporative demands, which can be intensified during dry periods. Therefore, we expect that the SPI shows a reduced duration of droughts compared to the scPDSI and SPEI, which include the potential evapotranspiration in their water balance. The same holds true for the SOIL index. Although the soil moisture in the model is closely connected to the hydrological cycle, reflecting the balance between the precipitation and actual evapotranspiration, the magnitude of actual evapotranspiration over the region is smaller than the potential evapotranspiration derived from the Thornthwaite method. Hence, the water balance involved in SOIL is affected in such a way that the drought duration is reduced compared to the scPDSI and SPEI. Lastly, droughts with a relatively long duration in the scPDSI are explained by the memory effect embedded in the calculation scheme of scPDSI (Palmer, 1965; Wells et al., 2004), which other indices that are obtained by being normalized with respect to certain statistical distribution families do not include. The scPDSI is an accumulating index; therefore, during the calculation process, the weighted value of preceding months is used to estimate the index for the current month, implying a persistence of the events. Hence, with the scPDSI, an intense yearly drought would likely induce a drought in the following year, and this effect can be exacerbated in the context of intense multi-year droughts.

Importantly, for the same indices, the distributions of the duration of droughts are statistically similar to the distributions in the control simulation at the 99 % confidence interval (Fig. 5a and b, and Table A1). This implies that the variability of droughts in the transient simulation is within the range given by the internal variability in the control simulation.

In terms of the timing of the occurrence of droughts over the period of 850–1849 CE (Fig. 5d), coherent changes among all indices are not identified, which is expected due to the different input variables and calculation schemes among drought indices. This fact also indicates that each index responds differently to the changes in precipitation and temperature, and hence potential evapotranspiration, caused by the externally forced variability, e.g., the volcanic forcing.

To further assess a potential connection between the drought indices and volcanic eruptions, a wavelet coherence analysis is applied (Fig. 6). The analysis shows that significant co-variability between the simulated drought indices (SOIL and scPDSI) and eruptions are found during periods with strong and frequent volcanic eruptions, for instance, around the 1257 Samala and 1600 Huaynaputina eruptions. For small eruptions, the signals of co-variability are not uniform among the eruptions, with some showing significant co-variability while others do not. In addition, the phase relationships between the eruptions and the drought indices also vary among the eruptions (not shown). This non-uniformity of co-variability between the small eruptions and the drought indices is a strong indication that no physical connection between them exists, i.e., the significant co-variability is merely due to statistical artifacts. OWDA does not show a strong significant co-variability during the 1257 Samala eruption, which was the strongest eruption in the last millennium (Gao et al., 2008). Still, OWDA shows, similar to CESM, a significant co-variability during the period of the Little Ice Age (around 1400–1600 CE).

The wavelet coherence analysis is clearly useful to distinguish the effects of strong and small eruptions on the variability of drought indices. However, the analysis poses some problems in handling discontinuous time series with a sporadic occurrence of the events, such as the volcanic eruptions. Filtering certain frequency bands from this kind of discontinuous time series smears out the effects of eruptions (i.e., an eruption starts earlier and lasts longer than in reality), adding some non-physical artifacts in the time series. Some of these are also reflected in Fig. 6, showing that the significant co-variability occurs earlier than the actual eruption years.

Hence, for a more detailed analysis on causal effects of volcanic eruptions on drought variability, the superposed epoch analysis is applied to the 16 largest eruptions and the 16 smallest eruptions (Fig. 7; for the list of the eruption years, see Table A2). The analysis shows that the increases in drought indices follow large eruptions, and this positive association lasts up to 3 years in CESM. On the other hand, no significant response of drought indices to small eruptions is noted. This finding is in line with Rao et al. (2017) and McConnell et al. (2020), who demonstrated wetter conditions in the Mediterranean region after strong eruptions. Thus, the analysis shows that large eruptions are associated with increases in drought indices, i.e., wet periods. In other words, the occurrence of yearly and multi-year Mediterranean droughts are not driven by the volcanic eruptions but instead by the internal variability.

In the next sections, we investigate the underlying dynamics using only the SOIL data as a drought indicator in order to understand the role of the internal variability in Mediterranean droughts. We use SOIL as it reflects the regional hydrological balance associated with the precipitation and

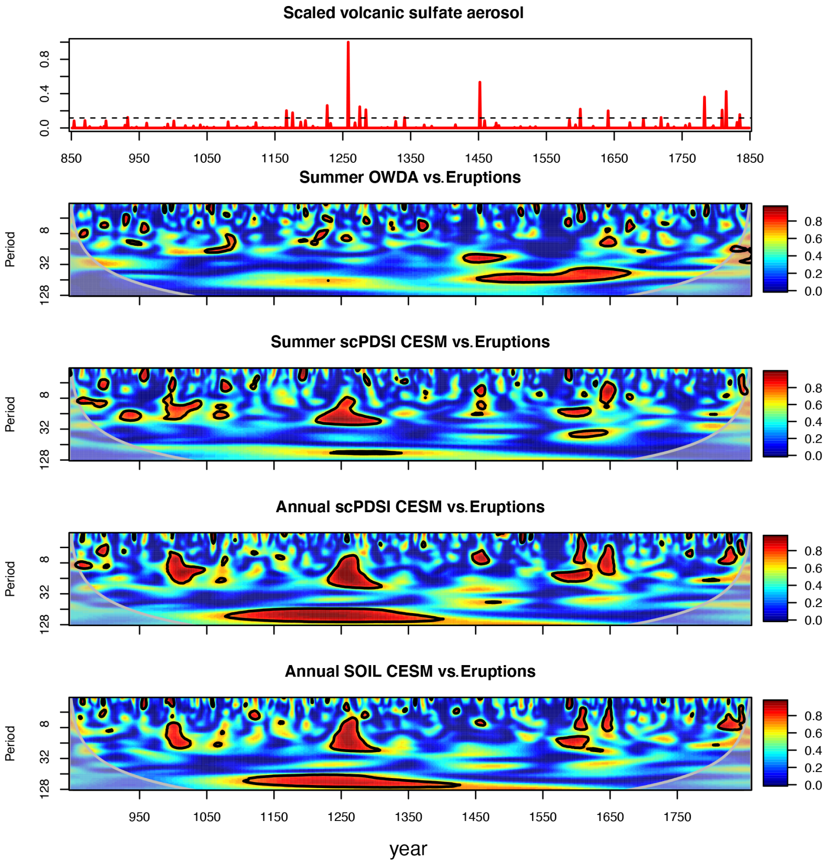

Figure 6. Time series of scaled total stratospheric sulfate aerosol injections for the volcanic eruptions in 850–1849 CE (Gao et al., 2008) (top panel). The dashed black line indicates the threshold for large eruptions with a stratospheric sulfate aerosol loading of more than 30 Tg. Wavelet coherence analysis between the time series of volcanic eruptions and the drought indices (lower panels). The red shaded regions are where the coherences of two time series are statistically significant at the 95 % confidence level, as estimated from Monte Carlo resampling of the time series.

evapotranspiration. Another advantage of this index is that the variable is a direct output from the model; thus, it does not require any further steps (except for calculating the anomalies) or statistical assumptions as other indices do. In addition, SOIL overlaps full or a partial drought periods given by the other three indices without significantly underestimating the multi-year duration of droughts. The droughts in SOIL overlap 36 %, 25 %, and 29 % of the droughts in scPDSI, SPEI, and SPI, respectively. In addition, SOIL and each of the other indices are statistically correlated at 1 % confidence level for the entire period of 850–1849 CE with Pearson correlation coefficients of 0.81 (thus, 66 % of variance) with scPDSI, 0.78 (0.61 %) with SPEI, and 0.86 (74 %) with SPI. Hence, the results in the following sections can be partially transferred to the other indices. To guarantee the transferability, the analysis in the next sections was repeated with each of the drought indices, showing similar results as for SOIL (therefore, these figures are not shown).

3.3 Atmospheric circulation associated with Mediterranean droughts (850–1849 CE)

In this section, the atmospheric circulation associated with Mediterranean droughts is investigated by using SOIL in the control and transient simulations up to 1849 CE. The control simulation presents 7.25 droughts per century with a mean duration of 3.06 years, and the transient simulation shows 8 droughts per century with a mean duration of 2.81 years.

To get a first glance of the atmospheric circulation during drought conditions, we analyze the mean circulation conditions during all short (1-year and 2-year duration) and long (more than 3-year duration) Mediterranean droughts together. Figure 8 shows the anomalies of geopotential height at 850 hPa and surface temperature during Mediterranean

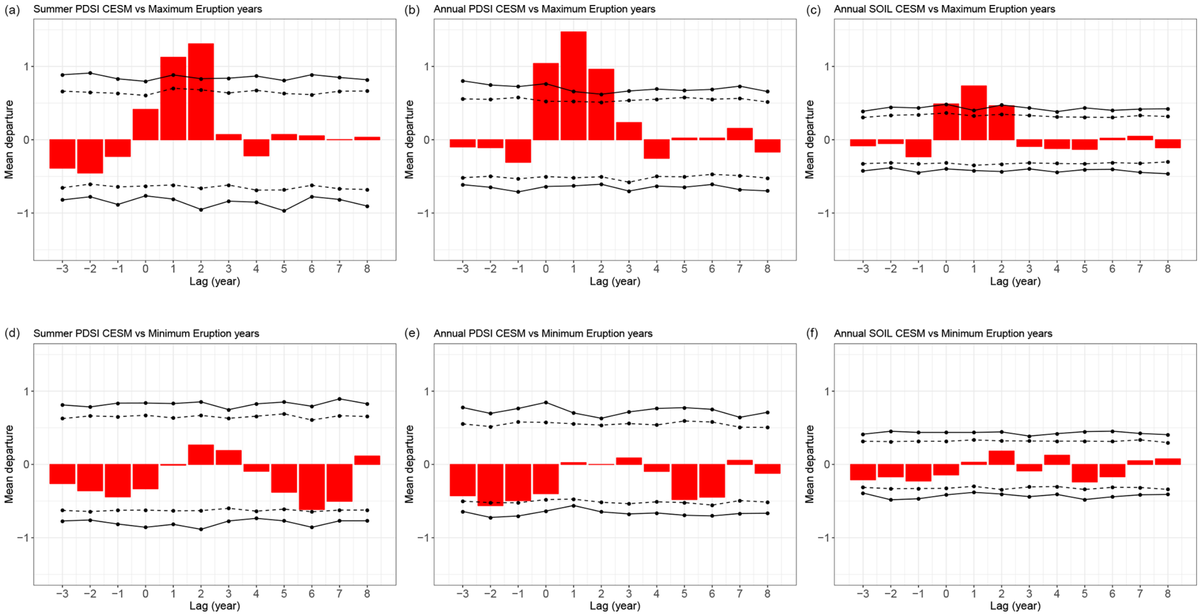

Figure 7. Superposed epoch analysis between the yearly drought indices in CESM (summer scPDSI, annual scPDSI, and SOIL) and years of eruptions for **(a–c)** the 16 largest eruptions and **(d–f)** the 16 smallest eruptions. The upward-pointing bars indicate the positive changes and downward-pointing bars show the negative changes before and after the eruptions. Continuous lines indicate the 99 % confidence interval and dashed lines the 95 % confidence interval from the bootstrap resampling of the time series. The list of the eruptions used for the analysis is in Table A2.

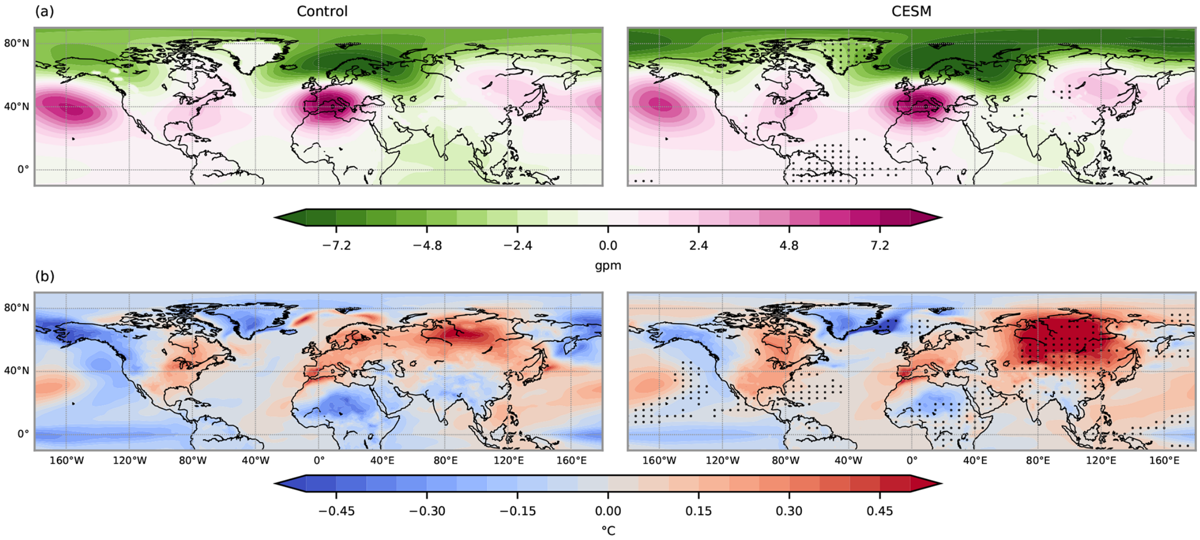

Figure 8. **(a)** Mean geopotential height anomaly at 850 hPa and **(b)** mean surface temperature anomaly for the control (left) and transient (right) simulations during Mediterranean droughts in 850–1849 CE. Black dots on the composites of the transient simulation indicate the regions where the distributions between the control and transient simulations are statistically different from each other at the 5 % confidence level according to the Mann–Whitney U tests.

droughts for each simulation. The structures of geopotential height and temperature anomalies during Mediterranean droughts are similar, with a high-pressure system centered over central Europe accompanied by a positive temperature anomaly. This high-pressure anomaly, which from now on is called the drought high, is found in all heights from 850 to 300 hPa (figures not shown), indicating a barotropic nature of this atmospheric circulation system. Additionally, a low-pressure anomaly is situated over the area of Scandinavia to Russia. Thus, the atmospheric circulation shows a northeasterly shift of the westerlies over Europe, and thus moist air masses from the North Atlantic are passed around the Mediterranean.

Outside the European continent, a negative temperature anomaly over the tropical equatorial Pacific and a positive anomaly over the North Pacific are prominent in both simulations. These temperature patterns resemble the cold phase of the ENSO and the positive phase of the Pacific Decadal Oscillation (PDO), respectively. Besides, a positive geopotential height anomaly at the midlatitudes and a negative anomaly at the high latitudes over the North Atlantic region is another pattern that both simulations share in common during droughts. This pattern is similar to the positive phase of the NAO; however, the southerly center of action is shifted to central Europe, which also partially resembles the East Atlantic Pattern (EA). The distributions of these common patterns are also statistically similar between both simulations, indicating that they are derived from the same statistical population. Thus, the simulations share common mechanisms associated with droughts, mainly driven by the internal variability of the climate system in the model. This reaffirms the result in the previous section.

Some statistically significant dissimilarities between the control and transient simulations are noticeable mostly in the temperature anomalies. Over the regions where the temperature anomalies are statistically different, the anomalies are rather weak, except the warming in Siberia. However, this positive temperature anomaly in Siberia is not associated with a geopotential height pattern, showing statistically indistinguishable geopotential height anomalies in the region between the control and transient simulations (Fig. 8). This indicates that there is no change in the circulation pattern over this region that can possibly be connected to the Mediterranean drought condition.

The drought high is a clear feature that appears during all droughts over the region. This pattern over central Europe and the western Mediterranean is similar to the pattern of the first mode of canonical correlation described by Xoplaki et al. (2003). In Xoplaki et al. (2003), this pattern is associated with the variability of temperature during the summertime in the Mediterranean region. In this study, the high-pressure system is present during all seasons of years with droughts, showing a relatively stronger intensity in winter and spring than in summer (Fig. 9). This is expected, as the variability of the geopotential height fields over Europe and the North Atlantic is reduced in summer compared to the other seasons because the meridional temperature gradient on the Northern Hemisphere is also reduced. Therefore, the main forcing of the atmospheric circulation is weakened. The findings show that the atmospheric conditions in wet seasons, i.e., winter and spring, are determinant in controlling the annual mean hydroclimate, indicating the importance of precipitation and dynamics during the wet season in annual-scale Mediterranean droughts (Lionello et al., 2006; Xoplaki et al., 2004; Zveryaev, 2004).

As expected, a decrease in precipitation occurs in all seasons during droughts: the winter and spring precipitation decreases by 13 % and the summer and autumn precipitation decreases by 11 % compared to non-drought periods. These changes in precipitation are comparable to the rates of the expected decrease in annual precipitation over the Mediterranean region in the future scenario. In the future, the regional precipitation is expected to reduce by 5 %–30 % from its present-day value (Dubrovský et al., 2014; Mariotti et al., 2008). The temperature shows a positive anomaly over the region in all seasons, with the strongest signals during summer and autumn, a finding which is in line with Xoplaki et al. (2003). The positive temperature anomaly indicates that Mediterranean droughts are more associated with anomalously warmer atmospheric conditions.

3.4 Dynamics of multi-year droughts

For the analysis on multi-year Mediterranean droughts, we focus on droughts with a minimum duration of 3 years. As shown in the previous section in Fig. 8, the drought high is a prominent atmospheric circulation pattern during Mediterranean droughts. The pattern resembles the positive NAO-like pattern, albeit with a shift to the northeast. At the same time, colder than normal conditions over the tropical equatorial Pacific are detected that are similar to La Niña-like conditions. Here, we investigate the origin and the evolution of Mediterranean long droughts associated with NAO, ENSO-like conditions, and drought highs using the transient simulation up to 1849 CE.

The phases of NAO and ENSO are defined with respect to the non-drought period: the values below the 25th (above 75th) percentile of NAO and ENSO during the non-droughts period are considered negative (positive) phases of NAO and ENSO, respectively (Fig. 10). The extreme NAO and ENSO are also defined in a similar way by taking the values below the 5th percentile for negative extremes and above the 5th percentile for positive extremes. Defining thresholds relative to the non-drought period facilitates the comparison between the two periods, showing whether (and how) these modes of variability during droughts differ from those during the opposite hydroclimate conditions. For simplicity, we call these relative negative and positive phases simply positive and negative NAO and ENSO without referring constantly to the fact that they are defined relative to the non-drought period.

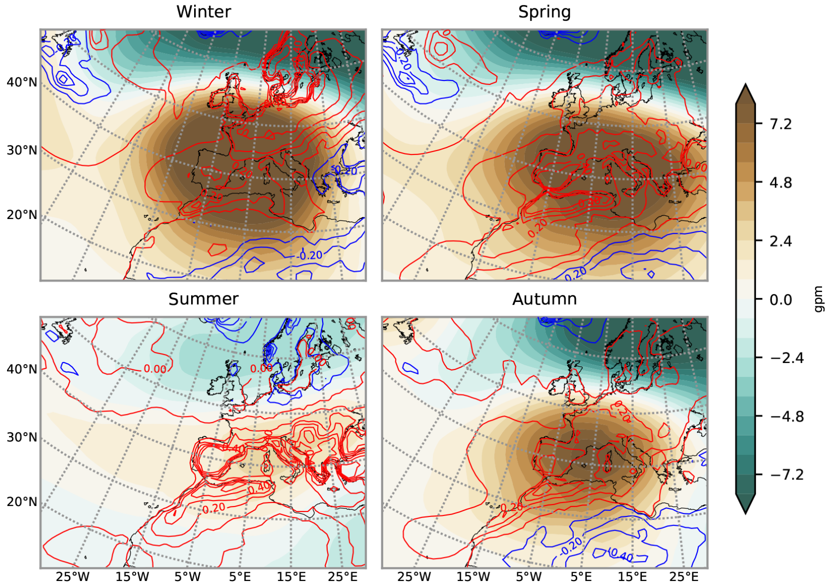

Figure 9. Mean geopotential height anomaly at 850 hPa (color shaded) and surface temperature anomaly (contours every 0.2 °C; positive in red and negative in blue) during Mediterranean droughts for each season in the transient simulation.

Considering all short and long droughts, the simulation shows that droughts occur more frequently during the positive phase of annual and winter NAO than during the non-drought period: 38 % of the drought years show the positive phase of annual NAO and 32 % for the winter, while the negative annual NAO occupies 16 % and 23 % in the winter. However, the positive NAO condition does not persist throughout the entire years of droughts. Rather, it fluctuates from the positive to negative phases during multi-year droughts. For the co-occurrence between droughts and phases of ENSO, we find that La Niña-like conditions are present in 37 % of total drought periods and El Niño-like conditions are present in 22 % of total drought periods. Similar to NAO, La Niña-like conditions do not persist throughout entire drought years.

The extreme positive NAO occurs slightly more frequently during droughts. In addition, the distributions of extreme positive NAO during droughts is statistically different from the distribution during the non-drought period at 5 % confidence level for both annual and winter NAO (p values from MW U test of 0.02 for annual and 0.002 for winter). However, for ENSO there is no statistically significant change in the distribution and frequency of extreme La Niña-like conditions during droughts.

To examine the behavior of the atmosphere during multi-year Mediterranean droughts, the frequency of modes of variability and mean composites of circulation during droughts are split into three stages: initiation, transition, and termination years (Sect. 2.3). The frequencies of occurrence of NAO and ENSO in each stage are presented in Fig. 10. The positive NAO occurs more frequently in the initiation years than in the transition and termination years of droughts. The positive NAO occupies 49 % of the initiation years. This shows that the occurrence of positive NAO almost doubles in the initiation years of droughts compared to the non-drought period (25 % of the occurrence of positive NAO). In the transition years, positive NAO decreases and finally falls to 29 % in the termination years. The frequency of extreme positive NAO also decreases over time. In the case of ENSO, the frequency of La Niña-like conditions is 40 % in the initiation years relative to the non-drought period. The occurrence of La Niña-like conditions increases slightly in the transition years, although this increase is not statistically significant with respect to the previous stage. Following this, it decreases to 20 % in the termination years. After the initiation years, there are increases in negative NAO and El Niño-like states. These changes in the frequencies of NAO and ENSO in each stage of droughts indicate a weakening role of large-scale circulation patterns at sustaining the persistence of droughts over time. As the intensities of droughts become more severe with their duration, some other factors need to be involved in sustaining the longevity of multi-year Mediterranean droughts from the transition to termination years.

The mean circulation and atmospheric conditions during the development of multi-year Mediterranean droughts are shown in Fig. 11 and are depicted by the specific humidity, temperature, and winds at 925 hPa level. In the initiation years, the southerly winds prevail over the southern Mediterranean region. These southerlies block the intrusion of the westerly systems from the North Atlantic, and together with the cyclonic winds in the East Atlantic distribute dry and

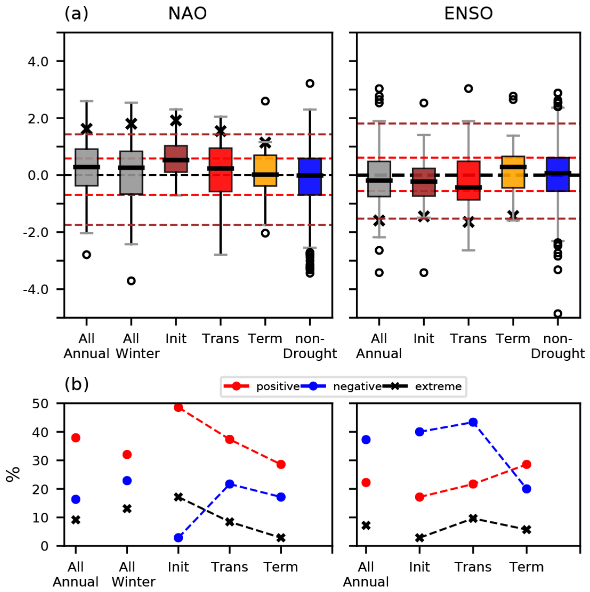

Figure 10. **(a)** Box plots of NAO and ENSO during multi-year Mediterranean droughts. Dashed red lines indicate the 25th and 75th percentiles of distributions of NAO and ENSO during non-drought periods that are taken as thresholds to discern relative negative or positive phases of NAO and ENSO. Dashed brown lines indicate the 5th and 95th percentiles of distributions that are taken as thresholds for extreme negative or positive NAO and ENSO. Black crosses represent the means of extreme positive NAO (values above the 95th percentile), and the means of extreme negative ENSO (values below the 5th percentile). **(b)** Frequencies of occurrence of positive and negative phases of NAO (left) and ENSO (right) in annual, winter, and each stage of droughts. Black crosses indicate the frequencies of occurrence of extreme positive NAO and extreme negative ENSO.

warm air masses from the East Atlantic, southern Mediterranean, and West Africa to the continent. In the transition years, a complete anticyclonic circulation associated with the high over central Europe and the Mediterranean region is developed. This anticyclonic system distributes the dry and warm air to the north and west of the continent and sustains dry and warm conditions over the region. During these years, the westerlies from the North Atlantic are clearly weakened. In the termination years, the anticyclonic circulation over Europe is not observed anymore, indicating a break-up of the high.

The mean circulation in each stage shows that the development of the high-pressure system, namely the drought high in Fig. 8, takes place in the transition years. This indicates that some mechanisms associated with this circulation are possibly important in determining the longevity of droughts after the initiation years. A possible candidate for an important process for the transition stage of Mediterranean droughts is the interaction among regional atmospheric and soil variables initiated by the anticyclonic circulation system over the region.

The presence of the atmosphere–soil interaction during the transition years is supported by the increases in frequencies of positive surface temperature (TS) and sensible heat flux (SH) and negative soil moisture (SOIL), evapotranspiration (EV), and latent heat flux (LH) anomalies during this period (Fig. 12). The mechanism associated with these regional atmospheric and soil variables is explained as follows: a decrease in precipitation supported by the positive NAO and/or La Niña-like conditions induce initial regional dryness and a stable atmospheric condition associated with the increase in geopotential high anomaly (GP) over the region. A positive GP induces an initial increase in the regional TS. This positive TS decreases SOIL and EV. The latter increases SH and decreases LH during the initiation year. During the transition years, the positive TS is even magnified due to the stable atmospheric condition that still persists (positive GP) and the increase in SH and loss of LH in the previous stage. TS in turn again increases SH, decreases EV and LH, and thus decreases SOIL. Over time, the complete high is developed and persists, again fueling this positive temperature–soil moisture feedback (Seneviratne et al., 2010; Yin et al., 2014). Thus, during the transition years, the means and occurrence of these variables associated with the feedback (positive TS, negative SOIL, negative EV, positive SH, negative LH) are clearly larger than their values during the initiation years (Fig. 12). This mechanism continues until the termination years. During the termination years, the positive GP and TS still prevail over the region, albeit with reduced anomalies. In addition, the magnitudes of other variables are reduced compared to the previous stage.

This result indicates that once the drought high is developed, the temperature–soil moisture feedback is a more important mechanism than the connection to NAO and La Niña-like patterns in order to sustain the continuous depletion of soil moisture. This means that although the large-scale circulation patterns help to support the regional dry conditions, after the initiation years their roles in sustaining droughts are diminished.

3.5 Historical and future condition on droughts: 1850 to 2099 CE

Here, the behavior of Mediterranean droughts and the associated mechanisms for the period 1850–2099 CE are presented. For an overview, the time series of the soil and precipitation anomalies (with respect to 1000–1849 CE) over the Mediterranean region for the period 1850–2099 CE are shown in Fig. 13. The simulation indicates that the region becomes drier in this period than in the past, showing pronounced decreases in soil moisture and precipitation. The reduction in these two variables is already apparent from the beginning of 1850 CE, concomitant with the anthropogenic increase in GHG. By the end of the 21st century, the region experiences

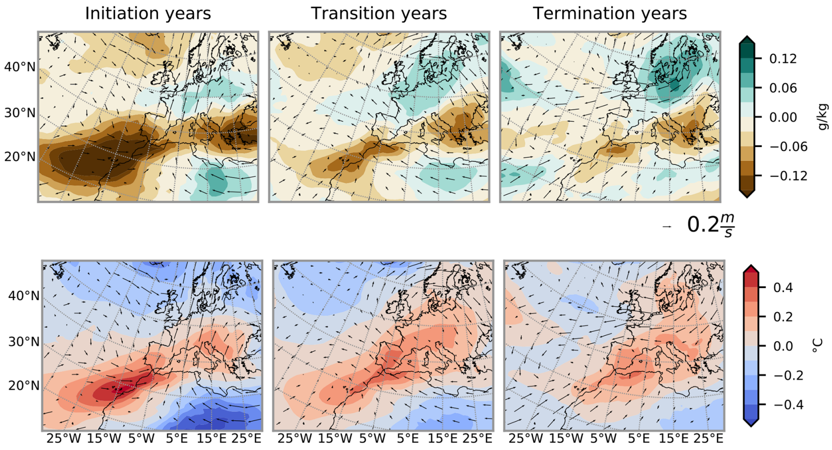

Figure 11. Evolution of atmospheric conditions in each stage of drought. Anomalies of (above) specific humidity and (below) temperature, both at 925 hPa during the initiation, transition, and termination years of droughts. Arrows indicate winds at 925 hPa.

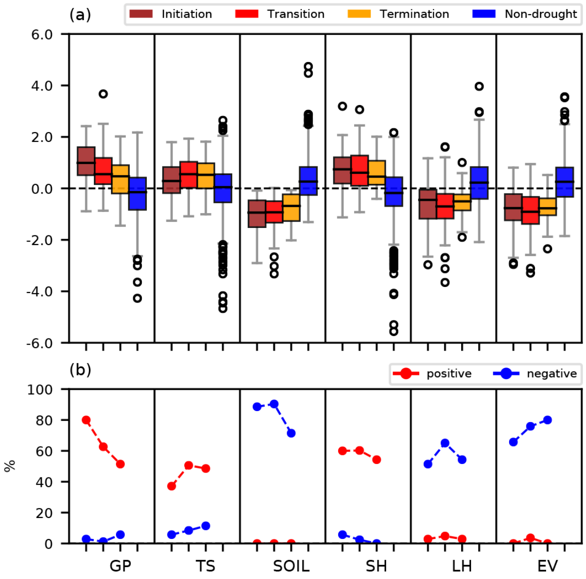

Figure 12. The same boxplot as Fig. 10 but for standardized regional atmospheric and soil variables over the region of study during Mediterranean droughts: anomalies of geopotential height at 850 hPa (GP), surface temperature (TS), soil moisture (SOIL), sensible heat flux (SH), latent heat flux (LH), and evapotranspiration (EV). **(b)** Frequencies of occurrences of positive and negative anomalies in each stage of droughts in order: initiation, transition, and termination years.

a continuous drought without any wet anomaly with respect to the 1000–1849 CE conditions. This indicates a shift of the mean climate of the region to a drier climate, and this transition has been initiated since the pre-industrial period and intensified under the RCP 8.5 scenario.

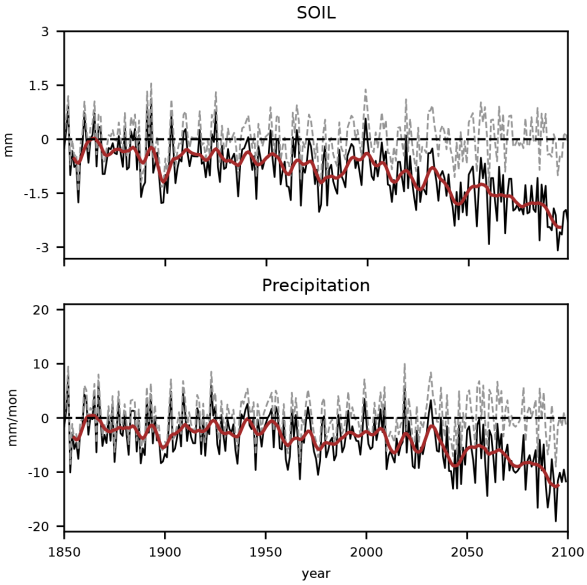

Figure 13. Time series of annual soil moisture (SOIL) and precipitation anomalies from 1850 to 2099 CE with respect to the 1000–1849 CE means. Brown lines indicate a 10-year running means, and dashed lines indicate the detrended time series. The values of the removed trends are presented in Fig. A1.

We examine whether the mechanisms associated with Mediterranean droughts described in the previous section are affected by the anthropogenic influences on climate and whether these changes contribute to the intensification of droughts and eventual aridification in the region occurring in this period. For this, the detrending method is applied to the simulation following the steps mentioned in the Sect. 2.2.

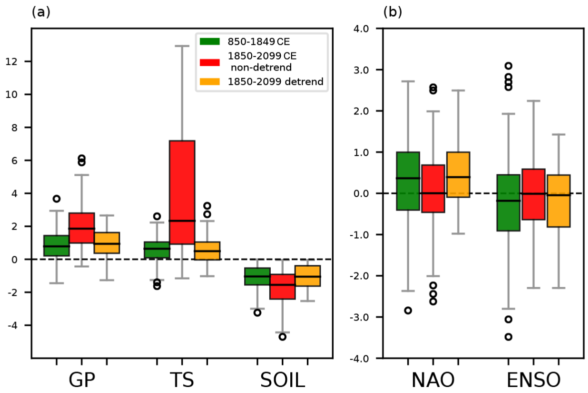

Figure 14. **(a)** Standardized regional variables: anomalies of geopotential height at 850 hPa (GP), surface temperature (TS), and soil moisture (SOIL) over the region of study. **(b)** Indices of large-scale circulation patterns: NAO and ENSO during Mediterranean droughts for the period of 850–1849 CE (green), non-detrended 1850–2099 CE (red), and detrended 1850–2099 CE (yellow). The GP, TS, and SOIL between the detrended 1850–2099 CE and the 850–1849 CE periods present p values from the Mann–Whitney U tests of 0.09, 0.02, and 0.29, respectively. For NAO and ENSO, the p values between these two periods are 0.19 and 0.29, respectively.

First, we analyze the non-detrended drought-related variables with the anthropogenic influences on them and then analyze the detrended variables to see the background climate during droughts when excluding the linear trends.

As for the period 850–1849 CE, droughts during the period 1850–2099 CE are associated with the intense positive geopotential height and temperature anomalies over central Europe and the Mediterranean. However, these features show more intense amplitudes in geopotential height (GP) and temperature (TS) anomalies than during the period 850–1849 CE (Fig. 14a). The variances of GP, TS, and SOIL are also enlarged compared to the past; therefore, their medians and extreme tails are also magnified, which implies that the dryness and its associated atmospheric conditions becomes more frequent and severe in 1850–2099 CE. The increases in GP and TS clearly intensify the above-mentioned interaction among regional atmospheric and soil variables, i.e., the positive temperature–soil moisture feedback. This intensification aids the longevity and intensity of droughts, which is reflected by a reduction in the surface soil moisture anomaly (Fig. 13). Additionally, the precipitation–soil moisture feedback is also involved: a continuous reduction in precipitation decreases the available soil moisture, inducing less evapotranspiration, which again leads to a reduction in precipitation (Seneviratne et al., 2010).

Related to the modes of variability, the frequencies of positive NAO and La Niña-like conditions during droughts also seem to be affected by the overall change in global temperature (Fig. 14b). Compared to 850–1849 CE, the non-detrended 1850–2099 CE period shows reduced frequencies of both positive NAO and La Niña-like conditions during droughts. This result is in line with the previously mentioned intensification of land–atmosphere feedbacks: in this situation where the GP and TS become intense, the regional atmospheric variables play a more dominant role in Mediterranean droughts and the importance of modes of variability is reduced, even during the initial stages of droughts. Hence, the role of positive NAO and La Niña-like conditions in different stages of droughts is diminished. However, the model biases in representing large-scale modes of variability, in particular ENSO, might be relevant. Many CMIP5 models have problems with realistically reproducing the cold SST in the eastern tropical Pacific. Therefore, these models would show fewer La Niña events in future warmer conditions (Seager et al., 2019). An overall increase in El Niño-like conditions here (Fig. 14b) can also be partially related to this bias. Nevertheless, considering this bias does not affect the result that the interaction among the regional variables is changed by the increase in temperature, causing more intensified regional land–atmosphere feedbacks during this period.

For the detrended variables, the GP anomalies and SOIL during droughts of the period 1850–2099 CE are statistically similar to the ones in the period 850–1849 CE (p-value of 0.09 for GP and 0.44 for SOIL). The same is also true for the NAO and ENSO during droughts (p values of 0.19 and 0.29 for each). The detrended TS over the region is statistically similar to the 850–1849 CE value but only at the 2 % confidence level (p value of 0.02). This indicates that the detrending method is not able to fully remove the strong effects of anthropogenic changes on temperature in future droughts. Nevertheless, the mean spatial composites of the detrended surface temperature and geopotential height at 850 hPa during Mediterranean droughts in the period 1850–2099 (Fig. 15) statistically agree with the ones in 850–1849 CE period (Fig. 7) over a large portion of the Mediterranean region.

Hence, when the anthropogenic effect is removed (i.e., the variables are detrended), the mechanisms involved in droughts remain unchanged during 1850–2099 CE. The comparison of non-detrended variables with detrended variables thus indicates that no factor other than the anthropogenic influence in temperature is the cause of the severe dryness in this period. In the future scenario, the intensities of both land–atmosphere feedbacks are magnified due to the increases in GP and TS caused by the increases in GHG, and these feedbacks become dominant in controlling the desiccation over the region.

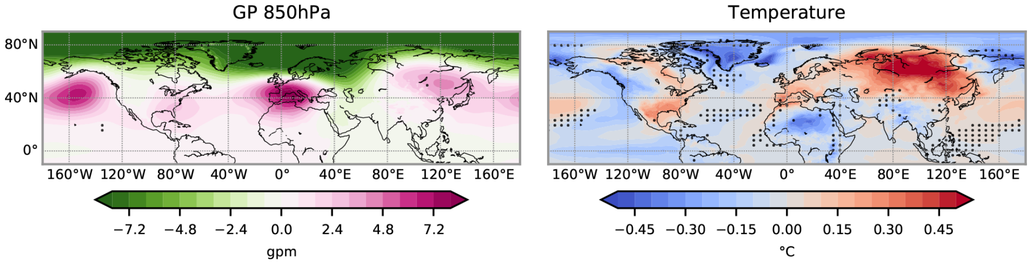

Figure 15. Detrended mean geopotential height anomaly at 850 hPa and surface temperature anomaly during Mediterranean droughts for the 1850–2099 CE. Black dots indicate the regions where the distributions between the detrended 1850–2099 CE and 850–1849 CE are statistically different at the 5 % confidence level (Fig. 8) from the Mann–Whitney *U* tests.

4 Conclusions

We have investigated the variability and mechanisms of multi-year droughts over the western and central Mediterranean region with pan-regional characteristics for the period of 850–1849 CE and whether these mechanisms associated with Mediterranean droughts have changed after the pre-industrial period from 1850 to 2099 CE with the anthropogenic increase in GHG. For this we used simulations from CESM (Lehner et al., 2015).

Firstly, the quantification of droughts is sensitive to the choice of drought index even in the paleoclimate context. For example, the scPDSI exhibits drought events with longer duration than other indices, such as SPEI, SPI, and soil moisture anomalies. Although the major mechanisms that induce multi-year droughts over the region remain similar due to the same overlapping periods and statistically significant correlations among indices, this discrepancy among indices can lead to different conclusions, mostly in the number and duration of past drought events. This shows that using just one unique index is still complicated, even in the paleoclimate context. Hence, the uncertainty associated with different indices must be taken into account when comparing indices in drought studies (Dai, 2011; Raible et al., 2017; Mukherjee et al., 2018), particularly in cases where only a single drought index is used and the focus is on the assessment of the duration of extreme hydrological events in past periods.

Secondly, we found that past Mediterranean droughts were mainly induced by the internal dynamics of climate system, supporting the finding of Xoplaki et al. (2018). The duration of droughts and the patterns of surface temperature and circulation over the Mediterranean during droughts in the control simulation are statistically similar to those in the transient simulation with external forcing. Moreover, a causal connection between volcanic eruptions and Mediterranean dry conditions is not identified. However, our result indicates a connection between large volcanic eruptions and wet periods over the region, supporting the findings of previous studies (McConnell et al., 2020; Rao et al., 2017). A distinct atmospheric pattern occurring during Mediterranean droughts is a barotropic high-pressure system accompanied by a positive temperature anomaly over central Europe and the Mediterranean region. This warm high persists during all seasons when droughts occur in the region, showing stronger intensity during winter and spring. This result emphasizes the importance of the wet cold seasons, i.e., winter and spring climate and circulation in annual Mediterranean droughts. Additionally, the positive NAO and La Niña are other patterns that occur more frequently during Mediterranean droughts.

Thirdly, the mechanisms associated with sustaining multi-year droughts change through the stages of droughts. We found that the large-scale circulation patterns, such as the positive NAO and negative ENSO, play a more important role during the early stage of droughts by providing dry conditions over the western and central Mediterranean region that are required to initiate such events. Therefore, the longevity of droughts is determined by the interaction of regional circulation variables, which involve stable atmospheric conditions, an increase in temperature, and changes in evapotranspiration and surface heat fluxes. Namely, this is the temperature–soil moisture feedback, which continues until the termination of droughts. During these transition years of droughts, the role played by the large-scale patterns is reduced. Hence, the persistence and duration of multi-year droughts should not be fully attributed to the states of large-scale circulation patterns, such as NAO and ENSO, as the roles of regional feedback and circulations regarding droughts become as important as (or more important than) large-scale modes of variability after the initial development of droughts.

It is important to note that the inherent model biases in representing ENSO and NAO (Bellenger et al., 2014; Fasullo et al., 2020) can have some implications in our results on the frequencies of ENSO and NAO at different stages of droughts. The model may produce too frequent and strong La Niña conditions and positive NAO during droughts due to its amplified variability (decadal for ENSO and seasonal for NAO). Moreover, due to the uncertainty associated with the changes in these modes in the future scenario, caution is required when interpreting the connection between droughts and modes of variability in the future warming scenario. Many CMIP5 models show an overall warming of the tropical equatorial Pacific reducing the west–east gradient of SST, which is different from what is observed in the present period (Seager et al., 2019). This model bias to the observation implicates reduced La Niña conditions in CMIP5 models in a warmer world. Nonetheless, this problem does not affect our conclusion: the roles of ENSO and NAO become weaker with the longevity of droughts, while the regional circulation and feedback become more dominant at maintaining the persistence of droughts, which is also found in the future warming scenario.

Fourthly, the decreases in soil moisture and precipitation anomalies have already been detected since the pre-industrial period concomitantly with the anthropogenic increase in GHG. This means that the intensification of droughts and the shift of the mean climate over the region to a drier climate already started during the pre-industrial era. This regional desiccation is principally caused by the anthropogenic increase in GHG, which induces the intensification of interactions between the regional atmospheric and soil variables, associated with the temperature–soil moisture and precipitation–soil moisture feedbacks. If the increase in temperature and decrease in precipitation continue, the region will suffer from a continuous aridification instead of droughts, as droughts are the deviation from the mean hydrological condition.

Fifthly, it is important to mention that our analysis is based on a single-model output and that this raises questions related to single-model studies, such as boundary condition problems and model-dependent biases and physics (PAGES Hydro2k Consortium, 2017). Nevertheless, for a small confined area that surrounds a large body of water (the Mediterranean Sea) and where the land coverage is limited, a finer horizontal resolution is needed to represent the regional climate and the mesoscale processes that are involved more realistically. In the end, our study provides a useful understanding of the long-term variability and mechanisms of Mediterranean droughts by analyzing the entire last millennium. We addressed the influences of external and internal variability on Mediterranean droughts and the different roles of the large-scale modes of variability and regional circulation during the different stages of multi-year droughts.

Lastly, we emphasize again the importance of assessing different drought indices in the paleoclimate context and also in the present and future warming scenario. The reason is that most of the commonly used offline drought indices, such as scPDSI, are based on a water balance that only considers the atmospheric moisture supply and demand, and these indices tend to overestimate drought risks in the future warming scenario (Berg et al., 2017; Mukherjee et al., 2018; Swann et al., 2016). Moreover, Berg et al. (2017) found that the upper-level soil moisture indicates droughts, whereas the mean 3 m soil moisture shows wet or relatively weak dry conditions compared to the surface level. In our study, we used the upper 10 cm soil moisture anomaly that partially reflects the water stress on plants. However, the upper 10 cm of the soil is not enough to fully assess the complex atmosphere–soil–vegetation interaction and the variability in the deeper levels of the soil. In addition, the upper 10 cm soil moisture used here also magnifies drought risks to some extent, in a similar manner to other offline drought indices. Nevertheless, the Mediterranean is one of the regions where the depletion of soil moisture still occurs both at the surface and in the mean 3 m soil level, though the amplitude of the rate of decrease is reduced in the 3 m soil moisture compared to the rate in the surface soil moisture (Berg et al., 2017).

As a next step, more studies on drought metrics need to be conducted in order to assess the future drought risk in the region properly. In addition, as vegetation is known to have more complex responses to the changing climate and droughts (Swann, 2018; Swann et al., 2016), the role of vegetation in extreme hydrological events should be investigated to get a more comprehensive view of drought mechanisms and their changes in the future. The Mediterranean region is considered one of the most vulnerable regions under future warming scenarios (e.g., Giorgi and Lionello, 2008; Lehner et al., 2017), and human impacts can modify the natural mechanisms and propagation of droughts, increasing droughts risks and water shortage issues over the region (Van Loon et al., 2016). Hence, more studies on the topics related to droughts and permanent future aridification in the Mediterranean region, including the role of vegetation during this period, are necessary to develop a better preparedness for upcoming changes.

Appendix A

Table A1. P values from the Mann–Whitney U tests between the drought indices in the control and transient simulations.

	Control (400-year) vs. Transient (850–1849 CE) simulations
scPDSI-summer	0.31
scPDSI-annual	0.35
SPEI	0.5
SPI	0.1
SOIL	0.43

Table A2. Years and total stratospheric sulfate aerosol injection of the 16 largest and 16 smallest volcanic eruptions in 850–1849 CE from Gao et al. (2008).

Largest eruptions		Smallest eruptions	
Year	Total stratospheric sulfate aerosol loading (Tg)	Year	Total stratospheric sulfate aerosol loading (Tg)
1258	257.91	1050	2.79
1452	137.5	1045	2.77
1815	109.72	1060	2.57
1783	92.96	1150	2.12
1227	67.52	1132	2.03
1275	63.72	987	1.92
1600	56.59	1794	1.88
1284	54.69	1316	1.83
1809	53.74	1503	1.72
1167	52.12	1158	1.56
1641	51.60	1213	1.56
1176	45.76	939	1.30
1835	40.16	1307	1.18
933	31.83	1358	1.09
1719	31.48	1142	0.82
1341	31.14	945	0.58

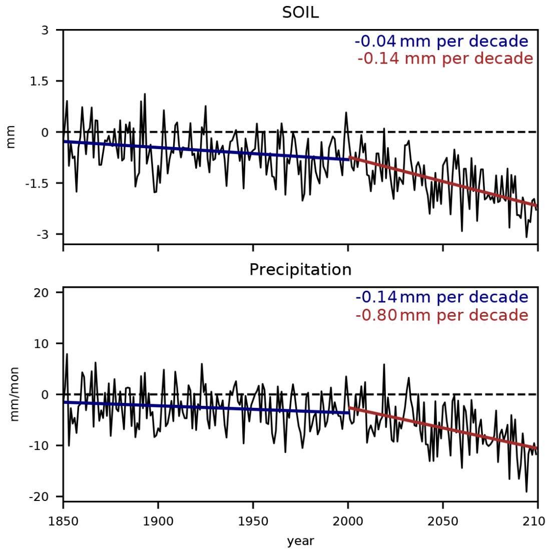

Figure A1. Time series of annual soil moisture (SOIL) and precipitation anomalies from 1850 to 2099 CE with respect to the 1000–1849 CE means for the detrending method. The least-squares method is applied to two separate time periods: 1850–2000 CE and 2001–2099 CE. The trends and their values for each period are also shown.

Code availability. Two R packages were used to calculate the drought indices: the scPDSI (https://CRAN.R-project.org/package=scPDSI, Zhong et al., 2018) and the SPEI (Vicente-Serrano et al., 2009). The biwavelet (https://github.com/tgouhier/biwavelet, Gouhier et al., 2018) was used for the wavelength coherence analysis, and burnr (https://CRAN.R-project.org/package=burnr, Malevich, 2018) was used for the superposed epoch analysis.

Data availability. The summer scPDSI from the Old World Drought Atlas are available at https://www.ncdc.noaa.gov/paleo-search/study/19419 (Cook et al., 2015) and the sea surface temperature ERSST v5 (Huang et al., 2017a) are available at https://doi.org/10.7289/V5T72FNM (Huang et al., 2017ba). The 20th Century Reanalysis V2 (https://psl.noaa.gov/data/gridded/data.20thC_ReanV2.html; Compo et al., 2011) and UDel_AirT_Precip data (https://psl.noaa.gov/data/gridded/data.UDel_AirT_Precip.html; Willmott and Matsuura, 2001) are provided by the NOAA/OAR/ESRL PSL, Boulder, Colorado, USA. The CESM simulations (Lehner et al., 2015) are available on request from the University of Bern.

Author contributions. WMK and CCR discussed and set up the initial research idea. WMK performed the analysis and drafted the manuscript under the supervision of CCR. CCR provided critical feedback on the results and the manuscript. Both authors contributed to the interpretation and discussion of the results and edited the manuscript together.

Competing interests. The authors declare that they have no conflict of interest.

Acknowledgements. The study is funded by the Swiss National Science Foundation (SNSF, grant 200020_172745). We acknowledge that some simulations were performed at the Swiss National Super Computing Centre (CSCS). Support for the 20th Century Reanalysis Project dataset is provided by the U.S. Department of Energy, Office of Science Innovative and Novel Computational Impact on Theory and Experiment (DOE INCITE) program, and Office of Biological and Environmental Research (BER); by the National Oceanic and Atmospheric Administration Climate Program Office; and by the National Oceanic and Atmospheric Administration Climate Program Office, and by the NOAA Physical Sciences Laboratory. The 20th Century Reanalysis V2 and UDel_AirT_Precip data are provided by the NOAA/OAR/ESRL PSL, Boulder, Colorado, USA, from their website at https://psl.noaa.gov/. The authors greatly thank the editor Hugues Goosse and the anonymous reviewers for their constructive feedbacks and insightful comments. The comments from the reviewers helped us to improve the analysis and the presentation of the results.

Financial support. This research has been supported by the Swiss National Science Foundation (SNSF) (grant no. 200020_172745).

Review statement. This paper was edited by Hugues Goosse and reviewed by two anonymous referees.

References

Alpert, P., Neeman, B., and Shay-El, Y.: Climatological analysis of Mediterranean cyclones using ECMWF data, Tellus A, 42, 65–77, https://doi.org/10.3402/tellusa.v42i1.11860, 1990.

Babst, F., Bodesheim, P., Charney, N., Friend, A. D., Girardin, M. P., Klesse, S., Moore, D. J. P., Seftigen, K., Björklund, J., Bouriaud, O., Dawson, A., DeRose, R. J., Dietze, M. C., Eckes, A. H., Enquist, B., Frank, D. C., Mahecha, M. D., Poulter, B., Record, S., Trouet, V., Turton, R. H., Zhang, Z., and Evans, M. E. K.: When tree rings go global: challenges and opportunities for retro-and prospective insight, Quaternary Sci. Rev., 197, 1–20, https://doi.org/10.1016/j.quascirev.2018.07.009, 2018.

Barnston, A. G. and Livezey, R. E.: Classification, seasonality and persistence of low-frequency atmospheric circulation patterns, Mon. Weather Rev., 115, 1083–1126, https://doi.org/10.1175/1520-0493(1987)115<1083:CSAPOL>2.0.CO;2, 1987.

Bellenger, H., Guilyardi, É., Leloup, J., Lengaigne, M., and Vialard, J.: ENSO representation in climate models: From CMIP3 to CMIP5, Clim. Dynam., 42, 1999–2018, https://doi.org/10.1007/s00382-013-1783-z, 2014.

Berg, A., Sheffield, J., and Milly, P. C.: Divergent surface and total soil moisture projections under global warming, Geophys. Res. Lett., 44, 236–244, https://doi.org/10.1002/2016GL071921, 2017.

Brönnimann, S.: Impact of El Niño–southern oscillation on European climate, Rev. Geophys., 45, RG3003, https://doi.org/10.1029/2006RG000199, 2007.

Brönnimann, S., Xoplaki, E., Casty, C., Pauling, A., and Luterbacher, J.: ENSO influence on Europe during the last centuries, Clim. Dynam., 28, 181–197, https://doi.org/10.1007/s00382-006-0175-z, 2007.

Champion, A. J., Hodges, K. I., Bengtsson, L. O., Keenlyside, N. S., and Esch, M.: Impact of increasing resolution and a warmer climate on extreme weather from Northern Hemisphere extratropical cyclones, Tellus A, 63, 893–906, https://doi.org/10.1111/j.1600-0870.2011.00538.x, 2011.

Coats, S., Smerdon, J. E., Seager, R., Cook, B. I., and González-Rouco, J. F.: Megadroughts in southwestern North America in ECHO-G millennial simulations and their comparison to proxy drought reconstructions, J. Climate, 26, 7635–7649, https://doi.org/10.1175/JCLI-D-12-00603.1, 2013.

Coats, S., Cook, B. I., Smerdon, J. E., and Seager, R.: North American pancontinental droughts in model simulations of the last millennium, J. Climate, 28, 2025–2043, https://doi.org/10.1175/JCLI-D-14-00634.1, 2015.

Coats, S., Smerdon, J. E., Cook, B., Seager, R., Cook, E. R., and Anchukaitis, K. J.: Internal ocean-atmosphere variability drives megadroughts in Western North America, Geophys. Res. Lett., 43, 9886–9894, https://doi.org/10.1002/2016GL070105, 2016.

Compo, G. P., Whitaker, J. S., Sardeshmukh, P. D., Matsui, N., Allan, R. J., Yin, X., Gleason, B. E., Vose, R. S., Rutledge, G., Bessemoulin, P., Brönnimann, S., Brunet, M., Crouthamel, R. I., Grant, A. N., Groisman, P. Y., Jones, P. D., Kruk, M. C., Kruger, A. C., Marshall, G. J., Maugeri, M., Mok, H. Y., Nordli, Ø., Ross, T. F., Trigo, R. M., Wang, X. L., Woodruff, S. D., and Worley, S. J.: The twentieth century reanalysis project, Q. J. Roy. Meteor. Soc., 137, 1–28, https://doi.org/10.1002/qj.776, 2011 (data available at: https://psl.noaa.gov/data/gridded/data.20thC_ReanV2.html, last access: 20 April 2021).

Cook, B. I., Anchukaitis, K. J., Touchan, R., Meko, D. M., and Cook, E. R.: Spatiotemporal drought variability in the Mediterranean over the last 900 years, J. Geophys. Res.-Atmos., 121, 2060–2074, https://doi.org/10.1002/2015JD023929, 2016a.

Cook, B. I., Cook, E. R., Smerdon, J. E., Seager, R., Williams, A. P., Coats, S., Stahle, D. W., and Díaz, J. V.: North American megadroughts in the Common Era: Reconstructions and simulations, WIRES Clim. Change, 7, 411–432, https://doi.org/10.1002/wcc.394, 2016b.

Cook, E. R., Seager, R., Kushnir, Y., Briffa, K. R., Büntgen, U., Frank, D., Krusic, P. J., Tegel, W., van der Schrier, G., Andreu-Hayles, L., Baillie, M., Baittinger, C., Bleicher, N., Bonde, N., Brown, D., Carrer, M., Cooper, R., Čufar, K., Dittmar, C., Esper, J., Griggs, C., Gunnarson, B., Günther, B., Gutierrez, E., Haneca, K., Helama, S., Herzig, F., Heussner, K.-U., Hofmann, J., Janda, P., Kontic, R., Köse, N., Kyncl, T., Levanič, T., Linderholm, H., Manning, S., Melvin, T. M., Miles, D., Neuwirth, B., Nicolussi, K., Nola, P., Panayotov, M., Popa, I., Rothe, A., Seftigen, K., Seim, A., Svarva, H., Svoboda, M., Thun, T., Timonen, M., Touchan, R., Trotsiuk, V., Trouet, V., Walder, F., Ważny, T., Wilson, R., and Zang, C.: Old World megadroughts and pluvials during the Common Era, Sci. Adv., 1, e1500561, https://doi.org/10.1126/sciadv.1500561, 2015 (data available at: https://www.ncdc.noaa.gov/paleo-search/study/19419, last access: 20 April 2021).

Dai, A.: Drought under global warming: a review, WIRES Clim. Change, 2, 45–65, https://doi.org/10.1002/wcc.81, 2011.

Deser, C., Hurrell, J. W., and Phillips, A. S.: The role of the North Atlantic Oscillation in European climate projections, Clim. Dynam., 49, 3141–3157, https://doi.org/10.1007/s00382-016-3502-z, 2017.

Dubrovský, M., Hayes, M., Duce, P., Trnka, M., Svoboda, M., and Zara, P.: Multi-GCM projections of future drought and climate variability indicators for the Mediterranean region, Reg. Environ. Change, 14, 1907–1919, https://doi.org/10.1007/s10113-013-0562-z, 2014.

Dünkeloh, A. and Jacobeit, J.: Circulation dynamics of Mediterranean precipitation variability 1948–98, Int. J. Climatol., 23, 1843–1866, https://doi.org/10.1002/joc.973, 2003.

Fasullo, J. T., Phillips, A., and Deser, C.: Evaluation of Leading Modes of Climate Variability in the CMIP Archives, J. Climate, 33, 5527–5545, https://doi.org/10.1175/JCLI-D-19-1024.1, 2020.

Field, C. B., Barros, V., Stocker, T. F., and Dahe, Q.: Managing the risks of extreme events and disasters to advance climate change adaptation: Special Report of Working Groups I and II of the Intergovernmental Panel on Climate Change (IPCC), Cambridge University Press, Cambridge, UK, 2012.

Franke, J., Frank, D., Raible, C. C., Esper, J., and Brönnimann, S.: Spectral biases in tree-ring climate proxies, Nat. Clim. Change, 3, 360–364, https://doi.org/10.1038/nclimate1816, 2013.

Gao, C., Robock, A., and Ammann, C.: Volcanic forcing of climate over the past 1500 years: An improved ice core-based index for climate models, J. Geophys. Res.-Atmos., 113, D23111, https://doi.org/10.1029/2008JD010239, 2008.

García-Herrera, R., Garrido-Perez, J. M., Barriopedro, D., Ordóñez, C., Vicente-Serrano, S. M., Nieto, R., Gimeno, L., Sorí, R., and Yiou, P.: The European 2016/17 Drought, J. Climate, 32, 3169–3187, https://doi.org/10.1175/JCLI-D-18-0331.1, 2019.

Giorgi, F.: Climate change hot-spots, Geophys. Res. Lett., 33, L08707, https://doi.org/10.1029/2006GL025734, 2006.

Giorgi, F. and Lionello, P.: Climate change projections for the Mediterranean region, Global Planet. Change, 63, 90–104, https://doi.org/10.1016/j.gloplacha.2007.09.005, 2008.

Gouhier, T. C., Grinsted, A., and Simko, V.: R package biwavelet: Conduct Univariate and Bivariate Wavelet Analyses (Version 0.20.17), available at: https://github.com/tgouhier/biwavelet (last access: 1 October 2020), 2018.

Grinsted, A., Moore, J. C., and Jevrejeva, S.: Application of the cross wavelet transform and wavelet coherence to geophysical time series, Nonlin. Processes Geophys., 11, 561–566, https://doi.org/10.5194/npg-11-561-2004, 2004.

Haywood, A. M., Valdes, P. J., Aze, T., Barlow, N., Burke, A., Dolan, A. M., von der Heydt, A. S., Hill, D. J., Jamieson, S. S. R., Otto-Bliesner, B. L., Salzmann, U., Saupe, E., and Voss, J.: What can Palaeoclimate Modelling do for you?, Earth Systems and Environment, 3, 1–18, https://doi.org/10.1007/s41748-019-00093-1, 2019.

Hoerling, M., Eischeid, J., Perlwitz, J., Quan, X., Zhang, T., and Pegion, P.: On the Increased Frequency of Mediterranean Drought, J. Climate, 25, 2146–2161, https://doi.org/10.1175/JCLI-D-11-00296.1, 2011.

Huang, B., Thorne, P. W., Banzon, V. F., Boyer, T., Chepurin, G., Lawrimore, J. H., Menne, M. J., Smith, T. M., Vose, R. S., and Zhang, H.-M.: Extended reconstructed sea surface temperature, version 5 (ERSSTv5): upgrades, validations, and intercomparisons, J. Climate, 30, 8179–8205, https://doi.org/10.1175/JCLI-D-16-0836.1, 2017a.

Huang, B., Thorne, P. W., Banzon, V. F., Boyer, T., Chepurin, G., Lawrimore, J. H., Menne, M. J., Smith, T. M., Vose, R. S., and Zhang, H.-M.: NOAA Extended Reconstructed Sea Surface Temperature (ERSST), Version 5 [data set], NOAA National Centers for Environmental Information, https://doi.org/10.7289/V5T72FNM, 2017b.

Hurrell, J. W.: Decadal trends in the North Atlantic Oscillation: regional temperatures and precipitation, Science, 269, 676–679, https://doi.org/10.1126/science.269.5224.676, 1995.

Krichak, S. O. and Alpert, P.: Decadal trends in the east Atlantic–west Russia pattern and Mediterranean precipitation, Int. J. Climatol., 25, 183–192, https://doi.org/10.1002/joc.1124, 2005.

Lehner, F., Joos, F., Raible, C. C., Mignot, J., Born, A., Keller, K. M., and Stocker, T. F.: Climate and carbon cycle dynamics in a CESM simulation from 850 to 2100 CE, Earth Syst. Dynam., 6, 411–434, https://doi.org/10.5194/esd-6-411-2015, 2015.

Lehner, F., Coats, S., Stocker, T. F., Pendergrass, A. G., Sanderson, B. M., Raible, C. C., and Smerdon, J. E.: Projected drought risk in 1.5 °C and 2 °C warmer climates, Geophys. Res. Lett., 44, 7419–7428, https://doi.org/10.1002/2017GL074117, 2017.

Li, W., Li, L., Ting, M., and Liu, Y.: Intensification of Northern Hemisphere subtropical highs in a warming climate, Nat. Geosci., 5, 830–834, https://doi.org/10.1038/ngeo1590, 2012.

Lionello, P., Malanotte-Rizzoli, P., Boscolo, R., Alpert, P., Artale, V., Li, L., Luterbacher, J., May, W., Trigo, R., Tsimplis, M., Ulbrich, U., and Xoplaki, E.: The Mediterranean climate: An overview of the main characteristics and issues, in: Developments in Earth and Environmental Sciences, edited by: Lionello, P., Malanotte-Rizzoli, P., and Boscolo, R., vol. 4 of Mediterranean, Elsevier, 1–26, https://doi.org/10.1016/S1571-9197(06)80003-0, 2006.

Lionello, P., Trigo, I. F., Gil, V., Liberato, M. L., Nissen, K. M., Pinto, J. G., Raible, C. C., Reale, M., Tanzarella, A., Trigo, R. M., Ulbrich, S., and Ulbrich, U.: Objective climatology of cyclones in the Mediterranean region: a consensus view among methods with different system identification and tracking criteria, Tellus A, 68, 29391, https://doi.org/10.3402/tellusa.v68.29391, 2016.

Liu, W., Sun, F., Lim, W. H., Zhang, J., Wang, H., Shiogama, H., and Zhang, Y.: Global drought and severe drought-affected populations in 1.5 and 2 °C warmer worlds, Earth Syst. Dynam., 9, 267–283, https://doi.org/10.5194/esd-9-267-2018, 2018.

Ljungqvist, F. C., Seim, A., Krusic, P. J., González-Rouco, J. F., Werner, J. P., Cook, E. R., Zorita, E., Luterbacher, J., Xoplaki, E., Destouni, G., García-Bustamante, E., Aguilar, C. A. M., Seftigen, K., Wang, J., Gagen, M. H., Esper, J., Solomina, O., Fleitmann, D., and Büntgen, U.: European warm-season temperature and hydroclimate since 850 CE, Environ. Res. Lett., 14, 084015, https://doi.org/10.1088/1748-9326/ab2c7e, 2019.

Lloyd-Hughes, B.: The impracticality of a universal drought definition, Theor. Appl. Climatol., 117, 607–611, https://doi.org/10.1007/s00704-013-1025-7, 2014.

Malevich, S.: burnr: Fire-History Analysis in R, r package version 0.2.2, available at: https://CRAN.R-project.org/package=burnr (last access: 1 February 2021), 2018.

Mariotti, A., Zeng, N., and Lau, K.-M.: Euro-Mediterranean rainfall and ENSO – a seasonally varying relationship, Geophys. Res. Lett., 29, 1621, https://doi.org/10.1029/2001GL014248, 2002.

Mariotti, A., Zeng, N., Yoon, J.-H., Artale, V., Navarra, A., Alpert, P., and Li, L. Z.: Mediterranean water cycle changes: transition to drier 21st century conditions in observations and CMIP3 simulations, Environ. Res. Lett., 3, 044001, https://doi.org/10.1088/1748-9326/3/4/044001, 2008.

McConnell, J. R., Sigl, M., Plunkett, G., Burke, A., Kim, W. M., Raible, C. C., Wilson, A. I., Manning, J. G., Ludlow, F., Chellman, N. J., Innes, H. M., Yang, Z., Larsen, J. F., Schaefer, J. R., Kipfstuhl, S., Mojtabavi, S., Wilhelms, F., Opel, T., Meyer, H., and Steffensen, J. P.: Extreme climate after massive eruption of Alaska's Okmok volcano in 43 BCE and effects on the late Roman Republic and Ptolemaic Kingdom, P. Natl. Acad. Sci. USA, 117, 15443–15449, https://doi.org/10.1073/pnas.2002722117, 2020.

McKee, T. B., Doesken, N. J., and Kleist, J.: The relationship of drought frequency and duration to time scales, in: Proceedings of the 8th Conference on Applied Climatology, 17–22 January 1993, Anaheim, California, USA, vol. 17, 179–183, 1993.

Mishra, A. K. and Singh, V. P.: A review of drought concepts, J. Hydrol., 391, 202–216, https://doi.org/10.1016/j.jhydrol.2010.07.012, 2010.

Mukherjee, S., Mishra, A., and Trenberth, K. E.: Climate Change and Drought: a Perspective on Drought Indices, Current Climate Change Reports, 4, 145–163, https://doi.org/10.1007/s40641-018-0098-x, 2018.

Naumann, G., Alfieri, L., Wyser, K., Mentaschi, L., Betts, R., Carrao, H., Spinoni, J., Vogt, J., and Feyen, L.: Global changes in drought conditions under different levels of warming, Geophys. Res. Lett., 45, 3285–3296, https://doi.org/10.1002/2017GL076521, 2018.

Otto-Bliesner, B. L., Brady, E. C., Fasullo, J., Jahn, A., Landrum, L., Stevenson, S., Rosenbloom, N., Mai, A., and Strand, G.: Climate variability and change since 850 CE: An ensemble approach with the Community Earth System Model, B. Am. Meteorol. Soc., 97, 735–754, https://doi.org/10.1175/BAMS-D-14-00233.1, 2016.

PAGES Hydro2k Consortium: Comparing proxy and model estimates of hydroclimate variability and change over the Common Era, Clim. Past, 13, 1851–1900, https://doi.org/10.5194/cp-13-1851-2017, 2017.

Palmer, W. C.: Meteorological drought, U.S. Department of Commerce, Weather Bureau Research Paper 45, U.S. Weather Bureau, Washington, D.C., USA, 58 pp., 1965.

Parsons, L. A. and Coats, S.: Ocean-atmosphere trajectories of extended drought in Southwestern North America, J. Geophys. Res.-Atmos., 124, 8953–8971, https://doi.org/10.1029/2019JD030424, 2019.

Parsons, L. A., Loope, G. R., Overpeck, J. T., Ault, T. R., Stouffer, R., and Cole, J. E.: Temperature and precipitation variance in CMIP5 simulations and paleoclimate records of the last millennium, J. Climate, 30, 8885–8912, https://doi.org/10.1175/JCLI-D-16-0863.1, 2017.

Parsons, L. A., Coats, S., and Overpeck, J. T.: The continuum of drought in Southwestern North America, J. Climate, 31, 8627–8643, https://doi.org/10.1175/JCLI-D-18-0010.1, 2018.

Philandras, C. M., Nastos, P. T., Kapsomenakis, J., Douvis, K. C., Tselioudis, G., and Zerefos, C. S.: Long term precipitation trends and variability within the Mediterranean region, Nat. Hazards Earth Syst. Sci., 11, 3235–3250, https://doi.org/10.5194/nhess-11-3235-2011, 2011.

Previdi, M. and Liepert, B. G.: Annular modes and Hadley cell expansion under global warming, Geophys. Res. Lett., 34, L22701, https://doi.org/10.1029/2007GL031243, 2007.

Raible, C.: On the relation between extremes of midlatitude cyclones and the atmospheric circulation using ERA40, Geophys. Res. Lett., 34, L07703, https://doi.org/10.1029/2006GL029084, 2007.

Raible, C., Luksch, U., Fraedrich, K., and Voss, R.: North Atlantic decadal regimes in a coupled GCM simulation, Clim. Dynam., 18, 321–330, 2001.

Raible, C., Yoshimori, M., Stocker, T., and Casty, C.: Extreme midlatitude cyclones and their implications for precipitation and wind speed extremes in simulations of the Maunder Minimum versus present day conditions, Clim. Dynam., 28, 409–423, https://doi.org/10.1007/s00382-006-0188-7, 2007.

Raible, C. C., Luksch, U., and Fraedrich, K.: Precipitation and northern hemisphere regimes, Atmos. Sci. Lett., 5, 43–55, https://doi.org/10.1016/j.atmoscilet.2003.12.001, 2003.

Raible, C. C., Ziv, B., Saaroni, H., and Wild, M.: Winter synoptic-scale variability over the Mediterranean Basin under future climate conditions as simulated by the ECHAM5, Clim. Dynam., 35, 473–488, https://doi.org/10.1007/s00382-009-0678-5, 2010.

Raible, C. C., Bärenbold, O., and Gómez-Navarro, J. J.: Drought indices revisited – improving and testing of drought indices in a simulation of the last two millennia for Europe, Tellus A, 69, 1287492, https://doi.org/10.1080/16000870.2017.1296226, 2017.

Rao, M. P., Cook, B. I., Cook, E. R., D'Arrigo, R. D., Krusic, P. J., Anchukaitis, K. J., LeGrande, A. N., Buckley, B. M., Davi, N. K., Leland, C., and Griffin, K. L.: European and Mediterranean hydroclimate responses to tropical volcanic forcing over the last millennium, Geophys. Res. Lett., 44, 5104–5112, https://doi.org/10.1002/2017GL073057, 2017.

Schmidt, G. A., Jungclaus, J. H., Ammann, C. M., Bard, E., Braconnot, P., Crowley, T. J., Delaygue, G., Joos, F., Krivova, N. A., Muscheler, R., Otto-Bliesner, B. L., Pongratz, J., Shindell, D. T., Solanki, S. K., Steinhilber, F., and Vieira, L. E. A.: Climate forcing reconstructions for use in PMIP simulations of the Last Millennium (v1.1), Geosci. Model Dev., 5, 185–191, https://doi.org/10.5194/gmd-5-185-2012, 2012.

Seager, R., Liu, H., Henderson, N., Simpson, I., Kelley, C., Shaw, T., Kushnir, Y., and Ting, M.: Causes of Increasing Aridification of the Mediterranean Region in Response to Rising Greenhouse Gases, J. Climate, 27, 4655–4676, https://doi.org/10.1175/JCLI-D-13-00446.1, 2014.

Seager, R., Cane, M., Henderson, N., Lee, D.-E., Abernathey, R., and Zhang, H.: Strengthening tropical Pacific zonal sea surface temperature gradient consistent with rising greenhouse gases, Nat. Clim. Change, 9, 517–522, https://doi.org/10.1038/s41558-019-0505-x, 2019.

Seneviratne, S. I., Corti, T., Davin, E. L., Hirschi, M., Jaeger, E. B., Lehner, I., Orlowsky, B., and Teuling, A. J.: Investigating soil moisture–climate interactions in a changing climate: A review, Earth-Sci. Rev., 99, 125–161, https://doi.org/10.1016/j.earscirev.2010.02.004, 2010.

Sousa, P. M., Trigo, R. M., Aizpurua, P., Nieto, R., Gimeno, L., and Garcia-Herrera, R.: Trends and extremes of drought indices throughout the 20th century in the Mediterranean, Nat. Hazards Earth Syst. Sci., 11, 33–51, https://doi.org/10.5194/nhess-11-33-2011, 2011.

Spinoni, J., Naumann, G., Vogt, J. V., and Barbosa, P.: The biggest drought events in Europe from 1950 to 2012, J. Hydrol., 3, 509–524, https://doi.org/10.1016/j.ejrh.2015.01.001, 2015.

Spinoni, J., Naumann, G., and Vogt, J. V.: Pan-European seasonal trends and recent changes of drought frequency and severity, Global Planet. Change, 148, 113–130, https://doi.org/10.1016/j.gloplacha.2016.11.013, 2017.

Stevenson, S., Overpeck, J. T., Fasullo, J., Coats, S., Parsons, L., Otto-Bliesner, B., Ault, T., Loope, G., and Cole, J.: Climate variability, volcanic forcing, and last millennium hydroclimate extremes, J. Climate, 31, 4309–4327, https://doi.org/10.1175/JCLI-D-17-0407.1, 2018.

Swann, A. L.: Plants and drought in a changing climate, Current Climate Change Reports, 4, 192–201, https://doi.org/10.1007/s40641-018-0097-y, 2018.

Swann, A. L., Hoffman, F. M., Koven, C. D., and Randerson, J. T.: Plant responses to increasing CO_2 reduce estimates of climate impacts on drought severity, P. Natl. Acad. Sci. USA, 113, 10019–10024, https://doi.org/10.1073/pnas.1604581113, 2016.

Taylor, K. E., Stouffer, R. J., and Meehl, G. A.: An overview of CMIP5 and the experiment design, B. Am. Meteorol. Soc., 93, 485–498, https://doi.org/10.1175/BAMS-D-11-00094.1, 2012.

Thornthwaite, C. W.: An approach toward a rational classification of climate, Geogr. Rev., 38, 55–94, https://doi.org/10.2307/210739, 1948.

Trenberth, K. E.: The Definition of El Niño, B. Am. Meteorol. Soc., 78, 2771–2778, https://doi.org/10.1175/1520-0477(1997)078<2771:TDOENO>2.0.CO;2, 1997.

Trigo, R., Osborn, T., and Corte-Real, J.: The North Atlantic Oscillation influence on Europe: climate impacts and associated physical mechanisms, Clim. Res., 20, 9–17, https://doi.org/10.3354/cr020009, 2002.

Ulbrich, U., Leckebusch, G., and Pinto, J. G.: Extra-tropical cyclones in the present and future climate: a review, Theor. Appl. Climatol., 96, 117–131, https://doi.org/10.1007/s00704-008-0083-8, 2009.

Van Loon, A. F., Gleeson, T., Clark, J., Van Dijk, A. I. J. M., Stahl, K., Hannaford, J., Di Baldassarre, G., Teuling, A. J., Tallaksen, L. M., Uijlenhoet, R., Hannah, D. M., Sheffield, J., Svoboda, M., Verbeiren, B., Wagener, T., Rangecroft, S., Wanders, N., and Van Lanen, H. A. J.: Drought in the Anthropocene, Nat. Geosci., 9, 89–91, https://doi.org/10.1038/ngeo2646, 2016.

Vicente-Serrano, S. M.: El Niño and La Niña influence on droughts at different timescales in the Iberian Peninsula, Water Resour. Res., 41, W12415, https://doi.org/10.1029/2004WR003908, 2005.

Vicente-Serrano, S. M., Beguería, S., and López-Moreno, J. I.: A Multiscalar Drought Index Sensitive to Global Warming: The Standardized Precipitation Evapotranspiration Index, J. Climate, 23, 1696–1718, https://doi.org/10.1175/2009JCLI2909.1, 2009.

Vicente-Serrano, S. M., Beguería, S., López-Moreno, J. I., Angulo, M., and El Kenawy, A.: A new global 0.5 gridded dataset (1901–2006) of a multiscalar drought index: comparison with current drought index datasets based on the Palmer Drought Severity Index, J. Hydrometeorol., 11, 1033–1043, https://doi.org/10.1175/2010JHM1224.1, 2010.

Vicente-Serrano, S. M., Lopez-Moreno, J.-I., Beguería, S., Lorenzo-Lacruz, J., Arturo Sanchez-Lorenzo, García-Ruiz, J. M., Azorin-Molina, C., Morán-Tejeda, E., Revuelto, J., Ricardo Trigo, Coelho, F., and Espejo, F.: Evidence of increasing drought severity caused by temperature rise in southern Europe, Environ. Res. Lett., 9, 044001, https://doi.org/10.1088/1748-9326/9/4/044001, 2014.

Vicente-Serrano, S. M., Van der Schrier, G., Beguería, S., Azorin-Molina, C., and Lopez-Moreno, J.-I.: Contribution of precipitation and reference evapotranspiration to drought indices under different climates, J. Hydrol., 526, 42–54, https://doi.org/10.1016/j.jhydrol.2014.11.025, 2015.

Wallace, J. M. and Gutzler, D. S.: Teleconnections in the Geopotential Height Field during the Northern Hemisphere Winter, Mon. Weather Rev., 109, 784–812, https://doi.org/10.1175/1520-0493(1981)109<0784:TITGHF>2.0.CO;2, 1981.

Wang, W., Ertsen, M. W., Svoboda, M. D., and Hafeez, M.: Propagation of drought: from meteorological drought to agricultural and hydrological drought, Adv. Meteorol., 2016, e6547209, https://doi.org/10.1155/2016/6547209, 2016.

Watterson, I.: The intensity of precipitation during extratropical cyclones in global warming simulations: a link to cyclone intensity?, Tellus A, 58, 82–97, https://doi.org/10.1111/j.1600-0870.2006.00147.x, 2006.

Wells, N., Goddard, S., and Hayes, M. J.: A Self-Calibrating Palmer Drought Severity Index, J. Climate, 17, 2335–2351, https://doi.org/10.1175/1520-0442(2004)017<2335:ASPDSI>2.0.CO;2, 2004.

Wilhite, D.: Understanding the Phenomenon of Drought, Drought Mitigation Center Faculty Publications, available at: https://digitalcommons.unl.edu/droughtfacpub/50 (last access: 1 April 2020), 1993.

Willmott, C. J. and Matsuura, K.: Terrestrial air temperature and precipitation: Monthly and annual time series (1950–1999) Version 1.02, Center for Climatic Research, University of Delaware, Newark, USA, 2001 (data available at: https://psl.noaa.gov/data/gridded/data.UDel_AirT_Precip.html, last access: 20 April 2021).

Xoplaki, E., González-Rouco, J. F., Luterbacher, J., and Wanner, H.: Mediterranean summer air temperature variability and its connection to the large-scale atmospheric circulation and SSTs, Clim. Dynam., 20, 723–739, https://doi.org/10.1007/s00382-003-0304-x, 2003.

Xoplaki, E., González-Rouco, J., Luterbacher, J., and Wanner, H.: Wet season Mediterranean precipitation variability: influence of large-scale dynamics and trends, Clim. Dynam., 23, 63–78, 2004.

Xoplaki, E., Luterbacher, J., Wagner, S., Zorita, E., Fleitmann, D., Preiser-Kapeller, J., Sargent, A. M., White, S., Toreti, A., Haldon, J. F., Mordechai, L., Bozkurt, D., Akçer-Ön, S., and Izdebski, A.: Modelling Climate and Societal Resilience in the Eastern Mediterranean in the Last Millennium, Hum. Ecol., 46, 363–379, https://doi.org/10.1007/s10745-018-9995-9, 2018.

Yin, D., Roderick, M. L., Leech, G., Sun, F., and Huang, Y.: The contribution of reduction in evaporative cooling to higher surface air temperatures during drought, Geophys. Res. Lett., 41, 7891–7897, https://doi.org/10.1002/2014GL062039, 2014.

Zhong, R., Chen, X., Wang, Z., and Lai, C.: scPDSI: Calculation of the Conventional and Self-Calibrating Palmer Drought Severity Index, r package version 0.1.3, available at: https://CRAN.R-project.org/package=scPDSI (last access: 1 November 2019), 2018.

Zhu, Y., Liu, Y., Wang, W., Singh, V. P., Ma, X., and Yu, Z.: Three dimensional characterization of meteorological and hydrological droughts and their probabilistic links, J. Hydrol., 578, 124016, https://doi.org/10.1016/j.jhydrol.2019.124016, 2019.

Zveryaev, I. I.: Seasonality in precipitation variability over Europe, J. Geophys. Res.-Atmos., 109, D05103, https://doi.org/10.1029/2003JD003668, 2004.

Chapter 4

Statistical characteristics of extreme daily precipitation during 1501BCE – 1849CE in the Community Earth System Model

Woon Mi Kim, Richard Blender, Michael Sigl, Martina Messmer and Christoph Raible

Published in *Climate of the Past*, Volume 17, 2031 – 2053, 2021

The chapter is published under the link:
`https://doi.org/10.5194/cp-17-2031-2021`

4.1 Abstract

In this study, we analyze extreme daily precipitation during the pre-industrial period from 1501 BCE to 1849 CE in simulations from the Community Earth System Model version 1.2.2. A peak-over-threshold (POT) extreme value analysis is employed to examine characteristics of extreme precipitation and to identify connections of extreme precipitation with the external forcing and with modes of internal variability. The POT analysis shows that extreme precipitation with similar statistical characteristics, i.e., the probability density distributions, tends to cluster spatially. There are differences in the distribution of extreme precipitation between the Pacific and Atlantic sectors and between the northern-high and southern-low latitudes.

Extreme precipitation during the pre-industrial period is largely influenced by modes of internal variability, such as El Niño-Southern Oscillation (ENSO), the Pacific North American, and Pacific South American patterns among others, and regional surface temperatures. In general, the modes of variability exhibit a statistically significant connection to extreme

precipitation in the vicinity to their regions of action.The exception is ENSO, which shows more widespread influence on extreme precipitation across the Earth. In addition, the regions where extreme precipitation is more associated either by a mode of variability or by the regional surface temperature are distinguished. Regional surface temperatures are associated with extreme precipitation over lands at the extratropical latitudes and over the tropical oceans. In other regions, the influences of modes of variability are still dominant.

Effects of the changes in the orbital parameters on extreme precipitation are rather weak compared to those of the modes of internal variability and of the regional surface temperatures. Still, some regions in central Africa, southern Asia, and the tropical Atlantic ocean show statistically significant connections between extreme precipitation and orbital forcing, implying that in these regions, extreme precipitation has increased linearly during the 3351-year pre-industrial period.

Tropical volcanic eruptions affect extreme precipitation more clearly in the short term up to a few years, altering both the intensity and frequency of extreme precipitation. However, more apparent changes are found in the frequency than the intensity of extreme precipitation. After eruptions, the return periods of extreme precipitation increase over the extratropical regions and the tropical Pacific, while a decrease is found in other regions. The post-eruption changes in the frequency of extreme precipitation are associated with ENSO, which itself is influenced by tropical eruptions.

Overall, the results show that climate simulations are useful to complement the information on pre-industrial extreme precipitation, as they elucidate statistical characteristics and long-term connections of extreme events with natural variability.

4.2 Introduction

Extreme daily precipitation, which often causes devastating flood events, is a difficult phenomenon to study due to its rare occurrence and short-lived nature. At regional scale, extreme precipitation events are caused by meso- and synoptic-scale processes (Pfahl and Wernli, 2012; Pfahl, 2014) and at global scale, they are influenced by large-scale modes of variability, such as El Niño-Southern Oscillation (ENSO) or the North Atlantic Oscillation (NAO) among others (Kenyon and Hegerl, 2010; Sun et al., 2015). In recent years, the topic has attracted more and more attention as the behavior of extreme precipitation is expected to change differently to that of mean precipitation in a warmer world (Allen and Ingram, 2002; Trenberth et al., 2003; Pall et al., 2007). While mean precipitation is expected to follow largely the “wet gets wetter, and dry gets drier” rule (Trenberth et al., 2003; Chou and Neelin, 2004; Chou et al., 2009), extreme precipitation is projected to increase over the entire globe (Trenberth et al., 2003; Donat et al., 2016; Fischer and Knutti, 2016). The “wet gets wetter, and dry gets drier” pattern denotes the intensification of the global hydrological cycle, which is controlled by a tropospheric energy budget (Boer, 1993; Allen and Ingram, 2002; Yang et al., 2003). Nevertheless, it is also noted that this pattern for the future mean precipitation is more heterogeneous over land areas in observations and climate models (Roderick et al., 2014; Byrne and O'Gorman, 2015) and breaks in the tropics in CMIP5 models (Chadwick et al., 2013).

Unlike changes in mean precipitation which are largely regulated by the available energy budget, changes in extreme precipitation are constrained by the available maximum low-level atmospheric moisture at a given temperature following the Clausius–Clapeyron (C-C) relationship (Allen and Ingram, 2002; Pall et al., 2007). The reasoning is as follows: the low-level atmosphere can hold more moisture with increasing temperatures, which in turn leads to an increase in extreme precipitation (Trenberth et al., 2003; Pall et al., 2007; Fischer and Knutti, 2016). The rate of increase of extreme precipitation given by C-C is 6-7% per 1 degree of warming. This relationship holds mostly true over higher latitudes where the air is usually closer to saturation and relative humidity is roughly constant (Allen and Ingram, 2002). Mean increases in extreme precipitation are projected for many terrestrial regions by climate models in the Coupled Model Intercomparison Project (CMIP5) under different climate change scenarios (Kharin et al., 2013; Scoccimarro et al., 2013; Wang et al., 2017; Donat et al., 2019). However, at regional scale, the changes are uncertain and vary from region to region (O'Gorman, 2012; Kharin et al., 2013; Pfahl et al., 2017).

Observations indicate that the frequency and intensity of extreme daily precipitation events have already increased over large parts of the continents during the 20th century (Asadieh and Krakauer, 2015; Donat et al., 2016, 2019; Myhre et al., 2019; Papalexiou and Montanari, 2019). These changes are coherently captured by many CMIP5 models (Donat et al., 2016, 2019), though overall, significant inter-model spread is found in the historical period and even more in climate projections (Scoccimarro et al., 2013; Donat et al., 2016; Wang et al., 2017; Donat et al., 2019). Additionally, the models show some bias in the magnitude of extreme daily precipitation (Stephens et al., 2010; Kopparla et al., 2013). The discrepancies between observations and climate models are potentially associated with the model-dependent sensitivity of extreme precipitation to the increase in temperature (Donat et al., 2016) and the model parameterization of subgrid scale physical processes which are relevant for extreme precipitation (e.g., Champion et al., 2011; Van Haren et al., 2015; Scher et al., 2017).

Many studies focus on the understanding of the nature of extreme daily precipitation in the historic period covering the last 50 to 100 years and their changes until the end of the 21st century under climate change scenarios (e.g., Asadieh and Krakauer, 2015; Donat et al., 2016, 2019; Wang et al., 2017; Myhre et al., 2019). Studying extreme events in the historical period is a reasonable approach as the analysis of such events with short duration requires continuous records of daily precipitation and such records are only provided by the modern instrumental observations and model simulations. Nevertheless, to understand the entire nature of these complex and rare events, it would be ideal to investigate their characteristics and long-term variability in the past when the anthropogenic influences on the climate were not present yet.

Reconstructions of past climate events based on natural proxies and historical documents can provide a glimpse of the nature of extreme precipitation and floods in the past (e.g., Brázdil et al., 2012; Kjeldsen et al., 2014; Machado et al., 2015; Steinschneider et al., 2016;

Zheng et al., 2018). For instance, lake sediment records indicate that the frequency of floods has increased during the Little Ice Age in the Mediterranean French Alpine region (Wilhelm et al., 2012). This period is also coherent with increased flood occurrences in central Europe described in the 500-year documentary records on river catchments (Glaser et al., 2010). Frequent floods in this period seem to be associated with large-scale atmospheric circulation patterns such as the Atlantic low and Russian high (Jacobeit et al., 2003). In the semi-arid regions in the western United States, the frequency of extreme precipitation is inferred from tree ring-based reconstructions of the summer Palmer Drought Severity Index for the last 500 years (Steinschneider et al., 2016). The reconstruction indicates that the regions present a low-frequency variability of extreme precipitation that ranges over ample frequency bands, showing a variability from 2 to 30 years. Natural proxies and historical reconstructions are undoubtedly invaluable sources of information on extreme events for periods prior to the start of the modern instrumental era. However, they also pose some limitations: they are not continuous in time and scarcely distributed across the globe, therefore, providing more local aspects of such events.

Nowadays, earth system models that describe the physical processes within the climate system provide abundant and continuous data of global atmospheric variables, not only for the historical and future periods but also for the past (Schurer et al., 2013; Jungclaus et al., 2017; PAGES Hydro2k Consortium, 2017). As these state-of-the-art climate models are already utilized to understand the present mechanisms and future changes of extreme daily precipitation, they can also help to explore the past natural variability of extreme precipitation, assuming that the corresponding transient external forcing is properly adapted in simulations for the past (Schmidt et al., 2011; Jungclaus et al., 2017).

The purpose of this study is to analyze and characterize extreme daily precipitation for the period 1501 BCE to 1849 CE (before the industrial revolution) using the Community Earth System Model version 1.2.2. We base our analysis on simulations, which are either driven by orbital forcing alone or by all external forcing functions, including the new continuous volcanic record (Sigl et al., 2021). These simulations allow to distinguish between signals of orbital and volcanic forcing and internal variability. For the analysis, we employ the peak-over-threshold extreme value analysis (Coles et al., 2001) to characterize the 3351 year pre-industrial extreme daily precipitation on a global scale, to assess its long-term connection to externally forced variability, such as the changes in radiation driven by the orbital parameters and volcanic eruptions, to internal variability associated with large-scale circulation patterns, and to surface air temperature. The peak-over-threshold analysis is an amply used method to understand the characteristics of extreme events. For instance, the method has been used to study the characteristics and recurrence periods of wind storm related variables (Della-Marta et al., 2009; Blender et al., 2017) and extreme precipitation (Sugahara et al., 2009; Thiombiano et al., 2017) in different locations, and the association of extreme events with large-scale modes of variability (Silva et al., 2016; Blender et al., 2017; Thiombiano et al., 2017).

This paper is organized as follows: in Sect. 4.3, we introduce the Community Earth System

Model, the set-up of the model simulations, and the observational data sets used to evaluate the model's ability to represent daily precipitation. Section 4.4 outlines the theoretical basis of the peak-over-threshold extreme value analysis and the methods employed for our analysis. The results are presented in Sect. 4.5 where we first evaluate the climate model against reanalysis data, then show the distribution of extreme daily precipitation globally, and finally, assess how the extreme daily precipitation is statistically related to orbital forcing changes, internal modes of variability, and volcanic forcing. Lastly, conclusive remarks are presented in Sect. 4.6.

4.3 Data

4.3.1 Description of the model, simulations, and observational data

The Community Earth System Model (CESM; Hurrell et al., 2013) version 1.2.2 is a fully coupled general circulation model that is composed of several component models: the Community Atmosphere Model version 5 (CAM5; Neale et al., 2010) for the atmosphere, the Community Land Model version 4 (CLM4; Lawrence et al., 2011) for the land which includes a prognostic carbon-nitrogen cycle, the Parallel Ocean Program version 2 (POP2; Smith et al., 2010) for the ocean, and the Community Ice Code version 4 (CICE4; Hunke et al., 2010) for the sea ice. The spatial resolutions of the simulations are 1.9° × 2.5° for the atmosphere and land, and 1° × 1° for the ocean and sea ice. The atmosphere is resolved at 30 and the land at 15 vertical levels. The ocean has 60 vertical levels. The time resolutions of the simulations are 6-hourly and monthly, and the 6-hourly precipitation is aggregated to a daily time resolution.

Table 4.1: Forcing values for the simulations. The time-varying forcing in the last column is presented in Fig. 4.1.

		spin-up simulation	**orbital-only simulation**	**full-forcing simulation**
time	[years]	1405	3351 (1501 BCE – 2008 CE)	3351 (1501 BCE – 2008 CE)
GHG				
CO_2	[ppm]	274.21	274.21	Bereiter et al. (2015) and Meinshausen et al. (2017)
CH_4	[ppb]	572.88	572.88	Joos and Spahni (2008) and Meinshausen et al. (2017)
N_2O	[ppb]	262.79	262.79	Joos and Spahni (2008) and Meinshausen et al. (2017)
VOL	[Tg]	no forcing	no forcing	Carn et al. (2016) and Sigl et al. (2021)
TSI	[Wm^{-2}]	1360.38	1360.38	Vieira et al. (2011) and Usoskin et al. (2014)
LULUC		850 CE conditions	850 CE conditions	Pongratz et al. (2008)

Using CESM, we perform two simulations covering the period 1501 BCE – 2008 CE (Table 4.1). The two simulations are branched off from the last year of a spin-up simulation with perpetual forcings. The spin-up simulation is performed with the orbital parameters and forcings set constant at 1501 BCE conditions, with a CO_2 level of 274.21 ppm (Bereiter et al., 2015), a CH_4 level of 572.88 ppb, a N_2O level of 262.79 ppb (Joos and Spahni, 2008), and a total solar irradiance (TSI) of 1360.38 Wm^{-2} (Vieira et al., 2011; Usoskin et al., 2014). The land use and land-use changes (LULUC) are set to conditions reconstructed for the year 850 CE (Pongratz et al., 2008). The spin-up simulation is run for 1405 years until it reaches an equilibrium state.

The first simulation that branches off the spin-up simulation includes orbital parameters that vary in time from 1501 BCE to 2008 CE. All other forcings are kept the same as in the spin-up period (Table 4.1). Hence, this simulation includes only the effect of the changes in the orbital parameters and internal climate variability. Hereinafter, this simulation is called the orbital-only simulation.

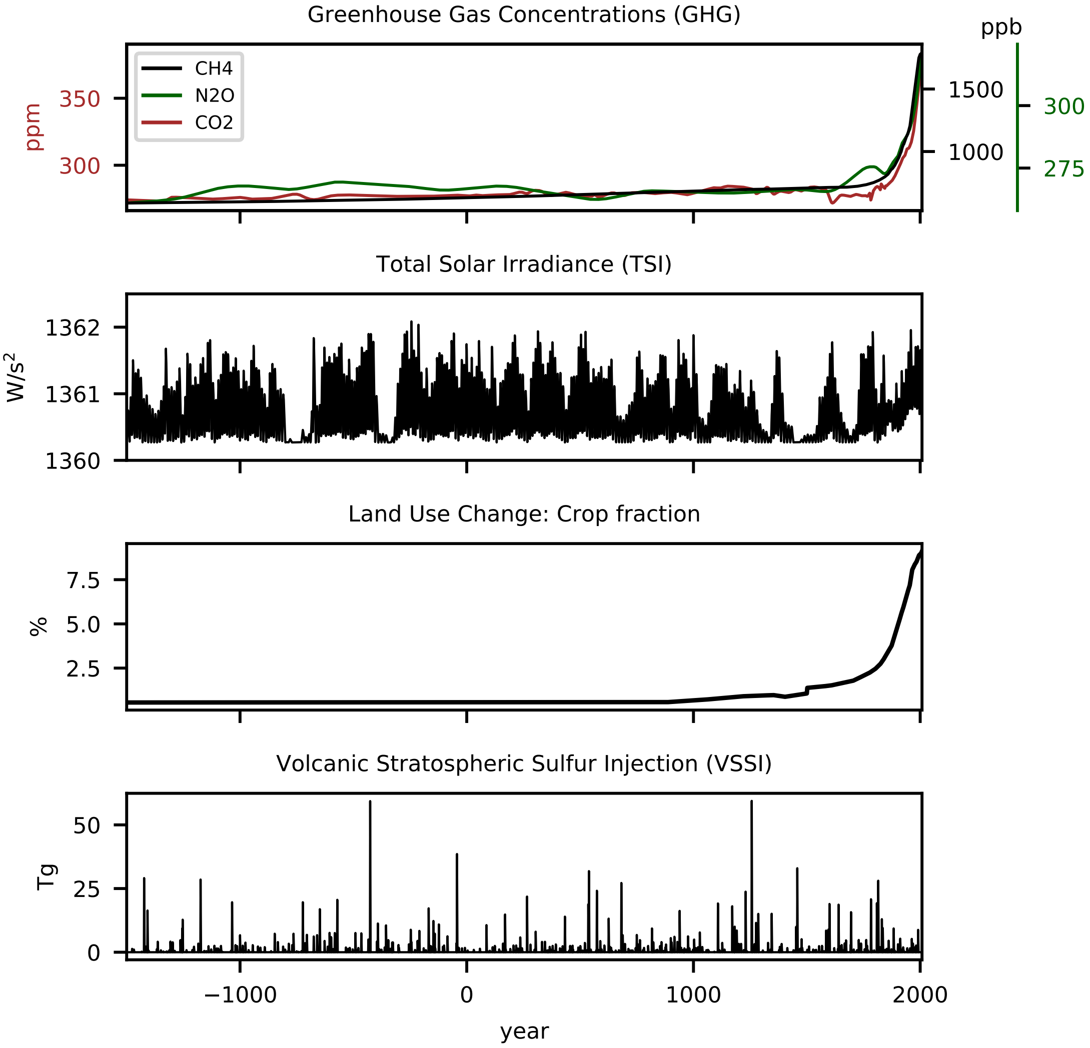

Figure 4.1: Time series of the external forcing included in the transient full-forcing simulation for 1501 BCE – 2008 CE.

The second simulation is run with all time-varying external forcings from 1501 BCE to 2008 CE (Fig. 4.1). The variables for the external forcings are the total solar irradiance (TSI), greenhouse gas concentrations (GHG), volcanic sulfate aerosols (VOL), and LULUC.

The TSI is reconstructed from $\Delta^{14}C$ (Usoskin et al., 2014, 2016; Vieira et al., 2011) and obtained from the Paleoclimate Modelling Intercomparison Project Phase 4 (PMIP4) database (https://pmip4.lsce.ipsl.fr/). For GHG up to 1849 CE, the annual records of CO_2 is obtained from Bereiter et al. (2015), and of CH_4 and N_2O from Joos and Spahni (2008). These annual time series are smoothed by cubic spline interpolation. After 1850 CE, the annual GHG is extended using the records from Meinshausen et al. (2017). LULUC up to 1500 CE is based on the reconstructions from Pongratz et al. (2008) and after this year, it is merged with the reconstruction from Hurtt et al. (2011). Prior to 850 CE, the LULUC is set constant to 850 CE values and it varies afterwards. This second simulation is denoted as the full-forcing simulation (see Table 4.1).

The record of volcanic sulfate aerosols from 1501 BCE to 1979 CE is obtained from Sigl et al. (2021), and afterward until 2008 CE from Carn et al. (2016). To incorporate this record into the transient simulation, we use the Easy Volcanic Aerosol Model version 1.2 (EVA; Toohey et al., 2016) to generate the temporal and latitudinal distribution of the volcanic aerosols. Then, two modifications are applied to this volcanic aerosol distribution to attain an atmospheric response for the 1991 Pinatubo eruption, which is similar to the respective response in Gao et al. (2008), the volcanic forcing used in Paleoclimate Modelling Intercomparison Project (PMIP) Last Millennium experiments (Schmidt et al., 2011; Lehner et al., 2015; Otto-Bliesner et al., 2016): First, the total volcanic aerosols are scaled by a factor of 1.49. By applying the scaling, more similar responses of atmospheric temperatures and incoming solar radiation to the eruptions in the here presented simulation and Gao et al. (2008) is ensured. A similar scaling approach was used by Zhong et al. (2018), but with a slightly higher scaling factor of 1.79, as they used the 1815 Tambora eruption as reference. Second, the timing of the maximum peaks of the eruptions is shifted by four months in time after the respective eruption following the approach in Gao et al. (2008). After this peak, the volcanic aerosols decay smoothly as estimated by the EVA model.

To evaluate the daily precipitation obtained by CESM, the precipitation of CESM is compared to that of ERA5, the latest reanalysis product of ECMWF, during the period 1979–2008 CE (Hersbach et al., 2020). ERA5 uses the 2016 version of the ECMWF numerical weather prediction model and the integrated forecasting system Cy41r2 data assimilation (Hersbach et al., 2020). From ERA, we use the total precipitation at a temporal resolution of an hour and at a spatial resolution of $0.75° \times 0.75°$. To be compared against CESM, the hourly precipitation of ERA5 is accumulated to daily precipitation sums and the spatial resolution is interpolated to the coarser grid resolution of $1.9° \times 2.5°$to be consistent with the resolution of CESM.

4.4 Methods

We apply the peak-over-threshold (POT) analysis to four datasets of daily precipitation anomalies: the CESM orbital-only and full-forcing simulations for the past period 1501 BCE–

1849 CE, the CESM full-forcing and the ERA5 reanalysis for the present period 1979–2008 CE. The daily precipitation anomalies are calculated by subtracting the multi-year daily means, i.e., the means of the entire 1501 BCE–1849 CE period for the CESM past simulations and 1979–2008 CE for the present period in CESM and ERA5, from each daily precipitation value.

For the 1501 BCE–1849 CE simulations, the 99^{th} percentiles relative to their distributions of the entire period are taken as a threshold to define extreme precipitation. For evaluation in the period 1979–2008 CE, the 95^{th} percentiles are selected as a threshold in order to obtain enough extreme events during this rather short period.

4.4.1 Peak-over-threshold extreme value analysis

The POT approach (Coles et al., 2001) states that the values y of a sequence of an independent random variable x, in our case, the precipitation anomalies, that exceed a certain threshold u, i.e., the 99^{th} or 95^{th} percentiles, are asymptotically distributed following a generalized Pareto distribution (GPD) with the density distribution function given as:

$$H(y) = \begin{cases} 1 - (1 + \frac{\xi y}{\sigma})^{-1/\xi} & \text{for} \quad \xi \neq 0 \\ 1 - \exp(-\frac{y}{\sigma}) & \text{for} \quad \xi = 0 \end{cases} \tag{4.1}$$

where $y = x - u$ are the positive exceedances of daily precipitation anomalies, σ is the scale parameter that characterizes the spread of the distribution and the scaling of the exceedances y, and ξ is the shape parameter that represents the upper-bound and tail behavior of the distribution (Sugahara et al., 2009; Blender et al., 2017). When ξ ¿ 0, the upper-bound is infinite and the distribution has a heavy tail. For $\xi = 0$, the upper-bound is also infinite, but the tail shape is lighter as the distribution decays exponentially. When ξ ¡ 0, the distribution has a finite upper-bound $y \leq -\sigma/\xi$ (above this upper-bound the probability vanishes) and a thin tail (Coles et al., 2001). When the number of exceedances is small and the estimated ξ is negative, there is a bias in the estimation of ξ towards a larger standard error (Blender et al., 2017). This occurs because since any sample has a finite maximum, there is a bias towards estimated distributions with an upper limit, hence the negative estimated shape parameter (Giles et al., 2016). The behaviors of the density distribution with different values of scale and shape are illustrated in Fig. 4.2.

Equation (4.1) describes the stationary GPD model, in which the scale and shape parameters remain constant. From the stationary GPD model, the T-year return level y_T associated with the return period T (Coles et al., 2001; Khaliq et al., 2006) can be estimated as:

$$y_T = \sigma[\zeta_u T^{\xi} - 1]/\xi \tag{4.2}$$

where $\zeta_u = P(X > u)$ is the ratio of exceedances in the sample, for the 95th percentile this

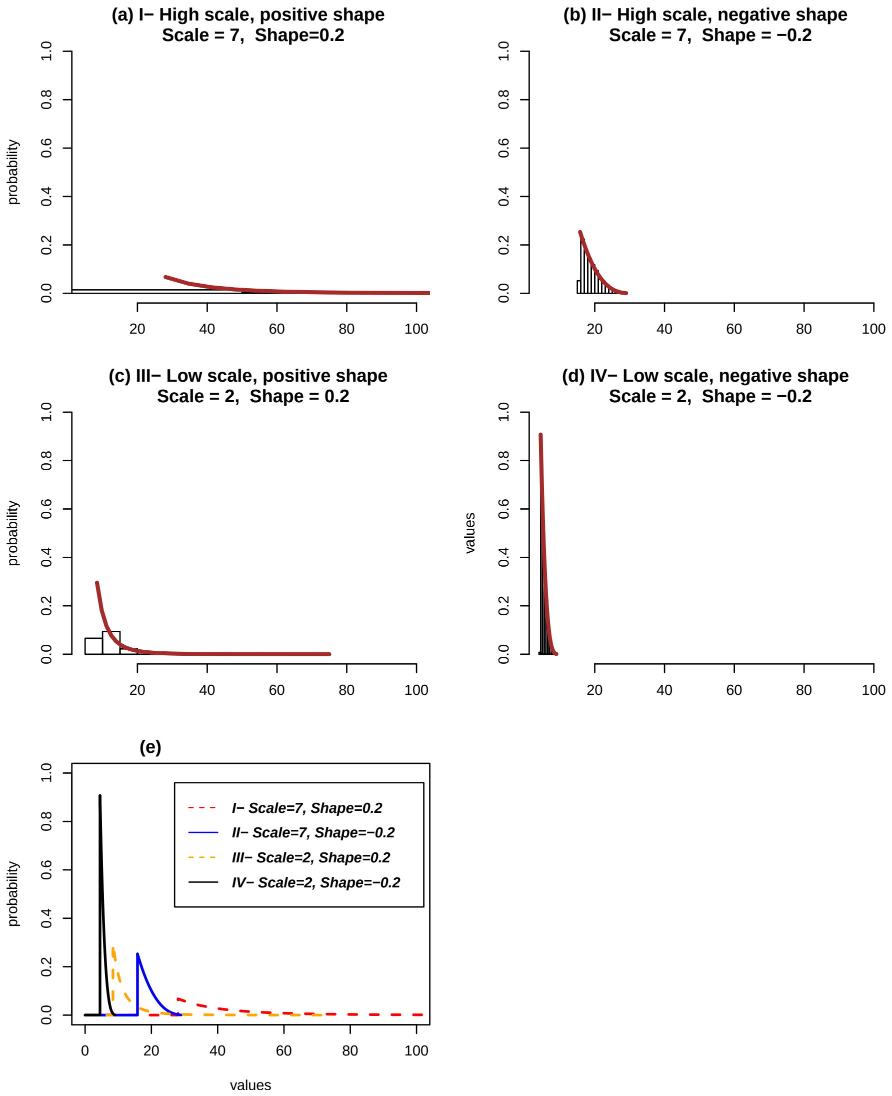

Figure 4.2: (a)-(d) Probability density distributions of extremes of a variable with different scale and shape parameters. (e) All distribution functions together.

is $\zeta_u = 0.05$ and for the 99th percentile $\zeta_u = 0.01$.

The POT analysis requires independent values among exceedances (Coles et al., 2001). Hence, the record of extremes needs to be de-clustered to reduce the persistence among the clustered extremes. For this, we de-cluster the extreme precipitation at each grid point by taking the maximum value within each cluster. Each cluster is composed of consecutive days of extremes and the extremes separated by a maximum of one day to other extremes. In other words, the minimum temporal distance allowed between the extremes within a cluster is one day, and between the clusters is two days (Coles et al., 2001). The result of the de-clustering can be quantified through an extremal index, which is the ratio between the number of extremes after being de-clustered and the initial number of extremes. These de-clustered exceedances are the values used for the analysis.

Then, a GPD is fit to the de-clustered extreme daily precipitation anomalies to generate a stationary GPD model with a specific scale and shape parameter at each grid point. The estimation of scale and shape parameters is performed using the maximum likelihood method (Coles et al., 2001; Sugahara et al., 2009).

The parameter estimation for a stationary GPD model through a maximum likelihood is given as follows: under the assumption that the exceedances $z_1, \ldots, z_{\mathrm{k}}$ are independent variables where k is the number of exceedances, the log-likelihood function l for the parameters σ and ξ is:

$$\begin{cases} l(\sigma,\xi) = -k\log(\sigma) - (1+\frac{1}{\xi})\sum_{i=1}^{k}\log(1+\frac{\xi z_i}{\sigma}) \qquad \text{for} \quad (1+\sigma^{-1}\xi z_i) > 0 \quad , \quad i = 1,...,k \\ l(\sigma) = -k\log(\sigma) - \sigma^{-1}\sum_{i=1}^{k} z_i \qquad \text{for} \quad \xi = 0 \end{cases} \tag{4.3}$$

Having the parameter vector β with $\beta = [\sigma,\xi]$, the maximization of the pair of log-likelihood $l(\sigma,\xi)$ with respect to the β is performed. This maximization leads to the maximum likelihood estimate of the scale σ and shape ξ. The maximization is done numerically, as no analytical solution is possible (Coles et al., 2001).

In the case of non-stationary GPD models (Coles et al., 2001; Blender et al., 2017), the scale and/or shape parameters vary linearly with time t, or with other external variables (covariates). In our analysis, we only allow scale parameters to change but shape parameters remain constant, similar to the approach used by Sugahara et al. (2009) and Blender et al. (2017). In our non-stationary GPD models, the scale parameter in Eq. (4.1) becomes

$$\sigma(t) = \sigma_0 + \sigma_1 t \quad \text{or} \quad \sigma(t) = \sigma_0 + \sigma_1 C(t) \tag{4.4}$$

with $C(t)$ being the time series of a covariate. Again GPDs are fit to the de-clustered extreme daily precipitation anomalies to generate non-stationary time- and covariate-GPD models. Time dependent scale and shape parameters for the non-stationary model are also estimated using the maximum likelihood method following Eq. (4.3), assuming $\sigma(t) = \sigma_0 + \sigma_1 C(t)$ or $\sigma(t) = \sigma_0 + \sigma_1 t$ (Coles et al., 2001; Sugahara et al., 2009). The parameter vector β in this case is $\beta = [\sigma_0,\sigma_1,\xi]$ (El Adlouni et al., 2007).

The performance of the non-stationary GPD model is measured relative to the stationary GPD model using the deviance statistics (Coles et al., 2001; Blender et al., 2017):

$$D = 2(L_1 - L_0) \tag{4.5}$$

where L_1 and L_0 are the log-likelihoods of the non-stationary and the stationary GPD model, respectively. The deviance statistics follows the χ^2_m distribution, and with $m = 1$ and a 99% confidence interval, a threshold for D is 6.634. Hence, the relative performance of the non-stationary GPD model is statistically significant at a 99% confidence interval when D is larger than 6.634. This indicates that the non-stationary GPD model is significantly better than the stationary GPD model at 99% confidence interval, and the non-stationary GPD explains the variability of extreme precipitation at a grid point better than the stationary GPD. If this is the case, we assume that there is an association between the corresponding covariate, or the time variable, with extreme precipitation at that grid point or region.

4.4.2 Non-stationary GPD models with external forcings, modes of internal variability and surface air temperature

We use several external forcings, modes of internal variability, and surface air temperature anomalies (TS) as covariates of the GPD models for the 1501 BCE–1849 CE simulations. For the external forcings, we consider five variables in total: three orbital parameters combined in one variable (ORB; eccentricity (ECC), longitude of perihelion (PER) and obliquity (OBL); Berger, 1978), TSI, insolation (INS), clear sky net surface short wave radiation (FSN) and VOL (Fig. 4.3). ORB and TSI are annually resolved one-dimensional time series. INS and FSN are the output variables from the model simulations and resolved monthly and spatially at each grid point. The VOL forcing is monthly and latitudinally resolved and is already described in Sect. 4.3.1. INS, FSN, and VOL are annually-averaged to obtain a yearly resolution. This procedure is applied to have consistent time resolutions among all external forcing variables and to exclude the effects of seasonality. Finally, all variables are normalized with respect to their 3351 year means and interpolated to a daily time resolution.

INS and FSN can be interpreted as the variables that reflect the combined effects of ORB and TSI on regional and global scales. Additionally, FSN also includes the effects of volcanic eruptions by exhibiting negative peaks on its time series after some strong eruptions, but only in the transient simulation (Fig. 4.3).

Each of these variables is included in the scale parameters of each individual GPD model in Eq. (4.1) using Eq. (4.4), except for ORB. For ORB, all three parameters are incorporated together in the scale parameter of one GPD model as:

$$\sigma(t) = \sigma_0 + \sigma_1 ECC(t) + \sigma_2 OBL(t) + \sigma_3 PER(t) \tag{4.6}$$

The resulting combined effect is that σ increases approximately linear with time t.

For the volcanic forcing, in addition to the analysis of the entire period, we also assess the short-term influence of volcanic eruptions on extreme precipitation. For this, we select a three-year period before (pre-eruption period) and a three-year period after (post-eruption period) all eruptions from the 1501 BCE – 1849 CE transient full-forcing simulation. Only the eruptions that fulfill the following conditions are included in the analysis: tropical eruptions that occur in January and exceed 2.66 Tg of volcanic stratospheric sulfur injection (VSSI). This reference VSSI is based on the El Chichon eruption in 1982 CE, whose effects on the radiation and climate were clearly detectable (Hofmann, 1987). We also assure that no other eruption has occurred 5 years before and after each of the selected eruptions. After applying

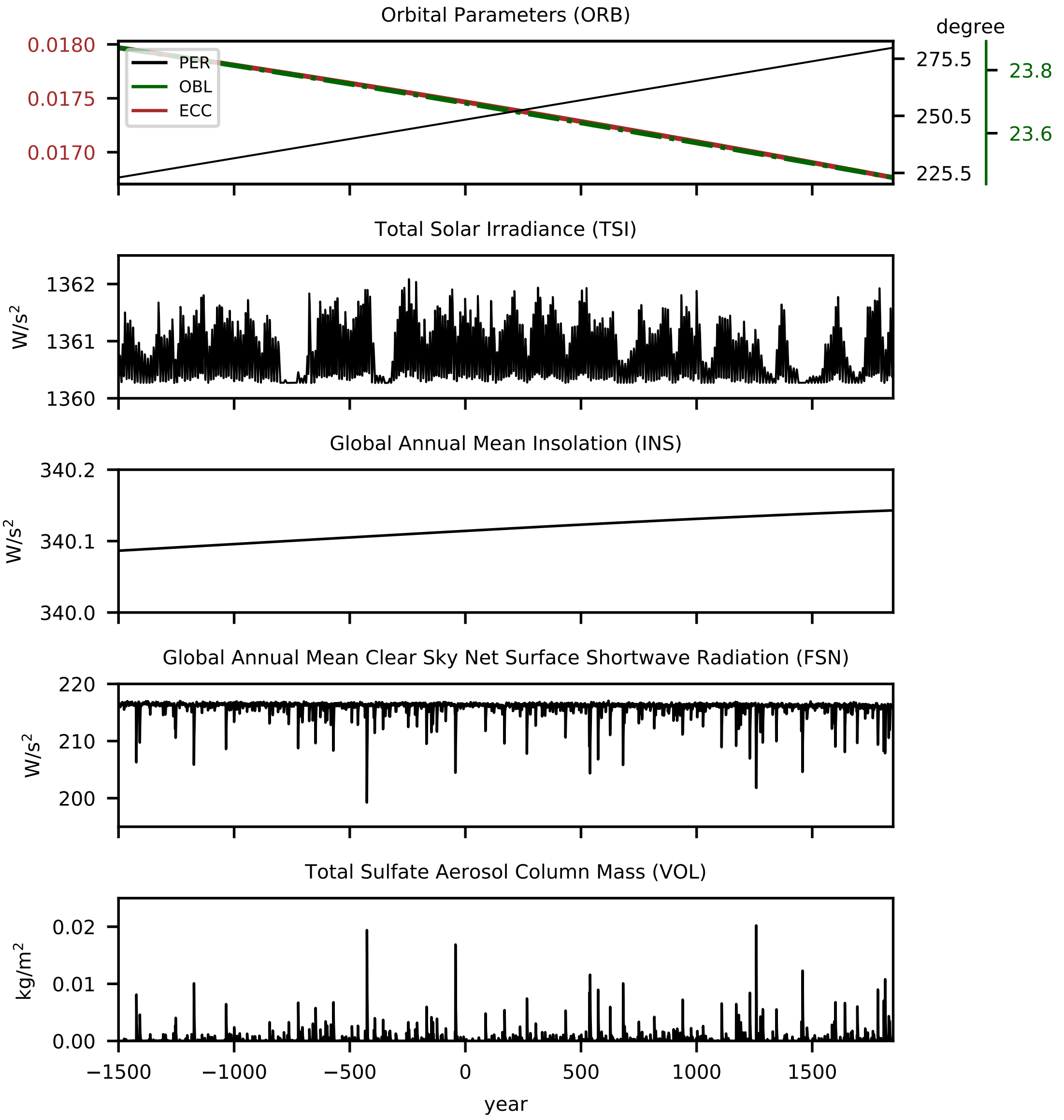

Figure 4.3: Time series of externally forced variability included as covariates in the non-stationary GPD models for the orbital-only and full-forcing simulations. Note that the VOL-covariate GPD model is only generated for the full-forcing simulation.

these criteria, the total number of eruptions included in the analysis is 57. These eruptions occur in the same month (January) and at similar latitudinal locations (tropical). Therefore, the asymmetric cooling due to extratropical eruptions (Oman et al., 2005; Schneider et al., 2009) and season-dependent climatic responses to tropical eruptions (Stevenson et al., 2017) are not considered for the analysis.

It is important to mention that all reconstructed external forcings such as TSI and volcanic eruptions contain inherent uncertainties derived from reconstruction models or methods and from the dating of events (Sigl et al., 2015; Jungclaus et al., 2017; Matthes et al., 2017). An attempt to reduce such uncertainties is an active research topic (e.g., Sigl et al., 2015; Matthes et al., 2017) that is beyond the scope of this study. A possible implication of uncertainties from the external forcings in our analysis is briefly discussed in the result section (Sect. 4.5.3).

A stationary GPD fit (Eq. (4.1)) is applied to the pre-eruption and post-eruption periods separately to estimate the return periods of extreme precipitation, then to assess the post-eruption changes in extreme precipitation. Additionally, the numbers of days and the intensities of extremes for these two periods are calculated. As strong volcanic eruptions influence the evolution of ENSO states (McGregor and Timmermann, 2011; Ohba et al., 2013; Wang et al., 2018; McGregor et al., 2020), we also identify imprints of ENSO on post-eruption extreme precipitation by splitting the years of eruptions (year 0) into three ENSO states, based on the Niño3.4 index: El Niño ($>$ 0.5 K), La Niña ($<$ -0.5 K) and neutral state ($\geq$ -0.5 K and $\leq$ 0.5 K). Then, the numbers of extremes in each ENSO state are counted and compared to the numbers in the same states during the year before the tropical eruptions.

To generate the non-stationary GPD models with the internal modes of variability as covariates, we use eight modes of variability: Eastern Atlantic–West Russian Pattern (EA-WR), North Atlantic Oscillation (NAO), Northern Annular Mode (NAM), Pacific Decadal Oscillation (PDO), Pacific North American (PNA) pattern, ENSO, Southern Annular Mode (SAM) and Pacific South American (PSA) mode. The procedures to calculate the modes of variability are explained in Sect. 4.7. These modes of variability are both captured by CESM and ERA5, as the patterns are comparably similar among the data sets (Figs. 4.14, 4.15, and 4.16). Then, we constrain the regions of action of some of these modes to only one hemisphere: EA-WR, NAO, NAM, PDO, and PNA are only associated with extreme precipitation in the Northern Hemisphere, while SAM and PSA only influence extreme precipitation in the Southern Hemisphere. There is no spatial restriction for ENSO; therefore, ENSO can be associated with extreme precipitation in both hemispheres. All of these modes have a monthly time resolution and each of them is inserted in a GDP model without an interpolation to the daily time resolution. For the internal variability, we assume that what influences the extreme daily precipitation is not the daily fluctuations of these modes but their monthly mean values.

TS is obtained by subtracting the 1501 BCE–1849 CE monthly means of surface air temperature from each monthly value in the simulations. Two kinds of TSs are considered for the non-stationary analysis: one is the globally-averaged means of TS (TS-G) and another is the spatially (latitude and longitude) gridded TS (TS-R). The former is to assess the influence of global temperature and the latter is to assess the influence of regional temperature on daily extreme precipitation. Both TSs are resolved monthly and similar to the modes of internal variability, they are not interpolated to daily time resolution. The influences of TSs are compared against to those of the modes of variability.

4.4.3 Statistical tests used for the model evaluation against ERA5

We compare the daily precipitation in CESM and ERA5 for the present period 1979–2008 CE in order to evaluate the model's ability to depict the daily precipitation. For this, we analyze the 30-year global and land averaged trends of the annual mean daily precipitation and the spatial means of the entire and extreme (the values above the 95^{th} percentiles) daily precipitation. The signs of the monotonic trends of the global and land averaged total daily precipitation are compared to each other and their statistical significance is calculated using the non-parametric Mann–Kendall trend (M-K) test (Mann, 1945; Wilks, 2011; e.g., Westra et al., 2013). Under the null hypothesis, the M-K test assumes no trend in the time series. The means of the total and extreme daily precipitation between CESM and ERA5 are compared using the non-parametric Mann–Whitney (M-W) U-test (Mann and Whitney, 1947; Wilks, 2011; e.g., Kim and Raible, 2021) at each grid point. The null hypothesis of the M-W test states an equal distribution of the two data sets. To assess the similarity of the spatial patterns, the Pearson r correlation coefficients are calculated using the spatial mean values of total and extreme precipitation between CESM and ERA5. The null hypothesis of the test assumes no correlation between two data sets. Hence, if the null hypothesis is accepted, no significantly similar spatial precipitation pattern between both datasets is observed.

4.5 Results

4.5.1 Comparison between ERA5 and CESM in the present period 1979–2008 CE

In this section, we compare the daily precipitation in ERA5 and CESM for the period 1979–2008 CE to evaluate the model's ability to represent the mean and extreme daily precipitation. For this comparison, we use the full-forcing simulation.

The 30-year global and land-only averaged annual means of the daily precipitation anomalies in ERA5 and CESM are shown in Fig. 4.4. During 1979–2008 CE, both ERA5 and CESM show a small but statistically significant positive trend for the global daily precipitation at a 99% confidence interval (Fig. 4.4a). However, when only the daily precipitation anomalies over land are considered, significant positive trends are absent in both data sets (Fig. 4.4b). ERA5 shows no statistically significant trend of the daily precipitation over land, while CESM indicates a slight negative but significant trend during this 30-year period. This difference in trends between the global and land averaged daily precipitation suggests that the changes in the mean daily precipitation over land during the last few decades are more heterogeneous than the global changes of daily precipitation resembling findings of Contractor et al. (2021).

Regarding the spatial distribution, some differences between ERA5 and CESM are evident, particularly in terms of the magnitudes of the mean daily precipitation (Fig. 4.5a). Compared to ERA5, CESM largely underestimates the daily precipitation over the tropical and North Pacific Oceans, India, central Asia, Australia, southern South America, almost all of Africa, and western North America. The model overestimates the daily precipitation over the tropical Atlantic, northern and central South America, and large parts of Europe among others. The differences in the magnitudes are also present in the extreme daily precipitation (daily precipitation above the 95^{th} percentiles relative to their 1979–2008 CE distributions) (Fig.

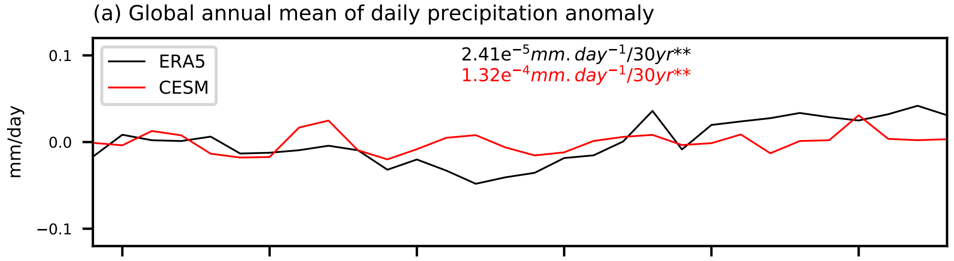
(a) Global annual mean of daily precipitation anomaly

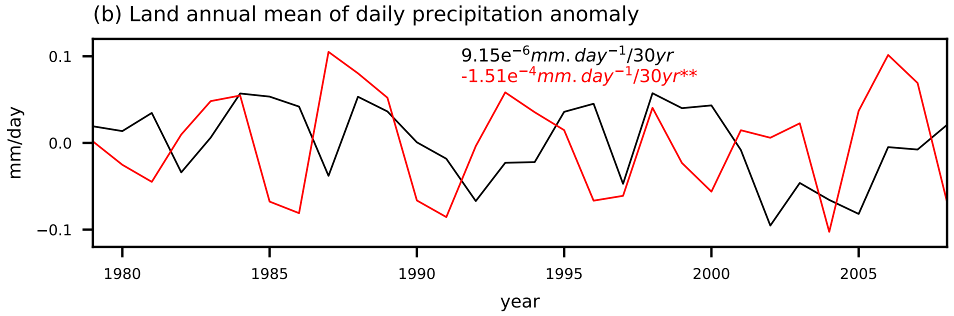
(b) Land annual mean of daily precipitation anomaly

Figure 4.4: Time series of annually-averaged mean daily precipitation over the (a) entire globe and (b) land-only in ERA5 (black) and CESM (red). The values on the figures indicate the trends and ** denote that the trends are statistically different to zero at the 99% confidence interval based on the Mann–Kendall trend tests.

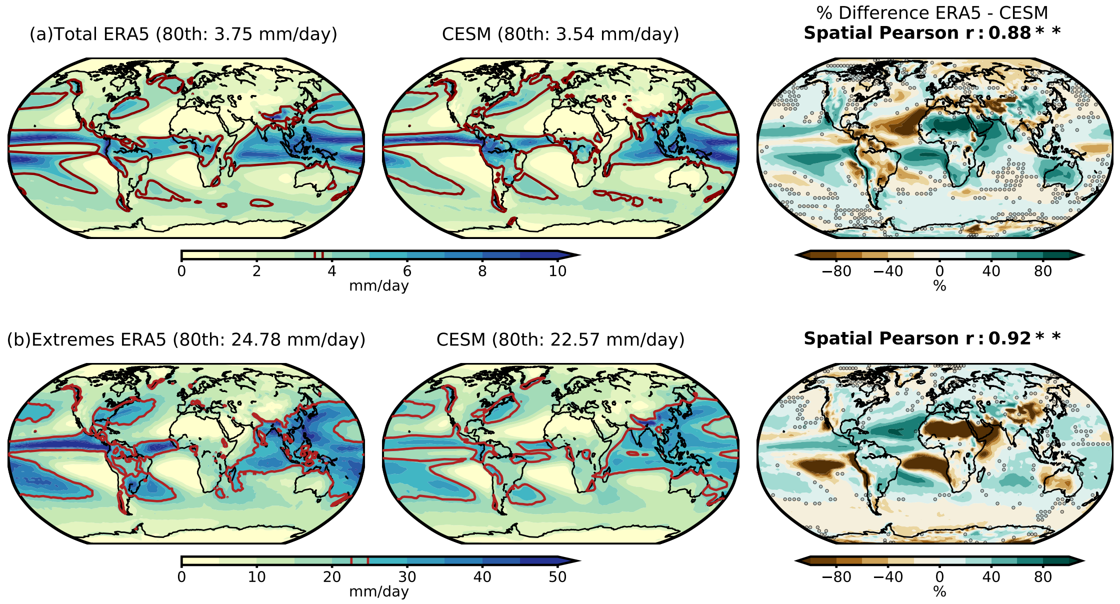

Figure 4.5: Mean values of ERA5 and CESM, and the percentages of difference between both datasets calculated as (ERA5 - CESM)/ERA5 for (a) the total daily precipitation and (b) the extreme daily precipitation (daily precipitation above the 95th percentiles relative to 1979–2008CE distributions). The brown line indicates the 80^{th} percentile level to discern wet regions (above the 80^{th} percentile) from others. Dotted regions in the difference plots indicate where the distributions of total or extreme precipitation are statistically similar at the 99% confidence interval based on the M-W U-tests. Pearson r coefficients between the spatial mean values of ERA5 and CESM are denoted in bold on the difference plots accompanied with ** when the r are statistically significant at the 99% confidence interval.

4.5b). However, CESM overestimates extreme daily precipitation in regions where the mean daily precipitation is underestimated and vice versa. The discrepancy between the reanalysis or the observation and the model simulation in the magnitudes of the mean and extreme daily precipitation is a known problem in many climate models (Stephens et al., 2010; Flato et al., 2014). This discrepancy demonstrates again the difficulties of models to realistically represent physical processes related to precipitation, mainly associated with short-lived and spatially small scale events (e.g., Champion et al., 2011; Van Haren et al., 2015; Scher et al., 2017).

Regardless of these differences in the magnitudes of the mean and extreme daily precipitation, CESM represents relatively well the spatial patterns of mean daily precipitation. CESM distinguishes properly the drier from wetter regions, which are identified as the regions with precipitation values below and above the spatial 80th percentile of the total mean precipitation, respectively (brown contour line in Fig. 4.5). The spatial Pearson correlation coefficients of the mean total and extreme precipitation between ERA5 and CESM are 0.88 and 0.92, respectively, and both values are statistically significant at the 99% confidence interval. These values demonstrate that the model is able to realistically represent the mean total and extreme spatial pattern of daily precipitation.

The POT analysis is applied to the extremes in ERA5 and CESM, and estimated parameters of the stationary GPD models from the analysis are presented in Fig. 4.6. The extremal indices, which are the ratios between the numbers of de-clustered extremes and initial extremes, show reduced numbers of extremes over the tropical oceans after de-clustering. In some regions in the tropics, the de-clustering method leaves only around 40% of the initial numbers of extremes, indicating that the reduction of extreme events is particularly strong over this latitudinal belt, a known region of convective organization with temporal clustering. Over the extratropics, the extremal indices range from 0.8 to 1, meaning that de-clustering does not strongly affect the number of extremes in these regions. The extremal indices illustrate that over the tropics, mainly over the oceans, clustered precipitation events that last for several days are common, while short-lived extreme precipitation events are prevalent over the extratropics. Hence, de-clustering causes a strong reduction in the number of extremes in the tropics, which is more pronounced in the CESM simulation.

The scale parameters in ERA5 and CESM, which indicate the spread of extreme precipitation, largely follow the spatial pattern of the mean extreme daily precipitation in Fig. 4.5b. The parameters show higher values over wetter regions and comparably lower values over other regions. This behavior of the scale parameters is expected as the parameter is related to the scaling of the exceedances in the density distribution, which is associated with the mean values of the extremes in Fig. 4.5b (see also Fig. 4.2). Hence, the difference in the scale parameters between ERA5 and CESM is expected, as both data sets present different mean extreme precipitation.

For the shape parameter, CESM shows more regions with negative shape parameters than ERA5 and more standard errors from the parameter estimation over these regions. As mentioned in Sect. 4.4.1, this occurs due to the small sample size for the parameter estimation over the regions where the shape parameters are negative (Blender et al., 2017). Excluding these regions, ERA5 and CESM share some positive values over the same regions and some

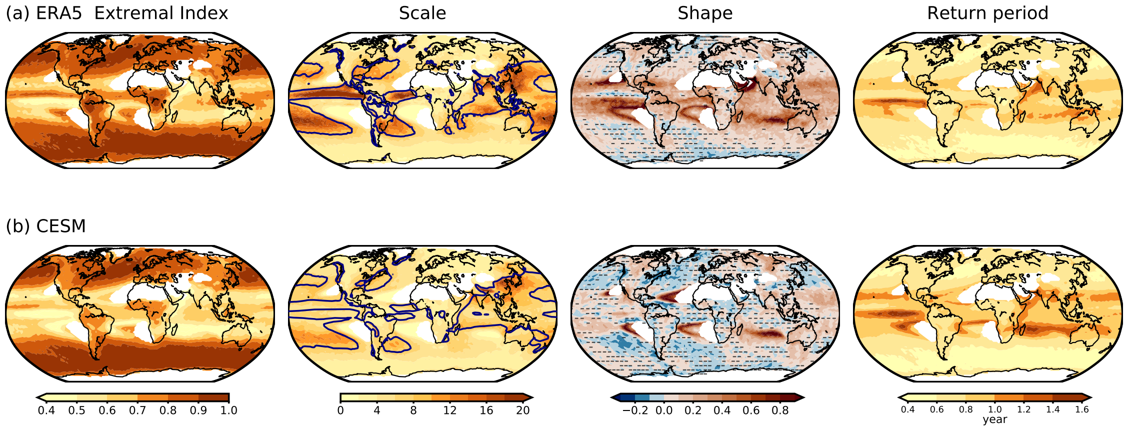

Figure 4.6: Extremal indices, parameters of the stationary GPD models, and return periods of the extreme thresholds in Fig. 4.5 for (a) ERA5 and (b) CESM. Striped regions indicate where the standard errors from the parameter estimation are higher than the estimated values. The dark blue line on the composite of the scale parameters denotes wet regions in Fig. 4.5. The regions where the annual total precipitation is less than 250 mm are excluded from the analysis and marked as white.

coherent regions with relatively high shape parameters in the Indian Ocean, the southern Atlantic, and Pacific Oceans.

The return periods of extreme precipitation in both CESM and ERA5 largely follow the pattern of the extremal indices. It exhibits long return periods over the tropics where the extremal indices are lower and short return periods over the extratropics where the extremal indices are higher. This behavior of the return periods is expected, as a low number of extremes indicates a low occurrence of events, therefore, an increased return period of the events. Note that the return period over the tropics should be interpreted as a return period of a clustered event instead of a return period of a single or a short-lived precipitation event.

In summary, some differences between ERA5 and CESM exist in the parameters of the GPD models due to differences in the mean extreme daily precipitation. Still, the spatial patterns of the GPD parameters and return periods of simulated extreme daily precipitation anomalies resemble the patterns of the reanalysis, presenting coherent regions with maximum and minimum parameter values. Wet and dry regions and the regions with maximum and minimum GPD parameters are in general coherent between ERA5 and CESM. This indicates that the model represents the large-scale spatial patterns of the mean and extreme precipitation relatively well. The focus of this study is on the long-term changes and characteristics of extreme daily precipitation on a global scale rather than on the characteristics or impacts of a handful single events. Therefore, we use the daily precipitation from CESM as it is in the next section, i.e., without applying any further corrections, such as bias correction (e.g., Chen et al., 2020) or downscaling methods (e.g., Yang et al., 2012). Still, we take into account the differences between ERA5 and CESM in the magnitudes of extreme precipitation when interpreting our results and discussing possible implications in the conclusions.

4.5.2 Distribution of extreme daily precipitation for the period 1501 BCE–1849 CE in CESM

Here, the POT analysis is applied to the time series of extreme daily precipitation in the 3351 year orbital-only and full-forcing transient simulations to generate the stationary GPD models at each grid point and to illustrate the characteristics of the distribution of extreme precipitation. The thresholds for the extremes (the 99^{th} percentiles of daily precipitation relative to their distributions of the entire period), the means of all precipitation above the extreme percentile limit, and extremal indices are presented in Fig. 4.7. The parameters of the stationary GPD models from the full-forcing simulation are shown in Fig. 4.8. The POT analysis of the orbital-only simulation exhibits similar results; thus, the corresponding figures are not shown here.

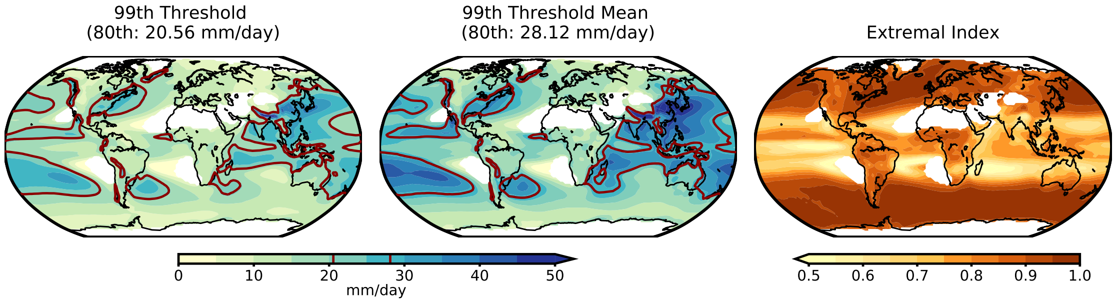

Figure 4.7: The thresholds for extreme precipitation (defined as the 99^{th} percentiles of daily precipitation relative to the 3351-year distributions), means of the values above these thresholds, and extremal indices in the 1501 BCE–1849 CE full-forcing simulation. Brown line indicates the spatial 80^{th} percentile level to discern wet regions (above the 80^{th} percentile) from others.

The spatial patterns of the mean extreme precipitation and extreme indices (Fig. 4.7) are similar to those during the present period in Fig. 4.5b, discerning the wetter and drier regions. Similar to results found in Fig. 4.6, the scale parameters (Fig. 4.8a), which describe the spread of the distribution or scaling of the extremes, largely follow the spatial pattern of the mean extreme precipitation with higher values over the wetter regions in the Pacific and Indian Oceans, south and east Asia, east and west coasts of North America among others. Relatively lower values of the scale parameter are found in Europe, Africa, and northern South America.

For the shape parameters (Fig. 4.8b), the regions with higher estimation errors (striped area) are reduced compared to Fig. 4.6. This is expected because the numbers of extreme precipitation events increase so that the parameter estimation is more reliable. Positive shape parameters dominate over the tropical and west Pacific and Indian Oceans. Over land, the wetter regions in Asia, the southeast coast of South America, and the east and west coasts of North America dominate more negative values. Similar to Fig. 4.5, the spatial pattern of the return periods (Fig. 4.8c) exhibit high return periods located over the tropics and relatively lower values over the extratropics.

The scale and shape parameters together (Fig. 4.8d) describe the generalized Pareto distributions that characterize the density distributions of extreme precipitation at each grid

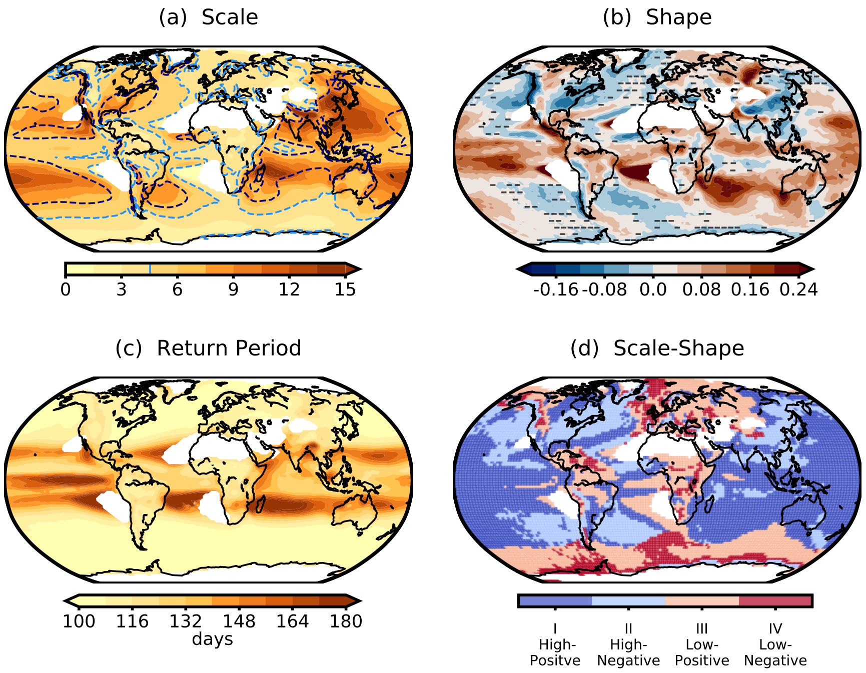

Figure 4.8: (a) Scale, (b) shape parameters of the stationary GPD models, (c) return periods of extreme thresholds (see Fig. 4.7), and (d) the combination of the scale and shape parameters with: above (High) and below (Low) the median of the scales, and positive and negative shape parameters. On the composite of scale parameters in (a), the wet region in Fig. 4.7 is denoted as dashed dark blue line, and the median of scale parameters is overlaid as dashed light blue line. Again, the regions where the annual total precipitation is less than 250 mm are marked as white.

point. The density distribution of extreme precipitation is separated into four types given in Fig. 4.2: I) high scale - positive shape characterized by a higher spread, heavy tail and no-upper bound of extremes (Fig. 4.2a); II) high scale - negative shape characterized by a high spread, thin tail and an upper-bound (Fig. 4.2b); III) low scale - positive shape characterized by a low spread, heavy tail and no upper-bound (Fig. 4.2c); and finally, IV) a low scale - negative shape is characterized by a low spread, thin tail and an upper-bound of extremes (Fig. 4.2d). High and low values of scale parameters are defined as the values above and below the median of all scale parameters in Fig. 4.8a. In Fig. 4.8d, clustering of the same types of distribution is noticeable. For instance, the type I (high scale - positive shape) dominate over the west and the tropical Pacific Ocean; the type II (high scale - negative shape) are located over the south and north Pacific and Atlantic Oceans, south and east Asia, and eastern North America; the type III (low scale - positive shape) are found over some regions in the Southern Ocean, northern Asia, Amazon, and Africa; lastly, the type IV (low scale - negative shape) distributions occur over some regions in the Southern Ocean and in the northernmost Atlantic Ocean. In general, over the ocean, the types of distribution seem to be more homogeneous than those over land. In addition, there are clear differences in the types of distribution between the Pacific and Atlantic sectors and between the northern high and southern low latitudes. To conclude, the results show that the POT analysis is able to identify the large-scale characteristics of extreme precipitation by separating distinct and coherent regions for similar types of distributions.

4.5.3 Association of extreme precipitation with external forcings including the tropical volcanic eruptions

To assess the long-term influence of externally forced variability on extreme precipitation, the time series of the variables mentioned in Sect. 4.4.2 (Figs. 4.3, 4.14, and 4.15) are included as covariates in the non-stationary GPD models (Eq. (4.4)). Then, the deviance statistics D (Eq. (4.5)) are calculated to quantify the performance of the covariate GPD models in the orbital-only and full-forcing simulations relative to the stationary GPD models in Fig. 4.8.

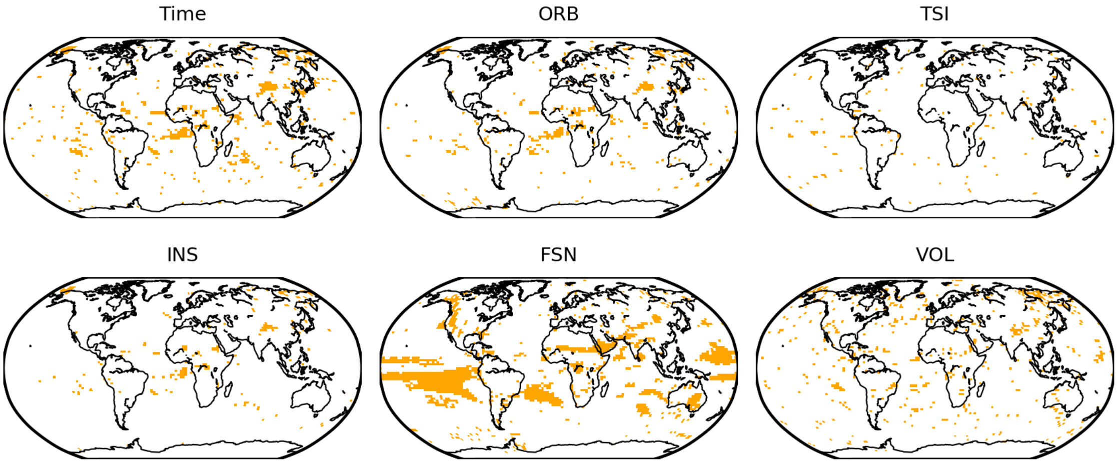

Figure 4.9: The external-forcing-GPD models that explains the variability of extreme precipitation better than the stationary GPD model in Fig. 4.11 at the 99% confidence interval in the full-forcing simulation.

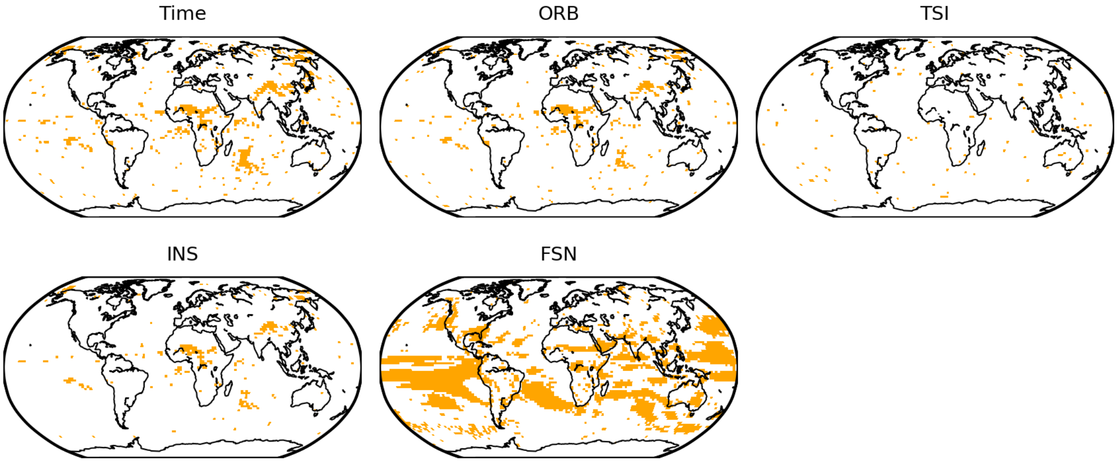

Figure 4.10: Same as Fig. 4.9 but for the orbital-only simulation.

The regions, where each covariate, the time and external forcing GPD models, outperform the stationary GPD models with the statistically significant D values (with D more than 6.634 at 99% confidence interval) is shown in Figs. 4.9 and 4.10 for each of the simulations. The regions where both orbital-only and full-forcing simulations share a common significant D are presented in Fig. 4.11. We assume that these regions with coherent D between the two simulations are where the extreme precipitation is truly influenced by the covariates.

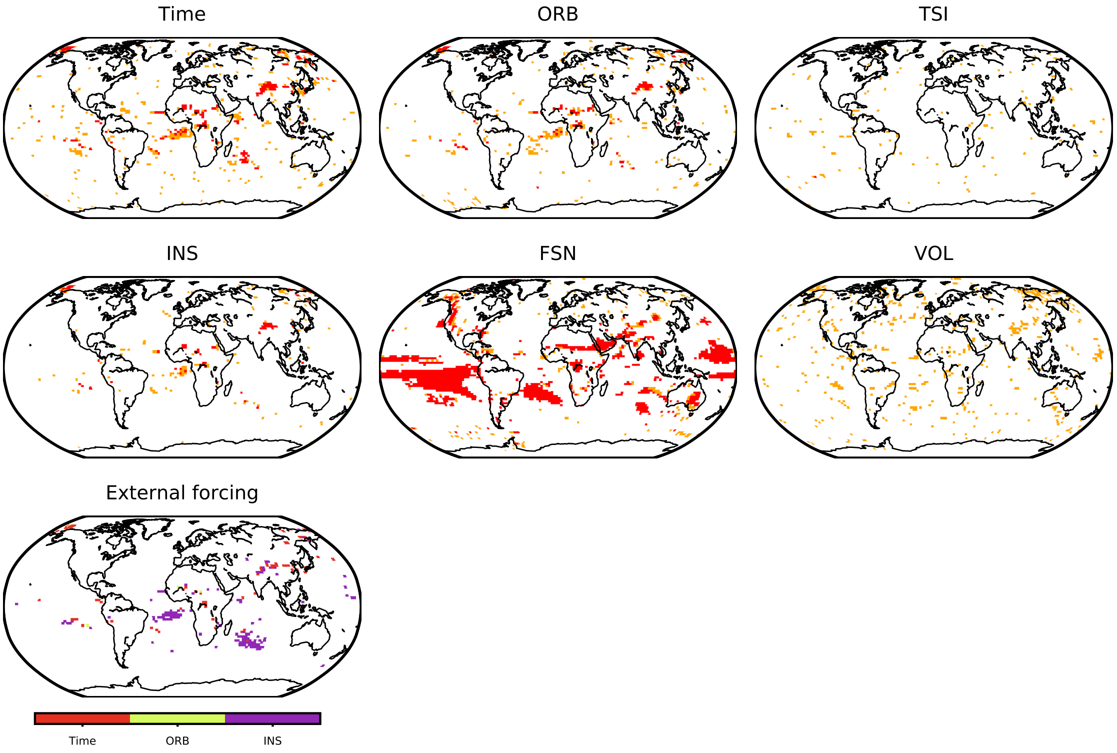

Figure 4.11: The external-forcing-GPD models that outperform the stationary GPD models at the 99% confidence interval based on the D statistics and explain better the variability of extreme precipitation. Orange shades indicate the regions where the D statistics in the full-forcing simulation are statistically significant and red shades where both full-forcing and orbital-only simulations present significant D statistics. Note that the VOL-covariate model is not generated for the orbital-only simulation.

The time, ORB, and INS share some common regions over the tropical Atlantic, the Indian Ocean, central Asia, and central Africa. These variables present a time series with a monotonic linear trend. Thus, over these regions, there is a linear increase in extreme precipitation during 1501 BCE–1849 CE. The influence of TSI is spread randomly across the globe, implying no robust association of this variable with the variability of extreme precipitation. FSN, which considers the overall changes in the net surface shortwave radiation, exhibits similar regions of association with extreme precipitation to those in ORB and INS, mostly over the tropics. Still, the regions of association of FSN with extreme precipitation are larger, as additional internal effects involved in the surface radiation balance and not only the external forcing are included in this covariate. For example, the regional temperature variability affected by internal variability has an impact on FSN. Overall, the roles of the external forcing in the variability of extreme precipitation during 1501 BCE–1849 CE are constrained to certain small regions shown in Fig. 4.11.

The VOL shows a random spread similar to TSI. This relatively limited influence of volcanic aerosols on extreme precipitation can be related to the time scale of the influence of volcanic eruptions on the climate. It is known that the effect of volcanic eruptions on precipitation is only in the short-term, in the range of a few years (Robock, 2000; Iles et al., 2013; Iles and

Hegerl, 2014). Hence, volcanic eruptions may not alter the long-term variability of extreme precipitation analyzed here. Considering the time scale of the effects of volcanic eruptions on precipitation, short-term influences of volcanic eruptions on extreme precipitation are specifically analyzed by taking the periods of three years before and three years after the eruptions (Sect. 4.4.2).

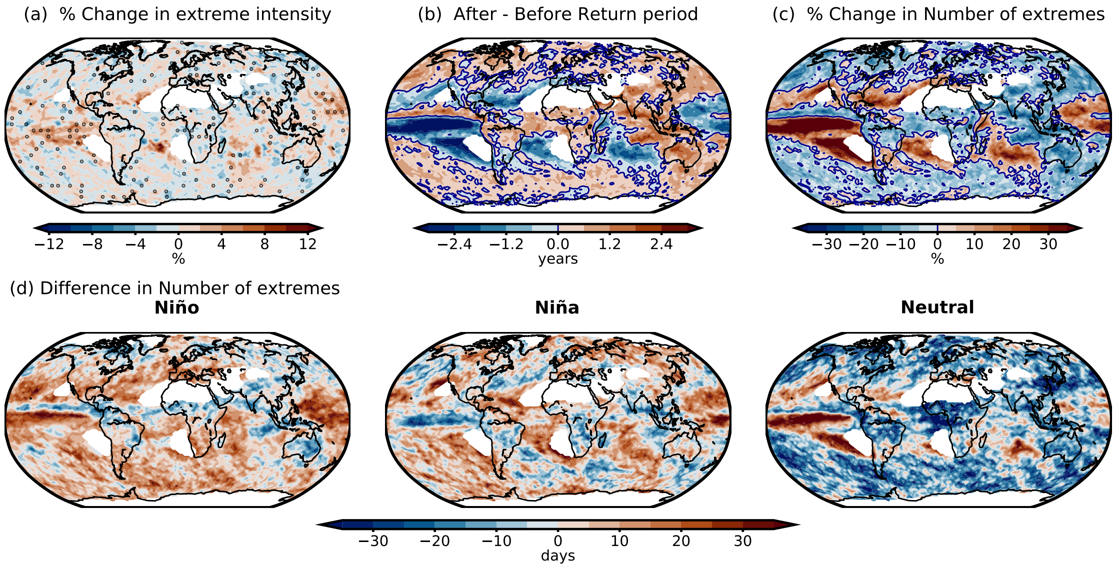

Figure 4.12: (a) Rates of change in the mean extreme precipitation, (b) differences in return periods, and (c) rates of change in the number of extreme precipitation during the period of three years after the tropical volcanic eruptions relative to three years before the tropical eruptions. The dotted regions in (a) indicate where the distributions of extreme precipitation between the pre- and post-eruption periods are statistically similar at the 99% confidence interval based on the M-W U-test. (d) Rates of change in the number of extremes in different ENSO states during the years of tropical eruptions (year 0) relative to the same ENSO states during the year before the tropical eruption.

The differences in mean, return period, and number of extreme precipitation between the post- and pre-eruption periods are shown in Fig. 4.12. In terms of the intensity of extreme precipitation (Fig. 4.12a), the tropical equatorial Pacific region presents a statistically significant increase after eruptions. Other regions with significant increases or decreases are spread across the globe. It is noted that the post-eruption changes in the intensity of extreme precipitation are not as evident as the changes in the number of extreme precipitation (Fig. 4.12b and c). The return periods of extremes in Fig. 4.12b indicate a decrease after eruptions in the tropics, west Indian Ocean, and lands in the mid-latitudes, including the southern US, central South America, and central and southern Europe. An increase is found in Asia, Australia, Africa, northern Europe, northern South America, and northern North America. These changes in the return periods reflect the changes in the number of extreme precipitation (Fig. 4.12c): where the return periods decrease, the number of extreme daily precipitation increases, and vice versa. Moreover, the percentages of changes in the number of extremes are clearly higher than those in the intensity of extremes. This result indicates that except for the tropical ocean and some small isolated regions, tropical eruptions influence more clearly the frequency than the intensity of extreme precipitation.

The patterns of the return period and the number of extremes in Fig. 4.12b and c resemble the precipitation anomaly pattern induced by El Niño events (Dai and Wigley, 2000), which is mainly characterized by an increase in precipitation over the tropical equatorial Pacific Ocean and the tropical regions from America to Africa, and a decrease over the eastern Pacific sector including Australia and Indonesia. Although, there is a lack of consistency among natural climate proxies in the responses of ENSO to tropical volcanic eruptions during the last millennium (Dee et al., 2020), model-based studies largely demonstrated that tropical volcanic eruptions alter the states of ENSO and can lead to El Niño-like conditions after the peaks of eruptions (McGregor and Timmermann, 2011; Wang et al., 2018; McGregor et al., 2020). Moreover, precipitation responses to volcanic eruptions are magnified during El Niño state after eruptions (Stevenson et al., 2016).

Fig. 4.12d exhibits the differences in the number of extreme precipitation during each of the ENSO states between the year of eruption (year 0) and the year before the eruption. Increases in the number of extremes are noticeable over a large part of the globe during El Niño phases in year 0, also over regions where the number of extremes increases in Fig. 4.12c. During La Niña, the anomalies are opposite to those during El Niño, presenting negative values over the tropical Equatorial Pacific, central South America, and southern Africa. During the neutral state, an increase in the frequency is evident over the tropical equatorial Pacific region, same as during El Niño phases, while in other regions, decreases in the frequency are found. All ENSO states show a reduction in the number of extremes over the Asian monsoon region in year 0. The result indicates that the increases and decreases in the frequency of extremes over large parts of the globe in Fig. 4.12a and b are explained by different ENSO states, mostly by El Niño and the neutral condition, influenced by tropical eruptions. Besides, the decreases in extremes in the high-latitudes are also connected with the cooling caused by the volcanic eruptions, as extreme precipitation depends on the change of the atmospheric moisture availability, which is modulated by the atmospheric temperature (Pall et al., 2007; Myhre et al., 2019).

4.5.4 Association of extreme precipitation with large-scale circulation patterns and surface air temperature

The same procedure as in the previous section (Sect. 4.5.3) is repeated to find the association between the extreme precipitation and the modes of internal variability. At each grid point, the D statistics which are higher than 6.634 (Eq. (4.5)) of all modes of variability are compared among each other, and the one with the maximum D statistics is selected. Hence, the mode of variability with the maximum D statistics is the variable that explains best the occurrence of extreme precipitation compared to other modes of variability and stationary conditions.

Fig. 4.13a shows the regions where the orbital-only and the full-forcing simulations coherently influence extreme precipitation through the same mode of variability. In general, the modes of internal variability GPD models outperform the stationary models across the globe. This result indicates that modes of variability play a more important role in explaining the long-term variability of extreme precipitation in the pre-industrial period than the natural external

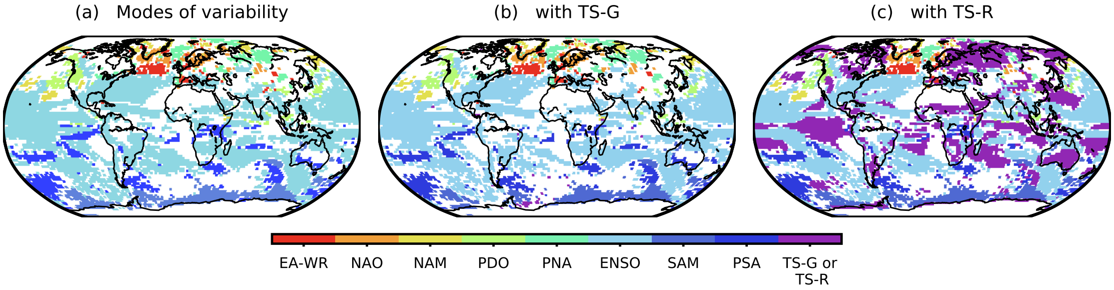

Figure 4.13: The non-stationary GPD models with (a) the modes of variability, (b) the modes of variability and TS-G, and (c) the modes of variability and TS-R as covariates that outperform all other GPD models (the modes-of-variability, TS-G or TS-R, and stationary GPD models) at 99% confidence interval, hence, explain best the variability of extreme precipitation. The regions where both orbital-only and full-forcing simulations share the same statistically significant D statistics are shown.

forcings do. In general, the modes of variability exhibit a significant connection to extreme precipitation in the vicinity to their regions of action. For instance, SAM is dominant in the Southern Ocean, and NAO and NAM in the North Atlantic region. The influence of ENSO is broader. Over land, ENSO dominates most of the Southern Hemisphere, eastern North America, southern Asia, and the eastern Mediterranean region. Although the connection between ENSO and extreme precipitation is strong and important (Kenyon and Hegerl, 2010), we also assume that this dominance of ENSO is partially related to the bias in CESM towards an overestimation of ENSO amplitudes (Stevenson et al., 2018). In Europe, the roles of EA-WR and PNA dominate over the western regions and NAM and NAO in the northern regions. In North America, PDO is the leading mode in the western regions and ENSO in the southeastern and central regions. Small areas are influenced by NAM and PNA. In the Southern Hemisphere, PSA and ENSO are dominant over land, while a slight influence of SAM is found over north-western Australia.

The result does not vary much when TS-G is included as covariate (Fig. 4.13b). Only a few sporadic points that denotes the influence of TS-G on extreme precipitation appear over the Southern Hemisphere, indicating that the changes in the global mean temperature affect little the long-term variability of extreme precipitation compared to the modes of variability. However, the influence of the surface temperature in Fig.4.13b changes when the regional temperature anomalies TS-R instead of TS-G are included as covariates (Fig. 4.13c). The dominance of TS-R over the modes of variability is highlighted in many land areas and the tropical oceans. The land areas where TS-R is more important are found largely at the extratropical latitudes in the Northern and Southern Hemispheres, covering a large part of northern Asia and North America, southern South America and Africa, Australia, the African transition zone, and the Arabian Peninsula. It is clear that over northern Asia, the influences of PNA and NAM that appeared previously in Fig. 4.13a and b are masked by those of TS-R. TS-R also prevails over the tropical Pacific, where ENSO takes place. In this region, the values of TS-R overlap with the NIÑO index, which is calculated as an average of the surface temperature anomalies of the same area. Hence, it is reasonable to interpret the predominance of TS-R in the tropical Pacific to be similar to the influence of ENSO. However, this pattern of TS-R simply indicates that the regional temperatures are statistically more associated with the regional extreme precipitation than the averaged temperature condition, thus the NIÑO index, over the area.

The here found associations of TS-R with extreme precipitation over land are in line with the preceding studies (Pendergrass et al., 2015; Sillmann et al., 2017; Sun et al., 2021), which have demonstrated that the present-day and future extreme precipitation are regulated by surface temperature. Here, it is also shown that TS-R does not outperform all the modes of variability over the entire land areas. There are regions, including some in the extratropics, where the modes of variability still play more important roles in regional extreme precipitation. Some of these regions are North America, northern South America, west- and southern Europe, and southern Asia, where ENSO, PDO, EA-WR, and PSA exhibit statistically significant associations.

Overall, the result indicates that both the modes of variability and regional temperature are more important than external forcings in the long-term variability of extreme precipitation during the pre-industrial 3351 years. Although the linear increase in extreme precipitation due to the externally forced variability is present in some regions, this influence is masked when internal variability and regional surface temperature are included. Moreover, this limited influence of external forcings on extreme precipitation signifies that the inherent uncertainties of external forcings have a minimal effect on the characterization of pre-industrial extreme precipitation.

4.6 Conclusions

We have examined the characteristics of pre-industrial extreme daily precipitation and its long-term changes and association to externally forced and internal variability during 1501 BCE–1849 CE. The period is of particular interest as the orbital parameters have progressively changed during the late Holocene (Wanner et al., 2008) and many civilizations had flourished and vanished during this period. Thereby, the role of changes in climate on these societal changes is also highly debated (e.g., Hodell et al., 1995; DeMenocal, 2001; Büntgen et al., 2011; McConnell et al., 2020). Our study is based on climate simulations from CESM1.2.2, which cover the period 1501 BCE–2008 CE, and the peak-over-threshold (POT) extreme value analysis is used to analyze extreme daily precipitation. The main findings of this study are the following:

First, regions with similar statistical distributions of extreme precipitation are identified using the POT analysis. We have distinguished the regions in four different density distributions of extreme precipitation, and these regions tend to cluster spatially. Clear differences in the distributions of extreme precipitation are observable between the Pacific and Atlantic sectors and between the northern-high and southern-low latitudes.

Second, past variability of extreme precipitation is strongly associated with large-scale modes of variability such as ENSO, NAM, PNA, EA-WR, and PSA, among others and regional surface temperature. Largely, the modes of variability present significant association with extreme precipitation in the vicinity to their regions of action. In this study, the regions where extreme precipitation is more associated either by a mode of variability or by the regional surface temperature are distinguished. Regional surface temperature is linked with extreme precipitation in general over lands at the extratropical latitudes and in the tropical oceans. In other regions, the influences of modes of variability are still dominant. Some limited regions show an association of extreme precipitation with changes in the insolation caused by changes in the orbital parameters during this period. This association is reflected by a linear increase in extreme precipitation. The POT analysis specifies geographical regions where the association with the climate variability is statistically significant, though it does not elucidate in which way the climate variability influences extreme precipitation. Understanding how each forcing and mode influences extreme precipitation is beyond the scope of this study, as additional dedicated sensitivity simulations and analysis would be required.

Lastly, changes in the frequency of extreme precipitation are remarkable after strong tropical eruptions. Significant changes after tropical eruptions occur in the return period. Hence, the frequency of extreme precipitation increases over the extratropical regions and the tropical Pacific and decreases in others. These post-eruption changes in the frequency of extreme precipitation are associated with the ENSO states, which are also influenced by the volcanic eruptions and agree with Stevenson et al. (2016). The influence of volcanic eruptions on extreme precipitation is only noticeable in the short term up to a few years (Iles et al., 2013; Iles and Hegerl, 2014; Stevenson et al., 2016). Statistically significant changes in the intensity of extreme precipitation are noted but are more heterogeneously distributed across the globe.

It is important to mention that some caveats need to be clarified in this study. There is a clear discrepancy between ERA5 reanalysis and CESM in representing the intensity of extreme precipitation. This is a problem that still many earth system models suffer from (Flato et al., 2014; Wang et al., 2017), and active research to reduce this difference is currently undertaken (Kopparla et al., 2013; Shields et al., 2016; Kawai et al., 2019). The fact that some regions over- or underestimate extreme daily precipitation may have implications for our results. For instance, the parameters of the generated statistical models are higher or lower than the values from the reanalysis. These differences in the parameter values can affect the estimation of return periods of extreme precipitation. However, we noted that the mean spatial patterns are rather similar between the two data sets. Therefore, the general conclusion on the global-scale spatial distributions of extreme precipitation should not be affected. Another point is that this analysis is based on a single climate model, CESM; therefore, the result is strongly influenced by the model-dependent internal variability (Fasullo et al., 2020). For instance, strong ENSO amplitudes in CESM may overrate the influences of this mode of variability on the global and regional extreme precipitation.

Nevertheless, this study provides a new approach to examine the nature of extreme daily precipitation in the past: we showed that continuous long climate model simulations help to partially understand the variability of extreme daily precipitation in the pre-industrial period. More volcanic eruptions are included from the newly available long record (Sigl et al., 2021; Dallmeyer et al., 2021), which can increase the robustness of the analysis of post-eruption extreme daily precipitation. Moreover, it is noted that the POT analysis is useful to discern regions where extreme precipitation is influenced by different climate factors.

Nowadays, understanding the variability of extreme precipitation is important to illustrate the entire natural mechanism of these rare events and to predict their future changes better. In the current context where the information on these events in the pre-industrial past is limited, studies based on available long climate simulations, such as the one employed here, can be a valuable contribution to complement the information on extreme precipitation. More modeling studies on extreme events in the past are needed to certify the results presented. This approach would clearly help us to understand the nature of these capricious, rare, and intense events in more detail, to improve the model-dependent representation of such events, and to distinguish the roles of the external and internal variability on them.

4.7 Supplement: calculation of modes of variability

Empirical Orthogonal Function analysis (EOF) (Hannachi et al., 2007) is used to derive the spatial patterns and the time series associated with the modes of internal variability in ERA5, CESM in 1979 – 2008 CE, and CESM during 1501 CE – 1849 CE. The EOF is applied to the sea surface temperature (SST) to infer the Pacific Decadal Oscillation (PDO) and the geopotential height at 500 hPa for other modes. The observational SST dataset is the ERSST v5 (Huang et al., 2017). The modes that are also detected as well by (Fasullo et al., 2020) which used the CMIP models including the CESM family models, and by (Lim, 2015) which used the reanalysis are considered.

For the Northern Annular Mode (NAM; Thompson and Wallace, 2000) and Pacific North American (PNA) pattern (Wallace and Gutzler, 1981), the EOF is applied over the region confined to 180°W – 180°E and 20° – 90°N; for the Southern Annular Mode (SAM; Marshall, 2003) and the Pacific South American (PSA) pattern (Mo and Paegle, 2001), the region over 180°W – 180°E and 20° – 90°S; for the North Atlantic Oscillation (NAO; Wallace and Gutzler, 1981) and Eastern Atlantic-West Russian pattern (EA-WR; Barnston and Livezey, 1987; Washington et al., 2000), the region over 70°W – 70°E and 20° – 85°N; and for the Pacific Decadal Oscillation (PDO; Trenberth and Hurrell, 1994), the region over 120°E – 75°E and 20° – 70°N. For NAM and SAM, the conventional EOF analysis is used, while for other, the rotated EOF (REOF) is applied. Among the resulting EOF patterns, those patterns whose root-mean-square-errors (RMSE) against the observational/reanalysis patterns are relatively low are chosen.

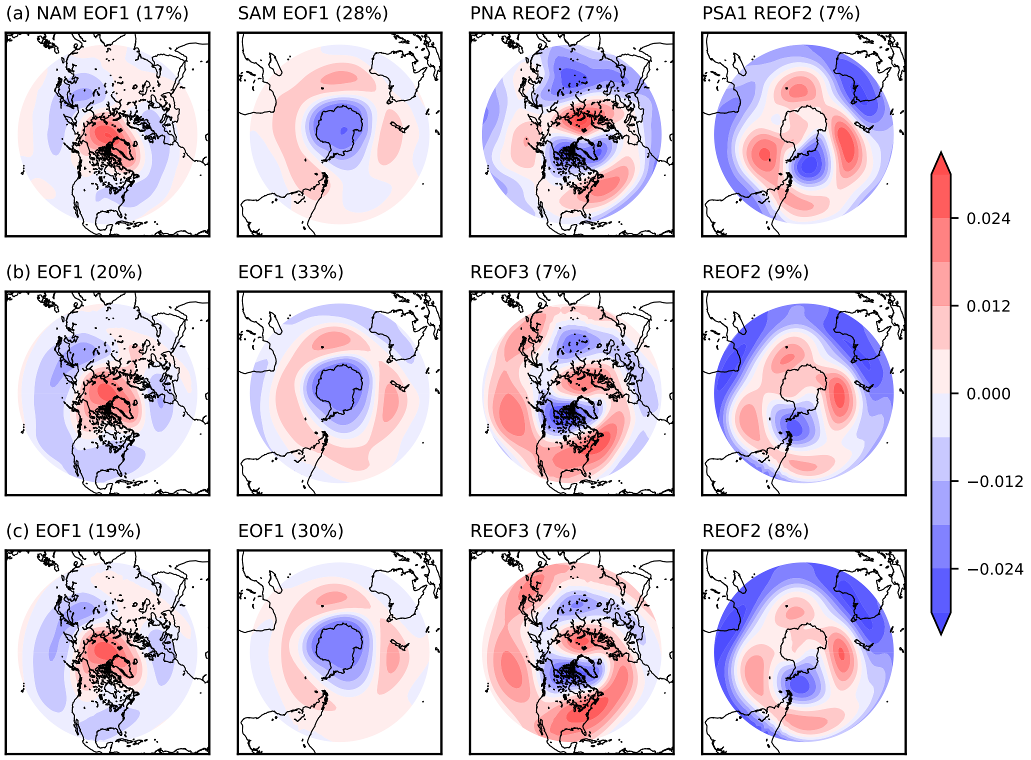

Figure 4.14: Modes of internal variability from (a) ERA5, (b) CESM 1979 – 2008 CE, and (c) CESM 1501 BCE – 1849 CE.

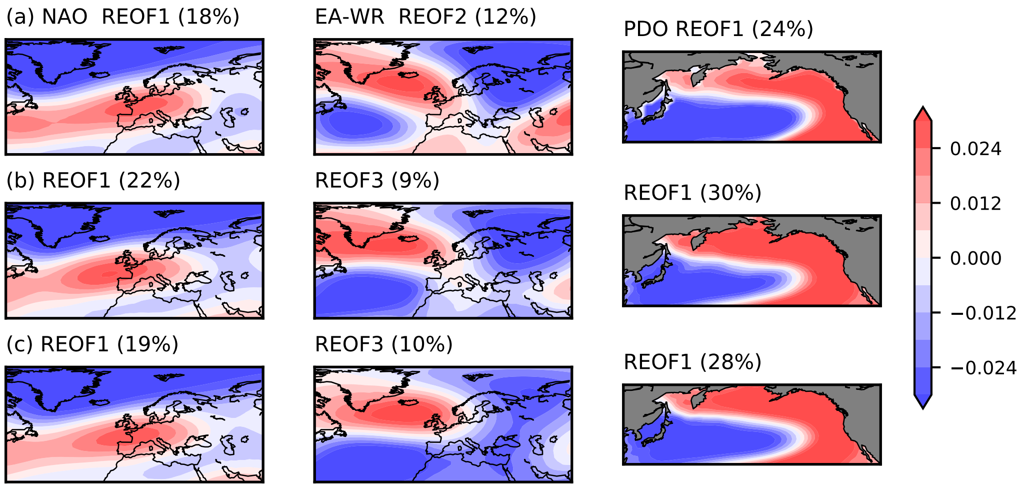

Figure 4.15: Continuation of Fig. 4.14

The RMSE is calculated as:

$$RMSE = \sqrt{\frac{\sum_{1}^{N}(X_i - Y_i)^2}{N}} \tag{4.7}$$

Where N is the total number of data, X_i is the time series of a variable from the observation, and Y_i is the time series of the same variable from the model simulation.

Unlike other indices, El Niño Southern Oscillation (ENSO) is computed as the mean SST over the Niño3.4 region in 170°W – 120°W and 5°S – 5°N (Trenberth and Stepaniak, 2001).

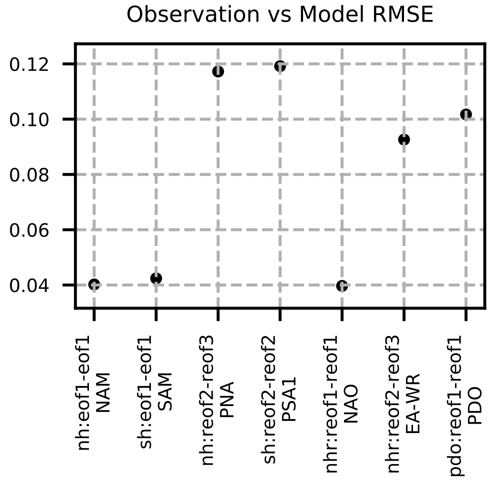

Figure 4.16: RMSE between the spatial patterns of the modes of variability of ERA5 and CESM for 1979–2008 CE (Fig. 4.14 and 4.15a and b.)

References

Allen, M. R. and Ingram, W. J.: Constraints on future changes in climate and the hydrologic cycle, Nature, 419, 228–232, doi:10.1038/nature01092, 2002.

Asadieh, B. and Krakauer, N. Y.: Global trends in extreme precipitation: climate models versus observations, Hydrology and Earth System Sciences, 19, 877–891, doi:10.5194/hess-19-877-2015, publisher: Copernicus GmbH, 2015.

Barnston, A. G. and Livezey, R. E.: Classification, seasonality and persistence of low-frequency atmospheric circulation patterns, Monthly weather review, 115, 1083–1126, doi:10.1175/1520-0493(1987)115⟨1083:CSAPOL⟩2.0.CO;2, 1987.

Bereiter, B., Eggleston, S., Schmitt, J., Nehrbass-Ahles, C., Stocker, T. F., Fischer, H., Kipfstuhl, S., and Chappellaz, J.: Revision of the EPICA Dome C CO2 record from 800 to 600 kyr before present, Geophysical Research Letters, 42, 542–549, 2015.

Berger, A.: Long-term variations of daily insolation and Quaternary climatic changes, Journal of Atmospheric Sciences, 35, 2362–2367, doi:10.1175/1520-0469(1978)035⟨2362:LTVODI⟩2.0.CO;2, 1978.

Blender, R., Raible, C. C., and Franzke, C. L. E.: Vorticity and geopotential height extreme values in ERA-Interim data during boreal winters: Vorticity and GPH Extremes, Quarterly Journal of the Royal Meteorological Society, 143, 634–640, doi:10.1002/qj.2944, 2017.

Boer, G.: Climate change and the regulation of the surface moisture and energy budgets, Climate Dynamics, 8, 225–239, URL `https://link.springer.com/content/pdf/10.1007/BF00198617.pdf`, 1993.

Brázdil, R., Kundzewicz, Z. W., Benito, G., Demarée, G., Macdonald, N., Roald, L. A., et al.: Historical floods in Europe in the past millennium, Changes in Flood Risk in Europe, edited by: Kundzewicz, ZW, IAHS Press, Wallingford, pp. 121–166, 2012.

Byrne, M. P. and O'Gorman, P. A.: The response of precipitation minus evapotranspiration to climate warming: Why the "wet-get-wetter, dry-get-drier" scaling does not hold over land, Journal of Climate, 28, 8078–8092, doi:10.1175/JCLI-D-15-0369.1, 2015.

Büntgen, U., Tegel, W., Nicolussi, K., McCormick, M., Frank, D., Trouet, V., Kaplan, J. O., Herzig, F., Heussner, K.-U., Wanner, H., Luterbacher, J., and Esper, J.: 2500 years of European climate variability and human susceptibility, Science, 331, 578–582, doi:10.1126/science.1197175, 2011.

Carn, S., Clarisse, L., and Prata, A. J.: Multi-decadal satellite measurements of global volcanic degassing, Journal of Volcanology and Geothermal Research, 311, 99–134, doi:10.1016/j.jvolgeores.2016.01.002, 2016.

Chadwick, R., Boutle, I., and Martin, G.: Spatial patterns of precipitation change in CMIP5: Why the rich do not get richer in the tropics, Journal of climate, 26, 3803–3822, doi:10.1175/JCLI-D-12-00543.1, 2013.

Champion, A. J., Hodges, K. I., Bengtsson, L. O., Keenlyside, N. S., and Esch, M.: Impact of increasing resolution and a warmer climate on extreme weather from Northern Hemisphere extratropical cyclones, Tellus A: Dynamic meteorology and oceanography, 63, 893–906, doi:10.1111/j.1600-0870.2011.00538.x, 2011.

Chen, H., Sun, J., and Li, H.: Increased population exposure to precipitation extremes under future warmer climates, Environmental Research Letters, 15, 034048, doi:10.1088/1748-9326/ab751f, publisher: IOP Publishing, 2020.

Chou, C. and Neelin, J. D.: Mechanisms of global warming impacts on regional tropical precipitation, Journal of climate, 17, 2688–2701, doi:10.1175/1520-0442(2004)017⟨2688:MOGWIO⟩2.0.CO;2, 2004.

Chou, C., Neelin, J. D., Chen, C.-A., and Tu, J.-Y.: Evaluating the “rich-get-richer” mechanism in tropical precipitation change under global warming, Journal of climate, 22, 1982–2005, doi:10.1175/2008JCLI2471.1, 2009.

Coles, S., Bawa, J., Trenner, L., and Dorazio, P.: An introduction to statistical modeling of extreme values, vol. 208, Springer, 2001.

Contractor, S., Donat, M. G., and Alexander, L. V.: Changes in Observed Daily Precipitation over Global Land Areas since 1950, Journal of Climate, 34, 3–19, doi:10.1175/JCLI-D-19-0965.1, publisher: American Meteorological Society Section: Journal of Climate, 2021.

Dai, A. and Wigley, T.: Global patterns of ENSO-induced precipitation, Geophysical Research Letters, 27, 1283–1286, doi:10.1029/1999GL011140, 2000.

Dallmeyer, A., Claussen, M., Lorenz, S. J., Sigl, M., Toohey, M., and Herzschuh, U.: Holocene vegetation transitions and their climatic drivers in MPI-ESM1. 2, Climate of the Past Discussions, pp. 1–55, doi:10.5194/cp-2021-51, 2021.

Dee, S. G., Cobb, K. M., Emile-Geay, J., Ault, T. R., Edwards, R. L., Cheng, H., and Charles, C. D.: No consistent ENSO response to volcanic forcing over the last millennium, Science, 367, 1477–1481, doi: 10.1126/science.aax2000, 2020.

Della-Marta, P. M., Mathis, H., Frei, C., Liniger, M. A., Kleinn, J., and Appenzeller, C.: The return period of wind storms over Europe, International Journal of Climatology: A Journal of the Royal Meteorological Society, 29, 437–459, doi:10.1002/joc.1794, 2009.

DeMenocal, P. B.: Cultural responses to climate change during the late Holocene, Science, 292, 667–673, doi:10.1126/science.1059287, 2001.

Donat, M. G., Lowry, A. L., Alexander, L. V., O’Gorman, P. A., and Maher, N.: More extreme precipitation in the world’s dry and wet regions, Nature Climate Change, 6, 508–513, doi:10.1038/nclimate2941, number: 5 Publisher: Nature Publishing Group, 2016.

Donat, M. G., Angélil, O., and Ukkola, A. M.: Intensification of precipitation extremes in the world’s humid and water-limited regions, Environmental Research Letters, 14, 065 003, doi:10.1088/1748-9326/ab1c8e, publisher: IOP Publishing, 2019.

El Adlouni, S., Ouarda, T. B., Zhang, X., Roy, R., and Bobée, B.: Generalized maximum likelihood estimators for the nonstationary generalized extreme value model, Water Resources Research, 43, doi:10.1029/2005WR004545, 2007.

Fasullo, J. T., Phillips, A., and Deser, C.: Evaluation of Leading Modes of Climate Variability in the CMIP Archives, Journal of Climate, 33, 5527–5545, doi:10.1175/JCLI-D-19-1024.1, 2020.

Fischer, E. M. and Knutti, R.: Observed heavy precipitation increase confirms theory and early models, Nature Climate Change, 6, 986–991, doi:10.1038/nclimate3110, number: 11 Publisher: Nature Publishing Group, 2016.

Flato, G., Marotzke, J., Abiodun, B., Braconnot, P., Chou, S. C., Collins, W., Cox, P., Driouech, F., Emori, S., Eyring, V., et al.: Evaluation of climate models, in: Climate change 2013: the physical science basis. Contribution of Working Group I to the Fifth Assessment Report of the Intergovernmental Panel on Climate Change, edited by Stocker, T., Qin, D., Plattner, Tignor, M., Allen, S., Boschung, J., Nauels, A., Xia, Y., Bex, V., and Midgley, P., pp. 741–866, Cambridge University Press, 2014.

Gao, C., Robock, A., and Ammann, C.: Volcanic forcing of climate over the past 1500 years: An improved ice core-based index for climate models, Journal of Geophysical Research: Atmospheres, 113, doi:10.1029/2008JD010239, 2008.

Giles, D. E., Feng, H., and Godwin, R. T.: Bias-corrected maximum likelihood estimation of the parameters of the generalized Pareto distribution, Communications in Statistics-Theory and Methods, 45, 2465–2483, doi:10.1080/03610926.2014.887104, 2016.

Glaser, R., Riemann, D., Schönbein, J., Barriendos, M., Brázdil, R., Bertolin, C., Camuffo, D., Deutsch, M., Dobrovolný, P., van Engelen, A., Enzi, S., Halíčková, M., Koenig, S. J., Kotyza, O., Limanówka, D., Macková, J., Sghedoni, M., Martin, B., and Himmelsbach, I.: The variability of European floods since AD 1500, Climatic Change, 101, 235–256, doi:10.1007/s10584-010-9816-7, 2010.

Hannachi, A., Jolliffe, I. T., and Stephenson, D. B.: Empirical orthogonal functions and related techniques in atmospheric science: A review, International Journal of Climatology: A Journal of the Royal Meteorological Society, 27, 1119–1152, doi:10.1002/joc.1499, 2007.

Hersbach, H., Bell, B., Berrisford, P., Hirahara, S., Horányi, A., Muñoz-Sabater, J., Nicolas, J., Peubey, C., Radu, R., Schepers, D., Simmons, A., Soci, C., Abdalla, S., Abellan, X., Balsamo, G., Bechtold, P., Biavati, G., Bidlot, J., Bonavita, M., Chiara, G. D., Dahlgren, P., Dee, D., Diamantakis, M., Dragani, R., Flemming, J., Forbes, R., Fuentes, M., Geer, A., Haimberger, L., Healy, S., Hogan, R. J., Hólm, E., Janisková, M., Keeley, S., Laloyaux, P., Lopez, P., Lupu, C., Radnoti, G., Rosnay, P. d., Rozum, I., Vamborg, F., Villaume, S., and Thépaut, J.-N.: The ERA5 global reanalysis, Quarterly Journal of the Royal Meteorological Society, 146, 1999–2049, doi:10.1002/qj.3803, 2020.

Hodell, D. A., Curtis, J. H., and Brenner, M.: Possible role of climate in the collapse of Classic Maya civilization, Nature, 375, 391–394, doi:10.1038/375391a0, 1995.

Hofmann, D. J.: Perturbations to the global atmosphere associated with the El Chichon volcanic eruption of 1982, Reviews of Geophysics, 25, 743–759, doi:10.1029/RG025i004p00743, 1987.

Huang, B., Thorne, P. W., Banzon, V. F., Boyer, T., Chepurin, G., Lawrimore, J. H., Menne, M. J., Smith, T. M., Vose, R. S., and Zhang, H.-M.: Extended reconstructed sea surface temperature, version 5 (ERSSTv5): upgrades, validations, and intercomparisons, Journal of Climate, 30, 8179–8205, doi:10.1175/JCLI-D-16-0836.1, 2017.

Hunke, E. C., Lipscomb, W. H., Turner, A. K., Jeffery, N., and Elliott, S.: CICE: the Los Alamos Sea Ice Model Documentation and Software User's Manual Version 4.1 LA-CC-06-012, T-3 Fluid Dynamics Group, Los Alamos National Laboratory, 675, URL `http://www.ccpo.odu.edu/~klinck/Reprints/PDF/cicedoc2015.pdf`, 2010.

Hurrell, J. W., Holland, M. M., Gent, P. R., Ghan, S., Kay, J. E., Kushner, P. J., Lamarque, J.-F., Large, W. G., Lawrence, D., Lindsay, K., Lipscomb, W. H., Long, M. C., Mahowald, N., Marsh, D. R., Neale, R. B., Rasch, P., Vavrus, S., Vertenstein, M., Bader, D., Collins, W. D., Hack, J. J., Kiehl, J., and Marshall, S.: The community earth system model: a framework for collaborative research, Bulletin of the American Meteorological Society, 94, 1339–1360, doi:10.1175/BAMS-D-12-00121.1, 2013.

Hurtt, G. C., Chini, L. P., Frolking, S., Betts, R., Feddema, J., Fischer, G., Fisk, J., Hibbard, K., Houghton, R., Janetos, A., et al.: Harmonization of land-use scenarios for the period 1500–2100: 600 years of global gridded annual land-use transitions, wood harvest, and resulting secondary lands, Climatic change, 109, 117–161, doi:10.1007/s10584-011-0153-2, 2011.

Iles, C. E. and Hegerl, G. C.: The global precipitation response to volcanic eruptions in the CMIP5 models, Environmental Research Letters, 9, 104 012, doi:0.1088/1748-9326/9/10/104012, 2014.

Iles, C. E., Hegerl, G. C., Schurer, A. P., and Zhang, X.: The effect of volcanic eruptions on global precipitation, Journal of Geophysical Research: Atmospheres, 118, 8770–8786, doi:10.1002/jgrd.50678, 2013.

Jacobeit, J., Glaser, R., Luterbacher, J., and Wanner, H.: Links between flood events in central Europe since AD 1500 and large-scale atmospheric circulation modes, Geophysical Research Letters, 30, doi: 10.1029/2002GL016433, 2003.

Joos, F. and Spahni, R.: Rates of change in natural and anthropogenic radiative forcing over the past 20,000 years, Proceedings of the National Academy of Sciences, 105, 1425–1430, doi:10.1073/pnas.0707386105, 2008.

Jungclaus, J. H., Bard, E., Baroni, M., Braconnot, P., Cao, J., Chini, L. P., Egorova, T., Evans, M., González-Rouco, J. F., Goosse, H., Hurtt, G. C., Joos, F., Kaplan, J. O., Khodri, M., Klein Goldewijk, K., Krivova, N., LeGrande, A. N., Lorenz, S. J., Luterbacher, J., Man, W., Maycock, A. C., Meinshausen, M., Moberg, A., Muscheler, R., Nehrbass-Ahles, C., Otto-Bliesner, B. I., Phipps, S. J., Pongratz, J., Rozanov, E., Schmidt, G. A., Schmidt, H., Schmutz, W., Schurer, A., Shapiro, A. I., Sigl, M., Smerdon, J. E., Solanki, S. K., Timmreck, C., Toohey, M., Usoskin, I. G., Wagner, S., Wu, C.-J., Yeo, K. L., Zanchettin, D., Zhang, Q., and Zorita, E.: The PMIP4 contribution to CMIP6–Part 3: The last millennium, scientific objective, and experimental design for the PMIP4 past1000 simulations, Geoscientific Model Development, 10, 4005–4033, doi:10.5194/gmd-10-4005-2017, 2017.

Kawai, H., Yukimoto, S., Koshiro, T., Oshima, N., Tanaka, T., Yoshimura, H., and Nagasawa, R.: Significant improvement of cloud representation in the global climate model MRI-ESM2, Geoscientific Model Development, 12, 2875–2897, doi:10.5194/gmd-12-2875-2019, 2019.

Kenyon, J. and Hegerl, G. C.: Influence of Modes of Climate Variability on Global Precipitation Extremes, Journal of Climate, 23, 6248–6262, doi:10.1175/2010JCLI3617.1, 2010.

Khaliq, M. N., Ouarda, T. B., Ondo, J.-C., Gachon, P., and Bobée, B.: Frequency analysis of a sequence of dependent and/or non-stationary hydro-meteorological observations: A review, Journal of hydrology, 329, 534–552, doi:10.1016/j.jhydrol.2006.03.004, 2006.

Kharin, V. V., Zwiers, F. W., Zhang, X., and Wehner, M.: Changes in temperature and precipitation extremes in the CMIP5 ensemble, Climatic Change, 119, 345–357, doi:10.1007/s10584-013-0705-8, 2013.

Kim, W. M. and Raible, C. C.: Dynamics of the Mediterranean droughts from 850 to 2099 CE in the Community Earth System Model, Climate of the Past, 17, 887–911, doi:10.5194/cp-17-887-2021, 2021.

Kjeldsen, T. R., Macdonald, N., Lang, M., Mediero, L., Albuquerque, T., Bogdanowicz, E., Brázdil, R., Castellarin, A., David, V., Fleig, A., Gül, G. O., Kriauciuniene, J., Kohnová, S., Merz, B., Nicholson, O., Roald, L. A., Salinas, J. L., Sarauskiene, D., Šraj, M., Strupczewski, W., Szolgay, J., Toumazis, A., Vanneuville, W., Veijalainen, N., and Wilson, D.: Documentary evidence of past floods in Europe and their utility in flood frequency estimation, Journal of Hydrology, 517, 963–973, doi:10.1016/j.jhydrol.2014.06.038, 2014.

Kopparla, P., Fischer, E. M., Hannay, C., and Knutti, R.: Improved simulation of extreme precipitation in a high-resolution atmosphere model, Geophysical Research Letters, 40, 5803–5808, doi:10.1002/2013GL057866, 2013.

Lawrence, D. M., Oleson, K. W., Flanner, M. G., Thornton, P. E., Swenson, S. C., Lawrence, P. J., Zeng, X., Yang, Z.-L., Levis, S., Sakaguchi, K., et al.: Parameterization improvements and functional and structural advances in version 4 of the Community Land Model, Journal of Advances in Modeling Earth Systems, 3, doi:10.1029/2011MS00045, 2011.

Lehner, F., Joos, F., Raible, C. C., Mignot, J., Born, A., Keller, K. M., and Stocker, T. F.: Climate and carbon cycle dynamics in a CESM simulation from 850 to 2100 CE, Earth system dynamics, 6, 411–434, doi:10.5194/esd-6-411-2015, 2015.

Lim, Y.-K.: The East Atlantic/West Russia (EA/WR) teleconnection in the North Atlantic: climate impact and relation to Rossby wave propagation, Climate Dynamics, 44, 3211–3222, doi:s00382-014-2381-4, 2015.

Machado, M. J., Botero, B. A., López, J., Francés, F., Díez-Herrero, A., and Benito, G.: Flood frequency analysis of historical flood data under stationary and non-stationary modelling, Hydrology and Earth System Sciences, 19, 2561–2576, doi:10.5194/hess-19-2561-2015, 2015.

Mann, H. B.: Nonparametric tests against trend, Econometrica: Journal of the econometric society, pp. 245–259, doi:10.2307/1907187, 1945.

Mann, H. B. and Whitney, D. R.: On a test of whether one of two random variables is stochastically larger than the other, The annals of mathematical statistics, pp. 50–60, doi:10.1214/aoms/1177730491, 1947.

Marshall, G. J.: Trends in the Southern Annular Mode from observations and reanalyses, Journal of climate, 16, 4134–4143, doi:10.1175/1520-0442(2003)016⟨4134:TITSAM⟩2.0.CO;2, 2003.

Matthes, K., Funke, B., Andersson, M. E., Barnard, L., Beer, J., Charbonneau, P., Clilverd, M. A., Dudok de Wit, T., Haberreiter, M., Hendry, A., et al.: Solar forcing for CMIP6 (v3. 2), Geoscientific Model Development, 10, 2247–2302, doi:10.5194/gmd-10-2247-2017, 2017.

McConnell, J. R., Sigl, M., Plunkett, G., Burke, A., Kim, W. M., Raible, C. C., Wilson, A. I., Manning, J. G., Ludlow, F., Chellman, N. J., et al.: Extreme climate after massive eruption of Alaska's Okmok volcano in 43 BCE and effects on the late Roman Republic and Ptolemaic Kingdom, Proceedings of the National Academy of Sciences, 117, 15 443–15 449, doi:10.1073/pnas.2002722117, 2020.

McGregor, S. and Timmermann, A.: The effect of explosive tropical volcanism on ENSO, Journal of climate, 24, 2178–2191, doi:10.1175/2010JCLI3990.1, 2011.

McGregor, S., Khodri, M., Maher, N., Ohba, M., Pausata, F. S., and Stevenson, S.: The effect of strong volcanic eruptions on ENSO, El Niño Southern Oscillation in a Changing Climate, pp. 267–287, doi: 10.1002/9781119548164.ch12, 2020.

Meinshausen, M., Vogel, E., Nauels, A., Lorbacher, K., Meinshausen, N., Etheridge, D. M., Fraser, P. J., Montzka, S. A., Rayner, P. J., Trudinger, C. M., Krummel, P. B., Beyerle, U., Canadell, J. G., Daniel, J. S., Enting, I. G., Law, R. M., Lunder, C. R., O'Doherty, S., Prinn, R. G., Reimann, S., Rubino, M., Velders, G. J. M., Vollmer, M. K., Wang, R. H. J., and Weiss, R.: Historical greenhouse gas concentrations for climate modelling (CMIP6), Geoscientific Model Development, 10, 2057–2116, doi:10.5194/gmd-10-2057-2017, publisher: Copernicus GmbH, 2017.

Mo, K. C. and Paegle, J. N.: The Pacific–South American modes and their downstream effects, International Journal of Climatology: A Journal of the Royal Meteorological Society, 21, 1211–1229, doi:10.1002/joc.685, 2001.

Myhre, G., Alterskjær, K., Stjern, C. W., Hodnebrog, , Marelle, L., Samset, B. H., Sillmann, J., Schaller, N., Fischer, E., Schulz, M., and Stohl, A.: Frequency of extreme precipitation increases extensively with event rareness under global warming, Scientific Reports, 9, 16 063, doi:10.1038/s41598-019-52277-4, number: 1 Publisher: Nature Publishing Group, 2019.

Neale, R. B., Chen, C.-C., Gettelman, A., Lauritzen, P. H., Park, S., Williamson, D. L., Conley, A. J., Garcia, R., Kinnison, D., and Lamarque, J.-F.: Description of the NCAR community atmosphere model (CAM 5.0), NCAR Tech. Note NCAR/TN-486+ STR, 1, 1–12, 2010.

Ohba, M., Shiogama, H., Yokohata, T., and Watanabe, M.: Impact of strong tropical volcanic eruptions on ENSO simulated in a coupled GCM, Journal of Climate, 26, 5169–5182, doi:10.1175/JCLI-D-12-00471.1, 2013.

Oman, L., Robock, A., Stenchikov, G., Schmidt, G. A., and Ruedy, R.: Climatic response to high-latitude volcanic eruptions, Journal of Geophysical Research: Atmospheres, 110, doi:10.1029/2004JD005487, 2005.

Otto-Bliesner, B. L., Brady, E. C., Fasullo, J., Jahn, A., Landrum, L., Stevenson, S., Rosenbloom, N., Mai, A., and Strand, G.: Climate variability and change since 850 CE: An ensemble approach with the Community Earth System Model, Bulletin of the American Meteorological Society, 97, 735–754, doi:10.1175/BAMS-D-14-00233.1, 2016.

O'Gorman, P. A.: Sensitivity of tropical precipitation extremes to climate change, Nature Geoscience, 5, 697–700, doi:10.1038/ngeo1568, 2012.

PAGES Hydro2k Consortium: Comparing proxy and model estimates of hydroclimate variability and change over the Common Era, Climate of the Past, 13, 1851–1900, doi:10.5194/cp-13-1851-2017, 2017.

Pall, P., Allen, M. R., and Stone, D. A.: Testing the Clausius–Clapeyron constraint on changes in extreme precipitation under CO2 warming, Climate Dynamics, 28, 351–363, doi:10.1007/s00382-006-0180-2, 2007.

Papalexiou, S. M. and Montanari, A.: Global and regional increase of precipitation extremes under global warming, Water Resources Research, 55, 4901–4914, doi:10.1029/2018WR024067, 2019.

Pendergrass, A. G., Lehner, F., Sanderson, B. M., and Xu, Y.: Does extreme precipitation intensity depend on the emissions scenario?, Geophysical Research Letters, 42, 8767–8774, doi:10.1002/2015GL065854, 2015.

Pfahl, S.: Characterising the relationship between weather extremes in Europe and synoptic circulation features, Natural Hazards and Earth System Sciences, 14, 1461–1475, doi:10.5194/nhess-14-1461-2014, publisher: Copernicus GmbH, 2014.

Pfahl, S. and Wernli, H.: Quantifying the relevance of cyclones for precipitation extremes, Journal of Climate, 25, 6770–6780, doi:10.1175/JCLI-D-11-00705.1, 2012.

Pfahl, S., O'Gorman, P. A., and Fischer, E. M.: Understanding the regional pattern of projected future changes in extreme precipitation, Nature Climate Change, 7, 423–427, doi:10.1038/nclimate3287, number: 6 Publisher: Nature Publishing Group, 2017.

Pongratz, J., Reick, C., Raddatz, T., and Claussen, M.: A reconstruction of global agricultural areas and land cover for the last millennium, Global Biogeochemical Cycles, 22, doi:10.1029/2007GB003153, 2008.

Robock, A.: Volcanic eruptions and climate, Reviews of geophysics, 38, 191–219, doi:10.1029/1998RG000054, 2000.

Roderick, M. L., Sun, F., Lim, W. H., and Farquhar, G. D.: A general framework for understanding the response of the water cycle to global warming over land and ocean, Hydrology and Earth System Sciences, 18, 1575–1589, doi:10.5194/hess-18-1575-2014, publisher: Copernicus GmbH, 2014.

Scher, S., Haarsma, R. J., Vries, H. d., Drijfhout, S. S., and Delden, A. J. v.: Resolution dependence of extreme precipitation and deep convection over the Gulf Stream, Journal of Advances in Modeling Earth Systems, 9, 1186–1194, doi:https://doi.org/10.1002/2016MS000903, 2017.

Schmidt, G. A., Jungclaus, J. H., Ammann, C. M., Bard, E., Braconnot, P., Crowley, T. J., Delaygue, G., Joos, F., Krivova, N. A., Muscheler, R., Otto-Bliesner, B. L., Pongratz, J., Shindell, D. T., Solanki, S. K., Steinhilber, F., and Vieira, L. E. A.: Climate forcing reconstructions for use in PMIP simulations of the last millennium (v1. 0), Geoscientific Model Development, 4, 33–45, doi:10.5194/gmd-4-33-2011, 2011.

Schneider, D. P., Ammann, C. M., Otto-Bliesner, B. L., and Kaufman, D. S.: Climate response to large, high-latitude and low-latitude volcanic eruptions in the Community Climate System Model, Journal of Geophysical Research: Atmospheres, 114, doi:10.1029/2008JD011222, 2009.

Schurer, A. P., Hegerl, G. C., Mann, M. E., Tett, S. F., and Phipps, S. J.: Separating forced from chaotic climate variability over the past millennium, Journal of Climate, 26, 6954–6973, doi:10.1175/JCLI-D-12-00826.1, 2013.

Scoccimarro, E., Gualdi, S., Bellucci, A., Zampieri, M., and Navarra, A.: Heavy Precipitation Events in a Warmer Climate: Results from CMIP5 Models, Journal of Climate, 26, 7902–7911, doi:10.1175/JCLI-D-12-00850.1, publisher: American Meteorological Society Section: Journal of Climate, 2013.

Shields, C. A., Kiehl, J. T., and Meehl, G. A.: Future changes in regional precipitation simulated by a half-degree coupled climate model: Sensitivity to horizontal resolution, Journal of Advances in Modeling Earth Systems, 8, 863–884, doi:10.1002/2015MS000584, 2016.

Sigl, M., Winstrup, M., McConnell, J. R., Welten, K. C., Plunkett, G., Ludlow, F., Büntgen, U., Caffee, M., Chellman, N., Dahl-Jensen, D., et al.: Timing and climate forcing of volcanic eruptions for the past 2,500 years, Nature, 523, 543–549, doi:10.1038/nature14565, 2015.

Sigl, M., Toohey, M., McConnell, J. R., Cole-Dai, J., and Severi, M.: HolVol: Reconstructed volcanic stratospheric sulfur injections and aerosol optical depth for the Holocene (9500 BCE to 1900 CE), doi:10.1594/PANGAEA.928646(DOIregistrationinprogress), last access = 5 May 2021, 2021.

Sillmann, J., Stjern, C. W., Myhre, G., and Forster, P. M.: Slow and fast responses of mean and extreme precipitation to different forcing in CMIP5 simulations, Geophysical Research Letters, 44, 6383–6390, doi:10.1002/2017GL073229, 2017.

Silva, A. T., Naghettini, M., and Portela, M. M.: On some aspects of peaks-over-threshold modeling of floods under nonstationarity using climate covariates, Stochastic environmental research and risk assessment, 30, 207–224, doi:10.1007/s00477-015-1072-y, 2016.

Smith, R., Jones, P., Briegleb, B., Bryan, F., Danabasoglu, G., Dennis, J., Dukowicz, J., Eden, C., Fox-Kemper, B., Gent, P., Hecht, M., Jayne, S., Jochum, M., Large, W., Lindsay, K., Maltrud, M., Norton, N., Peacock, S., Vertenstein, M., and Yeager, S.: The parallel ocean program (POP) reference manual ocean component of the community climate system model (CCSM) and community earth system model (CESM), LAUR-01853, 141, 1–140, 2010.

Steinschneider, S., Ho, M., Cook, E. R., and Lall, U.: Can PDSI inform extreme precipitation?: An exploration with a 500 year long paleoclimate reconstruction over the U.S., Water Resources Research, 52, 3866–3880, doi:https://doi.org/10.1002/2016WR018712, 2016.

Stephens, G. L., L'Ecuyer, T., Forbes, R., Gettelmen, A., Golaz, J.-C., Bodas-Salcedo, A., Suzuki, K., Gabriel, P., and Haynes, J.: Dreary state of precipitation in global models, Journal of Geophysical Research: Atmospheres, 115, doi:https://doi.org/10.1029/2010JD014532, 2010.

Stevenson, S., Otto-Bliesner, B., Fasullo, J., and Brady, E.: "El Niño like" hydroclimate responses to last millennium volcanic eruptions, Journal of Climate, 29, 2907–2921, doi:10.1175/JCLI-D-15-0239.1, 2016.

Stevenson, S., Fasullo, J. T., Otto-Bliesner, B. L., Tomas, R. A., and Gao, C.: Role of eruption season in reconciling model and proxy responses to tropical volcanism, Proceedings of the National Academy of Sciences, 114, 1822–1826, doi:10.1073/pnas.1612505114, 2017.

Stevenson, S., Overpeck, J. T., Fasullo, J., Coats, S., Parsons, L., Otto-Bliesner, B., Ault, T., Loope, G., and Cole, J.: Climate variability, volcanic forcing, and last millennium hydroclimate extremes, Journal of Climate, 31, 4309–4327, doi:10.1175/JCLI-D-17-0407.1, 2018.

Sugahara, S., Rocha, R. P. d., and Silveira, R.: Non-stationary frequency analysis of extreme daily rainfall in Sao Paulo, Brazil, International Journal of Climatology, 29, 1339–1349, doi:10.1002/joc.1760, 2009.

Sun, Q., Zhang, X., Zwiers, F., Westra, S., and Alexander, L. V.: A global, continental, and regional analysis of changes in extreme precipitation, Journal of Climate, 34, 243–258, doi:10.1175/JCLI-D-19-0892.1, 2021.

Sun, X., Renard, B., Thyer, M., Westra, S., and Lang, M.: A global analysis of the asymmetric effect of ENSO on extreme precipitation, Journal of Hydrology, 530, 51–65, doi:10.1016/j.jhydrol.2015.09.016, 2015.

Thiombiano, A. N., El Adlouni, S., St-Hilaire, A., Ouarda, T. B., and El-Jabi, N.: Nonstationary frequency analysis of extreme daily precipitation amounts in Southeastern Canada using a peaks-over-threshold approach, Theoretical and Applied Climatology, 129, 413–426, doi:10.1007/s00704-016-1789-7, 2017.

Thompson, D. W. and Wallace, J. M.: Annular modes in the extratropical circulation. Part I: Month-to-month variability, Journal of climate, 13, 1000–1016, doi:10.1175/1520-0442(2000)013⟨1000:AMITEC⟩2.0.CO;2, 2000.

Toohey, M., Stevens, B., Schmidt, H., and Timmreck, C.: Easy Volcanic Aerosol (EVA v1. 0): an idealized forcing generator for climate simulations, Geoscientific Model Development, 9, 4049–4070, doi:10.5194/gmd-9-4049-2016, 2016.

Trenberth, K. E. and Hurrell, J. W.: Decadal atmosphere-ocean variations in the Pacific, Climate Dynamics, 9, 303–319, doi:10.1007/BF00204745, 1994.

Trenberth, K. E. and Stepaniak, D. P.: Indices of el Niño evolution, Journal of climate, 14, 1697–1701, doi:10.1175/1520-0442(2001)014⟨1697:LIOENO⟩2.0.CO;2, 2001.

Trenberth, K. E., Dai, A., Rasmussen, R. M., and Parsons, D. B.: The Changing Character of Precipitation, Bulletin of the American Meteorological Society, 84, 1205–1218, doi:10.1175/BAMS-84-9-1205, publisher: American Meteorological Society Section: Bulletin of the American Meteorological Society, 2003.

Usoskin, I., Hulot, G., Gallet, Y., Roth, R., Licht, A., Joos, F., Kovaltsov, G., Thébault, E., and Khokhlov, A.: Evidence for distinct modes of solar activity, Astronomy & Astrophysics, 562, L10, doi:10.1051/0004-6361/201423391, 2014.

Usoskin, I., Gallet, Y., Lopes, F., Kovaltsov, G., and Hulot, G.: Solar activity during the Holocene: the Hallstatt cycle and its consequence for grand minima and maxima, Astronomy & Astrophysics, 587, A150, doi:10.1051/0004-6361/201527295, 2016.

Van Haren, R., Haarsma, R. J., Van Oldenborgh, G. J., and Hazeleger, W.: Resolution dependence of European precipitation in a state-of-the-art atmospheric general circulation model, Journal of Climate, 28, 5134–5149, doi:10.1175/JCLI-D-14-00279.1, 2015.

Vieira, L. E. A., Solanki, S. K., Krivova, N. A., and Usoskin, I.: Evolution of the solar irradiance during the Holocene, Astronomy & Astrophysics, 531, A6, doi:10.1051/0004-6361/201015843, 2011.

Wallace, J. M. and Gutzler, D. S.: Teleconnections in the geopotential height field during the Northern Hemisphere winter, Monthly weather review, 109, 784–812, doi:10.1175/1520-0493(1981)109⟨0784:TITGHF⟩2.0.CO;2, 1981.

Wang, T., Guo, D., Gao, Y., Wang, H., Zheng, F., Zhu, Y., Miao, J., and Hu, Y.: Modulation of ENSO evolution by strong tropical volcanic eruptions, Climate dynamics, 51, 2433–2453, doi:10.1007/s00382-017-4021-2, 2018.

Wang, X., Jiang, D., and Lang, X.: Future extreme climate changes linked to global warming intensity, Science Bulletin, 62, 1673–1680, doi:10.1016/j.scib.2017.11.004, 2017.

Wanner, H., Beer, J., Bütikofer, J., Crowley, T. J., Cubasch, U., Flückiger, J., Goosse, H., Grosjean, M., Joos, F., Kaplan, J. O., et al.: Mid-to Late Holocene climate change: an overview, Quaternary Science Reviews, 27, 1791–1828, doi:10.1016/j.quascirev.2008.06.013, 2008.

Washington, R., Hodson, A., Isaksson, E., and Macdonald, O.: Northern hemisphere teleconnection indices and the mass balance of Svalbard glaciers, International Journal of Climatology: A Journal of the Royal Meteorological Society, 20, 473–487, doi:10.1002/(SICI)1097-0088(200004)20:5⟨473::AID-JOC506⟩3.0.CO;2-O, 2000.

Westra, S., Alexander, L. V., and Zwiers, F. W.: Global increasing trends in annual maximum daily precipitation, Journal of climate, 26, 3904–3918, doi:10.1175/JCLI-D-12-00502.1, 2013.

Wilhelm, B., Arnaud, F., Sabatier, P., Crouzet, C., Brisset, E., Chaumillon, E., Disnar, J.-R., Guiter, F., Malet, E., Reyss, J.-L., Tachikawa, K., Bard, E., and Delannoy, J.-J.: 1400years of extreme precipitation patterns over the Mediterranean French Alps and possible forcing mechanisms, Quaternary Research, 78, 1–12, doi:10.1016/j.yqres.2012.03.003, 2012.

Wilks, D. S.: Statistical methods in the atmospheric sciences, vol. 100, Academic press, 2011.

Yang, F., Kumar, A., Schlesinger, M. E., and Wang, W.: Intensity of hydrological cycles in warmer climates, Journal of Climate, 16, 2419–2423, doi:10.1175/2779.1, 2003.

Yang, T., Li, H., Wang, W., Xu, C.-Y., and Yu, Z.: Statistical downscaling of extreme daily precipitation, evaporation, and temperature and construction of future scenarios, Hydrological Processes, 26, 3510–3523, doi:https://doi.org/10.1002/hyp.8427, 2012.

Zheng, J., Yu, Y., Zhang, X., and Hao, Z.: Variation of extreme drought and flood in North China revealed by document-based seasonal precipitation reconstruction for the past 300 years, Climate of the Past, 14, 1135–1145, doi:10.5194/cp-14-1135-2018, 2018.

Zhong, Y., Jahn, A., Miller, G., and Geirsdottir, A.: Asymmetric Cooling of the Atlantic and Pacific Arctic During the Past Two Millennia: A Dual Observation-Modeling Study, Geophysical Research Letters, 45, 12–497, doi:10.1029/2018GL079447, 2018.

Chapter 5

Extreme climate after massive eruption of Alaska's Okmok volcano in 43 BCE and effects on the late Roman Republic and Ptolemaic Kingdom

Joseph R. McConnell, Michael Sigl, Gill Plunkett, Andrea Burke, Woon Mi Kim, Christoph C. Raible, Andrew I. Wilson, Joseph G. Manning, Francis Ludlow, Nathan J. Chellman, Helen M. Innes, Zhen Yang, Jessica F. Larsen, Janet R. Schaefer, Sepp Kipfstuhl, Seyedhamidreza Mojtabavi, Frank Wilhelms, Thomas Opel, Hanno Meyer, and Jørgen Peder Steffensen

Published in *Proceedings of the National Academy of Sciences*, Volume 117, Number 27, 15443 – 15449, 2020.

The chapter is published under the link:
`https://doi.org/10.1073/pnas.2002722117`

Extreme climate after massive eruption of Alaska's Okmok volcano in 43 BCE and effects on the late Roman Republic and Ptolemaic Kingdom

Joseph R. McConnell[a,b,1], Michael Sigl[c,d], Gill Plunkett[e], Andrea Burke[f], Woon Mi Kim[c,d], Christoph C. Raible[c,d,e], Andrew I. Wilson[g,h], Joseph G. Manning[i,j,k], Francis Ludlow[l], Nathan J. Chellman[a], Helen M. Innes[f], Zhen Yang[l], Jessica F. Larsen[m], Janet R. Schaefer[n], Sepp Kipfstuhl[o], Seyedhamidreza Mojtabavi[o,p], Frank Wilhelms[o,p], Thomas Opel[q], Hanno Meyer[q], and Jørgen Peder Steffensen[r]

[a]Division of Hydrologic Sciences, Desert Research Institute, Reno, NV 89512; [b]Sir Nicholas Shackleton Visiting Fellow, Clare Hall, University of Cambridge, Cambridge CB3 9AL, United Kingdom; [c]Climate and Environmental Physics, Physics Institute, University of Bern, 3012 Bern, Switzerland; [d]Oeschger Centre for Climate Change Research, University of Bern, 3012 Bern, Switzerland; [e]School of Natural and Built Environment, Queen's University Belfast, Belfast BT7 1NN, United Kingdom; [f]School of Earth and Environmental Sciences, University of St Andrews, St Andrews KY16 9AL, United Kingdom; [g]Faculty of Classics, University of Oxford, Oxford OX1 3LU, United Kingdom; [h]School of Archaeology, University of Oxford, Oxford OX1 3TG, United Kingdom; [i]Department of History, Yale University, New Haven, CT 06520-8324; [j]Department of Classics, Yale University, New Haven, CT 06520-8266; [k]School of Forestry & Environmental Studies, Yale University, New Haven, CT 06511; [l]Trinity Centre for Environmental Humanities, Department of History, School of Histories & Humanities, Trinity College, Dublin 2, Ireland; [m]Department of Geosciences, University of Alaska Fairbanks, Fairbanks, AK 99775; [n]Volcanology Section, State of Alaska Division of Geological and Geophysical Surveys, Fairbanks, AK 99709; [o]Glaciology, Alfred-Wegener-Institut Helmholtz-Zentrum für Polar- und Meeresforschung, 27570 Bremerhaven, Germany; [p]Department of Crystallography, Geoscience Centre, University of Göttingen, 37073 Göttingen, Germany; [q]Polar Terrestrial Environmental Systems, Alfred-Wegener-Institut Helmholtz-Zentrum für Polar- und Meeresforschung, 14473 Potsdam, Germany; and [r]Physics of Ice, Climate, and Earth, University of Copenhagen, 1017 Copenhagen, Denmark

Edited by Ellen Mosley-Thompson, The Ohio State University, Columbus, OH, and approved May 20, 2020 (received for review March 6, 2020)

The assassination of Julius Caesar in 44 BCE triggered a power struggle that ultimately ended the Roman Republic and, eventually, the Ptolemaic Kingdom, leading to the rise of the Roman Empire. Climate proxies and written documents indicate that this struggle occurred during a period of unusually inclement weather, famine, and disease in the Mediterranean region; historians have previously speculated that a large volcanic eruption of unknown origin was the most likely cause. Here we show using well-dated volcanic fallout records in six Arctic ice cores that one of the largest volcanic eruptions of the past 2,500 y occurred in early 43 BCE, with distinct geochemistry of tephra deposited during the event identifying the Okmok volcano in Alaska as the source. Climate proxy records show that 43 and 42 BCE were among the coldest years of recent millennia in the Northern Hemisphere at the start of one of the coldest decades. Earth system modeling suggests that radiative forcing from this massive, high-latitude eruption led to pronounced changes in hydroclimate, including seasonal temperatures in specific Mediterranean regions as much as 7 °C below normal during the 2 y period following the eruption and unusually wet conditions. While it is difficult to establish direct causal linkages to thinly documented historical events, the wet and very cold conditions from this massive eruption on the opposite side of Earth probably resulted in crop failures, famine, and disease, exacerbating social unrest and contributing to political realignments throughout the Mediterranean region at this critical juncture of Western civilization.

ice core | volcano | Okmok | Rome | climate forcing

The assassination of Julius Caesar on the Ides of March in 44 BCE marked the beginning of a 17 y struggle for the future of the greater Mediterranean region— including the Roman Republic and Egyptian Ptolemaic Kingdom—that culminated in the rise of the Roman Empire. Although it is sometimes difficult to separate fact from myth associated with these transformative events, the thin surviving historical accounts credibly describe unusual atmospheric phenomena in the Mediterranean region from 44 BCE and China from 43 BCE (1), as well as anomalously inclement weather (2) and widespread famine (3) that provide a notable environmental background important to understanding the period's reorganization of political power that ultimately changed the course of history (4). Northern Hemisphere (NH) climate proxies show that 43 and 42 BCE were among the coldest of the past 2,500 y, coincident with the start of one of the coldest decades (5, 6), although no annually resolved climate proxy records exist for the Mediterranean region specifically. Moreover, ice core records of lead pollution in northcentral Greenland—a proxy of European lead/silver mining and smelting during antiquity and already low during the Crisis of the Roman Republic (7, 8)—declined during this decade, suggesting further deterioration of the Roman economy. Historians and scientists who study these ancient times have speculated that a large volcanic eruption most likely was the cause of these unusual atmospheric and climate events, although uncertain chronologies and low resolution in the available ice core and other records have to date limited understanding of the magnitude and extent of the climate anomaly and therefore its

Significance

The first century BCE fall of the Roman Republic and Ptolemaic Kingdom and subsequent rise of the Roman Empire were among the most important political transitions in the history of Western civilization. Volcanic fallout in well-dated Arctic ice core records, climate proxies, and Earth system modeling show that this transition occurred during an extreme cold period resulting from a massive eruption of Alaska's Okmok volcano early in 43 BCE. Written sources describe unusual climate, crop failures, famine, disease, and unrest in the Mediterranean immediately following the eruption—suggesting significant vulnerability to hydroclimatic shocks in otherwise sophisticated and powerful ancient states. Such shocks must be seen as having played a role in the historical developments for which the period is famed.

Author contributions: J.R.M., M.S., and C.C.R. designed research; J.R.M., M.S., G.P., A.B., W.M.K., N.J.C., H.M.I., J.F.L., J.R.S., S.K., S.M., F.W., T.O., H.M., and J.P.S. performed research; J.R.M., M.S., N.J.C., and Z.Y. analyzed data; and J.R.M., G.P., W.M.K., C.C.R., A.I.W., J.G.M., F.L., and N.J.C. wrote the paper.

The authors declare no competing interest.

This article is a PNAS Direct Submission.

See online for related content such as Commentaries.

[1]To whom correspondence may be addressed. Email: Joe.McConnell@dri.edu.

This article contains supporting information online at https://www.pnas.org/lookup/suppl/doi:10.1073/pnas.2002722117/-/DCSupplemental.

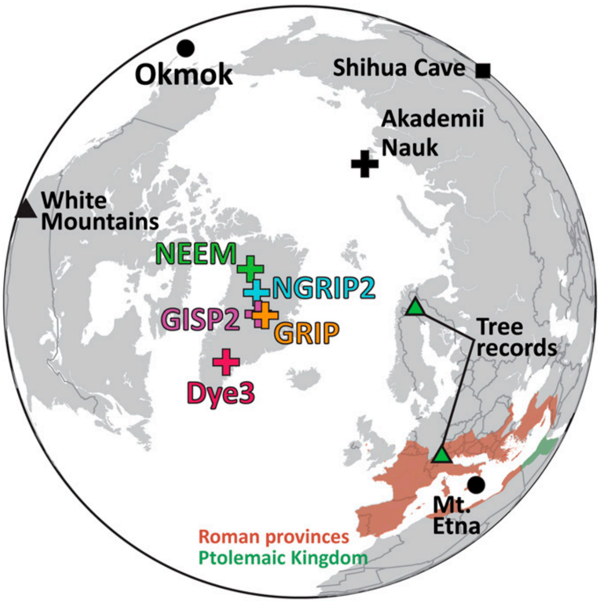

Fig. 1. Location map. Shown are drilling sites for the six Arctic ice core records evaluated in this study (pluses), the Okmok and Mount Etna volcanoes, tree (6, 11) and Shihua Cave (12) speleothem-based climate proxy records, and the extent of the Roman provinces and Ptolemaic Kingdom in 44 BCE.

potential effects on ancient societies. Speculation based primarily on the approximate timing and magnitude of known NH eruptions during this period suggested the most likely source volcano was Mount Etna (2) in Sicily or Shiveluch (9) in Kamchatka, with more recent speculation focused on Nicaragua's Apoyeque (5, 10).

Ice Core Evidence of a Massive Eruption in Early 43 BCE

We used records of volcanic fallout in six Arctic ice cores (Fig. 1 and *SI Appendix*, Fig. S1)—all synchronized to the same annual-layer-counted and verified timescale (7)—as well as climate proxies and Earth system modeling to develop a more complete understanding of the timing and magnitude of volcanism during this period and its effects on climate and history. We focused our interpretation on high-resolution measurements of volcanic fallout (*Materials and Methods*) in the North Greenland Ice Core Project 2 (NGRIP2) core on the recently developed and verified Desert Research Institute (DRI) NGRIP2 age scale that provides the most detailed and well-dated records of volcanic fallout for this period (Fig. 2) (7). Age uncertainties for this age scale previously were shown to be less than ±2 y during antiquity (7), although the exact coincidence between the massive fallout of radiatively important non-sea-salt sulfur (nssS) measured in NGRIP2 and the pronounced temperature anomaly in absolutely dated tree ring records (5) implies no dating uncertainty in the ice chronology at 43 BCE (Fig. 2). Throughout this study, 43 BCE corresponds to the period between 1,991 and 1,992 y before 1950 (ybp) (*SI Appendix*, Table S1).

The NGRIP2 measurements clearly delineate volcanic fallout from two distinct eruptions: the first starting in early (i.e., January or February) 45 BCE and the second in early 43 BCE. The nssS fallout from the first eruption suggests it was a powerful but short-lived event, with fallout returning to background levels by late 45 BCE. Comparisons to the array of four other Greenland

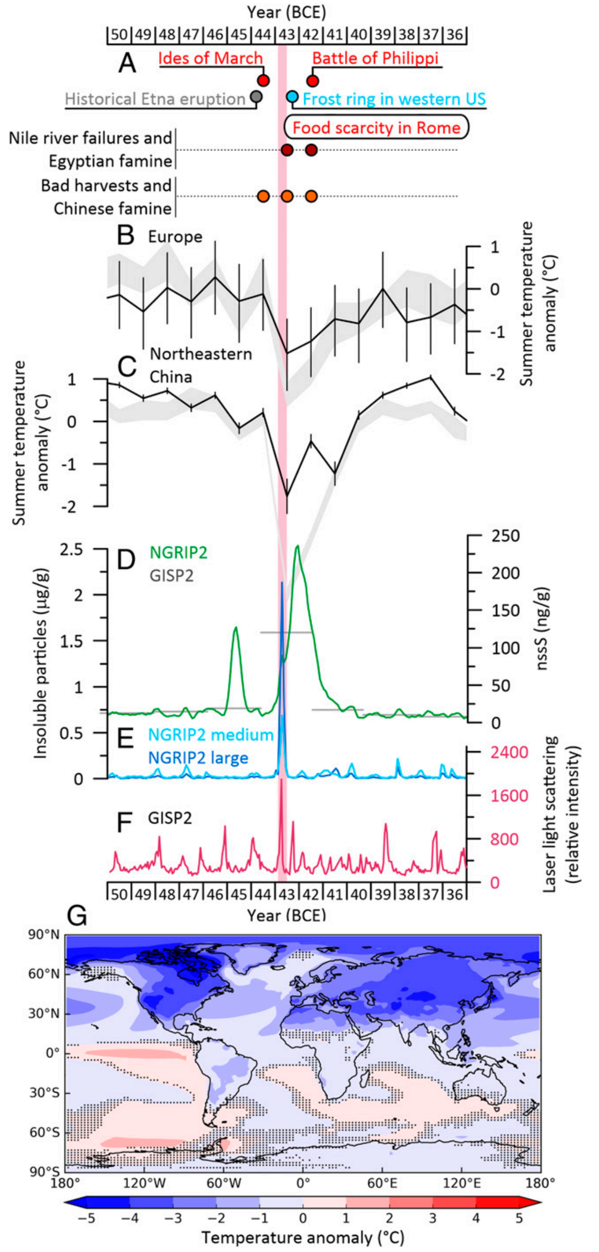

Fig. 2. Ice core, tree ring, and speleothem evidence for the 45 and 43 BCE eruptions and climate effects. (*A*) Selected historical and other events (see text). (*B*) Model-simulated (gray) and observed (black) summer temperature anomalies from European tree ring records with original 2σ uncertainties (6). (*C*) Model-simulated (gray) and observed (black) summer temperature anomalies from the Chinese Shihua Cave speleothem record with original maximum temperature uncertainties (12). Shading in *B* and *C* shows annual CESM ensemble SEs. (*D*) Continuous NGRIP2 and discrete (2 y) GISP2 nssS (9) concentrations. (*E*) NGRIP2 mass-equivalent insoluble particle concentrations for medium (2.5 to 5 μm) and large (5 to 10 μm) particles. (*F*) GISP2 LLS measurements (13). (*G*) Simulated 43 and 42 BCE average air -temperature anomalies (hashing shows anomalies that are not significant [2σ]). Annual and seasonal simulations for each year are shown in *SI Appendix*, Figs. S6 and S7. All records were aligned at the start of the 43 BCE volcanic event to be consistent with the DRI_NGRIP2 chronology. The vertical shaded bar shows the extent of the insoluble particle (i.e., tephra) spike at the start of volcanic fallout in the NGRIP2 record.

ice core records (*SI Appendix*, Fig. S1) show that fallout from the 45 BCE event was confined largely to northern Greenland, suggesting a nearby high-latitude source volcano (e.g., Iceland). In addition, proxy records (6) indicate no large-scale climate effects, so it is unlikely that this eruption had a significant influence on the midlatitude regions. The nssS fallout from the second event suggests that it was a massive eruption that started in early 43 BCE, with elevated volcanic fallout lasting more than 2 y. Increased nssS concentrations started in the NGRIP2 record in early winter and reached a temporary peak in spring and an overall maximum in late autumn of 43 BCE, before returning to background concentrations by spring 41 BCE (Fig. 2). Sulfur isotope ratios measured in fallout from the beginning of the 43 BCE event in Greenland Ice Sheet Project 2 (GISP2) ice (*Materials and Methods*) showed nonzero $\Delta^{33}S$ values (*SI Appendix*, Fig. S3) that result from oxidation in a high-ultraviolet environment consistent with plume ejection above the ozone layer in the lower stratosphere (14). Injection into the stratosphere is consistent with persistent, widespread climate effects.

Comparisons of volcanic acid deposition recorded in the five Greenland cores indicate moderately greater fallout in central Greenland during the 43 BCE event, contrasting with the 45 BCE event. Fallout deposition during the 2 y period was ~123 and ~110 kg/km^2 as sulfuric acid in the northern NGRIP2 and North Greenland Eemian Ice Drilling (NEEM) cores and ~131, ~135, and ~128 kg/km^2 in the GISP2 (15), GRIP (16), and Dye3 (16) cores to the south, respectively (*Materials and Methods*). In all six Arctic ice core records (Fig. 1), the 43 BCE event ranked among the largest observed during the past 2,500 y for acid-equivalent deposition. For example, it ranked second in NEEM (5), third in GRIP (16), second in GISP2 (15), fourth in Dye3 (16), and first in the combined NGRIP (17) and NGRIP2 (this study) nssS record for the past 2,500 y. Similarly, average nssS for the 2 y period of 43 and 42 BCE ranked fourth highest in the Russian Arctic (Akademii Nauk) ice core record (this study) from 500 BCE up to the Industrial Revolution and the start of widespread industrial sulfur pollution.

Volcanic Provenance

A sharp spike in 2.5 to 10 μm insoluble particle concentrations in NGRIP2 and in laser light-scattering measurements in GISP2 (13) coincided with the early stages of the 43 BCE volcanic nssS peak, suggesting deposition of volcanic tephra (18, 19) near the start of the eruption (Fig. 2 and *SI Appendix*, Fig. S1). Microprobe analyses (*Materials and Methods*) of 35 volcanic shards (*SI Appendix*, Fig. S4) filtered from corresponding GISP2 ice revealed geochemical characteristics (Fig. 3 and *SI Appendix*, Fig. S5) matching reference tephra from the andesite fall and pyroclastic density current units from the caldera-forming, volcanic explosivity index (VEI) 6, Okmok II (53.4 °N, 168.1 °W) eruption in Alaska (Fig. 1). The 43 BCE eruption date from Greenland ice cores is consistent with the 190 BCE to 50 CE (2σ, updated to international working group on radicarbon calibration curves IntCal13) (20) calibrated age range indicated by radiocarbon dates for organic material in the layers just below the initial proximal deposits of Okmok II. The geochemistry of the GISP2 shards and Okmok II reference tephra clearly is distinct from reference tephra from other potential volcanic eruptions in the first century BCE (Fig. 3 and *SI Appendix*, Fig. S5), providing nearly unambiguous evidence that the Okmok II eruption was the source of the 43 BCE event. The precise identification of the source location now provides a key input in efforts to better model and understand the event's effects on climate.

Northern Hemisphere Climate Effects

The 2 y cooling associated with the Okmok II eruption (Fig. 2) was among the most significant recorded in NH summer temperature proxies for the past 2,500 y. For example, 43 and 42 BCE ranked as the second and eighth coldest years in a recent tree ring–based assessment (5), respectively, while the decade from 43 to 34 BCE was the fourth coldest. Central and northern European climate reconstructions based on measurements in temperature-sensitive trees from Scandinavia and Austria (6) indicate marked regional summertime cooling of >3 °C and >2.5 °C in 43 and 42 BCE (Fig. 2), respectively. Similarly, an annually dated speleothem record of summer temperatures from Shihua Cave in northeastern China shows a pronounced 3 y reduction in summertime temperature of >2.0 °C starting in 45 BCE, coeval with 43 BCE within the 5 y dating uncertainty of the speleothem record (Fig. 2). A rare frost ring recorded in bristlecone pine trees from California's White Mountains indicates anomalous, below-freezing temperatures in early September 43 BCE (Fig. 2) during the late NH summer growing season (11).

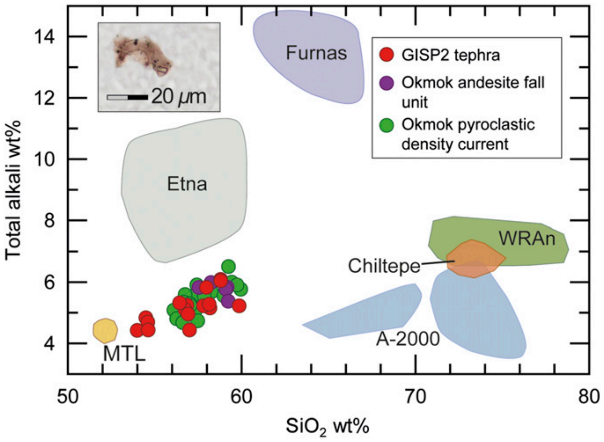

Fig. 3. Total alkali (Na_2O + K_2O) and silica compositions of tephra from GISP2 ice during the 43 BCE event compared with tephra from Okmok II and other potential source volcanoes. Filled circles show measurements (this study) of GISP2 and Okmok reference tephra. Shaded regions show tephra measurements from other potential first century BCE source volcanoes: Etna, Italy (21, 22); Chiltepe from Apoyeque, Nicaragua (23, 24); Masaya Triple Tuff (MTL), Nicaragua (23); A-2000, Askja, Iceland (25); White River Ash northern lobe (WRAn), Churchill, Canada (26); Furnas, Azores (27). *Inset* shows a tephra shard from the GISP2 sample. See *SI Appendix*, Fig. S5 for additional comparisons and analytical precision.

Using the exact location and the estimated eruption timing and sulfur yield of the Okmok II eruption, we used the Community Earth System Model (CESM, version 1.2.2) (28) to simulate the severity, extent, and persistence of the climate response (Fig. 2 and *Materials and Methods*). The simulations indicate pronounced, widespread NH cooling in 43 and 42 BCE, with simulated summer air temperature anomalies similar in magnitude and duration to the European tree ring (29) and Chinese (Shihua Cave) speleothem (12) climate proxy records that show 2 to 3 °C declines in summer air temperatures (Fig. 2). Chinese written records also document unusually cold weather in 43 and 42 BCE, including late spring and early autumn frosts (30). The CESM simulations suggest that cooling may have persisted into the early 30s BCE, as well as significant changes in global precipitation from the Okmok II eruption, including increases over the Mediterranean region and strong decreases over Asia and the high NH latitudes (*SI Appendix*, Figs. S6 and S7).

Climate Effects and Historical Linkages in the Mediterranean Region

Agreement between the few available annually resolved NH proxy records of summertime temperatures and the CESM-simulated temperature anomalies suggest that the model largely captures the temperature effects of radiative forcing associated with the early 43 BCE Okmok II eruption. Therefore, we used the simulated temperature and precipitation anomalies in the Roman provinces and Ptolemaic Kingdom (Fig. 4 and *SI Appendix*, Figs. S8 and S9), where no annually resolved climate proxies are available to investigate possible effects on ancient societies, though recognizing that accurately modeling precipitation is often particularly challenging. The effect of climate shocks on ancient societies most usually and directly occurred through diminished agricultural yields, with crop failures occurring because of insufficient or excessive rainfall at critical periods for plant growth (31) or because of unusual growing season temperatures. The environmental perception of anomalous weather and other volcanically induced phenomena (e.g., visually spectacular dimming or discoloration of the solar disk) as portents also endowed these events with a significance that made their appearance politically influential in ancient societies.

The ice core and climate proxy record evidence, as well as the Earth system model simulations, suggests that the atmospheric and climate phenomena described by ancient Mediterranean sources and recently evaluated by historians (1–3) can be separated into two groups. The first clusters around March and April 44 BCE and consists of atmospheric phenomena (solar dimming, halos, and parhelia) interpreted by ancient writers as signs and portents. Virgil, in his poem *Georgics* (1.466–73), said that the sun was darkened after Caesar's assassination, and the ancient commentator Servius added that "it is said, after Caesar had been killed in the Senate on the day before, the sun's light failed from the sixth hour until nightfall." Plutarch (*Life of Julius Caesar* 69.3–4) said not only that the sun was veiled and pale but also that it gave forth so little heat that fruits shriveled rather than ripened. Several authors mentioned seeing three suns in the sky (Dio Cassius, 45.17.5; Julius Obsequens, 68; Eusebius, *Chronicle*, Olympiad 184), a well-known phenomenon called "sun dogs" or parhelia caused by refraction of sunlight through ice crystals in the upper atmosphere in particularly cold weather. Dio and Obsequens added that there was a radiant colored halo around the sun, probably a "bishop's ring," a diffuse bluish-brown halo around the sun caused by sulfur-based aerosols from large volcanic eruptions. Other writers mentioned a solar halo that marked Octavian's arrival in Rome in early April 44 BCE (e.g., Seneca, *NQ* 1.2.1; Suetonius, *Augustus* 95; Velleius Paterculus, 2.59.6; Pliny, *NH* 2.98; Dio Cassius, 45.4.4; Obsequens, 68; Orosius, 6.20.5) and which was seized upon by Octavian and his supporters to suggest divine favor for his cause (1, 3). All these phenomena are consistent with the atmospheric effects of volcanic eruptions. However, given that they are reported as occurring before the probable date of the Okmok II eruption in 43 BCE, that all of the sources referring to them originate in Italy or the central Mediterranean, and that NH proxies show no large-scale climate effects, the comparatively minor, historically well documented eruption of Etna in 44 BCE is a plausible candidate for their cause.

The second group of ancient sources relates more directly to unusually cold weather and famine (3). These sources group from early 43 BCE to late 42 BCE and are consistent with the extreme climate effects (Fig. 4) of the massive, early 43 BCE Okmok II eruption indicated by volcanic fallout in the Arctic ice cores (Fig. 2). Although some sources suggest harsh winter weather in late 44 BCE, it is uncertain whether these passages reflect especially unusual winters in the southern Balkans or are more simply a commentary on the conditions that traditionally led armies to avoid movements in winter. Whether they also reflect the continuing aftereffects of the relatively minor eruption of Etna in 44 BCE 7 or 8 mo earlier is therefore similarly

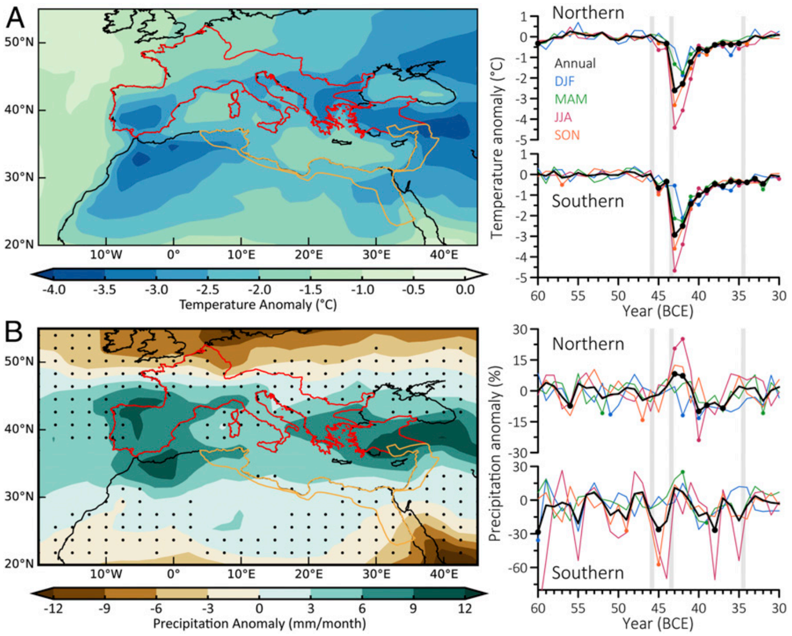

Fig. 4. Volcanically forced temperature and precipitation anomalies in the Mediterranean region from 60 to 30 BCE. (*A*) CESM-simulated average annual temperature and (*B*) precipitation anomalies for 43 and 42 BCE, with outlines of Roman provinces north (red) and south (orange) of the Mediterranean. Dots show areas where annual anomalies are not significant (2σ) relative to the 60 to 46 BCE background variability with no volcanic forcing. Also shown are time series of simulated annual and seasonal temperature and precipitation anomalies for northern and southern Roman provinces. Years with symbols are significant (2σ) relative to the background variability. Gray bars show dates of ice core–based volcanic sulfur injections (32) in the simulations, including the early 43 BCE Okmok II eruption.

uncertain. Plutarch's *Life of Brutus* (25.2–4) mentioned that on his way to Epidamnus (modern Durrës, Albania), Brutus marched in late 44 BCE through snowstorms and that he and his army suffered from boulimia, a disease brought on by fatigue, damp, and cold weather. Cicero, writing to Atticus in November 44 BCE, referred to stormy weather (*Att*. 16.11). Two additional letters of Cicero in February 43 BCE (*Ad Fam*. 9.24.3 and 12.5.2) refer to winter and cold (after the early 43 BCE Okmok II eruption indicated in the ice core records), and in a less precisely dated passage, Josephus (*Jewish Antiquities* 14.310) wrote of Antonius in the winter of 43/42 BCE, telling Hyrcanus about the severely cold climate of Macedonia (3).

More significant in registering the onset of major societal stress is a group of sources referring to famine in northern Italy in April 43 BCE and northern Greece in October 42 BCE, as well as additional reports of famine, food shortages, endemic disease, and civil unrest in Rome and other parts of Italy starting in 43 BCE and extending through 36 BCE (31). Plutarch in his *Life of Antony* (17.3) wrote that the greatest of the various hardships faced by Antony and his army in flight after their defeat at Mutina in April 43 BCE was famine, the army being reduced to eating wild fruit, roots, bark, and animals "never tasted before by men." Julius Obsequens (69) said that in 43 BCE a voice was heard at the oracle of Apollo (in Delphi, presumably), crying "madness of wolves in the winter; in the summer the grain is not harvested." The historian Appian said that there was also famine around the time of the Battle of Philippi, in October 42 BCE, as "Thessaly was no longer able to furnish enough supplies" (*Bellum Civile* 4.122), and later he said that Rome was "devastated by famine" (*Bellum Civile* 5.25) (3). While such hardships probably spring in part from conflict and political turmoil, our evidence now suggests an additional strong environmental context.

The CESM simulations suggest that the Okmok II eruption in early 43 BCE resulted in 0.7 to 7.4 °C seasonal cooling in specific regions of southern Europe and northern Africa, with cooling especially pronounced during summer and autumn (*SI Appendix*, Figs. S8 and S9). Although precipitation is often difficult to simulate accurately, model results also suggest that summer precipitation was 50 to 120% above normal throughout southern Europe and autumn precipitation was up to 400% percent of normal for specific regions, where normal is the average precipitation during the 60 to 46 BCE period with no volcanic forcing.

Other evidence for famine during this period comes from Egypt (3). Linkages between the agriculturally critical annual Nile River floods and political instability are well established (33–35), and particularly severe shocks to the Nile flood in the late 40s BCE are documented. The Okmok II eruption probably compounded the natural interannual variability of the Nile flood. Concomitant food shocks and the outbreak of disease are suggested in historical sources for the same years. Modern authorities agree that there were two famines in Egypt during the reign of Cleopatra, one of them occurring ca. 43 to 42 BCE. Seneca (*NQ* 4A.2.16) wrote that for two successive years, the 10th and 11th of Cleopatra's reign (43 and 42 BCE), the Nile did not flood. Appian seemed to confirm this, saying that in 43 BCE, Cleopatra declined to provide aid to Cassius on the grounds that Egypt was wracked by famine and pestilence (*Bellum Civile* 4.61), again (4.63) that Egypt was devastated by famine, and that around the time of the Battle of Philippi in October 42 BCE, Octavian and Antony could not obtain grain supplies from Egypt because "the country was exhausted by famine" (4.108). Although Seneca and Appian were writing one and two centuries after the events, respectively, their testimony is corroborated by a contemporary inscription from Thebes in southern Egypt (*OGIS* 194; TM 6325). This honors the local governor Kallimachos for his assistance in a time of dearth that clearly lasted more than a year. The text probably dates to 39 BCE (year 13 of Cleopatra's reign) but referred to the continuing famine and social distress of the late 40s BCE.

The CESM simulations suggest sharp cooling from the Okmok II eruption in the lower reaches of the Nile River basin in spring, summer, and autumn, with little or no temperature change in the upper reaches (*SI Appendix*, Figs. S8 and S9). The headwaters of the Blue Nile (and Atbara River) in the Ethiopian Highlands are the source of over 85% (36) of the annual Nile River floodwater, and connections are well described between explosive volcanism and the East African monsoon (33, 37) that is responsible for much of the summer precipitation in the Highlands. The CESM simulations presented here suggest generally wetter winter conditions in the lower reaches of the Nile and substantially drier winter, spring, and especially autumn conditions in the upper reaches, including the Blue Nile headwaters. Simulated summer precipitation in the Blue Nile headwaters, however, is unchanged or slightly higher as a result of the eruption.

The unusual atmospheric phenomena reported in Roman historical accounts in 44 BCE provide reasonable evidence for the presence of an aerosol veil in that year. We suggest that this probably was the result of the comparatively minor but local Mediterranean VEI 3 eruption of Mount Etna that year (2). Well-dated Arctic ice core records of volcanic fallout provide clear evidence suggesting a massive eruption of Alaska's Okmok volcano in early 43 BCE, thereby disassociating this eruption with the preceding aerosol veil based upon the best available documentary and ice core chronologies. This fallout coincided with a pronounced 2 y or longer period of much colder NH temperatures documented by climate proxy records and supported by Earth system climate modeling, with simulations also suggesting substantial changes in precipitation. In the Mediterranean region, these wet and extremely cold conditions during the agriculturally important spring through autumn seasons probably reduced crop yields starting in early 43 BCE and extending at least to early 41 BCE, compounding supply problems wrought by the ongoing political upheavals of the period. That this, indeed, occurred is known from reporting of widespread food shortages and famine in the Roman provinces and Ptolemaic Kingdom.

Natural disasters are known historically to create a "state of exception" in which business as usual becomes unfeasible and political and cultural norms are suspended, thereby providing room for rapid social and political change (38). While it is difficult to establish direct causal linkages, we thus postulate that this extreme climate shock—among the most severe of the past 2,500 y—contributed to reported social unrest and facilitated political change at this important juncture of Western civilization. For example, Sextus Pompeius's naval blockade of Italy from late 43 to 36 BCE cutting off grain supplies from important grain-growing regions in Sicily, Africa, and elsewhere (Appian, *Bellum Civile* 5.15, 18; Dio Cassius, 48.7.4) undoubtedly contributed to reported food shortages in Rome and throughout Roman Italy. Critical local food supplies (39), however, probably were already severely restricted by the extreme weather, and Sextus Pompeius can be seen as opportunistically using these circumstances to enhance political leverage arising from his blockade with constriction of much needed relief supplies. It is similarly challenging to establish direct links between Okmok II and the demise of the long-lasting Ptolemaic dynasty in Egypt, nominally accredited to the death of Cleopatra in 30 BC, following her naval defeat to Rome at the Battle of Actium in 31 BC. There can be little doubt, however, that Rome's interest in Egypt as its famed "breadbasket" was further magnified by the trials of the 40s BCE and that Egypt's own capacity to defend against Rome was diminished by the famine, disease, land abandonment, and reduced state income that followed the Okmok II eruption.

Materials and Methods

Measurements of Volcanic Fallout in Arctic Ice Cores. Detailed elemental, chemical, and other (e.g., dielectric profiling [DEP] and electrical conductivity [ECM] reflecting acidity, laser light scattering [LLS] reflecting volcanic tephra) ice core records reflecting volcanic fallout were evaluated for this study, with particular focus on the period from 50 to 30 BCE. Included were five Greenland ice cores [NGRIP2 (7): 75.1 °N, 42.3 °W; NEEM (40): 77.5 °N, 51.1 °W; GISP2 (9): 72.6 °N, 38.5 °W; GRIP (41): 72.6 °N, 37.6 °W; Dye3 (16): 65.18 °N, 43.49 °W] and one Russian Arctic [Akademii Nauk (AN) (42): 80.5 °N, 94.8 °E] core. Note that because of uncertainties in ice core chronologies between polar regions, an ~47 (±5) BCE volcanic fallout (nssS) event in Antarctica (5) cannot be attributed conclusively to Okmok II.

Ice core records of volcanic fallout included high depth resolution measurements of nssS and liquid conductivity in NGRIP2 (this study), NEEM (5, 40), and AN (this study), as well as size-resolved insoluble particle counts in NGRIP2 (this study) (*SI Appendix*, Fig. S1). Measurements were made with the unique continuous ice core analytical system at DRI using methods described elsewhere (19, 43). Additional ice core records included previously published, high depth resolution measurements of 1) DEP in NGRIP2 (44), NEEM (44), and GRIP (41); 2) ECM in GISP2 (45) and Dye3 (16); and 3) LLS in GISP2 (13). Note that the independently measured DEP records in NGRIP2 and NEEM were consistent with the continuous nssS and liquid conductivity measurements at DRI (*SI Appendix*, Fig. S1). We also evaluated discrete, 2 y sulfate concentration measurements in GISP2 (9). Measurement techniques used to develop these previously published records were described elsewhere (13, 16, 41, 44, 45).

DRI_NGRIP2 Ice Core Chronology. To enable comparisons between ice core volcanic fallout records, climate proxy information, and historical events, we used the precise DRI_NGRIP2 ice core chronology and synchronized all of the ice core records to that chronology. Development of the NGRIP2 chronology was described previously (7). Briefly, we used high depth resolution DRI measurements on the NGRIP2 core for multiparameter annual layer counting (*SI Appendix*, Fig. S2). Because the continuous DRI measurements began at 159.56 m, corresponding to ~1270 CE, annual layer counting started at unambiguous nssS fallout from the eruption of Samalas in 1257 CE (7). Evaluation of this independent chronology against well-established tree ring–based chronologies using multiannual (46) variations in cosmogenic nuclides (^{10}Be in ice, ^{14}C in wood) suggested uncertainty of less than ±2 y during antiquity. In addition, pronounced, short-lived cosmogenic nuclide increases in 994 CE and 775 CE recorded in both tree and ice core records (5) showed no offsets, indicating exact synchronization with the tree-based climate proxies at these specific dates (7). Moreover, recent evaluation of the DRI_NGRIP2 chronology using a newly discovered, short-lived cosmogenic nuclide event in the first millennium BCE (47) also showed no offset at 661 BCE (2,610 ybp). Comparisons to the published NS1-2011 chronology (5) based largely on similar continuous DRI measurements in the 411 m NEEM-2011-S1 intermediate core and 390.5 to 573.65 m in the NEEM bedrock core showed only minor differences (typically, ±2 y), well within the uncertainties of the published NS1-2011 chronology. For example, fallout from the massive 43 BCE eruption using the DRI_NGRIP2 chronology occurred 1 y earlier in 44 BCE using the NS1-2011 chronology.

Fallout measurements in all six Arctic ice cores (Fig. 1 and *SI Appendix*, Fig. S1) were synchronized at 43 BCE to allow comparisons. For NEEM, measurements on the NS1-2011 chronology were shifted by 1 y to align the 43 BCE event and an annual layer between 44 and 46 BCE on the original NS1-2011 deleted to align the 45 BCE event. Note that because of missing measurements, this annual layer was interpolated during development of the NS1-2011 chronology. For AN, pervasive surface melting and high marine biogenic inputs from the surrounding ocean made identification of volcanic sulfur spikes difficult. Acidity and nssS measurements were mapped to an existing chronology based primarily on tie points between heavy-metal concentrations in AN and the well-dated NGRIP2 record as previously described (8) and then shifted by ~2 y in this study to align the records at the start of the 43 BCE volcanic event. For GISP2, GRIP, and Dye3, measurements were mapped to the GICC05 timescale (48) and then compared to the NGRIP2 fallout record. Consistent with previous studies (5, 46), records on the GICC05 timescale (48) required a shift of ~10 y to align with the DRI_NGRIP2 chronology at the start of the 43 BCE event.

The speleothem-based summer temperature reconstruction from Shihua Cave (12), China, was shifted by 2.5 y to synchronize at 43 BCE to be consistent with NH tree ring–based climate proxies and the ice core fallout records on the DRI_NGRIP2 chronology (Fig. 2). This shift was well within the 5 y maximum counting error for the original speleothem chronology (12).

Tephra Analyses. To determine the provenance of the fallout, we obtained a sample of archived GISP2 ice (481.06 to 481.16 m) from the National Science Foundation Ice Core Facility (NSF-ICF) corresponding to the LLS spike at the start of the 43 BCE event (Fig. 2 and *SI Appendix*, Fig. S3). The sample (QUB-1991) was melted and analyzed for tephra at Queen's University Belfast. The sample was centrifuged to concentrate particulates and decanted, and the residue was transferred using plastic pipettes to a preground, labeled glass slide on a hot plate within a laminar flow bench and, when dry, covered in Buehler EpoxiCure 2 resin. The sample was scanned on a polarizing light microscope, and tephra shards were counted and recorded. A total of 35 shards was identified (*SI Appendix*, Fig. S4), consisting of small (long axis mean of 23 μm [ranging from 12 to 46 μm]), pale brown to brown, angular to subrounded glass (Fig. 3 and *SI Appendix*, Fig. S5), with variable microlite content. The slide was then ground and polished to expose the surfaces of the tephra shards for geochemical analyses. Major element geochemistry was determined using combined electron and wavelength dispersive spectrometry on a JEOL FEGSEM 6500F, with secondary glass standards analyzed in the same sessions to ensure acceptable operating conditions. Eleven major and minor elements were analyzed, following parameters previously outlined (49). Geochemical similarity to glass from the Okmok II caldera-forming eruption prompted analysis of reference glass from this event (*SI Appendix*, Fig. S5). Samples of lapilli (16JFLOK001F) and scoria (16JFLOK006A) from the eastern flank of Okmok corresponding to the second and third phases of the Okmok II event were ground, sieved, and prepared as thin sections on a glass slide for geochemical analysis on the JEOL FEGSEM 6500F under the same conditions as QUB-1991. All measurements were normalized to 100% to allow for water content.

Sulfur Isotope Analyses. GISP2 meltwater samples from 481.0 to 481.24 m were dried down, and the sulfate was isolated by column chemistry following established procedures (14). Sample sizes were small, with total sulfate ranging from 5 to 20 nmol. After purification, triple sulfur isotope (^{32}S, ^{33}S, ^{34}S) measurements were made by multicollector inductively coupled plasma mass spectrometry at the St Andrews Isotope Geochemistry laboratory at the University of St Andrews (14). Δ^{33}S values were calculated relative to the standard Vienna-Canyon Diablo Troilite (VCDT) as $\Delta^{33}S = \delta^{33}S + 1 - (\delta^{34}S + 1)^{0.515}$, where $\delta^{x}S = (^{x}S/^{32}S)_{sample}/(^{x}S/^{32}S)_{VCDT} - 1$, with x being either 33 or 34. Because of the small samples sizes, 1σ uncertainties on Δ^{33}S ranged from 0.06 to 0.15‰ (*SI Appendix*, Fig. S3), slightly larger than previously reported uncertainties of 0.05‰ (14).

Earth System Model Simulations. We used CESM (version 1.2.2) (28) to evaluate the impact of the volcanic eruptions on NH climate. The model consists of coupled components for the atmosphere, ocean, land, and sea ice and is run in 2° × 2° horizontal resolution in the atmosphere/land and 1° × 1° horizontal resolution in the ocean/sea ice. The vertical resolution of the atmosphere and ocean are 31 and 61 levels, respectively. A transient simulation started in year 1501 BCE was driven by orbital, solar (50), and greenhouse gas (51) forcing, as well as volcanic forcing. In 60 BCE, the transient simulation was branched to perform an ensemble of 10 CESM1.2.2 simulations. Small disturbances were introduced in the atmosphere at the first time step and run until 30 BCE with the prescribed volcanic forcing that included three NH eruptions in 45 BCE, 43 BCE (Okmok II), and 34 BCE.

Stratospheric volcanic sulfur injection estimates for the three eruptions between 60 and 30 BCE were taken from the eVolv2k database (32), which is based on quantification of Antarctic and Greenland sulfate depositional fluxes using bipolar ice core arrays. The eruption years were shifted by 1 y to align with the DRI_NGRIP2 chronology, and the default source locations from the eVolv2k database were adjusted to 64 °N (i.e., Iceland) for the 45 BCE eruption and to 54.4 °N for the Okmok eruption in 43 BCE. We also used an eruption date of January 1 based on a short time lag between the Okmok eruption and initial volcanic fallout in Greenland that started in early 43 BCE. Using the Easy Volcanic Aerosol (EVA) forcing generator (52) and volcanic sulfur injection from eVolv2k, we generated global aerosol distributions and the evolution of extratropical stratospheric aerosol optical depth at 550 nm. The space–time distribution of sulfate generated by EVA was converted to volcanic aerosol mass to be readable by CESM. Modifications to the prescribed aerosol distribution included 1) shifting peak sulfate injection in the stratosphere following (52) so that the atmospheric sulfate burden increased linearly until the fourth month after the eruption and then decreased exponentially according to the EVA model and 2) increasing the volcanic aerosol mass by 45% to reconcile CESM and EVA optical depths following (53) but using the 1991 Pinatubo eruption as a reference.

The model output consisted of monthly means that were combined to form a 10-ensemble average for evaluation of the volcanic climate effects.

We calculated annual and seasonal (December to February [DJF], March to May [MAM], June to August [JJA], and September to November [SON]) anomalies from the monthly ensemble means after removing the seasonal variability, with the anomalies relative to the 60 through 46 BCE background period with no volcanic forcing. We used a Student's t test (5% significance level or 2σ) to determine the significance of the anomalies relative to background variability during the reference period.

Data Availability. All high-resolution ice core measurements presented in this study are provided in Dataset S1. Tephra geochemistry measurements are provided in Dataset S2.

ACKNOWLEDGMENTS. National Science Foundation Grants 1925417, 1023672, and 0909541 to J.R.M. and 1824770 to J.G.M. and F.L. funded this research, in addition to support to A.I.W. and J.R.M. from the John Fell Oxford University Press (OUP) Research Fund and All Souls College, Oxford. Clare Hall, Cambridge, provided additional support to J.R.M. through the Sir Nicholas Shackleton Fellowship. F.L. also acknowledges support from an Irish Research Council Laureate Award (Climates of Conflict in Ancient Babylonia project, Award IRCLA/2017/303). Swiss National Science Foundation Grant 18001 funded C.C.R. and W.M.K. European Research Council Grant 820047 under the European Union's Horizon 2020 research and innovation program supported M.S. Marie Curie Career Integration Grant CIG14-631752 supported A.B. This work also benefitted from participation by some authors in the Past Global Changes Volcanic Impacts on Climate and Society working group. We thank the NGRIP and NEEM communities, M. Twickler, and the NSF-ICF for providing access to GISP2 samples, as well as students and staff in the DRI ice core group for assistance in the laboratory. R. Kreidberg provided editorial advice.

1. J. Ramsey, A. Licht, *The Comet of 44 B.C. and Caesar's Funeral Games*, D. Blank, Ed. (American Philological Association, Scholars Press, Atlanta, GA, 1997).
2. R. Stothers, M. Rampino, Volcanic eruptions in the Mediterranean before A.D. 630 from written and archaeological sources. *J. Geophys. Res.* **88**, 6357–6371 (1983).
3. P. Forsyth, In the wake of Etna, 44 B.C. *Class. Antiq.* **7**, 49–57 (1988).
4. D. Thompson, Cleopatra queen of Egypt. *Ancient Hist.* **17**, 11–15 (2018).
5. M. Sigl *et al*., Timing and climate forcing of volcanic eruptions for the past 2,500 years. *Nature* **523**, 543–549 (2015).
6. J. Luterbacher *et al*., European summer temperatures since Roman times. *Environ. Res. Lett.* **11**, 24001 (2016).
7. J. R. McConnell *et al*., Lead pollution recorded in Greenland ice indicates European emissions tracked plagues, wars, and imperial expansion during antiquity. *Proc. Natl. Acad. Sci. U.S.A.* **115**, 5726–5731 (2018).
8. J. R. McConnell *et al*., Pervasive Arctic lead pollution suggests substantial growth in medieval silver production modulated by plague, climate, and conflict. *Proc. Natl. Acad. Sci. U.S.A.* **116**, 14910–14915 (2019).
9. G. A. Zielinski *et al*., Record of volcanism since 7000 B.C. from the GISP2 Greenland ice core and implications for the volcano-climate system. *Science* **264**, 948–952 (1994).
10. K. Harper, In the shadow of Caesar. *Lapham's Q.* **12**, 210–217 (2019).
11. V. LaMarche, K. Hirschboeck, Frost rings in trees as records of major volcanic eruptions. *Nature* **307**, 121–126 (1984).
12. M. Tan *et al*., Cyclic rapid warming on centennial-scale revealed by a 2650-year stalagmite record of warm season temperature. *Geophys. Res. Lett.* **30**, 1617 (2003).
13. M. Ram, G. Koenig, Continuous dust concentration profile of pre-Holocene ice from the Greenland ice sheet project 2 ice core: Dust stadials, interstadials, and the Eemian. *J. Geophys. Res. Oceans* **102**, 26641–26648 (1997).
14. A. Burke *et al*., Stratospheric eruptions from tropical and extra-tropical volcanoes constrained using high-resolution sulfur isotopes in ice cores. *Earth Planet. Sci. Lett.* **521**, 113–119 (2019).
15. G. Zielinski, G. Mershon, Paleoenvironmental implications of the insoluble microparticle record in the GISP2 (Greenland) ice core during the rapidly changing climate of the Pleistocene-Holocene transition. *Geol. Soc. Am. Bull.* **109**, 547–559 (1997).
16. H. Clausen *et al*., A comparison of the volcanic records over the past 4000 years from the Greenland ice core project and Dye 3 Greenland ice cores. *J. Geophys. Res. Oceans* **102**, 26707–26723 (1997).
17. C. Plummer *et al*., An independently dated 2000-yr volcanic record from Law Dome, East Antarctica, including a new perspective on the dating of the 1450s CE eruption of Kuwae, Vanuatu. *Clim. Past* **8**, 1929–1940 (2012).
18. N. W. Dunbar *et al*., New Zealand supereruption provides time marker for the Last Glacial Maximum in Antarctica. *Sci. Rep.* **7**, 12238 (2017).
19. J. R. McConnell *et al*., Synchronous volcanic eruptions and abrupt climate change ∼17.7 ka plausibly linked by stratospheric ozone depletion. *Proc. Natl. Acad. Sci. U.S.A.* **114**, 10035–10040 (2017).
20. J. Larsen, C. Neal, J. Schaefer, J. Biget, C. Nye, *Late Pleistocene and Holocene Caldera-Forming Eruptions of Okmok Caldera, Aleutian Islands, Alaska*. **172**, 343–364 (2007).
21. L. Sadori, B. Narcisi, The Postglacial record of environmental history from Lago di Pergusa, Sicily. *Holocene* **11**, 655–671 (2001).
22. H. Vogel, G. Zanchetta, R. Sulpizio, B. Wagner, N. Nowaczyk, A tephrostratigraphic record for the last glacial-interglacial cycle from Lake Ohrid, Albania and Macedonia. *J. Quat. Sci.* **25**, 320–338 (2010).
23. S. Kutterolf *et al*., Pacific offshore record of plinian arc volcanism in Central America: 1. Along-arc correlations. *Geochem. Geophys. Geosyst.* **9**, Q02S01 (2008).
24. S. Kutterolf, A. Freundt, C. Burkert, Eruptive history and magmatic evolution of the 1.9 kyr plinian dacitic Chiltepe tephra from Apoyeque volcano in west-central Nicaragua. *Bull. Volcanol.* **73**, 811–831 (2011).
25. K. Barber, P. Langdon, A. Blundell, Dating the Glen Garry tephra: A widespread late-Holocene marker horizon in the peatlands of northern Britain. *Holocene* **18**, 31–43 (2008).
26. S. Preece *et al*., Chemical complexity and source of the White River Ash, Alaska and Yukon. *Geosphere* **10**, 1020–1042 (2014).
27. S. Wastegård, H. Johansson, J. Pacheco, New major element analyses of proximal tephras from the Azores and suggested correlations with cryptotephras in northwest Europe. *J. Quat. Sci.* **35**, 114–121 (2020).
28. J. Hurrell *et al*., The Community Earth System Model: A framework for collaborative research. *Bull. Am. Meteorol. Soc.* **94**, 1339–1360 (2013).
29. J. Esper, E. Duthorn, P. Krusic, M. Timonen, U. Buntgen, Northern European summer temperature variations over the Common Era from integrated tree-ring density records. *J. Quat. Sci.* **29**, 487–494 (2014).
30. D. Zhang, *A Compendium of Chinese Meteorological Records of the Last 3,000 Years*, (Jiangsu Education Publishing House, Nanjing, China, 2004).
31. P. Garnsey, *Famine and Food Supply in the Graecco-Roman World: Responses to Risk and Crisis*, (Cambridge University Press, Cambridge, UK, 1988).
32. M. Toohey, M. Sigl, Volcanic stratospheric sulfur injections and aerosol optical depth from 500 BCE to 1900 CE. *Earth Syst. Sci. Data* **9**, 809–831 (2017).
33. L. Oman, A. Robock, G. Stenchikov, T. Thordarson, High-latitude eruptions cast shadow over the African monsoon and the flow of the Nile. *Geophys. Res. Lett.* **33**, L18711 (2006).
34. J. G. Manning *et al*., Volcanic suppression of Nile summer flooding triggers revolt and constrains interstate conflict in ancient Egypt. *Nat. Commun.* **8**, 900 (2017).
35. E. Chaney, Revolt on the Nile: Economic shocks, religion, and political power. *Econometrica* **81**, 2033–2053 (2013).
36. A. M. Melesse, S. Bekele, P. McCormick, "Introduction: Hydrology of the Niles in the face of climate and land-use dynamics" in *Nile River Basin: Hydrology, Climate and Water Use*, A. M. Melesse, Ed. (Springer, Berlin, 2011), pp. vii–xvii.
37. C. Colose, A. LeGrande, M. Vuille, Hemispherically asymmetric volcanic forcing of tropical hydroclimate during the last millennium. *Earth Syst. Dyn.* **7**, 681–696 (2016).
38. M. R. Dove, *Anthropology of Climate Change: An Historical Reader*, (Wiley & Sons, Chichester, UK, 2014).
39. P. Erdkamp, *The Grain Market in the Roman Empire*, (Cambridge University Press, Cambridge, UK, 2005).
40. M. Sigl *et al*., A new bipolar ice core record of volcanism from WAIS Divide and NEEM and implications for climate forcing of the last 2000 years. *J. Geophys. Res. D Atmospheres* **118**, 1151–1169 (2013).
41. E. Wolff, J. Moore, H. Clausen, C. Hammer, Climatic implications of background acidity and other chemistry derived from electrical studies of the Greenland Ice Core Project ice core. *J. Geophys. Res. Oceans* **102**, 26325–26332 (1997).
42. T. Opel, D. Fritzsche, H. Meyer, Eurasian Arctic climate over the past millennium as recorded in the Akademii Nauk ice core (Severnaya Zemlya). *Clim. Past* **9**, 2379–2389 (2013).
43. J. R. McConnell, G. W. Lamorey, S. W. Lambert, K. C. Taylor, Continuous ice-core chemical analyses using inductively coupled plasma mass spectrometry. *Environ. Sci. Technol.* **36**, 7–11 (2002).
44. S. Mojtabavi *et al*., A first chronology for the East GReenland Ice-core Project (EGRIP) over the Holocene and last glacial termination. *Clim. Past Discuss.*, 10.5194/cp-2019-143 (2019).
45. K. Taylor, R. Alley, G. Lamorey, P. Mayewski, Electrical measurements on the Greenland ice Sheet project 2 core. *J. Geophys. Res. Oceans* **102**, 26511–26517 (1997).
46. F. Adolphi, R. Muscheler, Synchronizing the Greenland ice core and radiocarbon timescales over the Holocene – Bayesian wiggle-matching of cosmogenic radionuclide records. *Clim. Past* **12**, 15–30 (2016).
47. P. O'Hare *et al*.; ASTER Team, Multiradionuclide evidence for an extreme solar proton event around 2,610 B.P. (∼660 BC). *Proc. Natl. Acad. Sci. U.S.A.* **116**, 5961–5966 (2019).
48. I. Seierstad *et al*., Consistently dated records from the Greenland GRIP, GISP2 and NGRIP ice cores for the past 104 ka reveal regional millennial-scale delta O-18 gradients with possible Heinrich event imprint. *Quat. Sci. Rev.* **106**, 29–46 (2014).
49. S. Coulter *et al*., Holocene tephras highlight complexity of volcanic signals in Greenland ice cores. *J. Geophys. Res. D Atmos.* **117**, D21303 (2012).
50. G. Schmidt *et al*., Climate forcing reconstructions for use in PMIP simulations of the last millennium (v1.1). *Geosci. Model Dev.* **5**, 185–191 (2012).
51. F. Joos, R. Spahni, Rates of change in natural and anthropogenic radiative forcing over the past 20,000 years. *Proc. Natl. Acad. Sci. U.S.A.* **105**, 1425–1430 (2008).
52. C. Gao, A. Robock, C. Ammann, Volcanic forcing of climate over the past 1500 years: An improved ice core-based index for climate models. *J. Geophys. Res. D Atmos.* **113**, D23111 (2008).
53. Y. Zhong, A. Jahn, G. Miller, A. Geirsdottir, Asymmetric cooling of the Atlantic and Pacific Arctic during the past two millennia: A dual observation-modeling study. *Geophys. Res. Lett.* **45**, 12497–12505 (2018).

Chapter 6

Outlook and General Conclusion

This thesis offers insights into the variability and drivers of droughts in the Mediterranean region and extreme precipitation on the globe for the period 1501 BCE–2099 CE. In addition, the impacts of a large volcanic eruption on the climate and ancient Mediterranean society have been examined. The thesis is mainly based on the simulations performed with the Community Earth System Model (CESM). Additional sources, such as tree-ring-based drought reconstructions and observational records are also used complementing the model simulations. In addition, various statistical methods have been employed for the analysis of droughts and extreme precipitation.

Throughout the thesis, two research questions proposed in the introduction (Chapter 1) are answered:

(i) How do extreme hydrological events (droughts and extreme precipitation) vary over time, and how are they influenced by external and internal processes of the climate system?

The studies based on the CESM simulations indicate that before the Industrial Era, extreme hydrological events, either droughts in the Mediterranean or global extreme precipitation, are influenced by the internal variability of the climate system. Thereby, modes of variability are the principal drivers of past hydrological changes. For persistent Mediterranean droughts, ENSO, NAO, and the soil-atmosphere feedbacks are associated with anomalously dry conditions in the region. The roles of each of these drivers vary with the stages of evolution of droughts, and the soil-atmosphere feedbacks contribute more to the duration of droughts. For extreme precipitation, different modes of variability are associated with the long-term variability of extreme precipitation. The associated modes depend on the region. However, ENSO shows a widespread influence on extreme precipitation across the globe. Besides ENSO, regional temperatures play an important role in the variability of past extreme precipitation.

Among the external forcings, volcanic forcing is the most influential on the variability of extreme hydrological events in the past. Volcanic eruptions exert short-term influences on extreme hydrological events up to a few years. After some large volcanic eruptions, the

Mediterranean region experiences wet conditions. Large volcanic eruptions induce an El Niño-like response in the global pattern of extreme precipitation. It is also noted that the frequency of extreme precipitation is more affected than the intensity of the events.

For Mediterranean droughts, changes in their drivers in the future until 2099 CE are also analyzed under the business-as-usual mitigation scenario (RCP 8.5). Since the Industrial Era, a notable increase in the duration of droughts is detected, and this increase will be exacerbated by the end of the 21^{th} century. The cause of this change is attributed to the strengthened soil-atmosphere feedbacks due to the increase in atmospheric temperatures. The influences of internal variability on droughts are rather diminished in the future scenario.

(ii) How does an external process influence the climate, and what was the implication of this influence on an ancient civilization in Europe?

To answer this research question, the influence of a specific external forcing is considered: the volcanic forcing, particularly the influence of the Okmok eruption in 43 BCE on the climate and ancient Roman society.

The finding of this thesis implies that the 43 BCE Okmok eruption may have contributed to the societal disruptions in the Mediterranean region during the ancient Roman period. Documentary and proxy reconstructions indicate very cold and wet conditions that prevailed over the region after this large eruption. The massive cooling and wetness are also supported by the CESM simulations. This change in the climate possibly caused crop failures and famines that implicated societal unrest.

This investigation highlights the importance of an interdisciplinary approach in climate research. Data from different sources are combined to give a possible explanation of societal changes in the past. Moreover, this finding serves as an example that illustrates the impacts of such an abrupt change in the climate and associated extreme climate conditions on society. The result provides an understanding of societal responses to changes in the climate, a topic which is necessary to be assessed better with the current ongoing anthropogenic warming.

The studies on this thesis are based on various simulations performed with CESM. Hence, it is important to mention that model-dependent internal variability is a known problem for this kind of single-model-based approach. For instance, CESM largely overestimates the severity and frequency of ENSO than the observed values. The implications of this drawback are discussed in the conclusions of each chapter (Chapters 3 and 4). Nevertheless, this model's inherent problem does not affect the overall conclusion of this research about the influences of internal variability and external forcing on extreme hydrological events for the last three millennia and future 100 years.

Our studies provide a new approach to conduct investigations on past extreme climate events using a statistical method based on the extreme value theory and 3500-year-long transient climate simulations. More investigations on temporal and spatial variability of past extreme hydrological events and associated drivers are necessary to improve our understanding of these events. More knowledge on this topic will eventually lead to an improved projection of these events, hence, better preparedness for future changes.

Potential follow-up research can focus on assessing more specific changes in extreme precipitation during the climate periods in the Common Era such as the MCA and LIA. For droughts, spatio-temporal characteristics of the events in other regions still need to be assessed. One important aspect to address is how megadroughts in different regions that occurred during the same period (for instance, the North American and north European MCA megadroughts) were connected and what role the large-scale circulation played during these events. In addition, more multi-model, multi-proxy, and multidisciplinary approaches will be ideal to get a more complete description of past extreme hydrological events.

Appendix A

Systematic Identification of the Drivers of Regional Hydroclimate Variability in Southern Hemispheric Wet Seasons using a Causal Discovery Method

Woon Mi Kim, Christian L. E. Franzke, and Christoph C. Raible

In preparation

A.1 abstract

We analyze the drivers of hydroclimate variability in northeast Brazil and southeast Australia using a causal discovery algorithm (CDA). The CDA-based regression models are also generated to assess the predictive skills of this approach. Hydroclimate variability is quantified using the standardized precipitation index and standardized precipitation evapotranspiration index with different time-scales. The CDA highlights the influences of the tropical Atlantic and tropical Pacific on droughts in northeast Brazil. Droughts in southeast Australia are connected to the tropical Pacific and Southern Annual mode. For drought indices with long time-scales, the indices themselves are involved as drivers of hydroclimate conditions reflecting the persistence of long-lasting wet or dry events. The performance of the CDA-based prediction models increases with the time-scales of drought indices and decreases with the lead times of prediction. Overall, our analysis shows the usefulness of CDA to identify causal links in the regional hydroclimate in the southern Hemisphere.

A.2 Introduction

Drought is an extreme climate event characterized by a progressive depletion of the atmospheric and surface water balance (Dai, 2011). Since the mid 20th century, northeast Brazil and southeast Australia have experienced increases in the frequency and duration of droughts (Gallant et al., 2013; Brito et al., 2018), some with record-breaking multi-year lasting characteristics that caused severe socio-economic impacts (Kiem et al., 2016; Martins et al., 2018; Franzke and Torelló i Sentelles, 2020). Some of the examples are the 2011–2016 drought in northeast Brazil (Marengo et al., 2018) and the Millennium Drought (2001–2009) in southeast Australia (Van Dijk et al., 2013). Although, dry atmospheric conditions and regular occurrence of seasonal droughts are common climatological features in northeast Brazil (Marengo et al., 2017) and southeast Australia (Chiew et al., 2011), the causes of these severe droughts are partially attributed to anthropogenic greenhouse gas emissions (Cai et al., 2014; Field et al., 2014; Marengo et al., 2017).

The rainfall deficits over these regions are strongly connected to large-scale atmospheric and oceanic patterns. Droughts in northeast Brazil, including the 2011-2016 drought, are mainly explained by strong El Niño events (Hastenrath, 2000; Marengo et al., 2017) and a north-south gradient of the tropical Atlantic sea surface temperatures, with the warming in the north and cooling in the south (Hastenrath et al., 1984). Both of these factors induce a northward shift of the Intertropical Convergence Zone (ITCZ), which is an important source of rainfall for the region during the March-June rainy season (Hastenrath, 2006; Marengo et al., 2018).

Changes in rainfall over southeast Australia are connected to many large-scale circulation patterns, such as El Niño Southern Oscillation (ENSO), the Indian Ocean Dipole (IOD), the Southern Annular Mode (SAM) among others. Further, a remote connection to the North Pacific Ocean plays a role in the rainfall variability in southeast Australia (Risbey et al., 2009; Kiem et al., 2016; Risbey et al., 2018). Among all, ENSO is the most influential on rainfall variability in Australia (Risbey et al., 2009; Van Dijk et al., 2013) with El Niño events causing a decrease in rainfall over southern Australia. Besides, a positive phase of SAM is associated with a decrease in precipitation in austral winter and spring, whereas the same phase of SAM leads to an increase in precipitation in the austral summer (Hendon et al., 2007; Risbey et al., 2009). In addition, a positive PDO is associated to a long-term decline in rainfall (Power et al., 1999; Van Dijk et al., 2013), and a frequent absence of negative IOD events (Ummenhofer et al., 2009) or increases in positive IOD (Cai et al., 2009) are noted during the periods with reduced rainfall over the region.

Droughts strongly influence socio-economic conditions of these regions. Hence, assessing natural drivers of droughts are necessary to understand and distinguish their natural and anthropogenically forced mechanisms over these regions. Several statistical methods were developed to predict droughts over these regions. For northeast Brazil, Liu and Juárez (2001) predicted the Normalized Difference Vegetation Index by using ENSO indices and the SST over the tropical Atlantic as predictors in multivariate regression models. Lima and AghaKouchak

(2017) applied the canonical correlation analysis between the Palmer Drought Severity Index and the global SST to detect predictors prior to constructing regression models for the prediction of droughts in Amazonia. For southeast Australia, machine learning techniques are employed to predict the Standardized Precipitation Index (SPI) incorporating several atmospheric circulation patterns as predictors (Deo et al., 2017). Furthermore, a Markov chain model to predict the SPI (Rahmat et al., 2017), the random forest model to predict the Standardized Precipitation Evapotranspiration Index (SPEI; Dikshit et al., 2020) and artificial neural networks to predict the Effective Drought Index (Deo and Şahin, 2015) have been performed.

Here, we propose multivariate regression models based on a causal discovery algorithm (Ebert-Uphoff and Deng, 2012; Runge et al., 2014, 2019) in order to understand wet and dry fluctuations in the Southern Hemisphere. Causal discovery algorithms seek to identify cause–effect relationships among variables in spatial-temporal multivariate datasets (Ebert-Uphoff and Deng, 2012). We use the algorithm presented by Runge et al. (2012) and Runge et al. (2014). This novel approach is used to quantify joint causal links between regional hydroclimate and large-scale circulation patterns at different time lags, and to generate multivariate regression models and evaluate the predictions from these models. In the end, we discuss the usefulness of this method. We focus on the study of the hydroclimate variability during the rainy seasons using two drought indices, SPI and SPEI, in two regions of the Southern Hemisphere, where severe droughts have occurred more frequently in recent decades. These regions are northeast Brazil and southeast Australia.

A.3 Data and Methods

A.3.1 Drought and climate indices

We use two drought indices spanning the period 1957–2016: the SPI (McKee et al., 1993) and SPEI (Vicente-Serrano et al., 2009). The SPI uses only the monthly total precipitation record to identify meteorological droughts. The SPEI incorporates the water balance calculated as the difference between the precipitation and potential evapotranspiration to quantify agricultural droughts associated with depletion of soil moisture. The potential evapotranspiration for the SPEI are derived using the Hargreaves method (Hargreaves and Samani, 1985).

The necessary records to calculate drought indices are obtained from the Climatic Research Unit version 4.04 (CRU; Harris et al., 2020). The indices are calculated taking 1981–2010 as a reference period and for 1-, 3-, and 6-month time scales to characterize short- and long-term dry and wet periods. Therefore, we have in total six indices for the analysis: SPI-1, SPI-3, SPI-6, SPEI-1, SPEI-3, and SPEI-6 (Figs. A.1 and A.2)). The reason of analyzing the two types of drought indices and at different time scales is to assess separately causal parents involved in meteorological and agricultural, and short and long droughts. As droughts present different characteristics depending on their types and duration (Vicente-Serrano et al., 2012;

Tirivarombo et al., 2018), the causal drivers and the predictive skills may also differ.

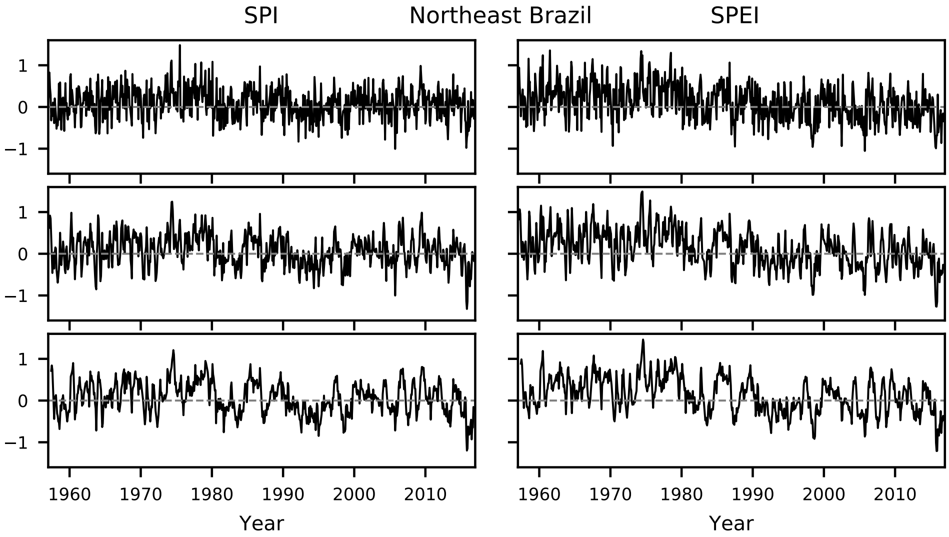

Figure A.1: Monthly SPI (left) and SPEI (right) for northeast Brazil

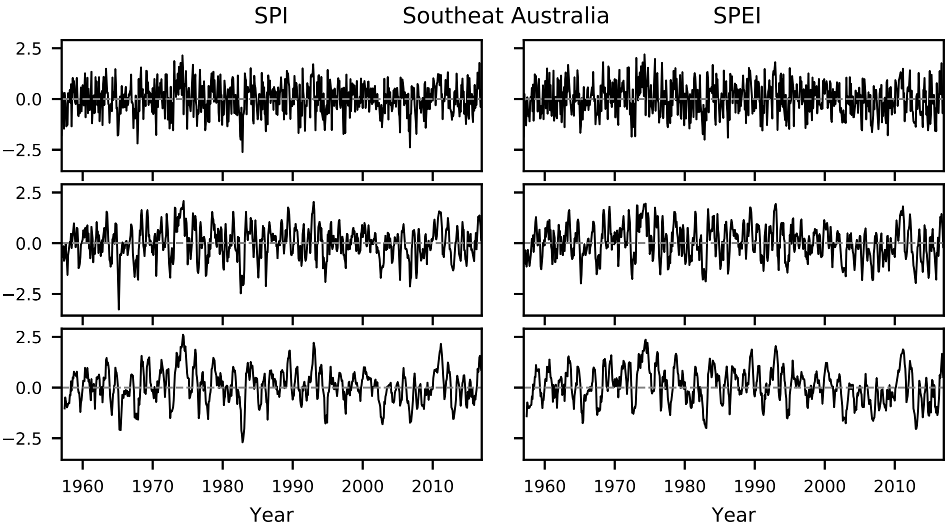

Figure A.2: Monthly SPI (left) and SPEI (right) for southeast Australia

The indices are calculated for each grid point of northeast Brazil, (20°–30°S/ 35°–60°W) and southeast Australia (30°–48°S/ 112°–152°E) (Figure A.3.a and b). Then, they are area-weighted averaged to be transformed to a single time series. When severe droughts occur in these regions, dry conditions extend over a large percentage of the confined areas (up to 83% of northeast Brazil and 94% of southeast Australia; Figure A.3.c). The large percentages of coverage support the use of a single area-weighted time series to illustrate the mean hydroclimate condition of each region.

As potential predictors, we take the nine climate indices listed in Table A.1 (Figs. A.4). All the indices are computed relative to 1981–2010 same as the drought indices. The drought and

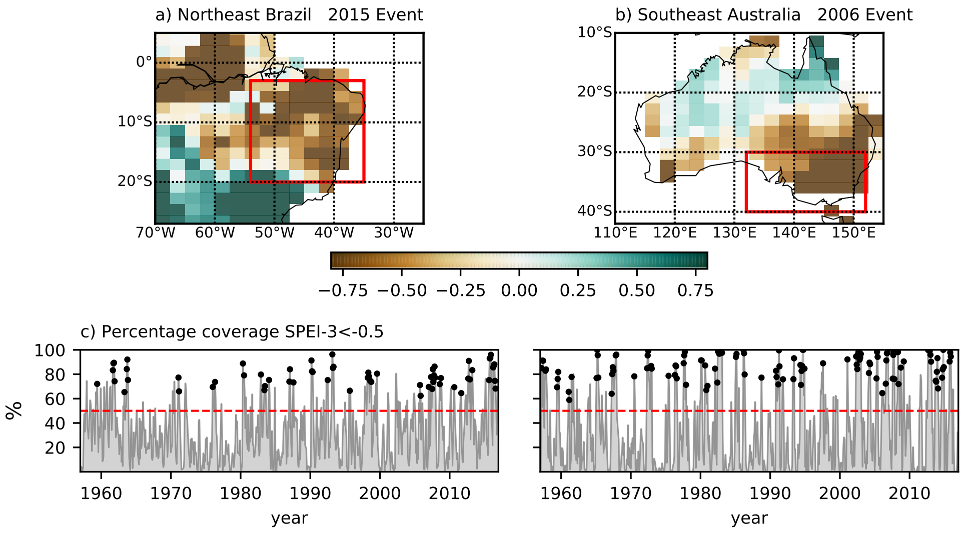

Figure A.3: Mean SPEI-3 during the droughts in (a) northeast Brazil in 2015, and (b) southeast Australia in 2006. The regions of study are marked in red rectangles. (b) Time series of coverage of regions with SPEI-3 below -0.5. Black dots indicates moderate droughts when the SPEI-3 is below -0.8.

Table A.1: Modes of climate variability used for the CDA

Mode of variability	Acronym	Method and region	Reference
Niño 1+2	**NIÑO1+2**	Anomaly of Tropical Pacific SST averaged over 0°-10°S, 90°-°80W	Huang et al. (2017) Trenberth and Stepaniak (2001)
Niño 3	**NIÑO3**	Anomaly of Tropical Pacific SST averaged over 5°N-5°S, 150°W-9°0W	”
Niño 4	**NIÑO4**	Anomaly of Tropical Pacific SST averaged over 5°N-5°S, 160°E-150°W	”
Indian Ocean Dipole	**IOD**	Difference between the averaged Indian Ocean SST over 10°S-10°N, 50°-70°E and 10°-0°S, 90°-110°E	Huang et al. (2017) Saji et al. (1999)
Pacific Decadal Oscillation	**PDO**	First principal component of the EOF in 20°-90°N in the north Pacific SST	Huang et al. (2017) Trenberth and Hurrell (1994)
Pacific South American Pattern 1	**PSA**	Second principal component of the rotated EOF in the 500 millibar height in 0°-90°S. Data from the NCEP/NCAR Reanalysis 1	Kalnay et al. (1996) Mo and Paegle (2001)
Southern Annular Mode	**SAM**	First principal component of the rotated EOF in the 500 millibar height in 0°-90°S. Data from the NCEP/NCAR Reanalysis 1	Kalnay et al. (1996) Marshall (2003)
Tropical North Atlantic	**TNA**	Anomaly of Tropical Atlantic SST averaged over 5.5°-23.5°N, 15°-57.5°W	Enfield et al. (1999) Huang et al. (2017)
Tropical South Atlantic	**TSA**	Anomaly of Tropical Atlantic SST averaged over 0°-20°S, 10°E-30°W	”

climate indices are only used during the wet seasons: for northeast Brazil, the wet season from November through May, and for southeast Australia, summer-autumn season from December through June. The CDA is applied to the wet season time series of each region.

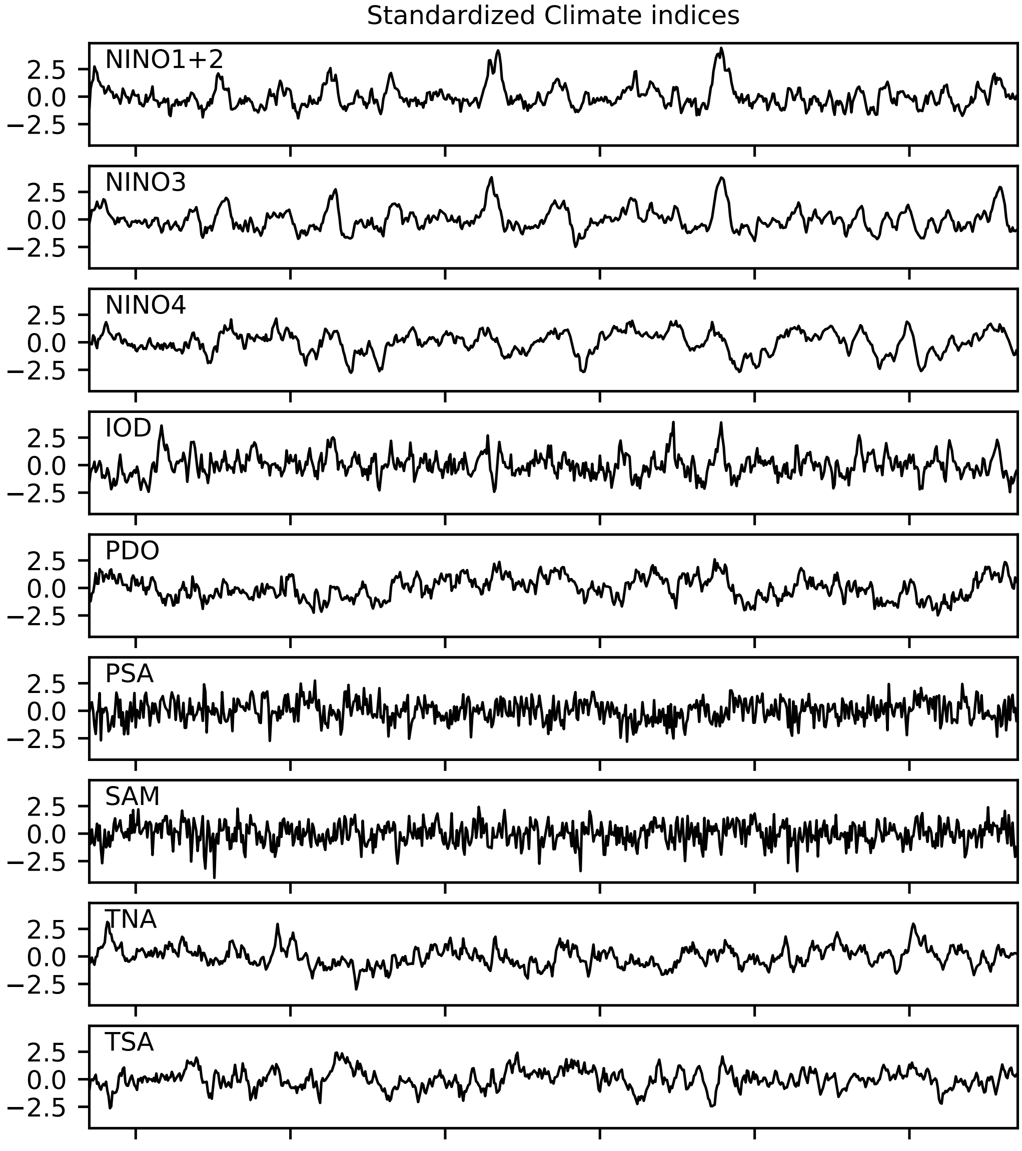

Figure A.4: Monthly standardized climate indices in table A.1 used as predictors in CDA

A.3.2 Causal Discovery Algorithm

The causal discovery algorithm (CDA) involves two main steps (Kretschmer et al., 2016; Runge et al., 2014): in the first step, we select proper causal parents (predictors X; in our study, the climate indices and the drought index itself with a certain time lag τ) that are statistically correlated at the 5% significance level and conditionally independent to the main actor (predictant Y; the drought index at time t). Therefore, a pairwise Pearson correlation (ρ) is calculated between the drought index at time t, Y_t, and an initial candidate predictor $X^i_{t-\tau}$ (Eq. A.1). This is repeated over all possible pairs of the drought index and initial candidate predictors. Then, only the predictors in which the correlations with the drought index are statistically significant at the 5% level are taken as candidate predictors for the next step.

$$C = \rho(Y_t, X^i_{t-\tau}) \quad ; \quad i = 1, \ldots, n \tag{A.1}$$

where n is the number of initial predictors.

Then, the conditional linear dependence is estimated between the drought index (Y_t) at time t and each of the candidate predictors ($X^i_{t-\tau}$) that survived from the previous step via iterative pairwise partial correlations (Eq. A.2) after excluding the effects of a common third driver. Next, the linear influence of a potential common driver from the drought index and a candidate predictor and leaving the residuals of each, and the Pearson correlation is calculated between both remaining residuals. Again, only the predictors which are significantly (at the 5% level) correlated with a drought index remain. This procedure is repeated for all possible pairs.

$$C_P = \rho(Y_t, X^i_{t-\tau} | Y^j_{t-\tau}) \quad ; \quad 1 \leq i, j \leq n \tag{A.2}$$

During this first step, the method attempts to eliminate possible spurious correlations caused by an indirect influence of some common drivers.

In the second step, the m causal parents $X^j_{t-\tau}$ identified in the first step are included in a multivariate linear regression analysis to generate a linear model for the drought index Y_t:

$$Y_t = \sum A_j X^j_{t-\tau} \quad ; \quad 1 \leq j \leq m \tag{A.3}$$

where A_j is the regression coefficient of each $X^j_{t-\tau}$ and quantifies the causal association of $X^j_{t-\tau}$ and Y_t. As we use the normalized variables, the generated regression model does not present any intercept term. Different to the causal discovery algorithm by Runge et al. (2014), we fix the time lag of the predictors at a specified τ. For the next part of the analysis, in which we develop predictive models, we refer to these fixed time lags τ as the lead times of the prediction.

Initially, we apply the CDA for the entire period of 1957–2016 for each region using ten predictors (nine climate indices in the table A.1 and the drought index itself), and with the τ, the time lag, from 1 to 6 months. Then, we examine the resulting regression coefficients to assess the performance of the algorithm to detect and quantify the causal association between drought indices and circulation patterns. Hence in total, we generate 24 regression models.

The predictive skill of the regression models based on CDA are measured using the leave-one-out cross-validation (e.g., Seppä et al., 2004). In this validation, one year in the period 1957–2016 is progressively taken out, while other years are used to generate a regression model to hindcast the drought index of the missing one year. The quality of the validation is further assessed by the root-mean-square-errors (RMSE), coefficient of determinants (R^2) and Brier Skill Scores (González-Rojí et al., 2019, BSS; e.g.,). The hindcast is comparable to the observation when RMSE and BSS is close to 0, and with a better parameter fit when R^2 is close to 1.

Figure A.5: Regression coefficients from the CDA between the drought and climate indices at different time lags for the period 1957–2016 over a) northeast Brazil and b) southeast Australia. Only the coefficients which are statistically significant at the 5% confidence level are shown. INDEX indicates the drought index itself.

A.4 Results

The CDA is applied to the drought and climate indices and the resulting regression coefficients are presented in Figure A.5. There are similarities in causal parents between the drought indices with the same time scale rather than the indices with the same type of drought. Namely, the SPI-1 shares similar causal parents to those of the SPEI-1, the SPI-3 with those of the SPEI-3, and the SPI-6 with those of the SPEI-6. This result indicates that the drivers involved in dry and wet episodes depend more on the duration than the type of drought. Nevertheless, there are still some differences in causal parents between the indices with the same time scale, and more differences are revealed between the SPI-1 and SPEI-1 in northeast Brazil, with the SPI-1 having a higher number of causal parents at longer time lags than the SPEI-1.

The magnitudes of the regression coefficients of the climate indices range between 0.1 to 0.3, while the magnitudes of the regression coefficients of the drought indices included as predictor range between 0.1 to 0.7. The result indicates that when a dry or wet episode lasts for a longer period, the past hydroclimate state plays a more important role than the remote influences of the modes of circulation at determining the current state. This suggests a positive feedback process which is associated with the persistence of long hydroclimate events that become more severe with their duration.

For the modes of climate variability, in northeast Brazil (Figure A.5a), TSA, IOD and some NIÑO indices are involved as causal parents of the drought variability at different time lags. TSA is positively associated with the drought indices at diverse time lags ranging from 2 to 6 months. An increase or a decrease in TSA reflects changes in the north-south gradient of the tropical Atlantic that affects the variability of precipitation over the region, a finding which agrees with previous studies (Hastenrath, 2006; Marengo et al., 2018). In case of NIÑO indices, NIÑO3 in the central and NIÑO1+2 in the east Pacific are negatively connected with the drought indices, indicating that the warming over the Tropical Equatorial Pacific causes more dry situations over northeast Brazil (Curtis and Hastenrath, 1995; Hastenrath, 2000). Both NIÑO1+2 and NIÑO3 show statistically significant links at relatively long time lags from 3 to 6 months, although the time lags of links vary with the drought indices. Unlike other NIÑOs, NIÑO4 presents significant connections with the drought indices at shorter time lags from 1 to 4 months and with a positive sign which is also different to the other two. In addition, both NIÑO4 and NIÑO3 are involved as the drivers of the SPEI-3 and SPEI-6 at 4-month time lag, and the SPI-6 at 3-month time lag, but with opposite signs. In this case, NIÑO4 may offset the influence of NIÑO3 on dry-wet variability of the region. However, NIÑO4 also shows the negative association with the SPI-1 at 5- and 6-month time lags and SPI-3 at 6-month time lag, same as the other NIÑOs. IOD is connected positively with the drought indices, in general, at shorter time lags from 1 to 4 months. A positive link between PDO and the drought indices is also noted for the SPI-3 and SPEI-3, SPI-6 and SPEI-6 at 4- and/or 5-month time lags.

For southern Australia (Figure A.5b), the CDA highlights the dominant roles of the tropical Pacific as the driver of the dry-wet variability. All NIÑO indices are involved as causal parents of all drought indices and in general with negative association at different time lags. This association indicates that the warming over the tropical Pacific increases dry conditions over the region and vice versa for wet condition, which is coherent with previous studies (Risbey et al., 2009; Van Dijk et al., 2013). NIÑO1+2 acts as a driver of drought indices at shorter time lags of 1 and 2 months, while the involvement of NIÑO3 and NIÑO4 are significant from 3 to 6-month time lags. Besides NIÑOs, IOD is negatively connected to the drought indices at 2-month time lags. SAM is positively associated mostly with the drought indices with the time scales of 3 and 6 month at diverse time lags, a result which indicates that a positive SAM during summer drives wet condition over the regions and vice versa (Risbey et al., 2009). The PDO influences inversely the drought indices at the time lags from 2 to 6 months. The PSA shows a negative association with the SPI-6 and SPEI-6 at 6-month, though with opposite sign with the SPI-1 at 5-month time lag.

Weak associations of some indices, such as PSA in northeast Brazil and TSA in southeast Australia, with the drought indices suggest limited influence of these modes of variability on the regional drought conditions of the region, moreover, that these associations might be merely artefacts of the data-driven regression analysis. Lastly, both in northeast Brazil and southeast Australia, when the drought indices themselves are included as predictors of dry-wet fluctuation, the values of their regression coefficients increase with the time scales of drought indices. The SPI-6 and SPEI-6 present statistically significant association with themselves at all time scales and with the highest coefficients, reflecting a strong persistent characteristic of long-lasting dry or wet events.

Overall, the causal links between the climate indices and wet-dry variability of these regions given by the CDA are coherent with the previous findings, which support the reliability of the CDA method. The analysis demonstrates that the causal links of climate indices and dry-wet variability over these regions depend on the duration of droughts and the time lags to determine drivers.

Next, the CDA-based regression models are generated using the climate and drought indices with the lead times from 1 to 6 months, and each drought index is hindcasted for 1957 – 2016 via the leave-one-out cross-validation. The performance skills of the CDA models are quantified through different means (Figure A.6): the RMSE between the climatological means of the observed and hindcasted drought indices, the RMSE between the observed and hindcasted drought indices for 1957–2016, R^2 of the regression models, and the BSS for negative drought indices.

The RMSE resulting from comparing the climatological means of the observed and hindcasted drought indices at different lead times (Figure A.6a) present relatively small values in all 12 months. The reason might be the small magnitudes of multi-year mean drought indices as the time series are normalized relative to the period 1981–2010. However, this also indicates that the hindcasted climatological means from the models do not differ much from those of the observations. Therefore, the models reflect relatively well the mean drought conditions given by the observation during the period 1957–2016.

For all hincasted drought indices, the RMSE exhibit lower values in northeast Brazil than in southeast Australia (Figure A.6b). In northeast Brazil, the RMSE of drought indices generally stays around 0.4, except for the SPI-3 at 1-month lead time and the SPI-1 and SPEI-1 at 5-month lead time which show the RMSE of about 0.5. In southeast Australia, the RMSE range between 0.4 and 0.9. The lower values of RMSE are at the lead times from 1 to 3 months for the SPI-3, SPEI-3 and SPEI-6. The RMSE of the SPI-1 and SPEI-1 exhibit no strong variation with the lead times, with values of 0.7 and 0.8, respectively.

The R^2 (Figure A.6c) that reflect the quality of the regression models, indicate that the CDA-based fits are not appropriate to generate the SPI-1 and SPEI-1 of both regions, exhibiting negative values in northeast Brazil and almost zero values in southeast Australia at all lead times. Nevertheless, the R^2 are positive for other drought indices and show the highest values, which indicates a better fit, for the SPI-6 and SPEI-6. For these cases, the values of R^2 decrease

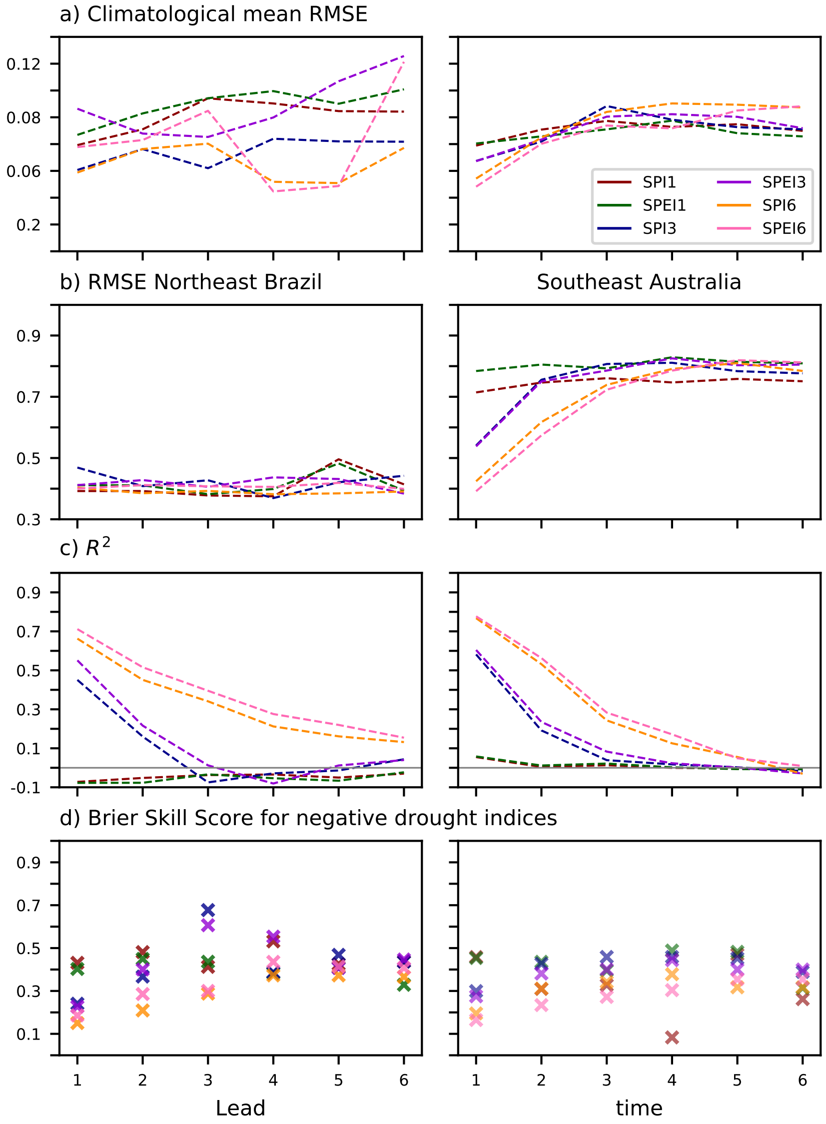

Figure A.6: a) RMSE between the climatological means of the observed and hindcasted drought indices, b) RMSE between the observed and hincasted drought indices for 1957–2016, c) R^2 of the regression models in b), and d) BSS for negative drought indices.

with the lead times.

BSS for dry episodes shows a similar result as for the RMSE (Figure A.6d). Largely, the BSS shows reduced values for the drought indices with the longer time scales, first with 6-, then with 3-month. The BSS also indicates that the performance of the models for dry episodes is better at short lead times of 1- and 2-month, and occasionally of 3-month.

Considering RMSE, R^2 and BSS together, the CDA-based regression models perform well for the drought indices with longer time scales and at shorter lead times. Furthermore, the performance and reliability of the models are good for the SPI-6 and SPEI-6, then for the SPI-3 and SPEI-3.

A.5 Conclusions

We analyzed causal links between drought indices and large-scale circulation patterns during the wet seasons in northeast Brazil and southeast Australia using a causal discovery algorithm (CDA) (Runge et al., 2014, 2019). Using the CDA, time lagged drivers of the regional hydroclimate variability are found and joint links of these drivers with drought indices are quantified.

We found that the CDA correctly detects the circulation patterns related to the hydroclimate variability over these regions, resembling previous findings. In northeast Brazil, the CDA reveals the importance of the tropical Atlantic SST gradient, ENSO, and IOD (Hastenrath, 2006; Marengo et al., 2018). In addition, the PDO is involved in the regional hydroclimate of this region. Droughts in southeast Australia are influenced by ENSO, IOD and SAM (Risbey et al., 2009; Van Dijk et al., 2013; Kiem et al., 2016). For the drought indices with longer time scales, their past information is also involved as drivers of the present hydroclimate conditions. This result reflects the persistent nature of long-lasting dry events indicating that memory effects need to be considered. Overall, drivers of drought indices in these regions depend on the time scale, namely the duration of events, and the considered time lag rather than the type of drought, either meteorological or agricultural.

Moreover, the regression models based on CDA perform better for drought indices with longer time scales, for instance the SPI-6 and SPEI-6 and at shorter lead times up to 3 months. One reason of this performance is related to the delayed responses of the regional hydroclimate to the large-scale climate circulation and to the memory effects.

A caveat of the CDA-based analysis employed in this study is that the causal links are derived assuming linear relationships among variables. Hence, if some variables affect non-linearly the variability of droughts, the CDA is not able to detect this. Nevertheless, the CDA provides a wide range of flexibility in terms of using the initial input data. Its first step to select statistically significant causal variables through direct and iterative pairwise partial correlations allows to detect proper variables which are statistically independent among each other and significantly correlated with the main target variable. This step reduces spurious associations among variables, and avoids subjective criteria at selecting the drivers to quantify a joint association. The method has shown its utility in understanding the causal drivers and their combined effects on dry and wet fluctuation in two drought-prone regions in the southern Hemisphere.

As these regions in the Southern Hemisphere are expected to experience an increase in droughts (Lehner et al., 2017; Naumann et al., 2018), in terms of the frequency and duration, more studies are needed to test and assess the stability of these flexible data-driven statistical models under changing climate conditions, such as future global warming.

References

Brito, S. S. B., Cunha, A. P. M., Cunningham, C., Alvalá, R. C., Marengo, J. A., and Carvalho, M. A.: Frequency, duration and severity of drought in the Semiarid Northeast Brazil region, International Journal of Climatology, 38, 517–529, doi:10.1002/joc.5225, 2018.

Cai, W., Cowan, T., and Raupach, M.: Positive Indian Ocean dipole events precondition southeast Australia bushfires, Geophysical Research Letters, 36, doi:10.1029/2009GL039902, 2009.

Cai, W., Purich, A., Cowan, T., van Rensch, P., and Weller, E.: Did climate change–induced rainfall trends contribute to the Australian Millennium Drought?, Journal of Climate, 27, 3145–3168, doi: 10.1175/JCLI-D-13-00322.1, 2014.

Chiew, F., Young, W., Cai, W., and Teng, J.: Current drought and future hydroclimate projections in southeast Australia and implications for water resources management, Stochastic Environmental Research and Risk Assessment, 25, 601–612, doi:10.1007/s00477-010-0424-x, 2011.

Curtis, S. and Hastenrath, S.: Forcing of anomalous sea surface temperature evolution in the tropical Atlantic during Pacific warm events, Journal of Geophysical Research: Oceans, 100, 15 835–15 847, doi: 10.1029/95JC01502, 1995.

Dai, A.: Drought under global warming: a review, Wiley Interdisciplinary Reviews: Climate Change, 2, 45–65, doi:10.1002/wcc.81, 2011.

Deo, R. C. and Şahin, M.: Application of the extreme learning machine algorithm for the prediction of monthly Effective Drought Index in eastern Australia, Atmospheric Research, 153, 512–525, doi:10.1016/j.atmosres.2014.10.016, 2015.

Deo, R. C., Kisi, O., and Singh, V. P.: Drought forecasting in eastern Australia using multivariate adaptive regression spline, least square support vector machine and M5Tree model, Atmospheric Research, 184, 149–175, doi:10.1016/j.atmosres.2016.10.004, 2017.

Dikshit, A., Pradhan, B., and Alamri, A. M.: Short-term spatio-temporal drought forecasting using random forests model at New South Wales, Australia, Applied Sciences, 10, 4254, doi:10.3390/app10124254, 2020.

Ebert-Uphoff, I. and Deng, Y.: Causal discovery for climate research using graphical models, Journal of Climate, 25, 5648–5665, doi:10.1175/JCLI-D-11-00387.1, 2012.

Enfield, D. B., Mestas-Nuñez, A. M., Mayer, D. A., and Cid-Serrano, L.: How ubiquitous is the dipole relationship in tropical Atlantic sea surface temperatures?, Journal of Geophysical Research: Oceans, 104, 7841–7848, doi:10.1029/1998JC900109, 1999.

Field, C., Barros, V., Dokken, D., K.J., M., M.D., M., T.E., B., M., C., K.L, E., Y.O., E., R.C., G., B., G., E.S., K., A.N., L., S., M., P.R., M., and L.L., W., eds.: Climate change 2014: impacts, adaptation, and vulnerability. Part A: global and sectoral aspects. Contribution of Working Group II to the Fifth Assessment Report of the Intergovernmental Panel on Climate Change., Cambridge University Press, 2014.

Franzke, C. L. and Torelló i Sentelles, H.: Risk of extreme high fatalities due to weather and climate hazards and its connection to large-scale climate variability, Climatic Change, 162, 507–525, 2020.

Gallant, A. J., Reeder, M. J., Risbey, J. S., and Hennessy, K. J.: The characteristics of seasonal-scale droughts in Australia, 1911–2009, International Journal of Climatology, 33, 1658–1672, doi:10.1002/joc.3540, 2013.

González-Rojí, S. J., Wilby, R. L., Sáenz, J., and Ibarra-Berastegi, G.: Harmonized evaluation of daily precipitation downscaled using SDSM and WRF+ WRFDA models over the Iberian Peninsula, Climate Dynamics, 53, 1413–1433, doi:10.1007/s00382-019-04673-9, 2019.

Hargreaves, G. H. and Samani, Z. A.: Reference crop evapotranspiration from temperature, Applied engineering in agriculture, 1, 96–99, 1985.

Harris, I., Osborn, T. J., Jones, P., and Lister, D.: Version 4 of the CRU TS monthly high-resolution gridded multivariate climate dataset, Scientific data, 7, 1–18, doi:10.1038/s41597-020-0453-3, 2020.

Hastenrath, S.: Interannual and longer-term variability of upper air circulation in the northeast Brazil-tropical Atlantic sector, Journal of Geophysical Research: Atmospheres, 105, 7327–7335, doi:10.1029/1999JD901104, 2000.

Hastenrath, S.: Circulation and teleconnection mechanisms of Northeast Brazil droughts, Progress in Oceanography, 70, 407–415, doi:10.1016/j.pocean.2005.07.004, 2006.

Hastenrath, S., Wu, M.-C., and Chu, P.-S.: Towards the monitoring and prediction of north-east Brazil droughts, Quarterly Journal of the Royal Meteorological Society, 110, 411–425, doi:10.1002/qj.49711046407, 1984.

Hendon, H. H., Thompson, D. W., and Wheeler, M. C.: Australian rainfall and surface temperature variations associated with the Southern Hemisphere annular mode, Journal of Climate, 20, 2452–2467, doi:10.1175/JCLI4134.1, 2007.

Huang, B., Thorne, P. W., Banzon, V. F., Boyer, T., Chepurin, G., Lawrimore, J. H., Menne, M. J., Smith, T. M., Vose, R. S., and Zhang, H.-M.: Extended reconstructed sea surface temperature, version 5 (ERSSTv5): upgrades, validations, and intercomparisons, Journal of Climate, 30, 8179–8205, doi:10.1175/JCLI-D-16-0836.1, 2017.

Kalnay, E., Kanamitsu, M., Kistler, R., Collins, W., Deaven, D., Gandin, L., Iredell, M., Saha, S., White, G., Woollen, J., et al.: The NCEP/NCAR 40-year reanalysis project, Bulletin of the American meteorological Society, 77, 437–472, URL `https://doi.org/10.1175/1520-0477(1996)077<0437:TNYRP>2.0.CO;2`, 1996.

Kiem, A. S., Johnson, F., Westra, S., van Dijk, A., Evans, J. P., O'Donnell, A., Rouillard, A., Barr, C., Tyler, J., Thyer, M., et al.: Natural hazards in Australia: droughts, Climatic Change, 139, 37–54, doi:10.1007/s10584-016-1798-7, 2016.

Kretschmer, M., Coumou, D., Donges, J. F., and Runge, J.: Using causal effect networks to analyze different Arctic drivers of midlatitude winter circulation, Journal of Climate, 29, 4069–4081, doi:10.1175/JCLI-D-15-0654.1, 2016.

Lehner, F., Coats, S., Stocker, T. F., Pendergrass, A. G., Sanderson, B. M., Raible, C. C., and Smerdon, J. E.: Projected drought risk in 1.5 C and 2 C warmer climates, Geophysical Research Letters, 44, 7419–7428, doi:10.1002/2017GL074117, 2017.

Lima, C. H. and AghaKouchak, A.: Droughts in Amazonia: spatiotemporal variability, teleconnections, and seasonal predictions, Water Resources Research, 53, 10 824–10 840, doi:10.1002/2016WR020086, 2017.

Liu, W. and Juárez, R. N.: ENSO drought onset prediction in northeast Brazil using NDVI, International Journal of Remote Sensing, 22, 3483–3501, doi:10.1080/01431160010006430, 2001.

Marengo, J. A., Torres, R. R., and Alves, L. M.: Drought in Northeast Brazil—past, present, and future, Theoretical and Applied Climatology, 129, 1189–1200, doi:10.1007/s00704-016-1840-8, 2017.

Marengo, J. A., Alves, L. M., Alvala, R., Cunha, A. P., Brito, S., and Moraes, O. L.: Climatic characteristics of the 2010-2016 drought in the semiarid Northeast Brazil region, Anais da Academia Brasileira de Ciências, 90, 1973–1985, doi:10.1590/0001-3765201720170206, 2018.

Marshall, G. J.: Trends in the Southern Annular Mode from observations and reanalyses, Journal of climate, 16, 4134–4143, doi:10.1175/1520-0442(2003)016⟨4134:TITSAM⟩2.0.CO;2, 2003.

Martins, E. S., Coelho, C. A., Haarsma, R., Otto, F. E., King, A. D., Jan van Oldenborgh, G., Kew, S., Philip, S., Vasconcelos Júnior, F. C., and Cullen, H.: A multimethod attribution analysis of the prolonged Northeast Brazil hydrometeorological drought (2012–16), Bulletin of the American Meteorological Society, 99, S65–S69, doi:10.1175/BAMS-D-17-0102.1, 2018.

McKee, T. B., Doesken, N. J., Kleist, J., et al.: The relationship of drought frequency and duration to time scales, in: Proceedings of the 8th Conference on Applied Climatology, vol. 17, pp. 179–183, American Meteorological Society Boston, MA, 1993.

Mo, K. C. and Paegle, J. N.: The Pacific–South American modes and their downstream effects, International Journal of Climatology: A Journal of the Royal Meteorological Society, 21, 1211–1229, doi:10.1002/joc.685, 2001.

Naumann, G., Alfieri, L., Wyser, K., Mentaschi, L., Betts, R., Carrao, H., Spinoni, J., Vogt, J., and Feyen, L.: Global changes in drought conditions under different levels of warming, Geophysical Research Letters, 45, 3285–3296, doi:10.1002/2017GL076521, 2018.

Power, S., Casey, T., Folland, C., Colman, A., and Mehta, V.: Inter-decadal modulation of the impact of ENSO on Australia, Climate Dynamics, 15, 319–324, 1999.

Rahmat, S. N., Jayasuriya, N., and Bhuiyan, M. A.: Short-term droughts forecast using Markov chain model in Victoria, Australia, Theoretical and Applied Climatology, 129, 445–457, doi:10.1007/s00704-016-1785-y, 2017.

Risbey, J. S., Pook, M. J., McIntosh, P. C., Wheeler, M. C., and Hendon, H. H.: On the remote drivers of rainfall variability in Australia, Monthly Weather Review, 137, 3233–3253, doi:10.1175/2009MWR2861.1, 2009.

Risbey, J. S., O'Kane, T. J., Monselesan, D. P., Franzke, C. L., and Horenko, I.: On the dynamics of austral heat waves, J. Geophys. Res., 123, 38–57, 2018.

Runge, J., Heitzig, J., Petoukhov, V., and Kurths, J.: Escaping the curse of dimensionality in estimating multivariate transfer entropy, Physical review letters, 108, 258 701, doi:10.1103/PhysRevLett.108.258701, 2012.

Runge, J., Petoukhov, V., and Kurths, J.: Quantifying the strength and delay of climatic interactions: The ambiguities of cross correlation and a novel measure based on graphical models, Journal of Climate, 27, 720–739, doi:10.1175/JCLI-D-13-00159.1, 2014.

Runge, J., Bathiany, S., Bollt, E., Camps-Valls, G., Coumou, D., Deyle, E., Glymour, C., Kretschmer, M., Mahecha, M. D., Muñoz-Marí, J., et al.: Inferring causation from time series in Earth system sciences, Nature communications, 10, 1–13, doi:10.1038/s41467-019-10105-3, 2019.

Saji, N., Goswami, B., Vinayachandran, P., and Yamagata, T.: A dipole mode in the tropical Indian Ocean, Nature, 401, 360–363, doi:10.1038/43854, 1999.

Seppä, H., Birks, H., Odland, A., Poska, A., and Veski, S.: A modern pollen–climate calibration set from northern Europe: developing and testing a tool for palaeoclimatological reconstructions, Journal of Biogeography, 31, 251–267, doi:10.1111/j.1365-2699.2004.00923.x, 2004.

Tirivarombo, S., Osupile, D., and Eliasson, P.: Drought monitoring and analysis: standardised precipitation evapotranspiration index (SPEI) and standardised precipitation index (SPI), Physics and Chemistry of the Earth, Parts A/B/C, 106, 1–10, doi:10.1016/j.pce.2018.07.001, 2018.

Trenberth, K. E. and Hurrell, J. W.: Decadal atmosphere-ocean variations in the Pacific, Climate Dynamics, 9, 303–319, doi:10.1007/BF00204745, 1994.

Trenberth, K. E. and Stepaniak, D. P.: Indices of el Niño evolution, Journal of climate, 14, 1697–1701, doi:10.1175/1520-0442(2001)014⟨1697:LIOENO⟩2.0.CO;2, 2001.

Ummenhofer, C. C., England, M. H., McIntosh, P. C., Meyers, G. A., Pook, M. J., Risbey, J. S., Gupta, A. S., and Taschetto, A. S.: What causes southeast Australia's worst droughts?, Geophysical Research Letters, 36, 2009.

Van Dijk, A. I., Beck, H. E., Crosbie, R. S., de Jeu, R. A., Liu, Y. Y., Podger, G. M., Timbal, B., and Viney, N. R.: The Millennium Drought in southeast Australia (2001–2009): Natural and human causes and implications for water resources, ecosystems, economy, and society, Water Resources Research, 49, 1040–1057, doi:10.1002/wrcr.20123, 2013.

Vicente-Serrano, S. M., Beguería, S., and López-Moreno, J. I.: A Multiscalar Drought Index Sensitive to Global Warming: The Standardized Precipitation Evapotranspiration Index, Journal of Climate, 23, 1696–1718, doi:10.1175/2009JCLI2909.1, URL `https://journals.ametsoc.org/doi/full/10.1175/2009JCLI2909.1`, 2009.

Vicente-Serrano, S. M., Beguería, S., Lorenzo-Lacruz, J., Camarero, J. J., López-Moreno, J. I., Azorin-Molina, C., Revuelto, J., Morán-Tejeda, E., and Sanchez-Lorenzo, A.: Performance of drought indices for ecological, agricultural, and hydrological applications, Earth Interactions, 16, 1–27, doi:10.1175/2012EI000434.1, 2012.

Appendix B

Technical setup of CESM 1.2.2 on the Cray XC40

This appendix provides a brief overview of the technical setup and performance of CESM 1.2.2 on a Cray XC40 Piz Daint (table B.1) at the Swiss National Supercomputer Centre in Lugano. CESM 1.2.2 was installed on the Cray XC40 in 2017.

Table B.1: Overview of Cray XC40 (Daint)

Processors	Multi-core Two Intel ® Xeon E5-2695 v4 @ 2.10GHz
Nodes	2 x 18 cores per node
Memory	64/128 GB
Operating System	Cray Linux Environment

CESM was compiled using the intel 19.1.1.217 compiler. In order to choose an optimal number of nodes to run the simulations, some performance tests were carried out by running the 1850 control simulation experiment (B1850C5CN) with various configuration of nodes (table B.2). The total number of nodes depends on the number of tasks allocated to each component in CESM. The B1850C5CN experiment simulates the climate at the 1850 condition and it includes a prognostic carbon-nitrogen cycle. The experiment was run with the horizontal resolutions of 1.9° × 2.5° in the atmosphere and approximately 1° over the ocean. After the tests, the final configuration of task allocation for each component in the CESM was set as shown in table B.3.

Table B.2: Speed-up and wall time with the intel compiler for CESM on XC40

Nodes	**Wall time (s)**	**Real speed-up**	**Ideal speed-up**
7	3749	1.00	1.00
11	2182	1.57	1.72
19	1365	2.71	2.75
37	1033	5.29	3.63

The chosen configuration in table B.3 yielded a model throughput of approximately 28 to 30 simulated years per day and a model cost of about 998 CPU hours per simulated year. A

Table B.3: Distribution of tasks for each component in CESM1.2.2 on the XC40 (Daint)

	Tasks	Root	Threads
Atmosphere	768	0	1
Land	336	0	1
Sea Ice	320	336	1
Ocean	480	768	1
Coupler	64	656	1
Total CPU	1248		
Maximum task per node	36		

model throughput is a measure of speed and a model cost is a measure of efficiency of runs. Although, this configuration did not greatly exceed other configurations in terms of the model cost, it resulted in a slightly better speed-up of simulations and a significant reduction in the wall time (table B.2).

The speed of performance and the reduction of wall time were important factors that we considered for a successful completion of long CESM simulations within the project period. Hence, we concluded that the chosen configuration provided a good compromises between the model costs, scalability and throughput, with an estimated time to complete one 3600-year transient simulation of approximately 4 months. Additional technical details on porting CESM 1.2.2 on different machines and initiating simulations can be found in CESM user's guide (`https://www.cesm.ucar.edu/models/cesm1.2/cesm/doc/usersguide/book1.html`).

Acknowledgements

Many thanks to ...

... my supervisor Prof. Dr. Christoph Raible for his continuous scientific and financial support during my Ph.D. Many active discussions on scientific topics I've had with him during these four years helped me deepen my knowledge of the climate and extreme climate events and my professional development. I enjoyed working in his research group, where I was able to interact with very nice people having some active scientific discussions.

... Prof. Dr. Fidel González Rouco for the external review of my thesis. I very appreciate his kindness in considering my defense schedule.

... Prof. Dr. Thomas Stocker for evaluating my thesis and financial support during my Ph.D.

... Prof. Dr. Fortunat Joos for being the chair of my defense.

... Prof. Dr. Michael Sigl, Dr. Richard Blender, and Prof. Dr. Christian Franzke for the valuable scientific discussions and collaborations.

... Martina Messmer, Santos Gonzalez-Rojí, Angélique Hameau, Altug Ekici, Ashley Dinauer, and Patricio Velásquez for scientific discussions and help with my work, also for the fun times and frustrations we have shared during these years. Special thanks to Martina and Patricio for proofreading my long texts and their kindness in supporting me with some technical issues. Thanks to Angélique for helping me with CESM and settle down in the new office during the first year of my Ph.D.

... Rene Bleisch and Gunnar Jansen for the technical support dealing with CESM and the never-ending storage issue.

... Doris Rätz and Bettina Schüpbach for all administrative complications.

... Pinhsin Hu, Hyunju Jung, Manuel Wifling, and Juhyeong Han for lively work- and non-work-related discussions and the fun times we spent together. Special thanks to Pinhsin for proofreading my texts and providing critical feedback.

... All colleagues at KUP who have shared joy during these four years.

... My parents, Ms. Myung-Ja Hwang and Mr. Young-Woon Kim, and my siblings, Sulbi, Yami, and Dani, for their unconditional support and companionship during my whole life and education.

Publications

McConnell, J. R., Sigl, M., Plunkett, G., Burke, A., Kim, W. M., Raible, C. C., Wilson, A. I., Manning J. G., Ludlow F., Chellman N. J., Innes H. M., Yang Z., Larsen J. F., Schaefer J. R., Kipfstuhl S. , Mojtabavi S. , Wilhelms F., Opel T., Meyer H., and Steffensen J. P.: Extreme climate after massive eruption of Alaska's Okmok volcano in 43 BCE and effects on the late Roman Republic and Ptolemaic Kingdom. *Proceedings of the National Academy of Sciences*, Volume 117(27), pp. 15443-15449, `https://doi.org/10.1073/pnas.2002722117`, 2020.

Kim, W. M., and Raible, C. C.: Dynamics of the Mediterranean droughts from 850 to 2099 AD in the Community Earth System Model. *Climate of the Past*, Volume 17(2), pp. 887–911, `https://doi.org/10.5194/cp-17-887-2021`, 2021.

Kim, W. M., Blender, R., Sigl, M., Messmer, M., and Raible, C. C.: Statistical characteristics of extreme daily precipitation during 1501 BCE – 1849 CE in the Community Earth System Model. *Climate of the Past*, Volume 17/(2), pp. 2031 – 2053, `https://doi.org/10.5194/cp-17-2031-2021`.

Kim, W. M., Franzke L.E.C., and Raible, C. C.: Systematic Identification of the Drivers of Regional Hydroclimate Variability in Southern Hemispheric Wet Seasons using a Causal Discovery Method. `https://www.essoar.org/doi/abs/10.1002/essoar.10507659.1`, in preparation.

Erklärung

gemäss Art. 28 Abs. 2 RSL 05

Name/Vorname:	Woon Mi Kim
Matrikelnummer:	17-134-552
Studiengang:	Climate Sciences
	Bachelor ☐ Master ☐ Dissertation ☒
Titel der Arbeit:	Extreme Hydrological Events during the last 3500 years and their Changes in the Future
Leiter der Arbeit:	Prof. Dr. Christoph Raible Dr. Thomas Stocker

Ich erkläre hiermit, dass ich diese Arbeit selbständig verfasst und keine anderen als die angegebenen Quellen benutzt habe. Alle Stellen, die wörtlich oder sinngemäss aus Quellen entnommen wurden, habe ich als solche gekennzeichnet. Mir ist bekannt, dass andernfalls der Senat gemäss Artikel 36 Absatz 1 Buchstabe o des Gesetzes vom 5. September 1996 über die Universität zum Entzug des auf Grund dieser Arbeit verliehenen Titels berechtigt ist.
Ich gewähre hiermit Einsicht in diese Arbeit.

Bern, 29. Oktober 2021